FEB 23 1949

THE PHYSICAL REVIEW

VOLUME 75 *Second Series* NUMBER 4

FEBRUARY 15, 1949

Published for the

AMERICAN PHYSICAL SOCIETY

by the

AMERICAN INSTITUTE OF PHYSICS
Incorporated

LANCASTER, PA., AND NEW YORK, N. Y.

THE PHYSICAL REVIEW

A journal of experimental and theoretical physics established by E. L. Nichols in 1893

Published by the American Institute of Physics for the

AMERICAN PHYSICAL SOCIETY

Officers

President

F. W. Loomis
University of Illinois
Urbana, Illinois

Vice-President

I. I. Rabi
Columbia University
New York, New York

Secretary

K. K. Darrow
Bell Telephone Laboratories
Office:
Columbia University
New York 27, New York

Treasurer

G. B. Pegram
Columbia University
New York 27, New York

Local Secretary for the Pacific Coast

J. Kaplan
University of California at Los Angeles
Los Angeles, California

Managing Editor

John T. Tate
University of Minnesota
Minneapolis, Minnesota

BOARD OF EDITORS

Editor
John T. Tate

Assistant Editor
J. W. Buchta

Associate Editors

E. J. Konopinski — H. A. Bethe — S. A. Goudsmit
H. H. Nielsen — L. A. Ridenour — E. M. Purcell
E. C. Pollard — W. H. Zachariasen — V. F. Weisskopf

Manuscripts for publication should be submitted to John T. Tate, University of Minnesota, Minneapolis, Minnesota. The authors' institutions are requested to pay publication charge of $4 per page which, if honored, entitles them to 100 free reprints. Instructions will be sent with galley proofs.

Proof and all correspondence concerning papers in the process of publication should be addressed to the Publication Manager, American Institute of Physics, 57 East 55 Street, New York 22, New York.

Subscription Price

United States and Canada $15.00
Elsewhere $16.50

Back Numbers

Complete set: Series 2,[1] Vol. 1, 1913–Vol. 74, 1948—$648.00
Yearly rate: $20.00
Single copies: $2.00 each, prior to July, 1929;
$1.00 each, July, 1929–December, 1941;
$2.00 each, January, 1942–December, 1946.
Current issue: $1.00 each.

Subscriptions and orders for back numbers should be addressed to Prince and Lemon Streets, Lancaster, Pennsylvania, or to the American Institute of Physics, 57 East 55 Street, New York 22, New York.

Changes of address in the case of members of the American Physical Society should be addressed to the Treasurer; in the case of other subscribers to the Business Manager, American Institute of Physics.

[1] For Series 1 inquire of Physics Department, Cornell University, Ithaca, New York.

The Physical Review is published semi-monthly at Prince and Lemon Streets, Lancaster, Pennsylvania.

Entered as second-class matter March 6, 1947, at the Post Office at Lancaster, Pennsylvania, under the Act of March 3, 1879.

Acceptance for mailing at special rate of postage provided for in paragraph 4, section 538, P. L. & R., authorized January 27, 1948.

THE
PHYSICAL REVIEW

A journal of experimental and theoretical physics established by E. L. Nichols in 1893

SECOND SERIES, VOL. 75, NO. 4 FEBRUARY 15, 1949

Relative Cross Sections for Nuclear Reactions Induced by High Energy Neutrons in Light Elements

WILLIAM J. KNOX
Radiation Laboratory, Physics Department, University of California, Berkeley, California
(Received November 1, 1948)

Various light elements from carbon to sulfur were bombarded in the high energy (about 90 Mev) neutron beam of the 184-inch cyclotron and decay curves were taken on the resulting activities. Relative cross sections for certain reactions were obtained by analyzing the decay curves into component activities and comparing the yields with the activity induced in a carbon monitor bombarded in the same beam. Values for 16 reactions are given with a probable error of about ±10 percent, as well as upper limits for six other reactions. An apparent regularity among these data is pointed out; cross sections for reactions differing by the ejection of an alpha-particle or its components differ by a factor of about three.

I. INTRODUCTION

WHEN a nucleus is bombarded with very high energy neutrons, a large variety of nuclear reactions can occur, resulting in the formation of most, if not all, the nuclear species below the bombarded nucleus. The cross sections for these reactions are of interest because they may give some idea of the nature of the mechanisms of nuclear reactions at high energies. In the region of light elements the activities of suitable half-life for convenient measurement are few enough that relative cross sections for the reactions producing these activities can be obtained from simple analysis of decay curves taken on the bombarded substances. The present work is a survey of relative cross sections obtained in this manner by bombarding elements from carbon to sulfur in the high energy neutron beam of the 184-inch cyclotron.

II. EXPERIMENTAL

The high energy neutron beam was produced by the action of 190-Mev deuterons on a ½-in. beryllium target. This beam emerges through an aluminum window in the wall of the cyclotron tank with a flux at the window of the order of 10^6 to 10^7 neutrons per cm^2 per second as determined by the C^{11} activity induced in a carbon sample, using the $C^{12}(n, 2n)C^{11}$ cross section.[1] The neutrons in the center of the beam have an energy distribution with a peak at 90 Mev and width at half-maximum of about 27 Mev.[2,3]

Materials to be bombarded were placed against the window near the center of the neutron beam in the form of foils or samples of powder contained in small bottles and were bombarded for a prescribed length of time with the cyclotron operating at a constant level. The size of the samples was such that the neutron flux was uniform over the area of exposure. In each bombardment a sample of graphite or polystyrene foil was included as a monitor and was bom-

[1] E. M. McMillan and H. F. York, Phys. Rev. **73**, 262 (1948).
[2] A. C. Helmholz, E. M. McMillan and D. C. Sewell, Phys. Rev. **72**, 1003 (1947).
[3] R. Serber, Phys. Rev. **72**, 1008 (1947).

barded at the same time and in the same position with respect to the beam as the sample under consideration. Attenuation of the beam by the samples themselves or by their containers was negligible because of the high energy of the neutrons and the relatively small amount of absorbing or scattering material involved. At the end of a bombardment, a foil or thin uniformly spread sample of the powder was mounted and the decay of the activities produced was followed on a G-M counter. Each foil or sample was accurately weighed. The samples were spread over an area of from 5 to 14 square centimeters on cardboard or paper backing in order to minimize back-scattering and were counted at geometries of from 3 to 30 percent. The carbon monitor was of the same shape as the sample and usually was counted at the same geometry. In a few cases when the geometries were different, a correction was determined and applied between a sample and its monitor. Much of the counting data, particularly that on the longer lived activities, was taken on traffic counters which automatically record the register reading at specified intervals.

Standard coincidence and background corrections were applied to all counting rates. The data were then plotted, and the decay curves were resolved into their component activities which were identified by their approximate half-lives. In most cases the longest lived component was readily identifiable, and the half-life indicated by the data was used in the resolution. In some cases a small amount of unidentified long lived activity, a few counts per minute above background, was subtracted out before resolution of the major long lived component. After subtraction of the long lived component if the half-life of the next component was indicated clearly enough for its identification, the component was resolved from the curve using the accepted value in the literature for its half-life. The same procedure was followed for further components if possible. A more detailed description of the individual decay curves is given below.

Each separated component of the decay curve was extrapolated back to the time at the end of the bombardment and a correction was applied for the difference in absorption between the given radiation and the C^{11} radiation in the monitor due to the counter window, air, and half the thickness of the sample. These corrections were of the order of 0 to 12 percent with the exception of the F^{18} correction in the magnesium samples mentioned below. The relative cross sections were calculated according to the formula

$$\sigma_1/\sigma_2 = A_1 T_2 (1-e^{-\lambda_2 t})/A_2 T_1 (1-e^{-\lambda_1 t}),$$

where A is the corrected activity in counts per unit time of a given component extrapolated back to the end of bombardment, λ is the decay constant, t is the length of bombardment, and T is the number of target atoms in the bombarded sample determined from the weight of the sample.

Experimental details regarding source materials used and decay curves obtained from each element bombarded are summarized in the following paragraphs.

Carbon

Samples of pure pulverized graphite or polystyrene foils of empirical composition $(CH)_n$ were used as monitors for all other samples. In both of these materials a single activity was produced which decayed with a half-life of 20 to 21 minutes for as long as the decay could be followed. This identified the activity as the well known 20.5-minute C^{11}.

Nitrogen

Be_3N_2 was used as a source of nitrogen because it contains a high percentage of nitrogen and because Be gives rise to no interfering activities of appreciable intensity in the half-life range investigated. Decay curves on this material showed the 20.5-minute C^{11} and a small amount of long lived activity which was unidentified. This long lived activity was presumably due to a small amount of unknown impurity in the Be_3N_2. No trace of it was apparent in later bombardments of BeO. After subtraction of the C^{11} activity a 10-minute component appeared which was presumed to be N^{13}. An appreciable amount of 2-minute activity was also produced and was attributed to O^{15} coming from a few percent of oxide impurity which the Be_3N_2 was known to contain. From the amount of this 2-minute com-

ponent in the decay curve and from the cross section determined for the production of O^{15} from O^{16}, the amount of oxide impurity was determined to be about 5 percent, and the correction to the cross sections due to this impurity was calculated and found to be about 3 percent.

Oxygen

BeO was used as a source of oxygen for the same reasons given for Be_3N_2 above. The decay curves showed well defined 20.5-min C^{11} and 2.1-minute O^{15} components and an intermediate component of about 10 minutes which was again assigned to N^{13}.

Fluorine

LiF was used as the source material because lithium, like beryllium, gives no interfering activities. The longest lived activity produced decayed with a half-life of about 111 minutes and was assigned to F^{18}. In two cases the decay of the F^{18} was followed continuously through five to seven half-lives after disappearance of the shorter lived components, and the values for the half-life were observed to be 110.7 and 111.3 minutes with an estimated probable error of 2 minutes. The shorter lived components had half-lives of the order of 1 to 20 minutes as expected for F^{17}, C^{11}, N^{13}, and O^{15} but these could not be quantitatively separated from each other.

Sodium

Sodium was bombarded in the form of $Na_2C_2O_4$. No attempt was made to resolve activities of half life 20 minutes or less because they were produced in the carbon and oxygen of the sample as well as the sodium. A considerable amount of 900 minute activity (Na^{24}) was produced and after subtraction F^{18} was easily identifiable. Since it was considered highly unlikely that Na^{24} would be produced from Na^{23} in appreciable quantities by capture of high energy neutrons, a sodium bombardment was made in which lead scatterers were placed around the sample in the neutron beam in order to increase the number of relatively low energy neutrons passing through the sample. This resulted in approximately tripling the apparent cross section for production of Na^{24} while the F^{18} cross section remained constant. Hence, it was obvious that the production of Na^{24} was sensitive to neutrons below the 20-Mev detection threshold of the carbon monitor and that it could not be regarded as a high energy reaction.

Magnesium

Thin metal discs of magnesium known to contain about 3 percent aluminum impurity were bombarded. Na^{24} and F^{18} were clearly resolvable and shorter lived activities were observed but could not be quantitatively separated. The magnesium disks were relatively thick to the soft F^{18} radiation, and a high absorption correction of from 30 to 40 percent was made to the corresponding cross section. Also a correction of a few percent as a result of the aluminum impurity was calculated using the cross sections determined for the production of Na^{24} and F^{18} in aluminum. The cross section for producing Na^{24} is to be considered as an upper limit because of the relatively low threshold for the reaction $Mg^{24}(n, p)Na^{24}$, combined with the possibility that the beam may contain an appreciable number of neutrons below the carbon threshold.

Aluminum

Thin aluminum foils of high purity were used for the aluminum cross sections. Na^{24} and F^{18} were again resolvable, and in addition a strong component of about 10 minutes was apparent which was attributed to Mg^{27}. It was assumed unlikely that this 10-minute component was due to any appreciable extent to the 10-minute N^{13} since the production of short lived activities in magnesium was so small. The cross sections given for the reactions producing Mg^{27} and Na^{24} from aluminum are only to be regarded as upper limits since the threshold energies for these reactions are low.

Silicon

Powdered high purity silicon was used as a target. Na^{24} and F^{18} were easily identified and subtracted out leaving a component of about 10 minutes which again was assigned to Mg^{27}. Also a considerable quantity of 2- to 2.5-minute activity appeared which was attributed to Al^{28}. It was assumed unlikely that this activity was

due to 2.1-minute O^{15} since O^{15} did not show up appreciably in Al and Mg bombardments. The cross section for the Al^{28} reaction is considered only as an upper limit because of its low threshold and because of the difficulty of resolving it accurately as the fourth component from the decay curve.

Phosphorus

The target material was amorphous red phosphorus. A few counts per minute of long lived unidentified activity presumably a result of impurity were subtracted out leaving a well defined 900-minute Na^{24} component. A very strong component of about 170 minutes was observed and was assumed to be Si^{31}. Some deviation from the 170-minute line toward shorter half-life occurred near its beginning and probably was due to a small amount of F^{18}. The Si^{31} reaction also has a low threshold and should be considered as an upper limit, since it was observed to be sensitive to scattering material in the beam. Unresolvable short lived components were also present in this decay curve.

Sulfur

High purity flowers of sulfur was used as the target material. The decay curves showed a small amount of activity of approximately 14-day half-life attributed to P^{32}, a 900-minute Na^{24} component, and a strong 170-minute Si^{31} component. The Si^{31} again showed a deviation toward shorter half-life near its beginning probably as a result of F^{18}, but the possible error from this source was estimated to be less than 10 percent. The cross section for the reaction producing P^{32} is again an upper limit because of its low threshold and because it was observed to be sensitive to scattering material in the beam.

TABLE I. Relative cross sections for reactions induced by 90-Mev neutrons.

		Product isotope								
		C^{11}	N^{13}	O^{15}	F^{18}	Na^{24}	Mg^{27}	Al^{28}	Si^{31}	P^{32}
Target element	C	1.00								
	N	0.40	0.32							
	O	0.31	0.12	0.90						
	F	—*	—	—	1.70					
	Na	—	—	—	0.75					
	Mg	—	—	—	0.75	(1.61)**				
	Al	—	—	—	0.21	(1.50)	(0.6)			
	Si	—	—	—	0.17	0.69	0.29	(2)		
	P	—	—	—	—	0.45	—	—	(0.8)	
	S	—	—	—	—	.0.21	—	—	0.30	(2)

* Blank spaces do not mean that the corresponding isotopes are not produced.
** Values in parentheses are upper limits only.

III. RESULTS AND DISCUSSION

Table I gives the values obtained for the cross sections of the various reactions observed,

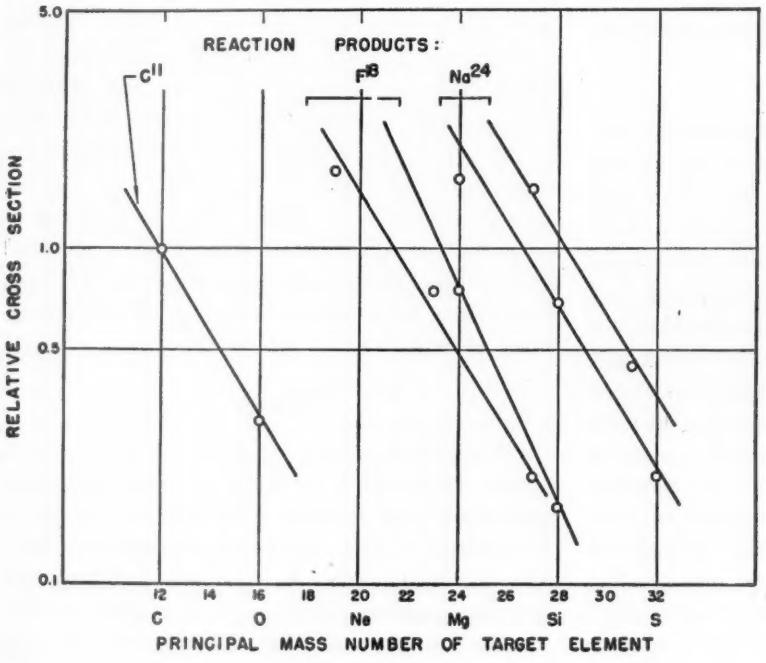

FIG. 1. Relative cross sections for some of the observed reactions, plotted on a logarithmic scale. Lines join cases which differ by the ejection of two protons and two neutrons; they are all drawn with the same slope except for one of the F^{18} lines. See the text for further discussions.

which are specified by giving the target element and the radioactive element produced in a bombardment. Each value is the average of several determinations, and the errors are estimated to be about ±10 percent. All values are given relative to the cross section for the $C^{12}(n, 2n)C^{11}$ reaction which has arbitrarily been taken as 1.00. The absolute value for this cross section has been separately determined as 0.022±0.004 barn.[1] The six values in parentheses should be considered as upper limits because of the low threshold energies for these reactions and because of the known presence of low energy reactions in the beam (see discussion above). The isotopic constitution of magnesium (79 percent Mg^{24}, 10 percent Mg^{25}, 11 percent Mg^{26}) is such that its cross sections are not readily assignable to a single type of reaction. Silicon (92 percent Si^{28}) and sulfur (95 percent S^{32}) are close enough to pure isotopes that the true cross sections for these isotopes probably lie within the range of probable errors given for the observed values. No correction has been made to the values given in the table for these isotopic mixtures. The remaining elements bombarded are essentially pure isotopes.

A decrease in cross section is apparent with increasing complexity of the reaction necessary to produce a given product element from various target elements, which is to be expected in general. More significantly, there seems to be a regularity among the relations between reactions which differ by the ejection of two neutrons and two protons (or an alpha-particle). Consider first the formation of O^{15} and C^{11} from oxygen; the ratio of cross sections is 2.9. The comparison can also be made in cases where the same product is made from different elements, as in the formation of C^{11} from carbon and oxygen, where the ratio is 3.2. Further relations of the latter sort occur in the formation of F^{18} and Na^{24}. For F^{18}, the cross section ratios are: F/Na=2.3, Na/Al=3.6, Mg/Si=4.4, and for Na^{24} they are Mg/Si=2.3, Si/S=3.3, Al/P=3.3. The mean of all these eight ratios is 3.2. (Note that two of the Na^{24} reactions have low thresholds, one of them being an (n, p) reaction. The agreement with the mean ratio may be fortuitous in these cases.) Figure 1 shows graphically some of the relations described above.

The ratio found here agrees with the value of 3.2 observed in a similar series of cross sections for the production of N^{17} from various elements by deuteron bombardment,[4] and roughly, with the value of 2.8 found in a comparison of the C^{11} yields from carbon and oxygen under proton bombardment.[5] This regularity is consistent with a simple theory involving constant relative emission probabilities for alpha-particles, protons and neutrons, and taking into account various possible paths between a given target and a given nucleus. However, a purely statistical model such as this does not appear competent to explain all features of the results, such as the rather puzzling lack of regularity among the four observed $(n, 2n)$ reactions. It is thus clear that a complete theoretical analysis must take account of individual nuclear properties, although the statistical model seems to give the correct trend in at least some cases.

The author wishes to express his appreciation to Professor E. M. McMillan for suggesting this problem. The work was performed under the auspices of the Atomic Energy Commission.

---

[4] W. W. Chupp and E. M. McMillan, Phys. Rev. **74**, 1217 (1948).

[5] E. M. McMillan and R. D. Miller, Phys. Rev. **73**, 80 (1948).

Note added in proof: Recently Professor McMillan has positively identified the pure gamma-emitter Be^{7} in carbon given a long bombardment with 190 Mev deuterons. Assuming that it gives one gamma-ray per ten disintegrations, the cross section for its formation was found to be ½ that for the formation of C^{11} in the same sample.

Thresholds for Several Photo-Nuclear Reactions

J. McElhinney,* A. O. Hanson, R. A. Becker, R. B. Duffield, and B. C. Diven
Physics Research Laboratory, University of Illinois, Champaign, Illinois

(Received November 1, 1948)

The x-rays from a 22-Mev betatron were used to observe the thresholds for 23 photo-nuclear reactions which are listed in Table I. The observed thresholds are compared with the mass data for the lighter elements and with those obtained from an empirical treatment of the masses for the heavier elements.

The excitation curves were extended up to 21 Mev in a few cases. These curves were very much alike except that for the Ta(γ, n) reaction. This curve showed an abrupt decrease in slope at about 18 Mev which indicates a much reduced cross section for photons above this energy.

INTRODUCTION

THE use of the 22-Mev betatron for the production of x-rays with an accurately controlled maximum energy has been described by Baldwin and Koch. Data on the excitation functions near thresholds were presented for photo-neutron reactions in N, C, O, Fe, Cu, Zn, Mo, and Ag.[1]

The present report describes additional work with a number of other elements. The preliminary results have already been reported briefly.[2] The experimental arrangement was essentially the same as that of the earlier work but the development of the betatron during the past few years has made the x-ray intensity available about 20 times greater. It was, therefore, profitable to repeat some of the previous work, in particular that on the light elements which serve to establish the energy scale.

Determination of X-Ray Energy

The energy of the electrons as they strike the x-ray target is controlled as in the previous work by the voltage across a condenser which is placed in series with a large resistance across one of the betatron coils. The voltage across this condenser is proportional to the integral of the applied voltage and to the magnetic field at the orbit. Since the radius of the target is fixed, the momentum of the electrons is proportional to the voltage across the condenser. The kinetic energy of the electron can be determined by adjusting the bias on a trigger circuit so that the orbit expander is fired at a predetermined value of this condenser voltage. The kinetic energy of the electrons or maximum x-ray energy can then be expressed in terms of the integrator bias by means of the relation,

$$T=[K(I-I_0)/\beta]-0.51 \text{ Mev}, \qquad (1)$$

where K is an empirically determined constant, I the integrator bias voltage; I_0 the zero error caused by contact potentials and other biases in the trigger circuit. β is the ratio of the velocity of the electron to that of light and can be taken as unity for all but the lowest energies used in this work.

The determination of the electron and x-ray energies by the simple considerations mentioned above is not quite accurate since the energy is changed by the additional flux introduced by the expander. If the electron orbit during acceleration is fixed, this additional pulse should be strictly proportional to the initial magnetic field at the time of the expansion and would not introduce any non-linear corrections in the energy scale. Estimates of the non-linear corrections resulting from this effect are of the order of 0.02 Mev and were neglected since these corrections are small compared to the uncertainties in determining actual threshold energies.

Another source of non-linearity in the energy scale based on the integrator bias may be introduced by a constant time delay between the firing of the trigger circuit and the firing of the expander circuit. These time delays were accurately measured and were taken into account

* Now at Los Alamos Scientific Laboratory, Los Alamos, New Mexico.

[1] G. C. Baldwin and H. W. Koch, Phys. Rev. **67**, 1 (1945); Phys. Rev. **63**, 462A (1943).

[2] R. A. Becker, A. O. Hanson, and B. C. Diven, Phys. Rev. **71**, 466A (1947); J. McElhinney, A. O. Hanson and R. B. Duffield, Bull. Am. Phys. Soc. **23**, 4 (1948).

in the estimated errors made in the process of expansion. There is, however, a similar error which could be introduced by a slight shift in phase between the effective integrator signal and the actual magnetic field in the betatron. Any significant error of this type can be detected by a change in the integrator bias voltage corresponding to a fixed nuclear threshold, such as that of copper, upon changing the amplitude of the exciting current in the main coils of the magnet. Actual tests for this type of error were not conclusive. Individual runs indicated changes in the bias settings for copper of from 0 to 0.3 percent.

Since the non-linear corrections were small and somewhat uncertain, it was thought that the most reliable energy scale could be obtained by using known fixed points to establish a linear relation between the integrator bias and the maximum x-ray energy. The fixed points examined for this purpose were the thresholds of beryllium and deuterium at low energies and that of carbon and nitrogen at the higher energies. The thresholds of beryllium and carbon could be quite accurately defined and served to establish the energy scale used in this work. This scale places the threshold for Cu^{63} at 10.9 ± 0.2 Mev which is the same as that used by Baldwin and Koch. A recent magnetic field measurement gave a value of 11.0 ± 0.2 Mev. A direct comparison of this copper threshold with that of N^{14} indicated a value of about 10.76 ± 0.2 Mev if the nitrogen threshold is taken as 10.51 Mev. The scale chosen seems to be a fair compromise between the various data and should serve until more reliable absolute values of some of these thresholds become available.

Experimental Arrangements

Since the method of observation of the excitation curves for various reactions depends on the nature of the induced activity, it is necessary to describe the results in each case individually. The data presented here were not all obtained at the same time, but were grouped in the following way.

1. Short period activities in Li, Mg, Al, Si, S, and Ca were detected by irradiating cylindrical samples at the monitor position shown in Fig. 1 and allowing them to drop over a Geiger counter at the end of a short irradiation. The scaled counts were recorded as a function of time by means of an Esterline Angus recording milliammeter. The analysis of the record provided a reliable measure of the amount of the short period activity present. This will be referred to as the drop method. These data do not give very sensitive measurements of the thresholds for the activities because of the low yields and the short counting times involved.

2. Long period activities and complete excitation curves for Mg, Cu, and Ta involved irradiations of the order of one hour. The induced radioactivity was again recorded on the recording milliammeters. With two recorders equipped with side pens it was possible to record the output of six counters simultaneously. The data for the individual activities were then taken from these records.

3. The use of rhodium neutron detectors to determine thresholds by the observation of neutrons from the reaction was first used in the case of bismuth, which gave no measurable radioactivity but was found to have a well-defined threshold for the emission of neutrons. This method was later used in the observation of the thresholds of beryllium, deuterium, and iodine.

4. The last set of measurements was made to check the energy scale against the thresholds of the light elements and included additional data on P, K, Fe, Br, Sb, and I.

In the first three sets of data all thresholds were determined only in terms of the Cu^{63}

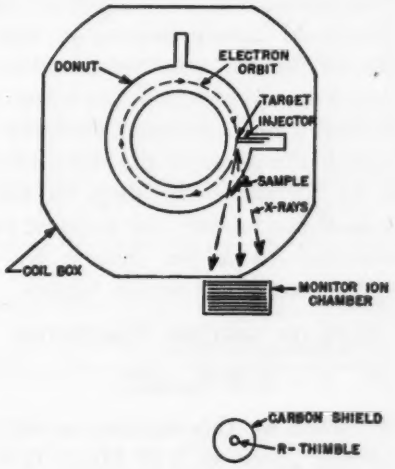

FIG. 1. Sample and monitor arrangements.

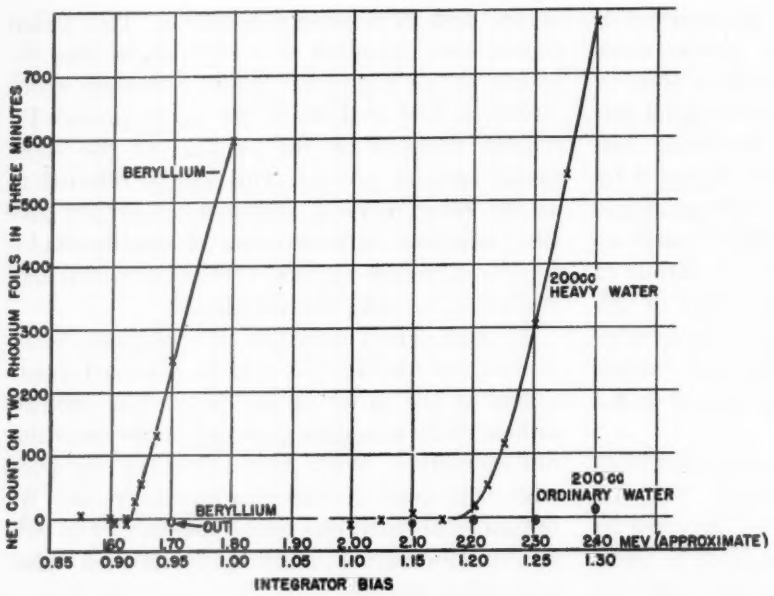

FIG. 2. Thresholds of deuterium and beryllium observed with rhodium neutron detector.

threshold as 10.9 Mev, with electrical checks on the linearity of the scale and the effective zero of the integrator bias scale. Although different trigger circuits were used at various times, it is not likely that these introduced inconsistencies which are comparable to the errors involved in estimating actual thresholds from the observed activities.

The x-ray intensity was occasionally measured by the use of a Victoreen roentgen meter. The *R*-thimble was surrounded by two inches of air-equivalent material such as carbon or hard rubber and was placed at the center of the x-ray beam at a distance of one meter from the target. The x-ray intensity measured in this manner was about 50*R* per minute at 20 Mev. In all threshold measurements it was most convenient to use the monitor chamber which was mounted on the betatron and whose output was read from a microammeter mounted on the control panel. For some of the data where it is desirable to normalize the data to the x-ray intensity in *R* per minute, the monitor readings were converted to *R* per minute by experimentally determined conversion factors.

DATA ON SPECIFIC REACTIONS

1. $H^2(\gamma, n)H^1$

The threshold for this reaction is well known and is usually given as 2.19 Mev.[3] It was observed in this case by placing 200 grams of heavy water in a bottle imbedded in paraffin near the x-ray target in the betatron. A rhodium foil was placed along one side of the heavy water container and covered with a slab of paraffin about $\frac{3}{4}$-inch thick. The samples were irradiated with x-rays at various integrator bias settings for two minutes. The rhodium foil was rolled up inside a cylinder, placed over a cylindrical Geiger counter, and the net count in the interval from $\frac{1}{2}$ to $3\frac{1}{2}$ minutes after the end of the irradiation was observed. The data are shown in Fig. 2. It is clear that the sensitivity of this method is sufficient to establish a convenient and accurate calibration point at the low energy end of the energy scale.

2. $Be^9(\gamma, n)Be^8$

This reaction has a threshold which is usually given as 1.63[3] Mev and serves the same purpose as deuterium as a check on the low end of the energy scale. The method was identical with that used for deuterium except that the heavy water was replaced with an equal mass of beryllium. The data are shown in the same figure. The threshold seems somewhat better defined than that of deuterium.

3. $Li^7(\gamma, p)He^6$ 0.8-second β^-

A cylinder of metallic lithium was irradiated at about the monitor position, and the 0.8-

[3] W. E. Stephens, Rev. Mod. Phys. **19**, 19 (1947).

second activity of He^6 was observed by means of a Geiger counter. The preliminary value of the threshold reported was obtained by placing the Geiger counter surrounded by lithium directly in the x-ray beam. The output of the counter was sent through a gating circuit so that the counts could be observed during the $\frac{3}{4}$-cycle following the x-ray burst. The results of these runs indicated a threshold of about 9.5 Mev for the short period activity. Although the sensitivity of this method is greater because of the increased counting time, it was felt that the backgrounds were less reliable than those for data taken with the counter out of the x-ray beam. The data taken by dropping the sample over a counter set up below the beam were taken a number of times, and one set of data is shown in Fig. 5. The activity seems to be definitely above background at 10.6 Mev, and the extrapolated threshold for this activity seems to lie at about 10.3 Mev. The mass data and disintegration energies give a value 10.1 Mev for the threshold,[4] but since this reaction involves the emission of protons, it is not likely that the reaction would be observed under the conditions of this experiment at energies much less than 0.5 Mev above the true threshold.

Tests were made to show that no error was made as a result of possible neutron capture in Li^7 forming the 0.88 second Li^8 activity. It is still possible that some of the observed activity may be produced by a secondary reaction in the lithium, such as $Li^6(\gamma, n)Li^5$ and $Li^6(n, p)He^6$, which would be energetically possible at about 8 Mev.

4. $C^{12}(\gamma, n)C^{11}$ 20.5-minute β^+

The threshold for this reaction was poorly defined in the earlier work[1] because of the low yield.

The substance used in the present data was thiophene-free benzene. Although this was the best of the substances tried, it still showed an appreciable background activity which is presumably due to the presence of small amounts of nitrogen or oxygen. About 50 cc of benzene was placed in a glass bottle and irradiated at various integrator settings for a period of 20 minutes. The irradiated benzene was poured into a container surrounding a Geiger counter. The data are shown in Fig. 3. The threshold can be seen to be no higher than 18.7 Mev on the scale which fixes the Cu^{63} threshold at 10.9 Mev. The threshold calculated from mass data and the disintegration energy of C^{11} is 18.7±0.1 Mev.

5. $N^{14}(\gamma, n)N^{13}$ 10-minute β^+

The accuracy of the original data on this threshold was also limited by the low x-ray intensity available. It was felt that better data on this reaction might serve as an additional check on the energy scale at about the threshold of copper.

Dicyandiamide powder ($C_2H_4N_4$) was placed in a container as near to the x-ray target as possible and irradiated for periods of 30 minutes. At the end of the irradiation the powder was transferred to three cylindrical containers which fit snugly over the three Geiger counters and counted for a period of 20 minutes. A copper cylinder mounted on the monitor chamber was irradiated simultaneously, so as to obtain an accurate comparison of the two thresholds.

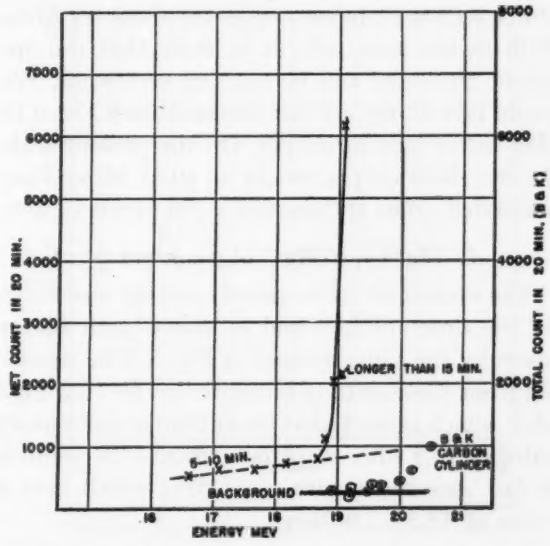

FIG. 3. Threshold of carbon as determined by activity in thiophene-free benzene. The data of Baldwin and Koch are shown on the same scale to indicate the increased activity obtained in the present experiments.

[4] The masses used in this work unless otherwise noted are those published in: H. A. Bethe, *Elementary Nuclear Theory* (John Wiley and Sons, Inc., New York, 1947).
A compilation of masses given by Mattauch will also be referred to. These are taken from J. Mattauch and S. Fluegge, *Nuclear Physics Tables and an Introduction to Nuclear Physics* (Interscience Publishers, Inc., New York, 1946).

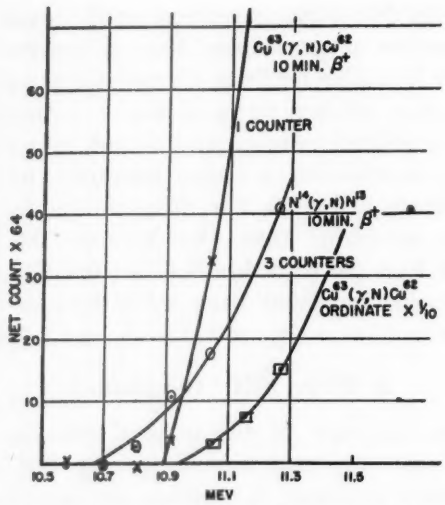

FIG. 4. Comparison of the thresholds for (γ, n) reactions in N^{14} and Cu^{63}.

The data are shown in Fig. 4. The ordinate for the nitrogen curve represents the net count from three counters in the interval of from 4 to 28 minutes after the irradiation. That for the copper curve represents the difference in the counts in the intervals from 5 to 17 and 17 to 29 minutes after the irradiation. The difference method of analyzing the copper data is desirable to eliminate possible confusion with the 12.8-hour activity which has a threshold of about 10.2 Mev.

The nitrogen activity is still too weak to define the threshold with high accuracy, but it can be seen to lie below copper by about 0.2 Mev. With higher sensitivity it is likely that the apparent threshold will be reduced somewhat. We would therefore place this threshold as 0.25 ± 0.10 Mev below that of copper. On the present scale the threshold energy would be 10.65 Mev. That calculated from the masses is 10.51 ± 0.1 Mev.

6. $Mg^{24}(\gamma, n)Mg^{23}$ 11.6-second β^+

The excitation curve near threshold was taken by the drop method and is shown with others taken by the same method in Fig. 5. The threshold from these data is estimated to be 16.2 ± 0.3 Mev, which is somewhat lower than a preliminary value of 16.5 Mev reported earlier. This value is in fair agreement with mass data which give a value of 15.5 ± 1.0 Mev.

7. $Mg^{25}(\gamma, p)Na^{24}$ 14.8-hour β^-

The experimentally determined threshold for this reaction is not expected to be well defined since the reaction will not occur with any probability until the energy of the protons is sufficient to penetrate a barrier of about three Mev. It was of interest, however, to compare the shape of the excitation function of this reaction with that of a (γ, n) reaction in the same element. A complete excitation curve was taken simultaneously with that of the 11.6-sec. (γ, n) activity. These data are shown in Fig. 6, and it can be seen that there is no marked difference in the shapes of the excitation functions except for the shift in the observed thresholds. The excitation curve near the threshold is shown in more detail in the inset of the same figure. The activity becomes observable at about 13 Mev. The proton binding energy calculated from the masses is 10.9 ± 1.0 Mev. When the barrier penetration is taken into account, the agreement of the observed value with the calculated value is satisfactory.

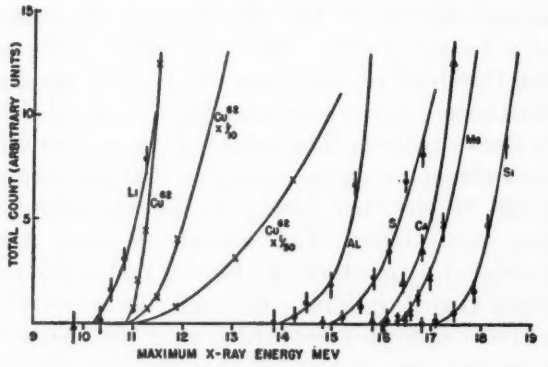

FIG. 5. Threshold for short period activities obtained by the drop method. The activation curve for Cu^{62} is sketched to various scales for comparison.

Since the 14.8-hour activity could be produced by an (n, p) reaction in Mg^{24}, it was of interest to determine whether this process contributed to the observed activity. Since the neutrons are distributed more isotropically than the x-rays, the Na^{24} activity induced as a function of the position of the sample would be different in two cases. Strips of copper and magnesium were placed across the center of the x-ray beam and irradiated. The counting rates in these two materials are shown in Fig. 7.

The angular distribution measured in this way was also useful in estimating the effective thickness of the x-ray target by comparing it with

the angular distributions calculated by Schiff.[5] One may note that the width of the x-ray beam as measured by the higher threshold reaction is somewhat less than that measured with the Cu detector.

A more sensitive way of estimating the magnitude of a possible (n, p) reaction was to irradiate a sample of phosphorus at the same position. The 170-minute Si^{31} activity indicated an excitation curve of the form shown in the inset of Fig. 6. Since the threshold for the $Mg^{24}(n, p)Na^{24}$ reaction is much higher than that for P^{31}, the strength of the (n, p) induced activity in magnesium would be several times lower than that indicated in the figure.

8. $Mg^{26}(\gamma, p)Na^{25}$ 62-second β^-

A complete excitation curve for this activity was taken simultaneously with that for Fe^{53} and is shown in Fig. 8. It can be seen to be almost identical in shape to that for Fe. The activity was observed down to values of about 15.5 Mev which would indicate that the threshold may be about 14 Mev. This is to be compared with 15.0 ± 1.6 Mev as calculated from mass data and disintegration energies and with 14.0 Mev using the theoretically estimated mass of Na^{25}.

A chemical separation was made which indicated that the 62-second activity was due to sodium and confirmed the earlier assignment of this isotope.[6]

An absorption measurement indicated a beta-energy of 3.4 Mev. The absorption data failed to show the two groups of 2.7 and 3.7 Mev reported by Bleuler and Zunti.[7]

9. $Al^{27}(\gamma, n)Al^{26}$ 7-second β^+

The excitation curve for this reaction was obtained by the drop method and is shown in Fig. 5. The threshold can be estimated to be about 14.0 ± 0.4 Mev. This value is somewhat lower than the preliminary value of 14.4 Mev[2], but is considerably greater than the value of 11.1 ± 1.0 which is based on values given for the masses.

10. $Si^{28}(\gamma, n)Si^{27}$ 5-second β^+

Metallic silicon crystals were held together by a small amount of paraffin to form a thick

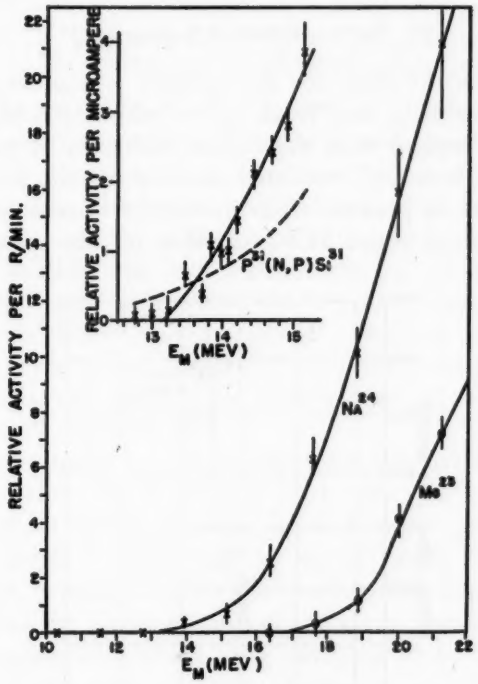

FIG. 6. Excitation curve for $Mg^{26}(\gamma, p)Na^{24}$.

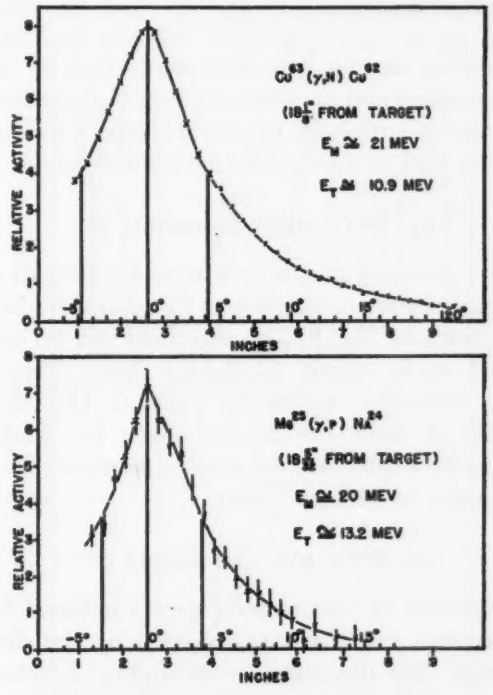

FIG. 7. Angular distribution of x-ray intensity as measured by copper and magnesium detectors.

[5] L. I. Schiff, Phys. Rev. 70, 87 (1946).

[6] Huber, Lienhard, Scherrer, and Waffler, Helv. Phys. Acta. 16, 33 (1943); 16, 431 (1943); 17, 139 (1944).

[7] E. Bleuler and W. Zunti, Helv. Phys. Acta. 20, 199 (1947).

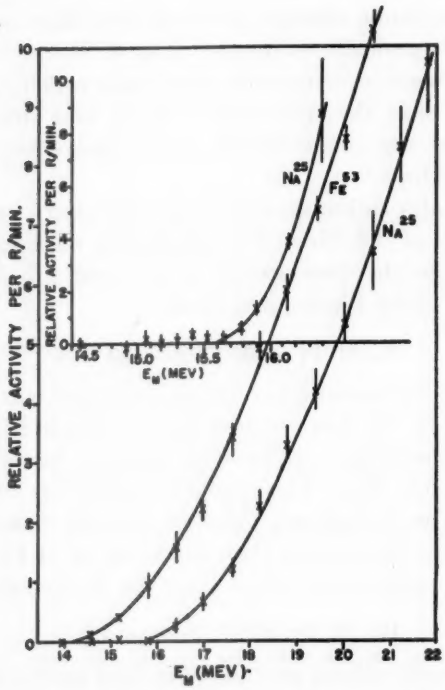

FIG. 8. A comparison of the activation curves for Na^{25} and Fe^{53}. The Na^{25} activity near threshold is shown in more detail in the inset.

cylindrical sample. The data were taken by the drop method and are shown in Fig. 5. These data indicate a threshold of about 16.8±0.4 Mev. Masses lead to a value of 16.0±1.0 Mev.

11. $P^{31}(\gamma, n)P^{30}$ 2.5-minute β^+

Red phosphorus was irradiated for periods of 4 minutes and counted for 10 minutes. The data are shown in Fig. 9. The threshold can be estimated to be about 12.35±0.2 Mev. This is again somewhat above the value of 11.1 Mev calculated from the masses given by Bethe. Mattauch's tabulation of masses, however, leads to a value of 12.2±0.5 Mev.

12. $S^{32}(\gamma, n)S^{31}$ 3.2-second β^+

Cylinders of cast sulphur were irradiated for 10 seconds and the data recorded by the drop method. The data are shown in Fig. 5, which indicates a threshold somewhat below 15.0 Mev. The value of the threshold is perhaps better stated as 14.8±0.4 Mev. The masses given by Bethe and by Mattauch again differ appreciably, leading to values of 16.7±0.5 and 14.9±0.5 Mev, respectively. The half-life was found to be 2.6 ±0.2 seconds, which is considerably lower than that usually given.

13. $K^{39}(\gamma, n)K^{38}$ 7.5-minute β^+

Potassium carbonate (K_2CO_3) powder was irradiated for 10-minute intervals and counted for periods of 18 minutes. The natural radioactivity of K^{40} gave rise to a rather large background. The threshold, as shown in Fig. 10, seemed fairly well defined as about 13.2±0.2 Mev. Masses are known very inaccurately. Those given lead to a value of 12.7±1.5 Mev.

14. $Ca^{40}(\gamma, n)Ca^{39}$ 1-second β^+

Samples of calcium fluoride (CaF_2) crystals were made up into a cylinder by a small amount of paraffin binder and irradiated for periods of two seconds. The data were obtained by the drop method. The short period made it difficult to obtain good accuracy, but the records showed definite indications of the short period at energies above 16.3 Mev. The resulting threshold is perhaps best stated as 15.9±0.4 Mev. The masses are again only approximately known. These lead to a value of 13.7±1.5 Mev.

15. $Fe^{54}(\gamma, n)Fe^{53}$ 8.9-minute β^+

The threshold for this activity was observed by Baldwin and Koch to be below 14.2 Mev. The present data were taken with pure electrolytic iron foil irradiated as close to the x-ray target as possible. The threshold was estimated to lie at about 13.8±0.2 Mev on the present

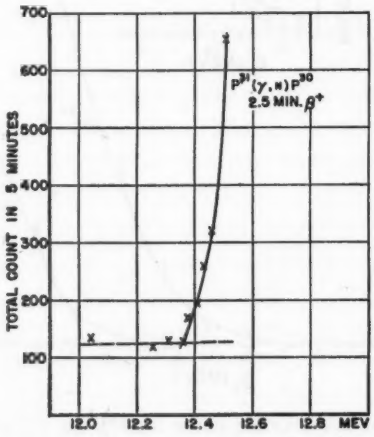

FIG. 9. Threshold curve for the $P^{31}(\gamma,n)P^{30}$ reaction.

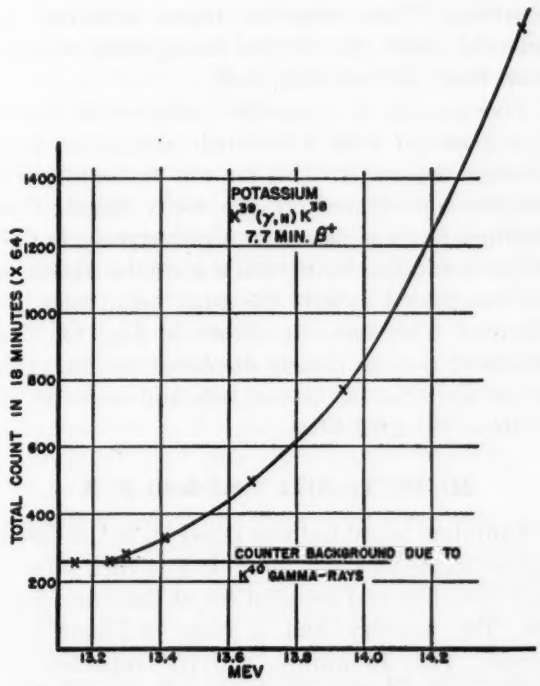

FIG. 10. Threshold curve for $K^{39}(\gamma, n)K^{38}$ reaction.

energy scale. A complete excitation curve for this activity taken simultaneously with that of $Mg^{26}(\gamma, p)Na^{25}$ is shown in Fig. 8.

16. $Cu^{65}(\gamma, n)Cu^{64}$ 12.8-hour $\beta^+\beta^-$

Copper samples $3\times2\times0.005$ inches were folded up, covered with cadmium and taped on to the donut so as to intercept the maximum x-ray flux. These were wrapped around a Geiger counter, and the activity was followed for about one half-life. The data are shown in Fig. 11. The shaded area represents the average neutron-induced activity in the sample, which to some extent limits the accuracy. The threshold for this activity can perhaps be best represented by a value of 10.2 ± 0.2 Mev.

A complete excitation curve for this activity was taken simultaneously with that for Cu^{63} which is shown in the same figure. The two curves are similar except for the energy shift. The errors attached to the Cu^{64} points are largely due to the interpretation of the x-ray intensity measurements, which were complicated by the close irradiation geometry. Since the activities were observed in the same copper sample the errors in the relative activities are much less.

17. $Cu^{63}(\gamma, n)Cu^{62}$ 10-minute β^+

Copper cylinders with $\frac{1}{16}$-inch walls, 4 inches long, and $\frac{3}{4}$ inch in diameter were placed in a cadmium holder on the monitor chamber and irradiated for periods of about five minutes and counted for about five minutes. This threshold was observed about thirty times during this work. The integrator bias setting for this threshold was found to be reproducible to better than 0.2 percent and was used as a calibration point on the energy scale at 10.9 Mev.

18. $Br^{79}(\gamma, n)Br^{78}$ 6.4-minute β^+

Samples of NaBr powder were irradiated for 10 minutes, transferred to a 1×2-inch lead tray (T), and placed between the poles of a small magnetron magnet as shown in Fig. 12. The simple magnetic separation made it possible to detect this positron activity above the large background resulting from the 18-minute beta-activity formed from Br^{81}. The counting rate in this case is only about 1 percent of that for the 18-minute activity but the threshold is still fairly well defined. It is definitely below 10.8

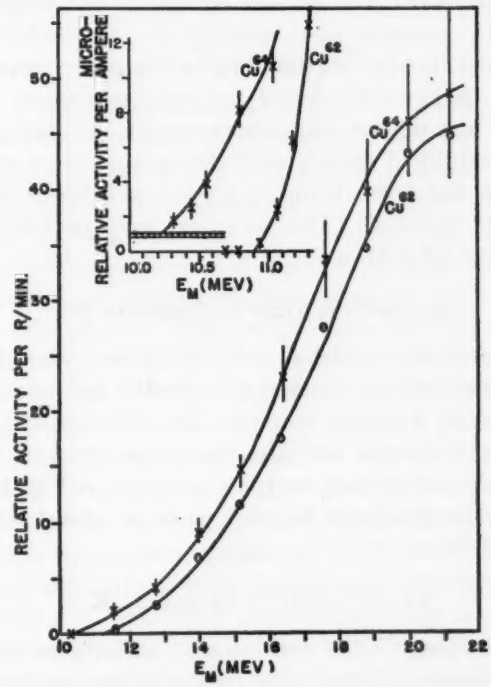

FIG. 11. Excitation curves for Cu^{64} and Cu^{62} taken simultaneously. The curves near threshold are shown in more detail in the inset.

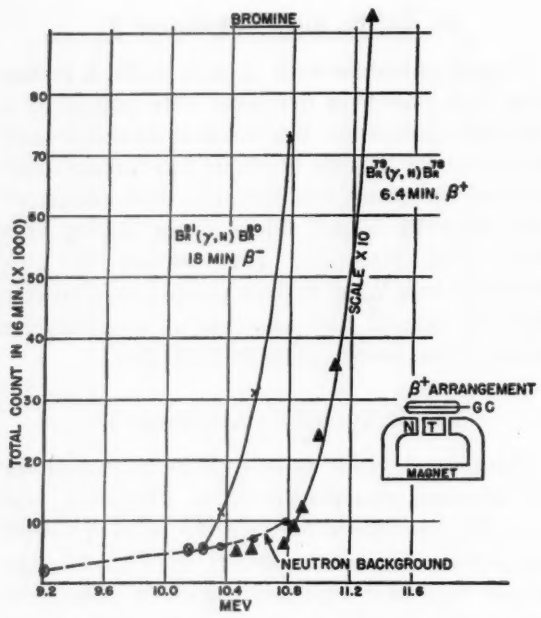

FIG. 12. Thresholds for induced activities in bromine.

Mev and is perhaps better expressed as 10.7 ±0.2 Mev.

19. $Br^{81}(\gamma, n)Br^{80}$ 18-minute β^-

The NaBr powder was irradiated for periods of 15 minutes and counted in a cylindrical powder holder surrounding a Geiger counter. The background caused by neutron capture in Br^{79} was determined simultaneously by placing an additional sample of NaBr outside the x-ray beam and normalizing at a point well below the (γ, n) threshold. The threshold may be stated as 10.2±0.2 Mev.

20. $Sb^{121}(\gamma, n)Sb^{120}$ 17-minute β^+

Antimony powder was irradiated for 15 minutes and transferred to a powder holder surrounding a Geiger counter. The activity had a clean 17-minute half-life. The total count in 20 minutes at various energies is shown in Fig. 13. The threshold can be seen to lie at about 9.25 ±0.2 Mev.

21. $I^{127}(\gamma, n)I^{126}$ 13-day β^- K

The long life of the induced activity in this case makes it impractical to obtain the threshold by observing the induced activity, and an attempt was made to observe the accompanying neutrons. These neutrons must, however, be detected above the normal background of neutrons from the betatron itself.

Five pounds of crystalline iodine were placed in a glass jar with a one-inch aluminum tube through the center. This jar was surrounded by paraffin and placed in the x-ray beam. One rhodium foil was placed in a polystyrene holder inside the iodine bottle while a similar rhodium foil was placed outside the x-ray beam near the "donut." The data are shown in Fig. 14. The threshold is most clearly displayed by the ratio of the activities in the two foils and seems to lie at about 9.3±0.2 Mev.

22. $Ta^{181}(\gamma, n)Ta^{180}$ 8.2-hour β^- K

Tantalum metal foil was taped on to the donut and irradiated for one hour. It was then formed into cylinders and counted for at least one half-life. The activity had a clean 8.2-hour half period. The 14-minute activity reported by Bothe and Gentner was not observed.[8] This activity may have been that of the 16-minute isomer of Ta^{182} reported by Seren, Friedlander, and Turkel,[9] which was too weak to be observable under the conditions of this experiment.

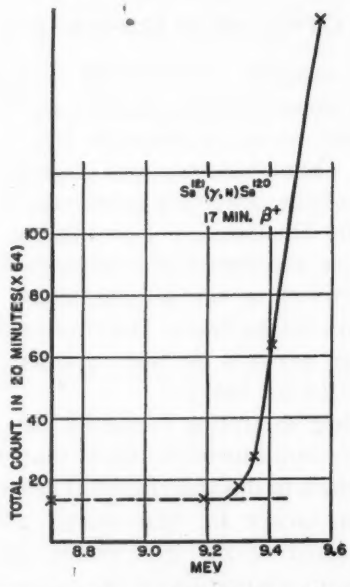

FIG. 13. Threshold for $Sb^{121}(\gamma,n)Sb^{120}$.

[8] W. Bothe and W. Gentner, Zeits. f. Physik. **105**, 236 (1937).
[9] L. Seren, H. N. Friedlander, and S. Turkel, Phys. Rev. **72**, 163 (1947).

The data on the excitation function for the 8.2-hour period are shown in Fig. 15. The threshold seems to lie below 7.8 Mev and may be stated as 7.7 ± 0.2 Mev.

A complete excitation curve taken simultaneously with that of copper is shown in the same figure. This excitation curve shows an abrupt change of slope at about 18 Mev which indicates a drop in the cross section for the formation of this activity at this energy. This feature of the curve is not characteristic of the monitor used since the copper was subject to the identical irradiation in each case and does not show a break at this point. Baldwin and Klaiber have shown that there is a similar break in the copper excitation curve at about 24 Mev. Cross sections based on the theoretical x-ray spectrum can be estimated only roughly. Those calculated by an empirical treatment of the data similar to that used by Baldwin and Klaiber[10] give the cross sections indicated in Fig. 16. The absolute cross section for tantalum may be larger than that indicated in the figure, since the decay scheme of Ta^{180} is not certain. It should be emphasized that, although the cross sections are consistent with our data and the theoretical spectrum, the nature of the data makes them relatively insensitive to the detailed shape of the cross sections. At higher energies a point by point analysis of the data indicated that the errors in the cross sections were much greater than the individual values represented by the curves in the figure.

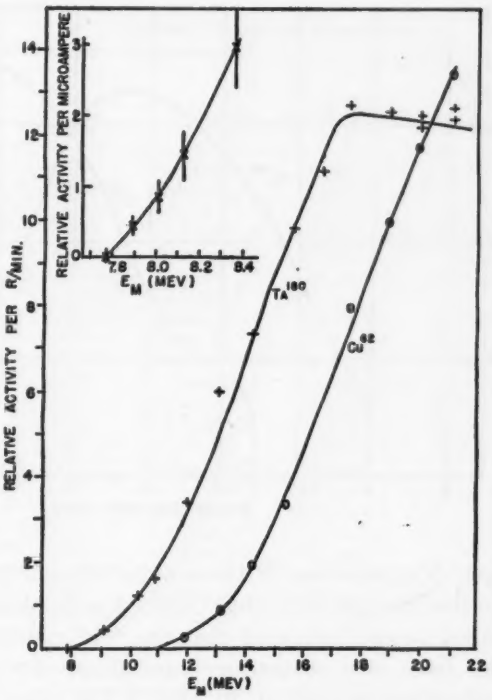

FIG. 15. Excitation curve for tantalum taken simultaneously with that for copper.

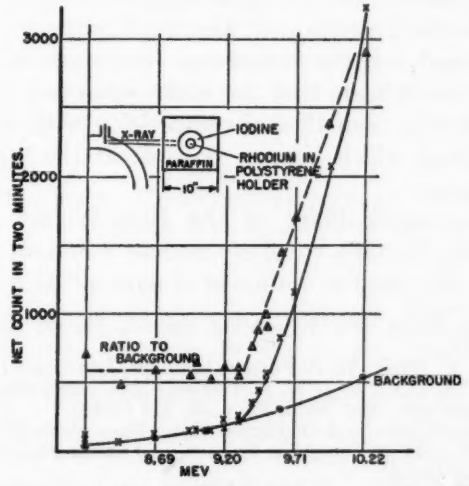

FIG. 14. Threshold for production of neutrons from iodine.

[10] G. C. Baldwin and G. S. Klaiber, Phys. Rev. **73**, 1156 (1948).

23. $Bi^{209}(\gamma, n)Bi^{208}$

A number of attempts failed to detect any radioactivity from this reaction. There has been some evidence which indicates the existence of a long life electron emission.[11]

The threshold for this reaction was determined by detecting the neutrons from an arrangement similar to that used for beryllium and deuterium. The intensity of neutrons from the betatron is still fairly low at these energies, so that the threshold can be distinguished from the rising background. The data are shown in Fig. 17. The threshold is estimated from the data to be 7.45 ± 0.2 Mev. The first measurement, which was taken with less satisfactory energy calibrations, gave a value of 7.3 Mev. It can be seen that the neutron background becomes significant at about 6.5 Mev. This energy is about that expected for the threshold for the most loosely bound neutron in the platinum x-ray

[11] J. J. Howland, D. H. Templeton, and I. Perlman, Phys. Rev. **71**, 552 (1947).

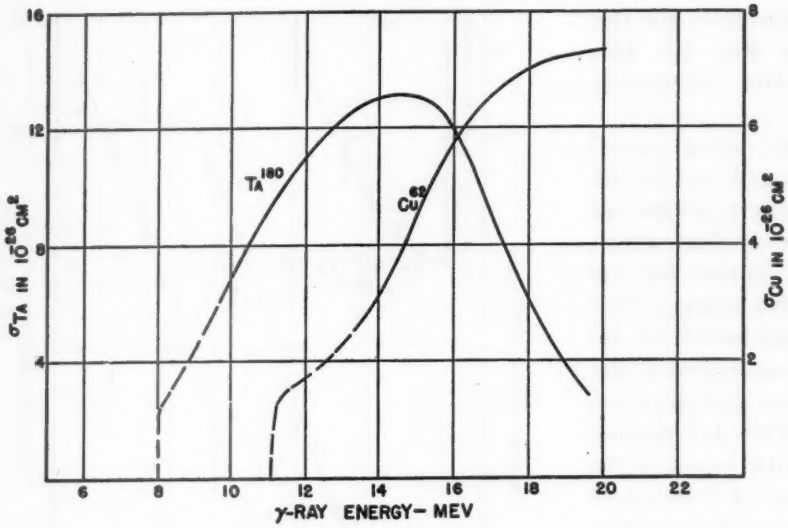

FIG. 16. Approximate cross sections for tantalum and copper as estimated from the excitation curves. The broken lines near the threshold are those obtained by estimating the effect of target thickness on the shape of the x-ray spectrum. The solid line portion of the curves are those calculated by using the theoretical spectrum as a function of energy and are approximately proportional to the derivative of product of E and excitation curves shown in Fig. 15.

target. A comparison of the number of neutrons from the betatron with that from a Ra-Be photoneutron source indicated that the total neutron yield from the betatron was about 5×10^8 neutrons per second at 20 Mev.[12] The number drops to about 10^5 neutrons per second at about 7 Mev. The general trend of the neutron-induced activities at higher energies is indicated by the background curve on the reduced scale.

DISCUSSION

Excitation Curves

It is found that the excitation curves near the threshold for all the reactions observed were very similar in shape and could be represented by a function $Y=kx^2$, where Y is the yield per unit of x-ray intensity measured by the ionization in a thick-walled ionization chamber, and x is the difference between the maximum x-ray energy and the observed threshold energy. This relation seemed to hold for a region of about 3 Mev. Since the effective thickness of the x-ray target is about 1.5 Mev, as estimated from the angular spread of the x-rays, the intensity of any isochromat in the x-ray spectrum in the region of maximum x-ray energy may be expected to increase with the energy below the maximum. If one assumes such a spectrum, the quadratic excitation functions observed would indicate that the cross sections rise abruptly to reasonably large values at a fraction of a Mev above threshold. This is in agreement with the results of Bothe and Gentner[13] which indicated that the cross section for Cu^{63} was about 2×10^{-26} and 5×10^{-26} cm^2 at 12 and 17 Mev, respectively.

The cross section for production of 10-minute copper activity averaged over the useful part of the x-ray spectrum at 20 Mev was estimated from ionization chamber measurements by the method discussed by Strieb, Fowler, and Lauritsen[14] and was found to be about 4×10^{-26} cm^2. This is in good agreement with Bothe and Gentner's values, but lower than that of other recent measurements.[15] The abrupt reduction of the cross sections at higher energies has not been satisfactorily explained. The small cross sections observed for the competing reactions[16] would seem to indicate that the explanation is a more subtle one than that of competition with other reactions which become possible at the higher energies.

The applicability of the Breit-Wigner dispersion formula to photo-nuclear reactions has been discussed in a number of papers.[17] Kalckar,

[12] We are indebted to M. Goldhaber for the loan of the calibrated neutron source.

[13] W. Bothe and W. Gentner, Zeits. f. Physik. **112**, 45 (1939).

[14] J. F. Streib, W. A. Fowler, and C. C. Lauritsen, Phys. Rev. **59**, 215 (1941); W. A. Fowler, C. C. Lauritsen, and T. Lauritsen, Rev. Mod. Phys. **20**, 236 (1948).

[15] H. Waffler and O. Hirzel, Helv. Phys. Acta **21**, 200 (1948); Skaggs, Laughlin, Hanson, and Orlin, Phys. Rev. **73**, 420 (1948).

[16] M. L. Perlman and G. Friedlander, Phys. Rev. **74**, 442 (1948).

[17] H. A. Bethe and G. Placzek, Phys. Rev. **51**, 450 (1937); F. Kalckar, J. R. Oppenheimer, and R. Serber,

Oppenheimer, and Serber reached the conclusion that the cross sections for the heavier elements should reach a maximum at energies where the level widths are of the same order as the level spacings and would decrease with further increases in the gamma-ray energies. It does not seem likely, however, that this treatment would explain the reductions in cross sections which are suggested by the data of Baldwin and Klaiber as well as by the present data for tantalum. Recently Goldhaber and Teller have suggested that the excitation curves could be accounted for by assuming a special type of resonance absorption in which the protons move in unison with respect to the remainder of the nucleus.[18]

Correlation of Threshold Data with Packing Fraction Curve

The experimental determinations of (γ, n) thresholds for light elements serve to check the energy scale, and, for masses above 20, serve to establish mass differences with somewhat greater accuracy than has been done previously. The observed thresholds and the binding energies obtained from the masses are summarized in Table I.

The masses above 40 are in most cases so poorly known that neutron binding energies can not be calculated directly with any accuracy. It is of interest, however, to correlate the observed binding energies with those calculated from the packing fraction by the method outlined by Bohr and Wheeler.[19] It has been found that the experimental data can be used to establish an approximate empirical relation to express the masses as a function of the atomic and mass numbers Z, and A.[20]

$$M(A,Z)=A-0.0081\cdot Z-0.00611\cdot A+0.014\cdot A^{\frac{2}{3}}+0.083[(A/2-Z)^2/A]+0.000627Z^2/A^{\frac{1}{3}}+\delta, \quad (2)$$

TABLE I. Observed thresholds.

Reaction	Observed activity	Observed thresholds (Mev)	Thresholds calculated from masses (Mev)
$H^2(\gamma, n)H^1$	Neutrons	2.20±0.05	2.19±0.03
$Be^9(\gamma, n)Be^8$	Neutrons	Calibration	1.63±0.03
$Li^7(\gamma, p)He^6$	0.85 β^-	9.8±0.5[a]	10.1 ±0.5
$C^{12}(\gamma, n)C^{11}$	20.5-min. β^+	Calibration	18.7 ±0.1
$N^{14}(\gamma, n)N^{13}$	10-min. β^+	10.65±0.2	10.51±0.1
$Mg^{24}(\gamma, n)Mg^{23}$	11.6-sec. β^+	16.2±0.3	15.5±1.0
$Mg^{25}(\gamma, p)Na^{24}$	14.8-hr. β^-	11.5±1.0[a]	10.9±1.0
$Mg^{26}(\gamma, p)Na^{25}$	62-sec. β^-	14.0±1.0[a]	15.0±1.6
$Al^{27}(\gamma, n)Al^{26}$	7-sec. β^+	14.0±0.4	11.1±1.0
$Si^{28}(\gamma, n)Si^{27}$	5-sec. β^+	16.8±0.4	16.0±1.0
$P^{31}(\gamma, n)P^{30}$	2.5-min. β^+	12.35±0.2	11.1±1.0
$S^{32}(\gamma, n)S^{31}$	3.2-sec. β^+	14.8±0.4	16.7±0.5
$K^{39}(\gamma, n)K^{38}$	7.5-min. β^+	13.2±0.2	12.7±1.5
$Ca^{40}(\gamma, n)Ca^{39}$	1-sec. β^+	15.9±0.4	13.7±1.5
$Fe^{54}(\gamma, n)Fe^{53}$	8.9-min. β^+	13.8±0.2	
$Cu^{65}(\gamma, n)Cu^{64}$	12.8-hr. $\beta^+\beta^-$	10.2±0.2	
$Cu^{63}(\gamma, n)Cu^{62}$	10-min. β^+	10.9±0.2	
$Br^{79}(\gamma, n)Br^{78}$	6.4-min. β^+	10.7±0.2	
$Br^{81}(\gamma, n)Br^{80}$	18-min. β^-	10.2±0.2	
$Sb^{121}(\gamma, n)Sb^{120}$	17-min. β^+	9.25±0.2	
$I^{127}(\gamma, n)I^{126}$	Neutrons	9.3±0.2	
$Ta^{181}(\gamma, n)Ta^{180}$	8.2-hr. β^-	7.7±0.2	
$Bi^{209}(\gamma, n)Bi^{208}$	Neutrons	7.45±0.2	

[a] These values are reduced from experimentally observed thresholds by approximately one-half the height of the barrier for proton emission.

where δ is zero for odd A, $-0.036/A^{\frac{1}{2}}$ for even A odd Z, and $+0.036/A^{\frac{1}{2}}$ for even A even Z. The neutron binding energy of a neutron in a nucleus of mass number A and atomic number Z is then

$$E_b(A,Z)=M(A-1,Z)+M_n-M(A,Z)\cong 83(Z^2/A^2)[1+0.0025A^{\frac{1}{3}}]-9.33/A^{\frac{1}{3}}-5.72+36/A^{\frac{1}{2}}\text{ millimass units.} \quad (3)$$

The positive value of δ used in this case holds for odd A odd Z, and even A even Z nuclei, which includes all nuclei observed in the present work.

Feenberg has attempted to evaluate the empirical relations in more detail and to take into

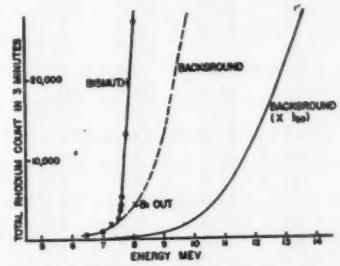

FIG. 17. Excitation curve for neutrons from bismuth. A more extensive curve indicating the effective background of neutrons from the betatron is shown on a reduced scale to higher energies.

Phys. Rev. **52**, 273 (1937); N. Bohr, R. Peierls, and G. Placzek, Nature **144**, 200 (1939); V. F. Weisskopf and D. H. Ewing, Phys. Rev. **57**, 472, Eq. (12) (1940), L. I. Shiff, Phys. Rev. **73**, 1311 (1948).

[18] M. Goldhaber and E. Teller, Phys. Rev. **74**, 1046 (1948).

[19] N. Bohr and J. H. Wheeler, Phys. Rev. **56**, 428 (1939); H. A. Bethe and R. F. Bacher, Rev. Mod. Phys. **8**, 82 (1936); C. F. Weizsacher, Zeits. f. Physik. **96**, 431 (1935); K. Way and E. P. Wigner, Phys. Rev. **73**, 1318 (1948).

[20] M. G. Mayer, Phys. Rev. **74**, 235 (1948); Mattauch and Flugge (reference 4, p. 100) give a similar equation.

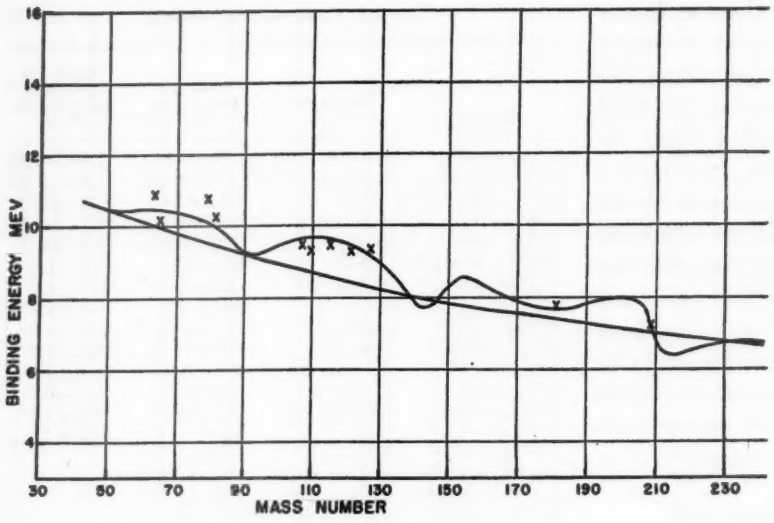

FIG. 18. Observed thresholds for (γ, n) reactions in odd nuclei. The solid lines represent the binding energy for odd A nuclei which lie at the bottom of the mass valley. The smooth curve is that calculated by use of Eq. (3). The irregular curve is based on Feenberg's curve for the mean excitation energy produced by the capture of a slow neutron.

account the fact that Z, for nuclei along the mass valley, is not a smooth function of the mass as assumed above.[21] He has calculated average neutron binding energies as a function of A. These are displayed in Fig. 4 of his paper. The binding energies for individual isotopes can be determined from Eq. (62) and the data shown in Figs. 3, 4, and 5 and Table 6 of the same paper. The binding energy for odd A odd Z and even A even Z nuclei which lie along the mass valley are shown by the irregular curve in Fig. 18. The additional binding energies for these types of nuclei which lie off the center of the valley are given approximately by the expression

$$\Delta E = 74/A[Z - Z_{(A-\frac{1}{2})}] \text{ Mev}, \qquad (4)$$

where $Z_{(A-\frac{1}{2})}$ is the value of Z corresponding to the most stable hypothetical nucleus having a mass of $(A-\frac{1}{2})$.

TABLE II. Observed and calculated thresholds.

Element	A	Z	Z_A	Binding energy Eq. 3	Binding energy Feenberg	Observed thresholds
Fe	54	26	24.5	12.6	12.6	13.8±0.2
Cu	63	29	28.5	11.1	11.1	10.9 cal.
Cu	65	29	29.3	10.0	10.0	10.2±0.2
Zn	64	30	28.9	11.7	11.9	11.6±0.4*
Se	82	34	36.0	8.0	8.3	9.8±0.5*
Br	79	35	34.8	10.0	10.8	10.7±0.2
Br	81	35	35.7	9.0	9.8	10.2±0.2
Mo	94	42	41.0	10.8	10.5	13.5±0.4*
Ag	107	47	46.7	9.6	10.1	9.5±0.5*
Ag	109	47	47.5	9.0	9.4	9.3±0.5*
In	115	49	49.5	8.7	9.4	9.5±0.5*
Sb	121	51	51.0	8.4	9.6	9.25±0.2
I	127	53	53.0	8.2	9.3	9.3±0.2
Ta	181	73	73.0	7.7	7.7	7.7±0.2
Bi	209	83	83.0	7.1	7.2	7.45±0.2

* Thresholds reported by Baldwin and Koch (see reference 1).

A comparison of the observed and calculated thresholds is given in Table II. This table includes all the observed thresholds reported for elements having atomic masses above 50. The odd A nuclei should have thresholds close to those calculated for elements lying along the mass valley. The agreement of the odd A thresholds with Feenberg's curve is good. It would be of interest to study the binding energies of other odd and even nuclei having A's of about 90, 140, and 210 to see if the strong variations in binding energy are confined to particular nuclei as suggested by Mayer[20] or if they can be fitted by more general fluctuations of binding energies as assumed by Feenberg.

The authors are indebted to R. T. Anderson and D. Riesen for assistance with these experiments and to H. Palevsky for the development and testing of the integrator circuits.

This work was assisted by the joint program of the Office of Naval Research and Atomic Energy Commission.

One of us (JM) wishes to acknowledge a National Research Council Fellowship held throughout much of this work.

[21] E. Feenberg, Rev. Mod. Phys. **19**, 239 (1947).

PHYSICAL REVIEW VOLUME 75, NUMBER 4 FEBRUARY 15, 1949

Neutron-Proton Scattering at 90 Mev

KEITH BRUECKNER, WALTER HARTSOUGH, EVANS HAYWARD, AND WILSON M. POWELL
Radiation Laboratory, Department of Physics, University of California, Berkeley, California
(Received November 8, 1948)

An experimental measurement of the angular distribution of protons scattered by neutrons in the neutron beam of the 184-inch Berkeley cyclotron has been made with a Wilson cloud chamber with magnetic field. The results show that the scattering is not isotropic in the center of mass system and that it is not symmetric about 90 degrees. The peak of protons in the forward direction indicates that a certain amount of charge exchange is taking place between the neutron and proton.

THE scattering of protons by neutrons of energies as high as 15 Mev has been studied by a number of observers.[1] Their results indicate that the scattering is isotropic in the center of mass system. Large changes in this distribution are to be expected when the de Broglie wave-length of the neutrons becomes smaller than the range of nuclear forces. In this experiment a hydrogen-filled Wilson cloud chamber was placed in the neutron beam from the 184-inch cyclotron and the scattering angles of the knock-on protons determined. Simultaneously, Hadley *et al.*[2] have been investigating this problem using counters. These experiments together are expected to give an accurate determination of the angular distribution of protons scattered by neutrons of energies near 90 Mev, the cloud chamber giving assurance that no large systematic error is being made and the counter experiments giving the higher statistical accuracy for which they are a more suitable tool.

Deuterons accelerated by the 184-inch cyclotron reach a half-inch beryllium target with an energy of approximately 190 Mev. A large fraction of the high energy neutrons produced appear in a beam in the forward direction. The intensity of this beam drops to half-value in approximately five degrees.[3] The energy distribution shows a maximum at 90 Mev. Both of these characteristics were predicted by Serber's stripping theory[4] for the deuteron and are particularly well adapted to the study of the scattering of protons by neutrons. The solid curve in Fig. 1 gives the calculated energy distribution of the neutrons in the beam. This energy distribution was checked by a measurement of the energy spectrum of the protons leaving a thin target in the forward direction.[5] It has been assumed that the energy distribution is the same for both neutrons and protons. This beam was collimated, as shown in Fig. 2, so that it passed through the center of the Wilson cloud chamber in a beam $\frac{5}{8}$ of an inch in diameter.

APPARATUS AND PROCEDURE

The cloud chamber (Fig. 3) was of the rubber diaphragm type measuring 16 inches in diameter and six inches deep with a useful depth (i.e., illuminated region) of about $3\frac{1}{2}$ inches. The neutrons entered through a 5-mil aluminum window in the wall of the cylinder. It was filled with about 110 cm of hydrogen and saturated with an alcohol-water mixture, 70 percent alcohol by volume.

The magnetic field was supplied by a pair of Helmholtz coils which, when carrying a current of 4000 amperes, produce a field of 14,000 gauss. This field drops only three percent six inches, from the center of the chamber. The power is supplied by a mine-sweeper generator, energized by a 150-hp motor; it is pulsed once every two minutes. It takes about 2 seconds for the current to rise to its maximum, where it remains steady for about 0.15 second before being turned off.

[1] Kruger, Shoupp, and Stallman, Phys. Rev. **52**, 678 (1937); T. W. Bonner, Phys. Rev. **52**, 685 (1937); P. I. Dee and C. W. Gilbert, Proc. Roy. Soc. **163**, 265 (1937); F. C. Champion and C. F. Powell, Proc. Roy. Soc. **183**, 64 (1944); J. S. Laughlin and P. G. Kruger, Phys. Rev. **73**, 197 (1947).
[2] Hadley, Kelly, Leith, Segrè, Wiegand, and York, Phys. Rev. **73**, 1114 (1948).
[3] Helmholtz, McMillan, and Sewell, Phys. Rev. **72**, 1003 (1947).
[4] Robert Serber, Phys. Rev. **72**, 1008 (1947).
[5] Chupp, Gardner, and Taylor, Phys. Rev. **73**, 742 (1948).

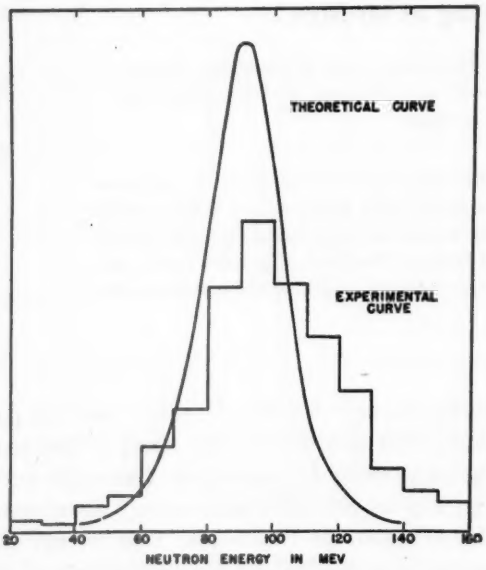

FIG. 1. The theoretical and experimental energy distributions. The experimental histogram is based on the data compiled in Table III and corrected for the variation of the scattering cross section with energy.

During this interval of steady current the cloud chamber is expanded, and the cyclotron is pulsed near the end of the sensitive time of the chamber. Very sharp tracks are produced in this manner. Turbulence is minimized by maintaining the chamber at a constant temperature of 19.3°C by means of a temperature-controlled, circulating water system. Two slow expansions were used between each fast expansion, the total time for a complete cycle being about 2 minutes. A clearing field of approximately 27 volts/cm was applied across the chamber and shorted out just before the expansion.

The illumination was obtained by discharging a pair of condenser banks of 256μf each at 1700 volts through a pair of General Electric FT422 flash tubes. The flash tubes were mounted behind a pair of cylindrical Lucite lenses to provide a parallel beam of light, and were placed in the space between the Helmholtz coils so that the chamber was illuminated at right angles to the line along which it was photographed (Fig. 3). Since the camera had no shutter, the length of the exposure was determined simply by the length of the flash, which was about 100μsec. The photographs were taken at f:16 with a stereocamera, using a pair of Leica lenses of 127-mm focal length separated by 4.5 inches and about 52 inches from the black velvet on the bottom of the cloud chamber. The film was Eastman Super XX and cut in 100-foot strips 1.81 inches wide.

A 10-foot paraffin collimating tube (Fig. 2) was placed between the concrete shielding of the cyclotron and the cloud chamber. This produced a neutron beam $\frac{5}{8}$ inch in diameter at the cloud chamber. A transit at the far side of the cyclotron was used to line up the tube and the target with the cloud chamber. A very intense light source behind the eyepiece of the transit projected the cross-hair through the collimating system onto the chamber window assuring accurate alignment. Two lines were drawn on the top glass of the chamber accurately parallel to within half a degree with the neutron beam. These marks appeared on each photograph and were used to determine the zero reading for the beam angle, β.

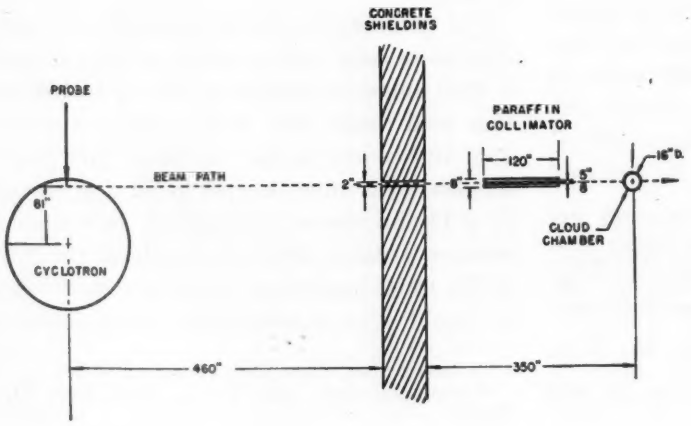

FIG. 2. The experimental arrangement showing the positions of the cloud chamber and collimator relative to the cyclotron and shielding.

REPROJECTION OF THE PHOTOGRAPHS

A double projector, Fig. 4, with an optical system identical with that of the stereocamera, threw a pair of life-size images of the cloud chamber on a special coated glass (Eastman Recordak green translucent screen type 75551). On the way to the screen the light passed through a piece of $\frac{3}{4}$-inch plate glass in order to correct for the distortions introduced by the $\frac{3}{4}$-inch top glass of the cloud chamber.

The procedure used in making the measurements involves first the adjustment of the film so that it is in the same relative position it had when the picture was taken. This was done by placing the green screen horizontal and at the proper height so that the distance between it and the projector lenses was 52 inches. Its position then corresponded to the bottom of the cloud chamber. Two wire crosses, sewn to the bottom of the chamber exactly eleven inches apart, served as fiducial marks. The projector lenses were closed down to f:8, and their focus adjusted so that the space between the fiducial marks was eleven inches for each projected image. Then the two images were brought into register by means of three fine screw adjustments on the film holder behind one of the projection lenses.

In order to obtain sufficiently brilliant projected images, it was necessary to use the Western Union concentrated arc lamp type 100. This made it possible to close down the projector lenses so that the reproduction was exact.

The reprojected track (Fig. 4) is superimposed on the measuring plate with the beginning of the track normal to the horizontal axis of rotation of the plate AA. The beam angle, β, is measured in the horizontal plane between the direction of the neutron beam and the horizontal projection of the tangent BB to the beginning of the track. The dip angle, α, in the vertical plane is measured to the tangent BB. The curvature is measured by matching it to one of a series of concentric arcs ruled on a Lucite template. A single line on the Lucite template perpendicular to all the arcs is simultaneously matched to the line AA to insure the accurate measurement of the angles α and β. The scatter angle, $\theta=\cos^{-1}\cos\alpha\cos\beta$, can then be calculated, and the energy E_n of the

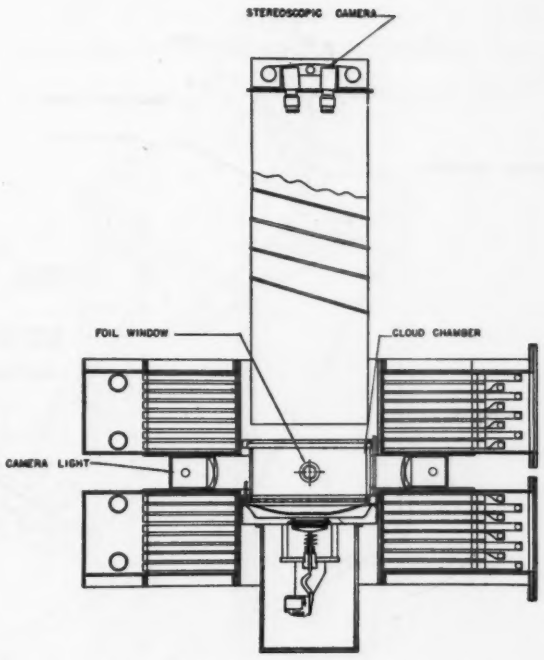

FIG. 3. A schematic drawing of the cloud chamber and Helmholtz coils.

incident neutron can be obtained from the measured radius of curvature, ρ_s, of the knock-on proton. Neglecting a small relativistic correction, the energy E_p of the proton is given by the expression

$$E_p=(e^2/2mc^2)(H\rho_H/\cos\alpha)^2,$$
$$E_n=(e^2/2mc^2)(H\rho_H/\cos^2\alpha)^2(1/\cos^2\beta),$$

where ρ_H is the curvature of the track if it is measured in the horizontal plane. It is related to the curvature, ρ_s, which is actually measured, by the expression $\rho_H^2=\rho_s^2\cos^4\alpha$.

PURPOSE AND LIMITS OF THE EXPERIMENT

Since the aim of the experiment is to measure the angular distribution of the protons scattered by neutrons of energies near 90 Mev, it was necessary to exclude events caused by lower energy neutrons. Hadley *et al.* set a lower limit for the neutron energies of 65 Mev. An examination of the experimentally determined energy distribution in Table III shows a minimum at 40 Mev. The number of neutrons between 40 and 65 Mev is sufficiently small so as not to invalidate a comparison between the two experiments. For these reasons a lower limit of 40 Mev was chosen

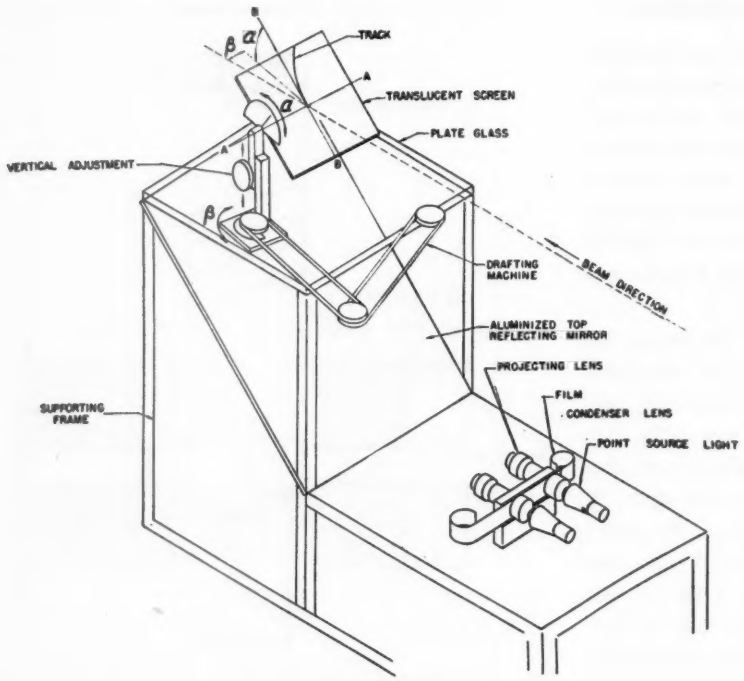

FIG. 4. A schematic drawing of the reprojection apparatus.

and higher energies determined merely as a check on the experimental accuracy as described below.

It was also necessary to set an upper limit to the scatter angle that would be included, since the particles scattered at large angles have short ranges and might be overlooked. Eighty-four degrees was chosen as the largest angle to be accepted in the data, because the range of the knock-on proton scattered at 85° by a 40-Mev neutron would be 0.8 cm. A track of this length would still have been observable, but a slightly shorter one would not.

EXPERIMENTAL CHECKS

Many auxiliary experiments have been performed as checks on the data. These are listed below.

1. The accuracy of these measurements depends on the assumption that all the neutrons producing events went through the chamber in the same direction. The validity of this assumption was checked by the observation that the ratio of the number of knock-on protons appearing outside the collimated beam to that in the beam was approximately one in a hundred. The volume occupied by the beam is small compared to the total illuminated volume of the chamber, so we may conclude that the number of knock-on protons produced by uncollimated neutrons is negligible.

2. The accuracy of the projecting apparatus was checked by taking pictures of a drafting triangle at various positions in the chamber and then measuring the angles by reprojection. The reprojected angles were found to be correct to within $\frac{1}{2}°$ for small dip angles and to within 1° for a dip angle of 60 degrees.

3. The question of whether high energy tracks were being missed because of their low ionization has been investigated. Since protons with energies of about 100 Mev knocked out of the glass were clearly visible, it has been assumed that none of those starting in the gas have been missed. As an additional check, an auxiliary camera was placed so that it viewed the cloud chamber at an angle such that each track scattered more light into it. No tracks were found in the pictures taken with the auxiliary camera that were not also clearly visible in the photographs taken with the stereocamera, although the tracks appeared to be considerably blacker.

4. It was also suggested that some nuclear disintegrations might be confused with knock-on protons. Such an event might consist of a proton

TABLE I. Comparison of angular distribution for two sets of data.

Neutron scatter angle	Cameras at 0 degrees 871 tracks Number observed	S.D.	Cameras at 45 degrees 893 tracks Number observed*	S.D.
12–40	93	9	100	10
40–60	105	10	117	11
60–80	113	11	112	11
80–100	105	10	109	11
100–120	127	11	126	11
120–140	133	12	143	12
140–160	128	11	109	11
160–180	57	8	54	7

* Multiplied by 871/893.

TABLE II. $(\Delta E/E)\times 100$ as a function of α and β for a 60-Mev neutron.

β	$\alpha=0$	20	40	60	70	80
0	15.4	14.3	12.7	17.7	32.6	65
20	14.8	13.8	12.2	17.7	31.8	65
40	13.0	12.3	11.5	17.6	32.0	64
60	10.9	10.6	10.9	17.7	32.0	64
70	10.5	10.5	11.3	18.2	32.0	64
80	13.7	13.8	14.7	20.5	34.0	65
85	23.4	23.6	24.2	28.1	38.7	67

TABLE III. Distribution in energy of incident neutrons.

Mev	Number of tracks	σ(barns)	$N/\sigma\times 10^{-3}$
20–30	37	0.40	0.9
30–40	20	0.28	0.7
40–50	42	0.20	2.1
50–60	49	0.16	3.1
60–70	92	0.130	7.1
70–80	118	0.112	10.5
80–90	194	0.093	20.9
90–100	217	0.081	26.8
100–110	153	0.072	21.2
110–120	110	0.066	16.7
120–130	72	0.060	12.0
130–140	29	0.054	5.4
140–150	17	0.049	3.5
150–160	12	0.046	2.6

TABLE IV. Data on angular distribution.

Neutron scatter angle	Number observed I	II	$I\times$geometrical correction	Cos interval	Intensity in arbitrary units I*	II
12–40	126	196	217	0.205	1.74±0.15	1.58±0.11
40–60	145	225	227	0.262	1.43±0.12	1.42±0.09
60–80	187	228	235	0.324	1.20±0.08	1.16±0.08
80–100	227			0.374	1.00±0.06	
100–120	256			0.329	1.28±0.08	
120–140	280			0.270	1.71±0.10	
140–160	240			0.179	2.21±0.14	
160–180	112			0.064	2.88±0.27	

* I—includes only proton tracks with dip angles less than 51 degrees. II—includes tracks of all dip angles. Errors are standard deviations based on the number of tracks.

TABLE V.

θ	$N(\alpha<50)$	N_1	$N(\alpha<50)f$
0–2	11		
3–4	24		
5–6	14		
7–8	26		
9–10	37		
11–12	44		
13–14	48		
15–16	58		
17–18	51		
19–20	39		
21–22	60		
23–24	52		
25–26	59		
27–28	50		
29–30	59		
31–32	53		
33–34	52		
35–36	35		
37–38	50		
39–40	66		
41–42	23		
43–44	49		
45–46	61		
47–48	41		
49–50	53		
51–52	45	53	52
53–54	42	44	52
55–56	19	40	37
57–58	35	45	48
59–60	32	46	46
61–62	30	42	45
63–64	39	53	60
65–66	31	49	48
67–68	27	49	44
69–70	18	32	30
71–72	33	47	54
73–74	28	42	47
75–76	21	34	36
77–78	11	24	19
79–80	11	17	19
81–82	11	17	20
83–84	11	15	20

track associated with a very short recoil nucleus. A set of pictures, taken with a cloud chamber filled with He and O_2, contained many stars resulting from the disintegration of O_2, but only two scattered protons. This number was commensurate with the number to be expected from the hydrogen in the vapor.

5. The data were thoroughly checked for turbulence, since this is one of the most important sources of error. Every fifth expansion was made without the magnetic field and with a block of paraffin in front of the chamber window so that there would be an ample number of protons in these pictures (Fig. 9a). If the tracks curved more than 1 mm in 20 cm, the pictures were excluded, and never fewer than 40 pictures in a turbulent strip were discarded in order to be

certain that there was no turbulence in the pictures taken when the magnetic field was on. Also, certain parts of the cloud chamber near the edges were found to be turbulent; therefore, tracks that started near the entrance and exit windows were omitted. The region of the cloud chamber from which tracks would be accepted was decided upon before the tracks were measured. This region was a cylinder with a diameter of about 1 inch and having a length of about 12 inches.

6. The data were selected and measured by two people independently. About one out of every 40 tracks was overlooked by one of the two observers; therefore, the chance that both would miss one is very small. Their measurements were reproducible to less than 1° in dip angle and $\frac{1}{2}$° in beam angle. If the discrepancy was larger, the track was remeasured twice, independently, and satisfactory agreement was always reached.

7. The data, which consist of 1764 knock-on protons, were taken in two sets; the first yielding 871 and the second, 893 protons. During the first set the two lenses of the camera straddled the direction of the beam, while for the second set the camera was rotated through 45°. This should have revealed the presence of any large systematic errors in the measurements. Turning the camera through 45° also increases the stereoscopic effect for those tracks scattered at large angles to the beam direction and thus makes the measurement of them more accurate. The angular distributions of the scattered protons in the two sets (Table I) were not found to differ significantly. The energy distributions based on 812 tracks (those with $\alpha>50°$ excluded) of the first set and on 246 of the second set were found to be in good agreement, so that the energies for the remaining protons were not measured except to distinguish recoils from neutrons with energies above and below 40 Mev.

8. Another check was made by comparing the estimated probable error in the energy with that obtained from the half-width of the experimental energy distribution. An approximate expression for the fractional error in the neutron energy may be obtained by differentiating the above expression for the neutron energy:

$$\Delta E/E=0.67[(2\Delta H/H)^2+(2\Delta\rho H/\rho H)^2 +(4\tan\alpha\Delta\alpha)^2+(2\tan\beta\Delta\beta)^2]^{\frac{1}{2}}.$$

$\Delta H/H$ is about ± 3 percent due to the radial variation of the field and to small errors in reading the ammeter. The fractional error in the radius of curvature, $\Delta\rho/\rho$, arises first from the error in measurement, ± 5 percent, and secondly from the "curvature" produced in the

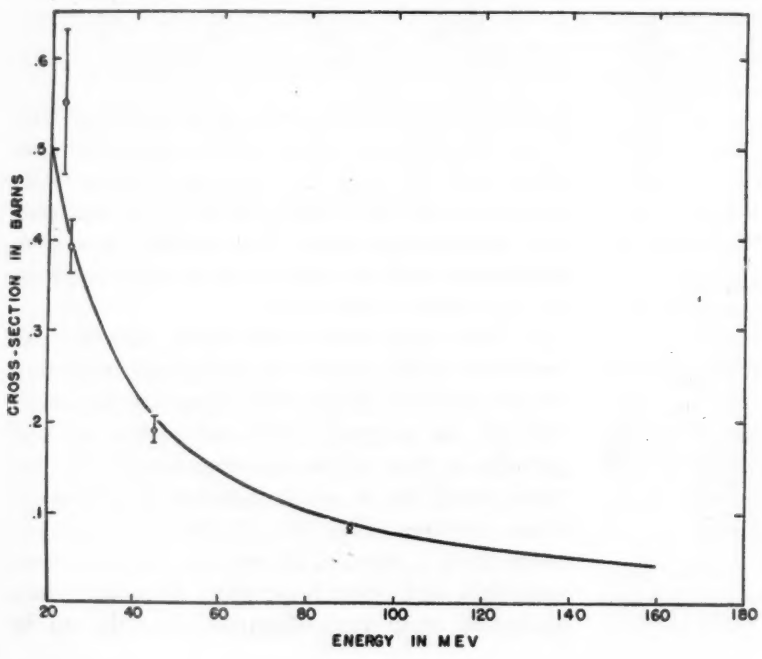

FIG. 5. The energy dependence of the scattering cross section used to obtain the energy distribution of the neutrons.

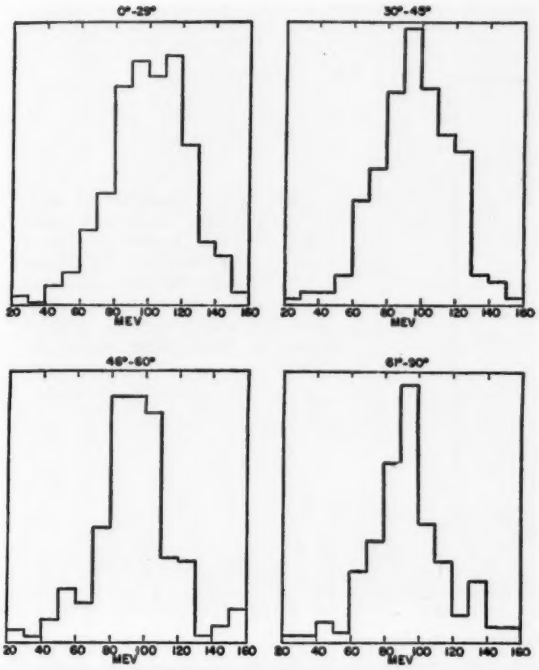

FIG. 6. The energy distribution for the angular intervals $\theta = 0$–29, 30°–45°, 46°–60°, and 61°–90°.

track by turbulence in the cloud chamber. This second error is given by ρ_H/ρ_T where ρ_T is the radius of curvature due to turbulence. This term depends on the energy and is most important for high energy tracks. In calculating the probable error ρ_T has been assumed to be 800 cm. The second term in the above expression may then be written:

$$[2(0.05)]^2+[(2\rho/800)\cos\beta]^2.$$

The estimate of the error in the dip angle, α, is based on the reproducibility of the measurements:

$$\begin{aligned} &\pm 1\tfrac{1}{2}^\circ \quad 0<\alpha<50^\circ \\ &\pm 2^\circ \quad \alpha=60^\circ \\ &\pm 2\tfrac{1}{2}^\circ \quad \alpha>60^\circ. \end{aligned}$$

The error in the beam angle, β, is $\pm 1°$; this includes the error in marking the beam direction on the top of the chamber as well as the error in measurement. The results obtained by substituting these estimates in the above formula are given in Table II for a 60-Mev neutron. The theoretical energy distribution of the neutrons is given in Fig. 1. The energies of the primary neutrons were experimentally obtained from the scatter angle and the curvature of about 1000 recoil protons. This energy distribution, if corrected for the variation of cross section with energy, gives the distribution in energy of the incident neutrons as shown in Table III. In order to compare the experimental energy distribution of the neutrons with the theoretical one, it is necessary to assume a cross section

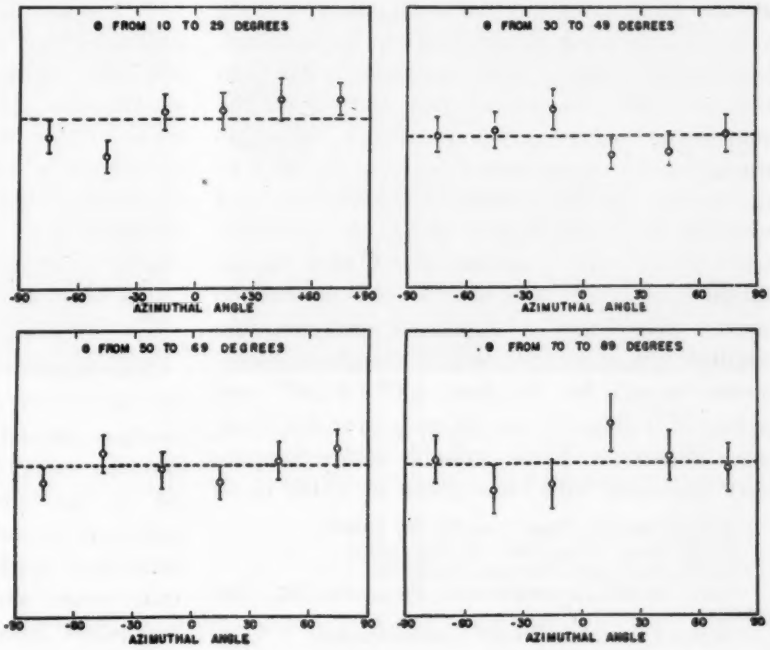

FIG. 7. The azimuthal distributions for four scattering angle intervals. The dotted lines represent the mean.

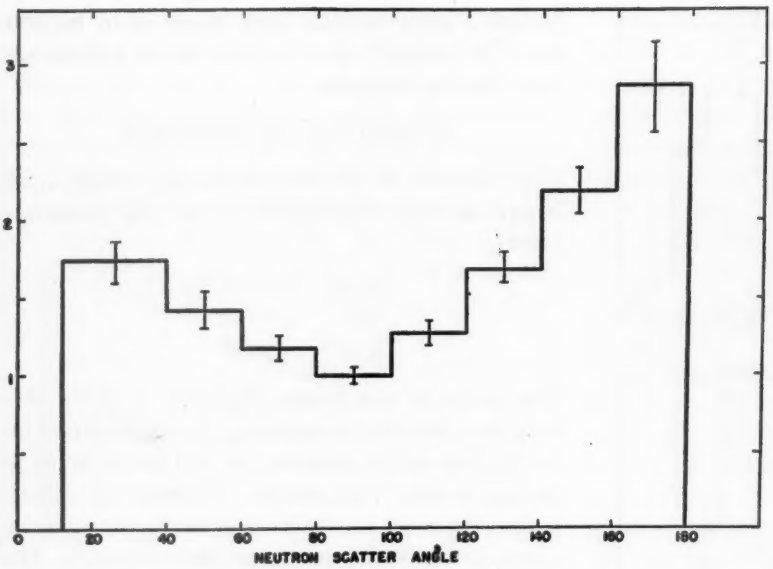

FIG. 8. The number of neutrons scattered per unit solid angle in the center of mass system. The standard deviations are based only on the number of tracks. Only those recoils due to neutrons with energies greater than 40 Mev have been included.

which varies with the energy of the neutrons. Figure 5 is a curve fitted to the experimental points of Sleator[6] at 23 Mev, Sherr[7] at 25 Mev, Segrè[8] at 45 Mev, and Cook, McMillan, and Sewell[9] at 90 Mev and extrapolated beyond 90 Mev by Christian.[10] This curve shows a cross section varying approximately as $1/E$ and is the one used for the purposes of this comparison. The histogram in Fig. 1 gives the experimentally determined energy distribution of neutrons after correction for the variation of energy with cross section. Only neutrons producing recoil protons with dip angles less than 50 degrees are included. In comparing theory and experiment it has been assumed that the actual distribution of the neutrons is that given by the theory. Since the spread in the experimental curve is due first to the spread in the theoretical distribution and secondly to experimental errors, the probable error in the energy measurements may be obtained by comparing the half-widths of the two curves. We obtain ± 13 percent. Selecting the angular group for which the energy measurements should be the best ($30° < \beta < 65°$ and $0 < \alpha < 25°$) (Fig. 5), we obtain a probable error of ± 10 percent. These probable errors compare very favorably with those given in Table II, so we conclude that no large systematic errors are being made.

8. If we assume that the angular distribution of the scattered protons does not depend critically on the neutron energy, we can check the accuracy of the measurements by comparing the experimental energy distributions at various scatter angles. Four such distributions are given in Fig. 6, again with dip angles greater than 50° excluded. They show only the expected spread in energy.

9. Finally, the azimuthal distribution (Fig. 7) indicates that no significant number of tracks has been missed or measured incorrectly. It should be emphasized that the errors in measurement of the incident neutron energy are large compared to the errors in the measurements of the scatter angle. The experimental angular distribution is, therefore, more reliable than the energy spectrum.

RESULT

The angular distribution has been measured for those protons corresponding to neutrons with energies exceeding 40 Mev and includes those protons scattered in the angular interval 0° to 84° in the laboratory system. Those particles scattered beyond 85° have such a short range that they might be overlooked; to be certain that none were missed, all those scattered beyond 84° have been excluded. 40 Mev has been

[6] William Sleator, Phys. Rev. **72**, 207 (1947).
[7] Rubby Sherr, Phys. Rev. **68**, 240 (1945).
[8] Emilio Segrè, private communication.
[9] Cook, McMillan, and Sewell, Phys. Rev. **72**, 1264 (1947).
[10] Richard Christian, private communication.

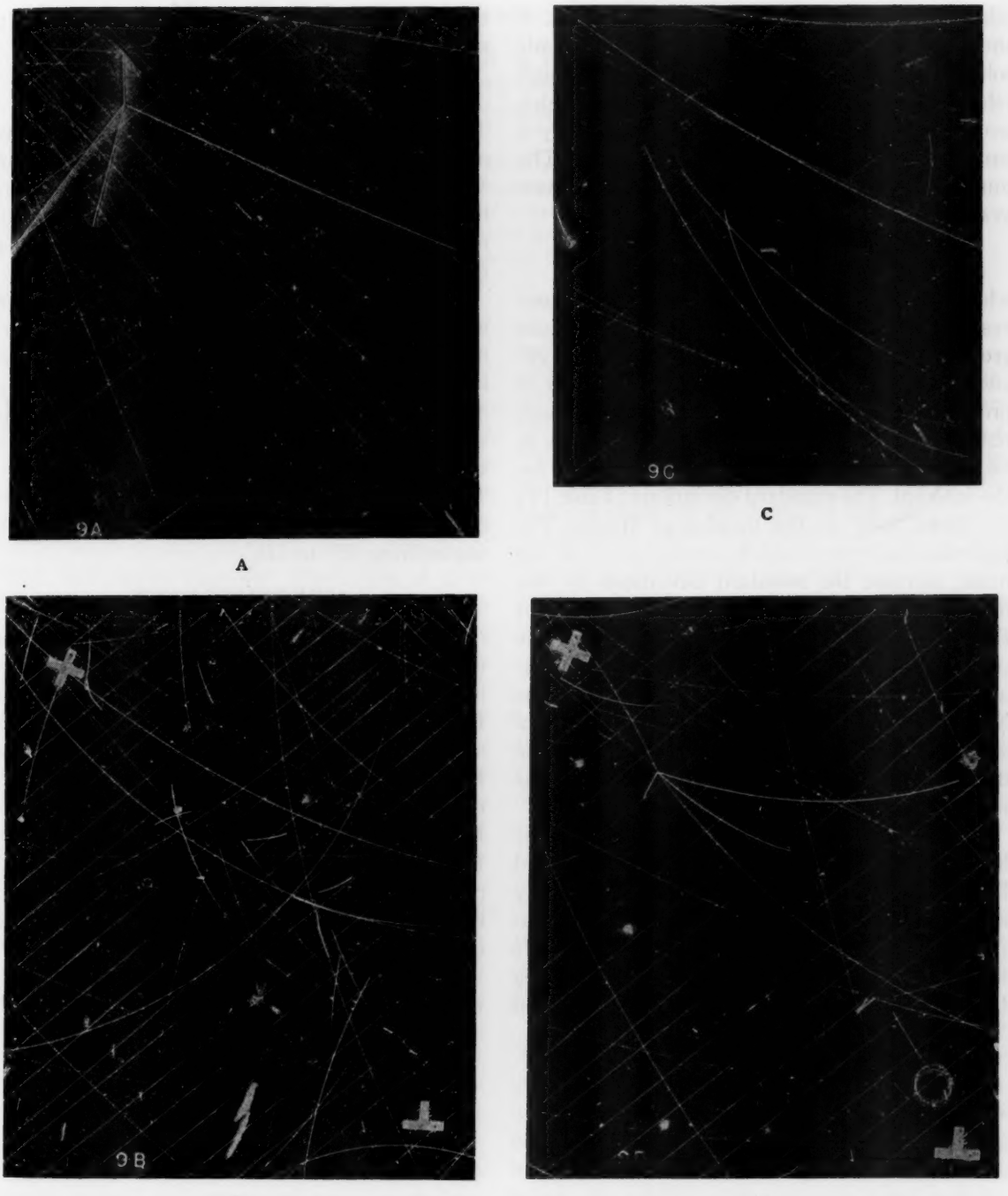

A C B D

FIG. 9. (A) A photograph taken without the magnetic field and with a block of paraffin in front of the chamber window. (B) and (C) show several examples of knock-on protons. (D) shows a nuclear disintegration. The straight parallel lines in all the pictures are the clearing field wires. In all cases the direction of the neutron beam is from the upper right-hand corner to the lower left.

chosen as the neutron energy below which tracks would not be accepted, because there are so few neutrons in the energy interval 35–45 Mev. Not more than 5 tracks could have been incorrectly included in or excluded from the data. The data, determining the angular distribution, are com-

piled in Table IV. The histogram in Fig. 8 shows the number of neutrons scattered per unit solid angle in the center of mass system. A small relativistic correction has been neglected which would move the experimental points only by a small fraction of their standard deviations. The number per unit solid angle in the center of mass system is

$$(dN/d\omega) = (dN/2\pi \sin 2\theta d\theta),$$

where θ is the scatter angle in the laboratory system. The data have been divided into eight groups; the first seven groups each include 20° and the last, 28 degrees. The relative number of protons scattered per unit solid angle has been obtained by dividing the number of particles in each group by the average value of the sine for the interval. The standard deviations (Table IV) are based only on the number of tracks. The experimental errors, which amount to 2° at the most, increase the standard deviations by not more than 25 percent for all the points except the one corresponding to 160°–180°. Here the process of averaging the $\sin 2\theta$ gives only a fair approximation because the variation of the sine is not linear over the interval. The amount of error introduced cannot be ascertained from the data; however, it is estimated to increase the indicated error by not more than 50 percent.

Those tracks that dip up or down from the horizontal by more than 50° have been excluded because it is difficult to measure them accurately enough to be certain that they are due to neutrons with energies greater than 40 Mev. We have corrected for this omission by multiplying by a suitable geometrical factor based only on the assumption that the scattering is azimuthally symmetrical:

$$f = 1 - [\pi/2 \cos^{-1}(\sin 50°/\sin\theta)].$$

Those points we obtain with the actual numbers of tracks scattered with dip angles greater than 50° are given in Table V. Although those points lie slightly below those obtained using the geometrical weighting factor, they agree well within the probable errors.

We conclude first that the scattering is not isotropic in the center of mass system; furthermore, the details of the distribution indicate that it is not symmetrical about 90°. Secondly, the peak of protons in the forward direction indicates that a certain amount of charge exchange is taking place between the neutron and proton. This work is in good agreement with that done by Hadley *et al.*[2] covering the neutron scatter angles from 65° to 180°.

ACKNOWLEDGMENTS

The authors wish to express their appreciation to Professor Ernest O. Lawrence for his interest in this work. Professor Emilio G. Segrè and Professor Robert Serber have made many valuable suggestions. Marguerite Hayward and Raymond E. Butler gave much essential technical assistance, John Swensson and Wallace Kilpatrick made many of the measurements. Paul Hernandez was responsible for the mechanical design of the major part of the equipment. Melvin E. Chun was in charge of the electrical equipment.

This paper is based on work performed under the auspices of the Atomic Energy Commission.

Magnetic Refraction of Neutrons at Domain Boundaries

D. J. HUGHES, M. T. BURGY, R. B. HELLER,* AND J. W. WALLACE
Argonne National Laboratory, Chicago, Illinois

(Received November 8, 1948)

In the course of experiments on the production of polarized neutrons, small-angle scattering (of the order of one minute) of neutrons in unmagnetized iron was observed. Further detailed experiments on the angular distribution, and variation with iron thickness, of the scattering have been performed. The results are compared with theory and are shown to be consistent with the hypothesis that the scattering is caused by magnetic refraction of the neutrons at domain boundaries.

INTRODUCTION

IN connection with a series of experiments on the polarization of neutrons,[1] a new effect was found which complicated the polarization results for some time. When the single transmission effect (E, the percentage increase in transmission of an iron block upon magnetization) was measured under conditions of good geometry, it was observed to increase appreciably. When the geometry was improved as much as possible with the equipment then in use (Fig. 1 of reference 1), the measured value of E for a block 1 cm thick became 13 percent instead of the 3 percent to be expected from neutron polarization alone. By using iron blocks of smaller thickness, d, it was found that the excess single transmission effect became relatively even more predominant, being about 1 percent for a 0.1-cm block for which the real E (being proportional to d^2) would be expected to be only 0.03 percent. The spurious single transmission effect could also be obtained for small magnetizing fields H, unlike the true effect which requires extremely high magnetization.

These early results made it quite clear that the new effect differed from the increased transmission caused by neutron polarization, and that it should be eliminated in order to study the latter. Measurements with different geometries showed that if the geometry were made bad enough so that all neutrons scattered by as much as 1° were included in the transmitted beam, then only the real transmission effect remained. It was thus shown that the new effect was a small-angle (less than 1°) scattering which took place in unmagnetized, but not in magnetized, iron. As the main interest at the time was in neutron polarization, the small-angle scattering was not investigated in any more detail than was necessary to eliminate its influence on the polarization effects. After the polarization work was finished, however, the scattering was investigated in more detail in order to determine its cause.

THEORETICAL CONSIDERATIONS

The fact that the small-angle scattering disappears with moderate magnetizing fields must mean that it is associated with the lining up of domains along the crystal axes (which takes place at low fields) and not with the rotation of the magnetic vector toward the applied field and away from the crystal axes (which takes place at high fields and which is necessary for neutron polarization). The cause of the scattering then must lie in the domain structure of unmagnetized iron.

As neutrons pass through polycrystalline iron they are scattered when they encounter a crystal grain at a Bragg angle. For thermal neutrons, however, the Bragg scattering occurs at angles of the order of 30° and greater, and hence will have nothing to do with the small-angle scattering. In addition, the neutron wave will be refracted at crystal boundaries and at domain boundaries. Of course the crystal boundaries do not change with magnetization and hence refraction at them cannot contribute to the effect. Refraction at domain boundaries, however, could cause the scattering and deserves more detailed investigation.

* Now at St. Louis University, St. Louis, Missouri.

[1] D. J. Hughes, J. R. Wallace, and R. H. Holtzman, Phys. Rev. 73, 1277 (1948).

The index of refraction of a crystal for neutron waves (for absorption small compared to scattering) is given[2,3] by

$$n^2-1=(\lambda^2 Na/\pi), \tag{1}$$

where λ is the neutron wave-length, N the number of nuclei per cm^3, and a the amplitude of coherent scattering. In the case of iron a is partly nuclear and partly magnetic in origin, being given by

$$a=a_n\pm a_m, \tag{2}$$

where a_n is the nuclear scattering amplitude (not spin-dependent) and a_m is the magnetic scattering amplitude which adds to, or subtracts from, the nuclear amplitude, depending on the orientation of the neutron spin with respect to the domain magnetization. In the general case the evaluation of a_m is quite complicated[2] because it involves the evaluation of the atomic form factor for the various scattering angles. However, if the neutron wave-length is so long that all the scattering is forward, or if only the forward direction is under consideration, as in the present case, the index is given simply by

$$n^2-1=(\lambda^2 Na_n/\pi)\pm(\mu B/E), \tag{3}$$

where μ is the neutron moment, B the magnetic induction, and E the neutron energy. Equation (3) gives the indices for the case of magnetization along the direction of incidence, for which case the difference of the indices is a maximum.

Thus there will be two indices of refraction in the iron, and the deviation experienced by a particular neutron at a domain boundary will depend on its orientation with respect to the magnetizations of the adjacent domains and on the orientation of the boundary. Upon magnetization, the boundaries, and hence the deviations, will disappear. The effect of the successive deviations will be to spread an initial collimated beam into a Gaussian whose width, σ, will increase with the square root of the thickness of iron traversed,

$$\sigma=\sigma_0(d/\delta)^{\frac{1}{2}}, \tag{4}$$

where σ_0 is the average (R.M.S.) deviation per domain boundary and δ the domain size. The average deviation depends on the distribution of shape, orientation, and magnetization direction of the domains, and it would be exceedingly difficult to compute accurately. The maximum deviation is, of course, given by twice the critical glancing angle for total reflection (θ_c) at a domain boundary where a_m changes sign. It follows from (3) that

$$\sin\theta_c=\theta_c=(2\mu B/E)^{\frac{1}{2}}, \tag{5}$$

a result which is independent of a_n and which agrees with the simple classical picture of a particle of energy E reflected at a boundary where its potential energy changes by $2\mu B$. Insertion of numerical values in Eq. (5) shows that the maximum deviation will be $2\theta_c=21.2'$ for thermal neutrons. The average deviation, σ_0, will depend on domain shape and orientation but will certainly be only a small fraction of $\theta_{\max}$. The average deviation might be expected to be exceedingly small if the domains were oriented in some regular manner, say with boundaries nearly normal to the neutron motion. In general, the multiply refracted neutrons will be unpolarized because of the random nature of the deviations. Only in the special case of single scattering at the critical angle would the neutron spin states be separated.[4]

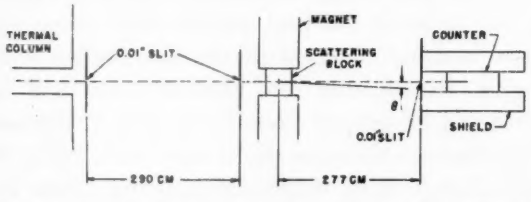

FIG. 1. Apparatus for measurement of magnetic small-angle scattering using slit geometry.

MEASUREMENTS

The first detailed investigations of the small-angle scatterings were made with apparatus very similar to that used for the polarization experiments, that is, with neutron beams of cylindrical cross section. It was found that if the direct beam were blocked by a cadmium disk at the neutron counter, so that only scattered neutrons were measured, then a negative single transmission

[2] O. Halpern, M. Hamermesh, and M. Johnson, Phys. Rev. 59, 981 (1941).
[3] M. Goldberger and F. Seitz, Phys. Rev. 71, 294 (1947).
[4] Scattering at the critical angle as a means of production of polarized neutrons has been considered by A. Achieser and J. Pomeranchuk, J. Exper. and Theoretical Physics, U.S.S.R. 18, 475 (1948).

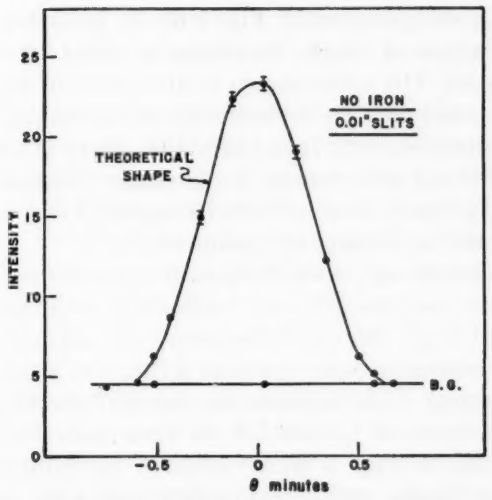

FIG. 2. Angular distribution of neutrons in the beam of Fig. 1 as detected with a 0.01-in. counter slit with no iron block in the beam.

resulted. However, attempts to measure the actual distribution of neutrons scattered outside the cadmium disk, using annular cadmium rings as diaphragms, showed only that the angles were much smaller than 1°. Further refinements decreased the upper limit until it was necessary to change to a slit geometry to obtain sufficient intensity for narrow angles.

The apparatus used to study the distribution of the scattered neutrons with the slit geometry is diagrammed in Fig. 1. A beam of neutrons from the thermal column of the Argonne heavy water pile is formed by two cadmium slits, 0.01″ wide, 1″ high, and 290 cm apart. The horizontal angular distribution in this beam is measured with a proportional counter 284 cm past the second slit. The counter and a third 0.01″-slit are moved in a horizontal direction by a micrometer screw to trace out the neutron distribution. The 0.01″-slits were the smallest that could be used without getting into undue background trouble.

The neutron distribution was first checked with no iron in the beam to see how it compared with that expected from the geometry of the slit system, the background being determined by placing cadmium over the central slit. Figure 2 shows the experimental points compared with the expected "theoretical" shape calculated from geometry. The agreement is excellent, and it is clear that any scattering present with the slits alone, such as air or room scattering, is negligible. The width of the direct beam pattern (half-width about $\frac{1}{4}'$) will complicate the determination of the true scattering distribution if the latter is of the order of 1′ or less. Contrary to early expectations, the scattering proved to be small enough so that the finite width of the direct beam complicated the analysis.

The distribution of the small-angle magnetic scattering was measured by placing a block of cold-rolled steel at the second slit between the poles of an electromagnet, as shown in Fig. 1, and measuring the neutron intensity with the iron magnetized and unmagnetized. The results, with background subtracted, are given in Fig. 3 for a 0.57-cm block. The points for "*H* on" fit the smooth curve which is the same curve as that of Fig. 2 calculated for the shape of the direct beam. In other words, there is no change in the shape of a beam caused by passage through a magnetized iron block, any small-angle scattering being negligible. About half the neutrons are scattered in the block, of course, but practically all go into Debye-Scherrer rings at large angles and do not change the observed beam shape. In addition, there is a slight amount of incoherent, isotropic scattering, but the fraction contained in the small angles studied here is negligible.

The results for the unmagnetized iron ("*H* off" in Fig. 3), however, show a very definite spreading of the beam extending out to several minutes. It is quite clear that the small-angle scattering is not much larger in magnitude than the geo-

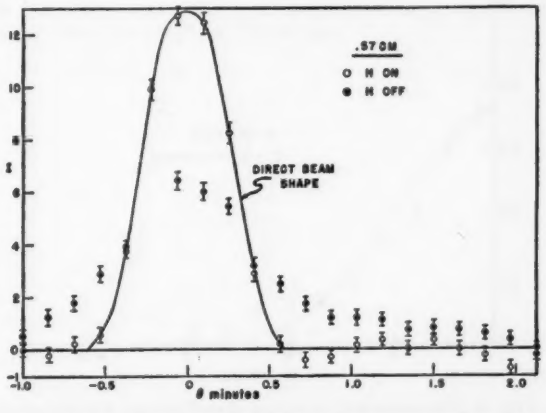

FIG. 3. Neutron distribution after passage through a magnetized ("*H* on") and an unmagnetized ("*H* off") iron block. The smooth curve is the same curve as shown in Fig. 2, adjusted by an intensity scale factor.

metrical spread of the direct beam, hence the shape of the curve of Fig. 3 will depend both on the distribution of the scattered neutrons and on the shape of the direct beam. It is noteworthy that intensity at the center of the pattern is much greater for H on than for H off. The ratio of these two intensities would be interpreted as the single transmission effect, related to neutron polarization, if the effect of small-angle scattering were unknown. It was just this increased single transmission effect with good geometry that led to the discovery of the small-angle scattering. For the 0.57-cm block, for instance, for which the true single transmission effect is about 1 percent, the good geometry of Fig. 3 would have led to an apparent single transmission effect of 100 percent. The errors shown on the points of Fig. 3 are based only on the statistics of the number of counts observed. It is likely that there is some additional error caused by irregular changes in background, for a uniform background was subtracted in plotting the points of Fig. 3.

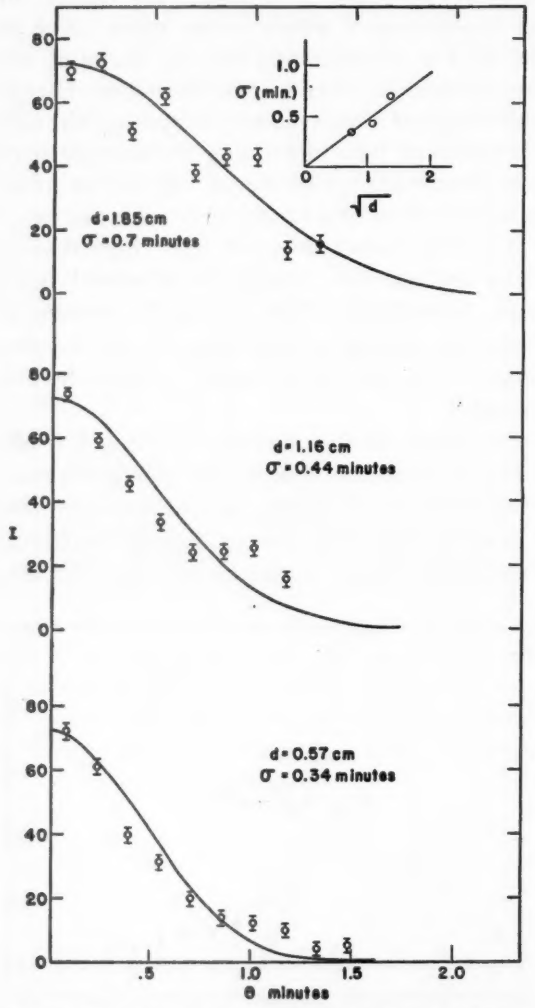

FIG. 4. Experimental neutron distributions for different block thicknesses, d, compared to curves calculated on the assumption that each part of the direct beam is spread into a Gaussian of width σ. The variation of the σ used for each block with d is also shown.

Even though it was difficult to obtain intensity above background, and sufficiently well separated from the direct beam at the same time, measurements were made as a function of block thickness d. In addition to the 0.57-cm block, thicknesses of 1.1 and 1.8 cm were used. Curves similar to Fig. 3 were obtained for both the other blocks, and it was qualitatively clear that the spread of the scattered neutrons increased with d. A more quantitative analysis of the different distributions will be given in the next section. Rough measurements made as a function of magnetizing field showed that the scattering disappeared with magnetizing fields of only a few hundred oersteds, thus verifying the earlier finding that the scattering disappeared as the domain walls disappeared.

DISCUSSION OF RESULTS

According to the theory that the scattering is caused by multiple refraction, it should be possible to fit the results by a Gaussian distribution whose width increases with the square root of d. The comparison with the experimental data was made by assuming that each part of the direct beam was split into a gauss and that the sum of these Gaussians would represent the scattered beam. In this way a series of curves for the scattered distribution was calculated, each corresponding to a particular width, σ, for the Gaussian. It was found that the scattered distributions for the various thicknesses were consistent with the shapes of the calculated curves and that σ increased with d. The experimental points for each block are shown in Fig. 4 with the calculated curves which best fit the results. Although the data are quite rough, the calculated shapes adequately account for the scattered distributions. The Gaussian width assumed for each block thickness is plotted as a function of $d^{\frac{1}{2}}$ in Fig. 4 also. As the errors involved in fixing σ for each curve are quite large, it can only be said that the

variation of σ with d is consistent with a $d^{\frac{1}{2}}$ relation and hence with the multiple refraction theory.

The most significant test of the refraction hypothesis is probably that of the numerical value of the scattering. From the curve of Fig. 4 it is seen that a σ of 0.46 corresponds to 1 cm of iron. For the particular iron used the domain size is known to be 3.4×10^{-3} cm, so that $(d/\delta)^{\frac{1}{2}}$ will be 17. From Eq. 4, σ_0 then turns out to be 0.027′. The question then is whether this value of σ_0, which is inferred from the experimental distributions, is consistent with the magnetic refraction hypothesis. Although the details of domain structure are unknown, it is possible to make an approximate calculation of the expected σ_0 without undue difficulty.

The maximum angle of deviation (21.2′) at a single scattering is, of course, much larger than the σ for a d of 1 cm (0.46′), hence the possibility must be considered in the calculation that the observed distribution is caused by single scattering rather than a superposition of small deviations. However, single deviations larger than 1′ occur only for glancing angles less than 0.3°. Because the probability of a domain boundary being oriented at such angles is very small, and because the area presented to the beam in such a case is small, the contribution of large single deviations is negligible. As the glancing angle increases, the deviation rapidly decreases (deviation $=E/B\cot\theta$ for glancing angle θ over 10′), but the probability of occurrence of the angle increases (as $\sin\theta\cos\theta$). The R.M.S. deviation per domain, σ_0, can be calculated from Eq. (3) if it is assumed that the domain boundaries are oriented at random and that the directions of magnetization on opposite sides of the boundary are at random. The resulting value, for one component of the deviation to correspond to the slit geometry, is

$$\sigma_0=0.029',$$

in satisfactory agreement with the observed value of 0.027′, considering the approximate nature of the calculation.*

Although the exceedingly low intensities caused by the necessity for fine beam collimation has made it difficult to get accurate data, it seems as if the hypothesis that the scattering is caused by multiple refraction at the domain boundaries adequately accounts for the results. The work thus demonstrates the presence of two indices of refraction for neutrons in iron, the difference in the indices being caused by magnetic scattering. It is possible that the small-angle scattering will be useful in investigating domain structure because of its relation to domain sizes, shape, and orientation.

We wish to express our thanks to O. Halpern, M. Hamermesh, W. Selove, and H. Snyder with whom we have had interesting discussions concerning the magnetic refraction of neutrons.

* *Note added in proof:* Since this article was written, it has been pointed out by O. Halpern (at the Physical Society Meeting in Chicago December 1948) that the refraction calculations are a special case of the more complete theory (to be treated in a forthcoming publication of Professor Halpern) of small angle effects including diffraction. The refraction treatment gives correct results when the angle of deviation is larger than the angle of diffraction; in the present experiments the angle of refraction is slightly larger than the angle of diffraction.

Electron-Neutrino Angular Correlation in the Beta-Decay of He^6

JAMES S. ALLEN,* H. R. PANETH, AND A. H. MORRISH
Institute for Nuclear Studies, University of Chicago, Chicago, Illinois
(Received November 8, 1948)

The recoil nuclei emitted during the beta-decay of He^6 have been detected by means of an electron multiplier tube, and the beta-rays counted by means of an end window Geiger counter. The energy spectrum of the recoils has been studied by recording coincidences between the two detectors as a function of the retarding potential between a set of grids in the path of the recoils. Beta-recoil ion coincidences have been observed when the angle between the directions of emission of the beta-particle and of the recoil ion was 180 degrees and also 162 degrees. In both cases the best agreement was obtained when the recoil spectra were compared with the curves predicted by the $1-(v/3c)\cos\theta$ electron-neutrino angular correlation.

I. INTRODUCTION

THE fact has recently been emphasized by Crane[1] and Sherwin[2] that the principal field to be exploited with neutrino recoil experiments is the determination of the neutrino-electron angular correlation functions. Hamilton[3] has published a paper giving the angular correlation functions expected for allowed and first forbidden transitions. Five different interactions between the nucleons and the electron-neutrino fields were considered. The point that Hamilton has emphasized is that the angular correlation changes much more, from one interaction to another, than does the shape of the beta-ray spectrum. Consequently, recoil experiments have something to offer in this direction which cannot be obtained as well from the usual beta-disintegration studies.

Sherwin[4] has reported the results of his investigations of the momentum spectra of the recoil ions from very thin, perhaps monolayer, sources of P^{32} and Y^{90}. He has concluded that the $1-(v/c)\cos\theta$ angular correlation expected for either the scalar or pseudoscalar interactions agreed with the experimental curves for P^{32}. However, a function of the form $[1-(v/c)\cos\theta]^2$ fitted the observed data reasonably well. In the case of Y^{90} he concluded that the $[1-(v/c)\cos\theta]^2$ correlation was preferred rather than the $[1-(v/c)\cos\theta]$ relation. The correlation functions are given in terms of the velocity of the electron v, the velocity of light c, and the angle between the directions of emission of the electron and neutrino.

The use of a radioactive gas rather than a monolayer source eliminates any possible distortion of the shape of the recoil spectrum due to energy lost by the recoils in escaping from the surface of the source. He^6 is an almost ideal isotope for use as a geasous source and may be produced in quantities sufficient for the study of the recoil spectra. The most convenient reaction for producing He^6 is $Be^9(n,\alpha)He^6$ with neutrons of energies greater than about 0.6 Mev. He^6 is assumed to decay through the emission of an electron and a neutrino according to the scheme, $He^6 \rightarrow Li^6 + \bar{e} + \nu$, with a single beta-spectrum[5] of maximum kinetic energy of 3.5 $\pm$0.6 Mev. The recoil spectrum corresponding to this beta-decay should consist of Li^6 ions with energies up to about 1410 ev.

II. PRODUCTION OF He^6

The He^6 was produced by neutron bombardment of one pound of 200-mesh beryllium powder in a can placed near the Be target of the University of Chicago cyclotron. According to the results of Sherr,[6] no appreciable production of N^{16} through the reaction $O^{16}(n,p)N^{16}$ will occur if neutrons emitted at 90° with respect to the deuteron beam are used. Since there was a possibility of this reaction occurring in the alcohol used as a carrier, the source was placed in a

* Now at the University of Illinois, Urbana, Illinois.
[1] H. R. Crane, Rev. Mod. Phys. 20, 278 (1948).
[2] C. W. Sherwin, Nucleonics 2, 16 (1948).
[3] D. R. Hamilton, Phys. Rev. 71, 456 (1947).
[4] C. W. Sherwin, Phys. Rev. 73, 216 (1948); 73, 1173 (1948).
[5] T. Bjerge and K. Broström, Nature 138, 400 (1936); Dansk. Math.-Fys. Medd. 16, 8 (1938).
[6] R. Sherr, Phys. Rev. 69, 21 (1946).

position such that mainly 90° neutrons entered the Be powder.

The He^6 gas was swept out of the powder by ethyl alcohol vapor and carried through about 50 feet of $\frac{1}{4}$-inch O.D. copper tubing to the recoil chamber. The radioactive gas diffused into the recoil chamber after the alcohol had been removed in a trap cooled with liquid nitrogen. The total pressure of the residual gases and the radioactive gas in the chamber during the experiments was about 5×10^{-6} mm of Hg. Attempts were made to localize the volume of the He^6 gas by introducing the gas through a jet into the recoil chamber. The results indicated that the He^6 was not concentrated by means of the various jets that were tried. Although the jet action might have been improved by the use of a recoil chamber of large dimensions plus large capacity pumps, it was decided that a more efficient use of the gas could be made without a jet system. In the final apparatus the pressure of the He^6 gas was nearly constant throughout the recoil chamber.

III. APPARATUS

A schematic diagram of one of the recoil chambers is shown in Fig. 1. The beta-rays were defined either by the system of slits in tube *AB* or by the openings in tube *DC*, and the accompanying beam of recoil ions was defined by the slits 1, 2, and 6. In order to reduce the scattering of the beta-rays, the slit systems were fabricated from aluminum. The tubes *AB* and *CD* were made gas tight by Al foils in order to prevent the He^6 gas from diffusing into the region near the Geiger counter. Side tubes were provided to equalize the pressure during the initial evacuation of the system.

The beta-rays from the decay of He^6 were recorded by an end window Geiger counter with a mica window of 5.8 mg/cm². This counter could be moved to a postion of either *A* or *D*. The first three electrodes of the electron multiplier used to count the recoil ions are shown in Fig. 1. Ions emerging from grid 6 were accelerated by a potential difference of 4.5 kv between this grid and the first electrode of the multiplier tube.

A retarding potential method was used for the energy analysis of the recoil ions. The retarding voltage was applied to grid 4 located between the grids 3 and 5 which were at ground potential. In addition, a fourth grid near the opening into the multiplier tube reduced, but did not eliminate entirely, the penetration into the retarding potential system by the field from the multiplier tube electrodes.

The entire recoil apparatus, including the multiplier tube and the can containing the beryllium powder, was evacuated by means of a three-stage oil diffusion pump. A pressure of 10^{-5} to 10^{-6} mm of Hg was maintained in the multiplier tube and recoil chamber. An increase in the concentration of the He^6 gas was obtained by a reduction of the pumping speed by use of a valve in the vacuum manifold. In practice the pumping speed was reduced until the pressure in the recoil chamber increased to about 10^{-5} mm of Hg.

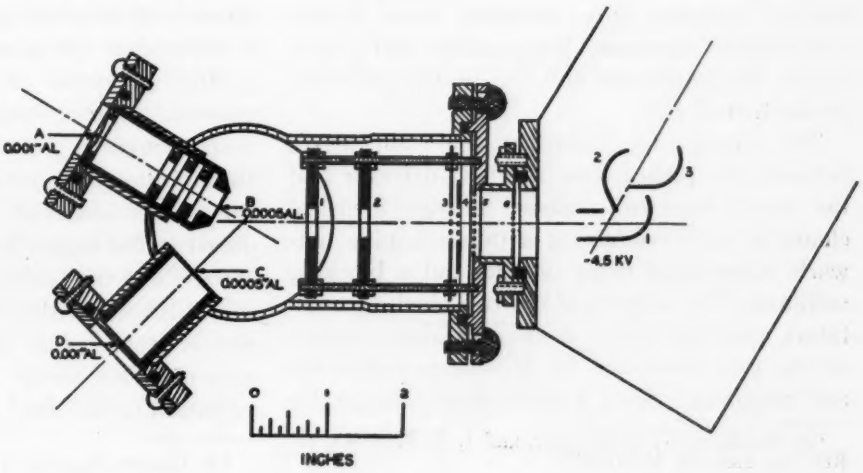

FIG. 1. A schematic diagram of the apparatus used for the retarding potential measurements of the energy spectrum of the recoil ions produced in the beta-decay of He^6. The recoils were counted by the electron multiplier tube and the beta-particles by a Geiger counter at window *A*. The retarding voltage was applied to grid 4.

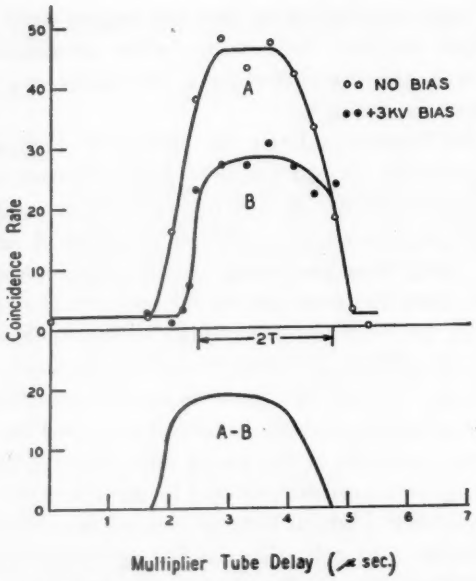

FIG. 2. The time response of the twofold coincidence circuit used during the measurements of the shape of the energy spectrum of the recoils emitted at 180 degrees from the beta-rays. The curve $A-B$ represents the number of coincidences resulting in recoil ions which could be stopped by the retarding voltage. The resolving time of the coincidence circuit is given by $2T$.

IV. COINCIDENCE CIRCUITS

The time of flight of the recoil ions, measured from the instant the beta-ray pulse was recorded, varied from about 0.45×10^{-6} sec. for 1400-volt recoil ions to 1.5×10^{-6} sec. for 100-volt recoils. In order to record the recoil spectrum from the maximum energy down to 100 volts or even lower, the minimum resolving time of the coincidence circuit was limited to a value of about 1×10^{-6} sec. This limitation of the resolving time proved to be most serious, since the high coincidence counting rate resulting from chance coincidences between beta-counts and recoil counts prevented the full use of the available production of He^6.

The circuits for recording the coincidences between the pulses from the beta-detector and the recoil detector consisted of two identical channels, each containing a pulse shaping network, a precision delay circuit, and a blocking oscillator. The outputs of the two blocking oscillators were fed into a diode coincidence circuit of the type described by Howland, Schroeder, and Shipman.[7] Since a continuously adjustable delay was needed, the multivibrator type of delay was used rather than a delay line. The delay multivibrators were of the cathode coupled type discussed by Chance.[8] In practice the delay in the channel connected to the Geiger counter was held constant at 10^{-5} sec., and the delay in the multiplier tube channel adjusted to obtain the required timing. The resolving time of the coincidence circuit was determined by the sum of the widths of the pulses from the two blocking oscillators. Resolving times ranging from 2×10^{-7} sec. to 2.2×10^{-6} were available.

The first measurements of the time response of the coincidence circuits were made with a coincidence chamber similar to that shown in Fig. 1, but having a beta-ray port in a position to permit the observation of coincidences caused by recoils emitted in a broad beam centered about 180 degrees with respect to the beam of disintegration electrons. The curves shown in Fig. 2 were obtained by recording the number of coincidences for various delays between the time of arrival of the pulses from the multiplier tube and the Geiger counter. Since the concentration of He^6 in the coincidence chamber did not remain constant during the course of an experiment, it was necessary to use either the Geiger counter or the multiplier tube as a monitor. The multiplier tube proved to be more reliable than the Geiger tube because of the extremely low background rate compared to the counting rate due to recoil ions produced near the first electrode of the multiplier tube.

Curve A of Fig. 2 represents the number of coincidences observed at various delays in the absence of a retarding potential, whereas curve B represents the number observed with a retarding potential of 3 kv. Since a retarding potential of this value should have been more than enough to prevent the recoils from passing through the grid system and into the multiplier, the counts observed resulted from recoils produced in the region between grid 5 and the first electrode of the tube. The disintegration electron in coincidence with a given recoil ion entered the Geiger tube after passing through the grid system. The curve $A-B$ represents the contribution to the total coincidence count from the

[7] B. Howland, C. A. Schroder, and J. D. Shipman, Jr., Rev. Sci. Inst. 18, 551 (1947).

[8] B. Chance, Rev. Sci. Inst. 17, 396 (1946).

region between grid 4 and the Al window in front of the Geiger counter. This explanation is in agreement with the observation that the low energy edge (short delay time) of curve $A-B$ is displaced to the left of the knee (at a delay of 2.5×10^{-6} sec.) of curve B by about 0.8×10^{-6} sec. This delay corresponds to the time required for a 300-volt Li^6 ion to travel the length of the coincidence chamber. Apparently, there are relatively few ions present in the recoil spectrum with energies less than 300 volts.

In Fig. 3 are shown a set of delay curves obtained with the Geiger counter at window A in the apparatus of Fig. 1. The cylinder in front of the counter did not have the system of slits as indicated in the diagram, but was closed at the inner end with an Al foil as shown in C. The curves have the same significance as those of Fig. 2. It was hoped that curve B would be absent with this arrangement, since disintegration electrons originating from the region between the multiplier tube and grid 4 could not enter the Geiger counter without having been scattered at least once. The presence of curve B can be explained in terms of electrons produced beyond grid 4 and entering the Geiger counter after having been scattered from the inner surface of the cylinder AB. Additional measurements indicated that most of the observed coincidences represented by curve $A-B$ were due to disintegrations occurring between slits 1 and 2 of Fig. 1.

V. COUNTING EFFICIENCY OF THE MULTIPLIER TUBE

Since the multiplier tube was operated with the first electrode at a potential of -4.5 kv with respect to the recoil chamber, the energy of the Li^6 ions arriving at this electrode varied from 4.5 kev to 5.9 kev. In order to interpret correctly the observed shape of the recoil spectra, a knowledge of the relation between the efficiency of the multiplier tube and the energy of the ions was required. This relation was obtained from an investigation of the efficiency of a multiplier tube used to count Li ions from a spodumene source. The method of measuring the efficiency of the tube was similar to that used by Allen[9] for an experiment on electron counting.

[9] J. S. Allen, Rev. Sci. Inst. **18**, 739 (1947).

When the discriminator bias of the scaler input circuit was set at a value low enough to permit essentially all the pulses to be recorded, the efficiency was observed to be constant for Li ions with energies from 2.5 to 6.5 kev. The energies referred to are those acquired by the ions upon arrival at the first electrode of the multiplier tube. Approximately 90 percent of the ions in this energy range striking the first electrode were recorded. In view of these results, it was possible to operate the multiplier tube in the He^6 experiment under conditions such that the counting efficiency was independent of the energy of the recoils.

VI. BETA-RAYS FROM He^6

A determination of the maximum energy of the He^6 beta-spectrum was made by the absorption method. The He^6 gas was pumped continuously through a cell consisting of a one-inch length of $\frac{7}{8}$-inch I.D. brass tubing. This cell had a 1-mil thick Al window at either end. Two end window Geiger counters were used, one as a monitor of the number of betas passing through

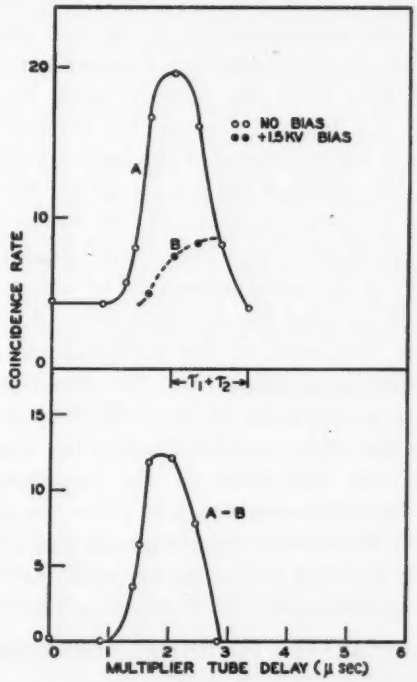

FIG. 3. The time response of the twofold coincidence circuit used during the measurements of the shape of the energy spectrum of the recoils emitted at 162 degrees from the beta-rays. The resolving time of the coincidence circuit is given by T_1+T_2.

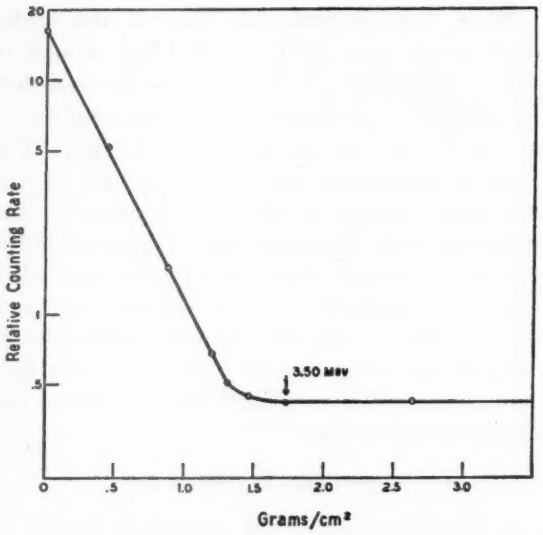

FIG. 4. Absorption in aluminum of the beta-rays from He^6. The counting rate beyond the end point of the spectrum is a background due to gamma-radiation from the cyclotron.

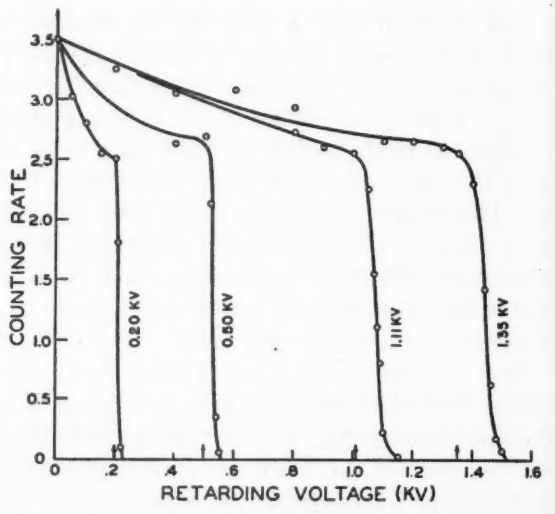

FIG. 5. A series of retarding potential curves for Li ions from a spodumene source. The initial energy of the ions is indicated on each curve. These curves were used to supply the corrections applied to the similar curves obtained for the recoil ions produced in the decay of He^6.

one of the windows and the other to measure the absorption of the beta-rays in Al.

The absorption in Al of the beta-rays of He^6 is shown in Fig. 4. A Feather analysis of the absorption curve gave an absorption limit of 1.74 g/cm² corresponding to an end point of 3.50 Mev, as calculated from Feather's equation, or 3.47 Mev from the relation given by Glendenin.[10] A value of 1.6 g/cm² has been reported by Sherr[11] for the range of the beta-rays of He^6. When the spread of the data near the end point of Sherr's curve is considered, the range of 1.74 g/cm² probably is within the experimental accuracy of his measurements. The value of 3.50 Mev will be used for the end point of the He^6 beta-ray spectrum in the computation of the recoil spectra resulting from this decay process. The largest deviation of the counting rate from a constant value was 3.6 percent for absorbers beyond the end point of the beta-spectrum. Since this departure was just twice the relative probable error in the counting rate, this counting rate was assumed to be a background due entirely to the gamma-radiation from the cyclotron.

VII. RETARDING POTENTIAL CORRECTIONS

Because of the use of the retarding potential method of energy analysis, the measured recoil spectra must be subjected to a considerable correction. The need for this correction is based upon the fact that the recoil ions go through the retarding potential grid system in parabolic paths and also experience a focusing action resulting from the inhomogeneous fields near the grid wires. As a result, the ion beam diverges, and a fraction of the beam fails to enter the multiplier tube. Jacobsen and Kofoed-Hansen[12] have emphasized the fact that the low energy end of the recoil spectrum will be greatly exaggerated if a suitable correction is not applied.

An attempt was made to determine the type of correction required with the retarding potential system shown in Fig. 1. A Pt filament coated with spodumene was placed inside the recoil chamber at the intersection of the lines AB and CD. Li ions were accelerated from this source to a coarse mesh grid and passed through the grid system in a broad beam. With this arrangement retarding potential curves were obtained for beams of Li ions of known energies. A series of retarding potential curves obtained in this manner is shown in Fig. 5. The initial energy of the ion beam is indicated on each curve. It is evident that corrections have to be applied to the observed cut-off potential and also to the

[10] L. E. Glendenin, Nucleonics **2**, No. 1, 12 (1948).
[11] R. Sherr, Phys. Rev. **69**, 21 (1946).
[12] J. C. Jacobsen and O. Kofoed-Hansen, Danske. Math.-Fys. Medd. **23**, paper 12 (1945).

shape of the curves in the region from zero retarding potential to the knee of a particular curve.

The procedure followed in applying the connections to the retarding potential curves of the recoils from the decay of He^6 was to multiply the applied retarding voltage by a correction factor obtained from the curves of Fig. 5. As a result, the corrected energy of the recoils was approximately 6 percent lower than that corresponding to the applied retarding potentials.

In order to compare the observed retarding potential curves with those predicted for various neutrino-electron angular correlation functions, a differential distribution curve giving the number of recoils per unit energy interval as a function of the recoil energy was computed for a given correlation function. By means of graphical integration the differential plot was converted into an integral, retarding potential curve. Since these computations had to be performed, it was more convenient to apply a correction to the theoretical curves rather than to the observed data. In effect, a hypothetical beam of recoil ions having a distribution predicted by a given angular correlation function was sent through the retarding potential system. The retarding potential curve expected from this operation was exaggerated at the low energy end by the appropriate correction and then compared with the observed data.

The actual form of the correction was obtained from the calibration data of Fig. 5 under the assumption that these curves represented the shape of the retarding potential curves of the corresponding energy intervals in the He^6 recoil spectrum. Later experiments indicated that the effective He^6 source was nearer the multiplier tube than the spodumene source. This would require somewhat larger corrections than those actually applied.

VIII. He^6 RECOIL SPECTRA

The first measurements of the shape of the spectrum of the recoils from the decay of He^6 were made with an apparatus similar to that of Fig. 1, but with a beta-ray port at 180 degrees with respect to the recoil counter. In order to determine the proper delay to be introduced between the Geiger counter and the multiplier tube the delay curves shown in Fig. 2 were used. The pulses from the multiplier tube were delayed by 3.3×10^{-6} sec. (measured from an arbitrary zero of time). With this delay, the total resolving time of 2.25×10^{-6} sec. for the response of both coincidence circuits was sufficient to allow practically the entire recoil spectrum to be recorded.

In the 180-degree arrangement the location of the effective He^6 source was made difficult by the fact that electron-recoil ion coincidences occurring at any point in a roughly cylindrical volume could be recorded. This volume was defined by the slit system, the retarding potential grids, and the Al window for the beta-rays. An estimate of the actual location of the source was obtained by recording the coincidence rate as a piece of Al foil was moved inside the recoil chamber from a position near the Geiger counter to a position near the retarding potential grids. The Al foil served as a baffle for the recoil ions, but was transparent to the beta-rays. As a result of this experiment it was concluded that

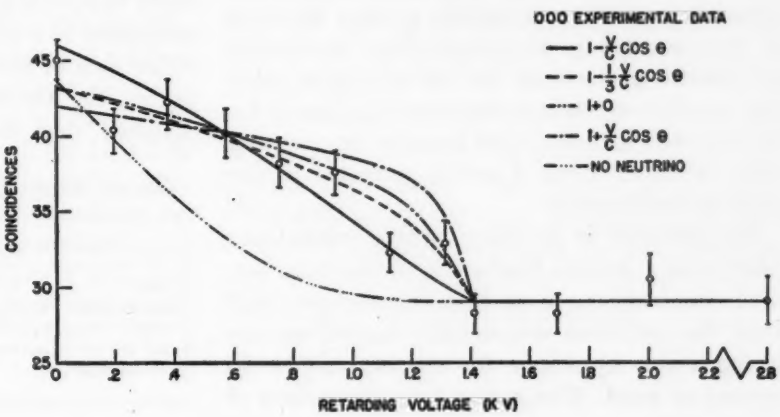

FIG. 6. Experimental and theoretical retarding voltage curves for the recoil ions produced in the decay of He^6. The beta-ray counter was in a position to record electrons emitted at an angle of $180°\pm15°$ with respect to the direction of the beam of recoil ions.

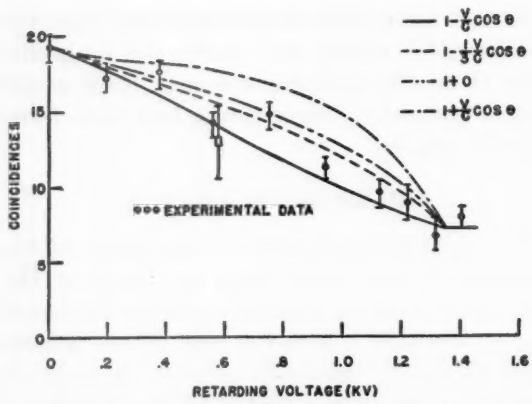

FIG. 7. Experimental and theoretical retarding voltage curves for the recoil ions from the decay of He^6. The beta-ray counter was in a position to record electrons emitted at an angle of $162°\pm8°$ with respect to the direction of the beam of recoil ions. The open circles represent data recorded without baffles in front of the Geiger counter. A measurement made with a set of baffles which reduced the beta-ray scattering is represented by the open square at a retarding voltage of approximately 0.6 kv.

most of the coincidences originated in a region extending from grid 3 to slit 1 of Fig. 1. In order to compute the retarding potential curves expected for various electron-neutrino angular correlation functions, it was assumed that the beta-rays entered the Geiger counter in a conical beam of 15 degrees half-width and that the recoil ions entered the multiplier tube in a beam of parallel rays.

The retarding potential curves for the recoils from the decay of He^6 as obtained with the 180-degree arrangement are shown in Fig. 6, where the number of coincidences per 3.2×10^4 multiplier tube counts is plotted against the retarding voltage. A correction has been applied to the applied voltage as described in Section VII. The constant number of coincidences observed for retarding potentials greater than 1.4 kv was due partly to coincidences originating between the grid system and the multiplier tube. The number of chance coincidences caused by the relatively high beta- and positive ion counting rates averaged about 4 and is included in the constant background.

The presence of the large chance coincidence count was a serious limitation to the accuracy of the experiment. In practice the neutron yield from the cyclotron occasionally varied enough during a run to change the chance rate by 50 percent or more. The rather large deviations of some of the experimental points from a smooth curve probably were caused by this variation in the chance coincidence rate. This effect could have been reduced by decreasing the rate of production of He^6, but with an almost corresponding decrease in the true coincidence rate.

The no neutrino curve of Fig. 6 was computed with the assumptions that the momentum of the nucleus is equal and opposite to that of the beta-particle and that the shape of the beta-spectrum is correctly given by the Fermi distribution. The additional curves were computed for four possible neutrino-electron angular correlation functions, including the case of a constant angular correlation. The computed curves have been corrected for the distortion of the shape of the recoil spectrum as a result of the use of the retarding potential method of energy analysis. The end point of the He^6 beta-spectrum was taken to be at 3.5 Mev in computing these curves.

Additional retarding potential measurements were made with the Geiger counter at window A of the recoil chamber shown in Fig. 1. In order to reduce the chance coincidence rate the resolving time of the coincidence circuits was reduced to a value of 1.3×10^{-6} sec. The delay curve for the coincidences observed with this arrangement is shown in Fig. 3. A delay of 2×10^{-6} sec. (arbitrary zero of time) in the multiplier tube circuit was used during the measurements of the recoil spectrum.

The data obtained with the slit system removed from the tube A–B are represented by the open circles in Fig. 7, where the number of coincidences per 6.4×10^4 multiplier tube counts has been plotted against the retarding voltage. With this arrangement most of the coincidences originated in a region extending about one cm on either side of slit 1 as shown in Fig. 1. In computing the theoretical curves of Fig. 7 it was assumed that the beta-rays coming from this

TABLE I. Expected correlations for allowed transitions.

Interaction	Correlation function
Scalar:	$P_1(\theta)=1-(v/c)\cos\theta$
Polar vector: Fermi rules.	$P_2(\theta)=1+(v/c)\cos\theta$
Tensor: Gamow-Teller rules.	$P_3(\theta)=1+(v/3c)\cos\theta$
Axial vector: Gamow-Teller rules.	$P_4(\theta)=1-(v/3c)\cos\theta$
Pseudoscalar:	$P_5(\theta)=1-(v/c)\cos\theta$

source entered the Geiger counter in a conical beam with apex at the center of this source. The beam had a half-width of 8 degrees, and the mean angle with the beam of recoil ions was 162 degrees. The computed curves have been corrected for the distortion expected through the use of the retarding potential method of energy analysis.

In order to reduce the scattering of the beta-rays from the inside surface of the tube in front of the Geiger counter, the system of defining slits shown in tube A–B was used with the Geiger counter at A. With this arrangement the half-width of the beam of beta-rays was 6 degrees, and the mean angle with the beam of recoil ions was 154 degrees. Although the coincidence rate was extremely low, coincidences were obtained at retarding potentials of 0, 600, and 1500 volts. The number of coincidences observed at a retarding potential of 600 volts is shown by the open square of Fig. 7. An appropriate adjustment of the ordinate scale has been made so that the numbers of coincidences observed at 0 and at 1400 volts agree with the corresponding values of the computed curves. The fact that the number of coincidences observed at 1500 volts agreed within the statistical error with that expected from chance coincidences indicated that the scattering of the beta-rays had been greatly reduced.

IX. CONCLUSIONS

Since the change of nuclear spin during the decay of He^6 is probably from $I=0$ to $I=1$, the transition is forbidden according to the selection rules of the original Fermi theory of beta-decay. In order to explain the fact that the experimental values of the lifetime and maximum beta-ray energy for this decay process indicate an allowed transition, it is necessary to assume Gamow-Teller selection rules. According to these rules an allowed transition is permitted for $\Delta I=1, 0$.

Hamilton[3] has calculated the expected correlation functions, giving the relative probability for the emission of a beta-particle and a neutrino with an angle θ between the two directions of emission. The correlations expected for allowed transitions are listed in Table I. If the Gamow-Teller selection rules explain the He^6 decay, either the $1+(v/3c)\cos\theta$ or the $1-(v/3c)\cos\theta$ correlation functions are possible choices of a function which should agree with the observed electron-neutrino angular correlation.

In the case of the 180-degree retarding potential curves shown in Fig. 6 the no neutrino curve is strongly contradicted by the experimental data. Because of the inaccuracy of the data it is not safe to say more than that the $1+(v/c)\cos\theta$, $1+(v/3c)\cos\theta$, and probably the $1-(v/c)\cos\theta$ correlations are ruled out. The best agreement is with the $1-(v/3c)\cos\theta$ correlation, although the isotropic distribution is not entirely ruled out. In the case of the 162-degree curves shown in Fig. 7, the best agreement is with a curve located between the $1-v/c\cos\theta$ and the isotropic distribution. The $1-(v/3c)\cos\theta$ correlation is a reasonably good choice for this curve. Because of the large statistical error in the datum represented by the open square, it is safe to conclude that only the curves above the $1-(v/3c)\cos\theta$ correlation curve are ruled out. However, since the average angle between the beta-rays and the recoil ions for this measurement was 154 degrees rather than 162 degrees, the data obtained at this angle should lie slightly below that obtained at 162° and represented by the open circles.

The results of this experiment seem to rule out the "no neutrino" assumption and give some indication of agreement with the $1-(v/3c)\cos\theta$ correlation predicted by the axial vector form of interaction which follows Gamow-Teller selection rules. As mentioned above, the He^6 decay is expected to be governed by this type of selection rule. It is hoped that further experiments with He^6 will lead to a more critical choice of the appropriate beta-interaction or combination of interactions.

This research was assisted by the joint program of the Office of Naval Research and the Atomic Energy Commission. The authors wish to thank Dr. Gerhardt Groetzinger for placing the University of Chicago cyclotron at their disposal, and also Mr. Scott and his cyclotron crew for their help in operating the machine.

Spin Dependence of Slow Neutron Scattering by Deuterons

E. FERMI AND L. MARSHALL
Argonne National Laboratory and Institute for Nuclear Studies, University of Chicago, Chicago, Illinois
(Received November 8, 1948)

The cross section of deuterium gas at liquid air temperature for neutrons of average wave-length 5.43A is found to be 21.3×10^{-24} cm² per molecule. The cross section of deuterium atoms for neutrons of a few volts is found to be 3.44×10^{-24} cm² per atom. These two values are used to obtain information on the spin dependence of the neutron scattering by the deuteron. It is found that the two scattering lengths a_4 and a_2, corresponding to neutron spin parallel or anti-parallel to the deuteron spin, have the same sign but may differ in magnitude by as much as a factor 2.

I. INTRODUCTION

THE purpose of the present experiment is to obtain information on the spin dependence of the slow neutron scattering by deuterium. The scattering properties of slow neutrons are determined by the scattering lengths[1] for the various spin orientations. The spins of the neutron and the deuteron can take two relative orientations with resultant spins $\frac{1}{2}$ and $\frac{3}{2}$. To these correspond two scattering lengths, a_2 for the doublet state, $S=\frac{1}{2}$, and a_4 for the quartet state, $S=\frac{3}{2}$. If these two quantities and their signs were known, the scattering properties of the deuterium nucleus would be completely characterized.

The corresponding two quantities for hydrogen have been obtained by determining separately the cross sections of the ortho- and parahydrogen. The most recent of these measurements is due to Sutton *et al.*[2]

Since no liquid hydrogen was available for the present work and the ortho- and paradeuterium could not be separated, a somewhat different method was used. The cross section of the deuterium molecule at liquid air temperature was measured, using neutrons of very long wave-length in order to emphasize the interference phenomena. The ratio of this cross section to that of deuterium for epithermal neutrons was compared with a value of the same ratio calculated as a function of a_4/a_2. From the comparison one can assign limits to the possible values of a_4/a_2.

Unfortunately, a_4/a_2 turns out to be not very different from one—a value for which the sensitivity of the method is extremely poor. Consequently, a_4/a_2 could be determined only within rather wide limits.

[1] E. Fermi and L. Marshall, Phys. Rev. **71**, 666 (1947).
[2] Sutton, Hall, Anderson, Bridge, De Wire, Lavatelli, Long, Snyder, and Williams, Phys. Rev. **72**, 1147 (1947).

II. DETERMINATION OF THE CROSS SECTION OF D_2 FOR FILTERED NEUTRONS

The deuterium gas was contained in a heavy-walled steel tube, the inside dimensions of which were 74.93 cm in length and 2.72 cm in diameter. In order to prevent condensation of water on the ends of the tube, when it was cooled to liquid air temperature, the ends of the tube were extended by false ends and the space in between was evacuated. The tube, together with the adjoining parts of the false ends, was immersed in liquid nitrogen. The temperature of the tube was measured by a thermocouple and was found to be quite constant at 77.5°K.

A beam of thermal neutrons from the thermal column of the Argonne heavy water pile was filtered through 40 cm of sintered BeO. This filter removes neutrons whose wave-length is less than 4.5A from the thermal beam.[1] The average wave-length of the neutron beam so obtained was determined in a separate experiment, which will be described below, and found to be 5.43A.

The neutron intensity transmitted by the deuterium was measured with a long BF_3 counter. The intensity was measured both with the tube empty and with the tube containing deuterium at a pressure of 406.9 cm Hg. Without deuterium the beam intensity was measured as 1672.1 ± 5 counts per minute with a background of 86 ± 2 c/min., corresponding to a net count of 1586 ± 6 c/min. With the deuterium in the tube the count was 781.9 ± 4 c/min. with a

background of 74.8±2 c/min., corresponding to a net count of 707±5 c/min.

From these data the cross section of the deuterium molecule at 77.5°K for BeO filtered neutrons is found to be $(21.3\pm0.2)\times10^{-24}$ cm².

The average wave-length of the BeO filtered neutrons used in this experiment was measured by a subsidiary experiment. The cross section of B^{10} in the form of BF_3 was measured for monochromatic neutrons of known wave-length obtained by reflection from a (1, 1, 1) face of a LiF crystal, and for the filtered neutrons. Assuming a $1/v$ law for the boron absorption, the average wave-length of filtered neutrons is then calculated. The particular face (111) of LiF was chosen, because for it the correction caused by high orders in the range of wave-lengths used is negligible.

In order to measure transmissions of the order of 0.5 for a large range of wave-lengths, two interconnected transmission tubes filled with $B^{10}F_3$ were used. One was 3.569 cm long and the other was 17.556 cm. The short transmission tube was used to measure the cross section of the filtered neutrons, and the long tube was used to measure the cross sections of the monochromatic neutrons whose wave-length ranged from 0.8A to 1.3A. The average wave-length, after correcting for air absorption and for scattering, was found to be 5.43A.

III. DETERMINATION OF THE CROSS SECTION OF D_2 FOR EPITHERMAL NEUTRONS

The cross section of deuterium for epithermal neutrons was measured for resonance neutrons of indium and silver. A beam of neutrons coming from the surface of the pile and which contained therefore a large amount of epithermal neutrons was used. A cadmium foil was inserted into the beam to absorb the thermal neutrons.

When a resonance detector like silver or indium is used, the activity induced is due to some extent to very high energy neutrons. One expects that the cross section of deuterium is smaller for such neutrons than for neutrons of a few volts. In order to minimize the contribution of the high energy neutrons, each measurement of induced activity is taken with and without a thin absorber made of the same element as the detector, and the difference is used. In this way, only neutrons belonging to the low resonance bands are counted.

The deuterium was in the form of 99.74 percent pure D_2O, the contaminant being H_2O. If the cross section of oxygen were well known, it could be directly subtracted, since for epithermal neutrons interference phenomena are negligible. In order to minimize the error introduced by inaccuracies in the oxygen cross section, the following method to cancel it was used. In one measurement, the absorber in the neutron beam was n moles of D_2O and n moles of Be. The intensity transmitted through this absorber was compared with the intensity transmitted in a second measurement in which the absorber was n moles of BeO. The difference in these two transmitted intensities is due to the deuterium only.

Actually, the absorbers used in the two measurements contained the following quantities:

Absorber 1	moles/cm²	Absorber 2	moles/cm²
D_2O	0.2999	BeO	0.3016
H_2O	0.0008	O_2	0.00004
Be	0.3051	N_2	0.00018

If R is the ratio of the intensity transmitted by absorber 2 to that transmitted by absorber 1, one finds

$$\ln R = 0.6023[0.5998\sigma_D + 0.0035\sigma_{Be} - 0.0010\sigma_O + 0.0016\sigma_H - 0.00036\sigma_N].$$

The σ's represent the cross sections of the respective elements in units of 10^{-24} cm². All cross sections except σ_D appear with very small coefficients so that an error in their values is unimportant. The values which were used were $\sigma_{Be}=6.1$, $\sigma_O=4.1$, $\sigma_H=21$, $\sigma_N=10$.

The measurement with silver gave

$$\ln R = 1.293\pm0.023.$$

That with indium gave

$$\ln R = 1.247\pm0.021.$$

The average of these two, 1.27±0.02, was then used to calculate σ_D. One finds $\sigma_D=3.44\pm0.06$.

IV. THEORY

The above experiments have determined the cross section of the deuterium molecule for neu-

trons of average wave-length 5.43A at 77.5°K ($\sigma(D_2)=21.3\times10^{-24}$ cm²) and of the deuterium atom for neutrons of a few volts ($\sigma(D)=3.44\times10^{-24}$ cm²).

These two cross sections can be expressed in terms of the scattering lengths a_2 and a_4 corresponding to antiparallel and parallel orientation of spins of the neutron and the deuteron, respectively.

$\sigma(D)$ is simply expressed by the formula

$$\sigma(D)=4\pi(\tfrac{2}{3}a_4^2+\tfrac{1}{3}a_2^2).$$

In this formula the factors $\frac{2}{3}$ and $\frac{1}{3}$ correspond to the probabilities of parallel and of antiparallel orientation. The calculation of the scattering cross section of the deuteron is more complicated and is similar to that made by Schwinger and Teller[3] for the scattering cross section of the hydrogen molecule. In the experiments the ortho-para ratio was unchanged from that at room temperature. On the other hand, the distribution of the rotational states was that for a temperature of 77.5°K. $\sigma(D_2)$ is an average of the values for the individual states corresponding to this distribution. The results of the calculation of the ratio $\sigma(D_2)/\sigma(D)$, not including the correction of the Doppler effect, are given below:

g	$\sigma(D_2)/\sigma(D)$
0.0	$5.76-1.92\delta+0.0035/g+0.035\delta/g$
0.2	$5.65-1.67\delta$
0.4	$5.23-1.58\delta$
0.6	$4.58-1.36\delta$
0.8	$3.85-0.98\delta$
1.0	$3.13-0.55\delta$
1.1	$2.81-0.36\delta$

In this table g is the relative velocity measured in units of $5\hbar/(2Mr)$ where M is the proton mass and r is the interatomic distance in the deuterium molecule, 0.747×10^{-8} cm. δ is the following function of a_2 and a_4:

$$\delta=(a_4-a_2)^2/(2a_4^2+a_2^2).$$

The cross section becomes infinite at zero velocity. However, the coefficient of the infinite terms is very small.

The Doppler correction was calculated using the formula

$$\sigma_{\text{eff}}=\frac{2\exp(-q^2/q_0^2)}{(\pi)^{\frac{1}{2}}q_0q^2}\int_0^\infty g^2\sigma(g)dg \times\sinh(2qg/q_0^2)\exp(-g^2/q_0^2),$$

where q is the velocity of the neutrons in units $5\hbar/(2Mr)$ and q_0 is the characteristic velocity of the Maxwell distribution written in the form $\exp(-q^2/q_0^2)$. For deuterium at 77.5°K, q_0 is 0.269. The integral is obtained by a numerical integration.

The following values were found for the ratio $\sigma(D_2)/\sigma(D)$ corrected for the Doppler effect:

q	$\sigma(D)_2/\sigma(D)$
0.3	$6.851-2.022\delta$
0.368	$6.047-1.768\delta$
0.4	$5.782-1.680\delta$

The effective wave-length of the neutrons used in the determination of $\sigma(D_2)$ was 5.43A, for which q is 0.346. By interpolation one finds, for $q=0.346$,

$$\sigma(D_2)/\sigma(D)=6.271-1.865\delta.$$

The measured value of this ratio is 21.3/3.44 or 6.19. Consequently, δ is very small.

$$\delta=0.04\pm0.10.$$

Since δ is essentially positive, this result enables one to assign to δ only an upper limit, namely, 0.14. If δ were zero, a_4 would be equal to a_2. To each value of δ there correspond two values of the ratio a_4/a_2, one greater and one less than one. For the upper limit, $\delta=0.14$, the two corresponding values of a_4/a_2 are 0.53 and 2.25. Since δ is between zero and 0.14, the ratio a_4/a_2 must lie between 0.5 and 2.3.

Therefore, it can be concluded that a_4 and a_2 have certainly the same sign. Their magnitudes, however, may differ by somewhat more than a factor 2. The sensitivity of this method is low when the value of a_4 is rather close to that of a_2. Consequently, only the above wide limits can be given for their ratio.

It is notable that deuterium does not share the peculiarities of hydrogen for which the two scattering lengths are of opposite sign and of such magnitudes that the neutron interference effects almost cancel as a result of the almost complete cancelation of the contributions of the two spin orientations.

[3] J. Schwinger and E. Teller, Phys. Rev. **52**, 286 (1937).

Mixed Cosmic-Ray Showers at Sea Level*

C. Y. CHAO**
Physics Department and Laboratory for Nuclear Science and Engineering, Massachusetts Institute of Technology, Cambridge, Massachusetts

(Received October 13, 1948)

A detailed analysis of 15 cloud-chamber photographs of mixed showers is given. This analysis gives the following results: (a) Mixed showers contain, in general, both slow and fast heavy particles in addition to the electron component. Some of the heavy particles can be identified as protons and some as mesons. (b) The electron component of the mixed showers consists sometimes of a single cascade shower and sometimes of several cascade showers. In cases where only a single cascade shower is present its axis is found to be within an angle of 2 or 3 degrees from the direction of the primary particle when this is observable. In cases where several cascade showers appear, one of them often propagates nearly in the direction of the primary particle when this is observable. (c) The simultaneous existence of several cascade showers with their axes diverging at fairly large angles indicates that several high energy electrons or photons are produced in the shower origin. (d) In three cases, an electron group is produced below the shower origin by a non-ionizing particle which seems to originate from the primary nuclear event. These particles may be photons. (e) In one case, two successive nuclear events are observed, which are separated by approximately 60 g/cm² of lead. (f) In one case, a star is produced by a penetrating shower particle after traversing approximately 30 g/cm² of lead.

I. INTRODUCTION

IT has been found recently that some of the cosmic-ray showers produced by penetrating particles consist both of energetic electrons and of particles heavier than electrons.[1,2] Such a shower has been given the name *mixed shower*. Many mixed showers were observed by W. B. Fretter[1] at sea level, and an extensive study of them at high altitude has been made by H. Bridge and W. Hazen.[3] We have also recently taken a series of cloud-chamber pictures for the investigation of shower production by penetrating particles at sea level.[4] In a total of 545 cloud-chamber pictures there were 19 mixed showers produced in the lead plates inside the cloud chamber. The apparatus is described in Section II of the present paper. A detailed analysis of 15 of the mixed showers is given in Section III, and a summary of the results in Section IV. The pictures of the remaining 4 mixed showers are not very clear and do not show points of special interest. Hence they are omitted. For comparison, we include the pictures of one very penetrating shower and of one electron shower.

II. APPARATUS

The cloud chamber was rectangular, 20 inches square and 11 inches deep. For 10 percent of the pictures the chamber contained 9 horizontal lead plates, 12 inches by 10 inches by $\frac{1}{2}$ inch. For the rest of the pictures the lowest lead plate was replaced with an aluminum plate $\frac{1}{16}$-inch thick. The illuminated depth of the chamber was 8 inches. Sterescopic pictures were taken with an angle of 12° between the two lines of sight.

A tray of 6 Geiger-Mueller counters, each 12 inches long and 1 inch in diameter, was placed just below the cloud chamber, and a second tray of 4 similar tubes was placed 18 inches below the first. The cloud chamber was expanded when any 4 tubes of the upper tray were discharged simultaneously with any two tubes of the lower tray. With this method of triggering, showers could be observed which were initiated by either ionizing or non-ionizing particles. A total of 545 pictures was obtained over a period in which the total sensitive time of the triggering apparatus was 184 hours. It is to be noted that the frequency of showers obtained depends largely on the counter arrangement, which selects

* Assisted by the joint program of the Office of Naval Research and the Atomic Energy Commission.

** On leave from Physics Department, National Central University and Institute of Physics, Academia Sinica, Nanking, China.

[1] W. B. Fretter, Phys. Rev. **73**, 41 (1948), also other references there.

[2] H. Bridge, W. Hazen, and B. Rossi, Phys. Rev. **73**, 179 (1948).

[3] H. Bridge and W. Hazen, Phys. Rev. **74**, 579 (1948).

[4] C. Y. Chao, Phys. Rev. **74**, 492 (1948).

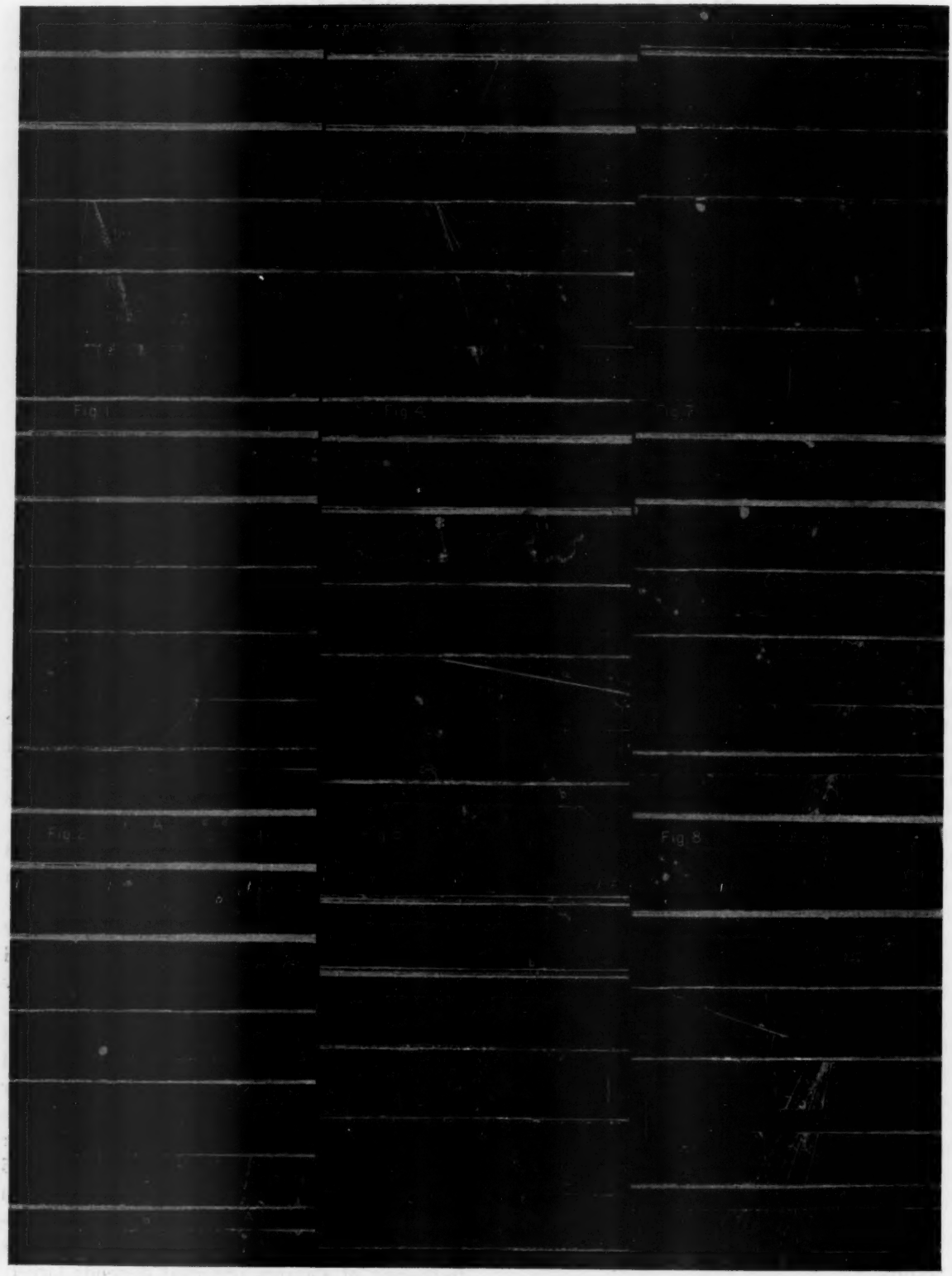

FIGS. 1–9. Shower Nos. 1–9.

showers of a certain type. Hence it is difficult to compare our results with those of others, with regard to the absolute rate of the events.

III. ANALYSIS OF THE SHOWER PICTURES

For convenience, the showers to be described are divided into the following groups:

(a) The first group contains those showers which have only one prominent electron sub-shower. There are 5 such cases (Shower Nos. 1–5).

(b) The second group contains those showers which have two or more electron sub-showers. There are 9 such cases (Shower Nos. 6–14).

(c) The third group contains one picture giving two showers produced in succession (Shower No. 15).

(d) The fourth group contains one very penetrating shower and one electron shower for comparison.

For identification of individual particles, we make use of the three criterions discussed in a paper by W. M. Powell.[5] They are: (a) the penetrating power of a particle in lead, (b) the rate of increase of ionization near the end of the range, and (c) the angle of scattering in lead. Criterion (a) makes it possible to distinguish between electrons and heavier particles. By means of (b) and (c), we can further distinguish between mesons and particles heavier than mesons. In the following analysis a particle is said to be heavily ionizing if it gives a track which is distinctly more intense than tracks of fast particles in the same location, and it is said to be penetrating if it traverses one or more half-inch lead plates without multiplication.

Group 1

Shower No. 1 (Fig. 1)

Origin.—The shower is produced in the 5th*** lead plate by the ionizing particle a, which is seen to traverse 3 lead plates without producing secondaries.

Heavily ionizing particles and penetrating particles.—The shower contains a heavily ionizing particle b making an angle of approximately 23° with the direction of the initiating particle in the plane of the picture. No penetrating particle is separately identifiable, possibly because the picture is not very clear.

Electronic component.—The electronic component has a single core making an angle of approximately 2° with the direction of the initiating particle. It contains about 40 electrons at the maximum, hence possesses an energy of about 4 Bev.[6]

Shower No. 2 (Fig. 2)

Origin.—The shower is produced in the 8th lead plate by the ionizing particle a, which is seen to traverse 4 plates without producing secondaries. The accompanying track x is more diffused and is therefore not simultaneous with the shower.

Heavily ionizing particles and penetrating particles.—The shower contains heavily ionizing particles b, c, and possibly d. Particle b goes upwards and has a δ-ray. From the energy and the angle of ejection of the δ-ray, the energy of particle b, assumed to be a proton, is estimated to be about 60 Mev. Since the shower starts at the last lead plate, penetrating shower particles can only be recognized if they go upwards. No such penetrating particles are found in this shower.

Electronic component.—The particles of group A, about 5 in number, are probably electrons because they have a narrow angular spread which is characteristic of electron groups. The pair f may or may not belong to the same group.

Shower No. 3 (Fig. 3)

Origin.—The shower is produced in the 6th lead plate, probably by the ionizing particle a, which is seen to traverse 2 plates without producing secondaries.

Heavily ionizing particles and penetrating particles.—The shower contains a heavily ionizing particle b, which penetrates one lead plate. Since particle b gives heavy ionization both above and below the 7th plate, it is probably a proton.

Electronic component.—The electronic component A contains about 10 particles below the 7th plate. It is excited by a non-ionizing particle which is probably produced in the primary interaction in the 6th plate. If this is the case, since

[5] W. M. Powell, Phys. Rev. 69, 385 (1946).

*** This is the actual plate number inside the chamber but not the number counted from the top of the figure since only the important part of the original negative is reproduced here.

[6] S. Belenky, J. of Phys. U.S.S.R. 8, 305 (1944).

the shower origin is located near the upper surface of the 6th plate, the particle which initiates the electron group traverses more than a half inch of lead before giving rise to the latter. It is rather unfortunate that in the other stereoscopic picture the track of particle *a* is covered by the bright background of one of the Lucite plate-supporters. The interpretation of this shower is thus made less reliable.

Shower No. 4 (Fig. 4)

Origin.—The shower is produced in the 5th lead plate most probably by the ionizing particle *a*, which is seen to traverse 4 plates without producing secondaries. The accompanying particle *x* seems to be simultaneous but is probably unrelated to the shower.

Heavily ionizing particles and penetrating particles.—The shower contains two penetrating particles, *b* and *c*. Since particle *c* gives heavy ionization both above and below the 4th plate, it is probably a proton. The shower contains two additional heavily ionizing particles, *d* and *f*, stopping in the 6th plate.

Electronic component.—The electronic component makes an angle of about 2° with the

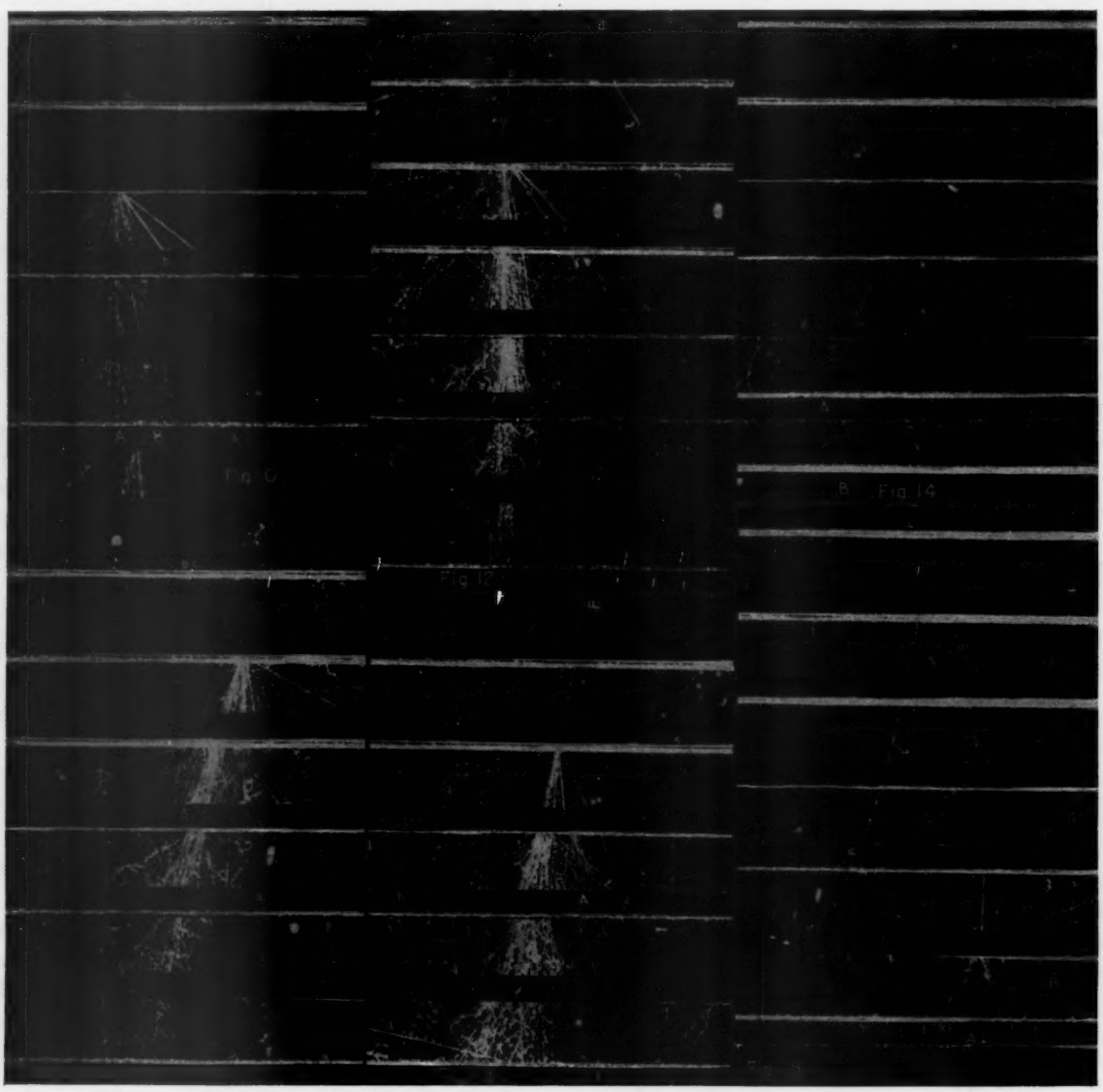

FIGS. 10–15. Shower Nos. 10–15.

direction of the initiating particle and contains about 30 particles below the 7th plate. The pair *g* may or may not be an electron pair. Perhaps it gives rise to group *h*.

Shower No. 5 (Fig. 5)

Origin.—The shower is produced in the 6th lead plate near the rear edge of the illuminated region and is inclined forward. Hence it cannot be established whether the initiating particle is or is not ionizing. The tracks below the 8th plate are slightly displaced towards the right because of convection currents.

Heavily ionizing particles and penetrating particles.—The shower contains one heavily ionizing particle, *a*, one penetrating particle, *b*, and possibly another penetrating particle, *c*. Particle *c* may be a meson, as is shown by the large deflection in the 7th plate and by its stopping in the 8th plate without giving heavy ionization above that plate.

Electronic component.—The electrons form a single group starting from the shower origin. There are about 15 to 20 particles in the group below the 8th plate.

Shower No. 6 (Fig. 6)

Origin.—The shower is produced in the 5th lead plate, probably by the ionizing particle *a*, which is seen to traverse 2 plates without producing secondaries. The accompanying tracks, *z* and *y*, are apparently simultaneous, but probably unrelated to the shower. The particle *b* going upwards is found to pass at a little distance in front of the shower origin. It may either have been scattered or produced by a secondary event.

Heavily ionizing particles and penetrating particles.—The shower gives a penetrating particle *c*. The particle is heavily ionizing below the 6th plate and then passes out of the illuminated region. There may be other penetrating particles which are not easily identifiable individually.

Electronic component.—The shower contains two electron groups (or subshowers). Group *A* has approximately 20 particles at the maximum, and group *B* approximately 10 particles. Their energies are, therefore, about 2 Bev and 1 Bev, respectively. The projected angle between them is about 21°. If the two groups were produced by an electron pair which is, in turn, created by a single photon, the average angle of emission of each electron would be of the order of mc^2/U, or about 0.03°. On the other hand, the average angle of scattering of an electron of 1 Bev through one-half inch of lead is about 1.5°. Hence the two groups cannot be produced by a single photon. The projected angle between the axis of group *A* and the direction of particle *a* is about 6°. There may be a small group *C* produced in the 6th plate and stopping in the 7th plate.

Shower No. 7 (Fig. 7)[****]

Origin.—The shower is produced in the 6th lead plate by the ionizing particle *a*, which is seen to traverse 4 plates without producing secondaries.

Heavily ionizing particles and penetrating particles.—The shower gives two penetrating particles, *b* and *c*, at the left side. Particle *b* is also heavily ionizing. The density of track *b* decreases as it proceeds because the particle travels from a well illuminated region to the edge of that region. Particle *c* gives a star in the 8th plate.

Electronic component.—The shower has two electron groups *A* and *B*. Each group contains about 20 electrons below the 8th plate. This would mean an initiating energy of about 2 Bev for each group. The projected angle between the two cores is about 15°, which is again much too large if the groups were initiated by a single photon. Group *A* makes an angle of about 2° with the direction of the initiating particle *a*.

Shower No. 8 (Fig. 8)

Origin.—The shower is produced in the 6th lead plate, most probably by the ionizing particle *a*, which is seen to traverse 5 plates without producing secondaries. Behind the track *a* there is another track which is seen separated from *a* in the other stereoscopic view. By reprojecting the stereoscopic pictures, this second track is found to pass at a small distance behind the shower origin. The shower contains two particles, *b* and *c*, going upwards. Since the track of particle *c* does not pass through the origin exactly when prolonged backwards, particle *c* may have been scattered in the lead plate or both particles *b* and *c* may have been produced in-

[****] This picture was published previously in reference 4 without a detailed analysis.

directly by one of the shower particles emerging from the origin. The two other pairs of tracks above the 6th plate probably also belong to the shower.

Heavily ionizing particles and penetrating particles.—The shower contains heavily ionizing particles *d*, *f*, *g*, *h*, and possibly also *i*, of which *d* is penetrating. It contains at least 3 other lightly ionizing penetrating particles, *j*, *k*, and *l*. Particle *d* gives rise to a δ-ray. From the energy and the angle of ejection of the δ-ray, the energy of particle *d*, assumed to be a proton, is estimated to be about 30 Mev below the 7th plate, or about 160 Mev in leaving the 6th plate. The density of the track is consistent with this result. Particle *h* passes out of the illuminated region at the rear. The light track which appears coincident with the track of *h* in this view is due to another particle. There is also a δ-ray on the track of *h*, but the angle of ejection of this δ-ray cannot be measured with sufficient accuracy to give a reasonable estimate of the energy of particle *h*.

Electronic component.—The electrons of the shower appear to form at least two groups *A* and *B*. The two groups contain about 15 and 10 particles, respectively, below the 8th plate, and their axes make an angle of about 6° in the plane of the picture. Group *A* is practically in the same direction as the particle *a*. Both groups *A* and *B* seem to start multiplication in the 7th plate. However, group *A* may have started multiplication in the 6th plate and so have the apparent form of the heavy track *i*. Group *B* seems to be produced by a non-ionizing particle emerging from the shower origin. Stereoscopic examination shows that the light track above group *B* in this view is not coincident with the axis of the group.

Shower No. 9 (Fig. 9)†

Origin.—The shower is produced in the 6th lead plate very close to the center of the illuminated region by a non-ionizing particle.

Heavily ionizing particles and penetrating par-

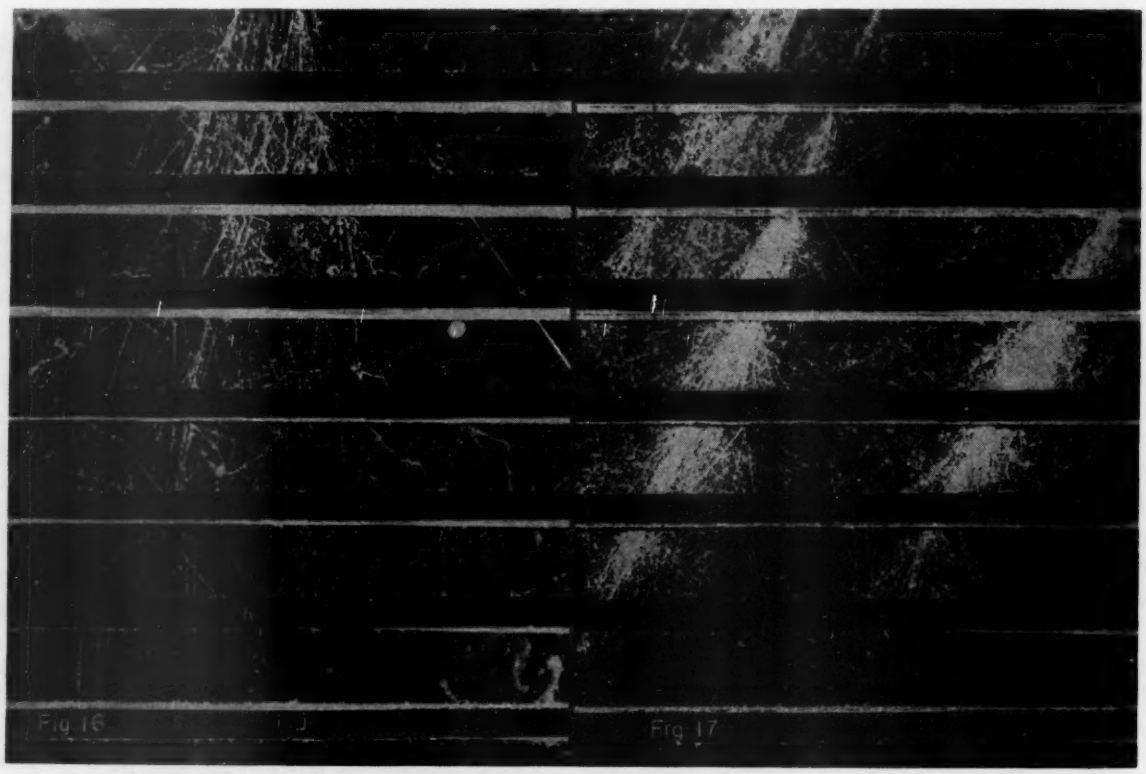

FIGS. 16 and 17. Shower Nos. 16 and 17.

† This picture was published previously in reference 4.

ticles.—The shower contains at least 3 heavily ionizing particles, *a*, *b*, and *c*. Particle *a* seems to traverse the 7th plate and to stop in the 8th plate. Particle *b* gives rise to a δ-ray, from which the energy of this particle, assumed to be a proton, is estimated to be about 60 Mev. Particle *b* may not belong to the shower, or both *b* and *c* may originate from a secondary process of one of the shower particles emerging from the primary origin. The general form of the shower shows that it must contain quite a number of penetrating particles. The penetrating particle *d*, which can be traced back to the shower origin stereoscopically, is seen to be a meson from the angles of deflection in the lead plates.

Electronic component.—The electrons can be attributed to two main groups, *A* and *B*, each containing about 15 particles below the 8th plate. The axes of the two groups make an angle of approximately 15° in the plane of the picture. There are two more small groups, *C* and *D*. Group *C*, containing about 5 particles, appears to be produced by a non-ionizing particle, which is probably emitted in the primary event. If this is the case, the initiating particle of group *C* must travel through more than a half-inch of lead before giving rise to the electron group.

Group 2

Shower No. 10 (Fig. 10)

Origin.—The shower is produced in the 5th lead plate by the ionizing particle *a*, which is seen to traverse 3 plates above the shower origin with only the production of a knock-on electron in the 4th plate.

Heavily ionizing particles and penetrating particles.—The shower contains two heavily ionizing particles, *b* and *c*. There is a light track below the end of track *c* in the figure. These two tracks are found to be unrelated to each other by stereoscopic examination. The general shape of the shower indicates that it contains a number of penetrating particles. The penetrating particle *d* traverses 3 lead plates.

Electronic component.—There seem to be at least two electron groups, *A* and *B*, each containing about 10 particles below the 7th plate. The axes of the two groups make an angle of about 10° in the plane of the picture. Group *A* is nearly in the same direction as the initiating particle and propagates through the 8th plate. (The tracks below the 8th plate are displaced toward the right by a convection current.)

Shower No. 11 (Fig. 11)

Origin.—The shower is produced in the 3rd plate, possibly by the ionizing particle *a*. The track *xx'* passes very close to the origin but is probably unrelated to the shower. The shower contains at least 3 particles, *b*, *c*, and *d*, going upwards.

Heavily ionizing particles and penetrating particles.—The shower contains at least two heavily ionizing particles, *b* and *f*, emerging from the origin. There is another heavily ionizing particle†† below the 8th plate, which may or may not belong to the shower. The shower possibly contains a number of penetrating particles, as seen from the general shape.

Electronic component.—The electrons seem to form two groups, the main group *A* containing about 50 particles at the maximum and a less distinct small group *B* containing about 15 particles at the maximum. The axes of *A* and *B* make projected angles of approximately 4° and 10°, respectively, with the direction of particle *a*.

Shower No. 12 (Fig. 12)

Origin.—The shower is produced in the 3rd lead plate probably by the ionizing particle *a*. This seems most likely, since it is observed that there is often a prominent electron group which propagates nearly in the direction of the initiating particle when the latter is observable. There are 3 particles, *b*, *c*, and *d*, going upwards.

Heavily ionizing particles and penetrating particles.—The shower contains a number of penetrating particles. Particles *d*, *f*, and *g* traverse at least one lead plate, *h* at least two plates, and *i* stops in the 8th plate. Particle *i* gives heavy ionization both above and below the 7th plate; it is, therefore, probably a proton. In addition to *i*, there are two heavily ionizing particles, *j* and *k*. There is another interesting particle, *l*, which gives rise to a δ-ray. Most likely, particle *l* is a meson or proton since it is not appreciably deflected by the collision.

†† The track of this particle is not in the figure.

Electronic component.—The electrons seem to belong to two groups, a larger group A propagating nearly in the direction of particle a and a smaller group B. The two groups have their axes making an angle of about 5° and largely overlap each other. They jointly give about 50 particles at the maximum below the 6th plate.

Shower No. 13 (Fig. 13)

Origin.—The shower is produced in the 4th lead plate by the ionizing particle a, which is seen to traverse 3 plates without producing secondaries. The tracks x and y are inclined at much larger angles toward the rear of the cloud chamber than the track a, and are therefore unrelated to the shower. Track x looks also older than the shower tracks.

Heavily ionizing particles and penetrating particles.—The shower contains at least two heavily ionizing particles, b and c, emerging from the origin. The heavily ionizing particles, d and f, may or may not belong to the shower. The shower contains a number of identifiable penetrating particles, g, h, i, and j. Particle h is probably a meson, as indicated by the large deflection in the 5th plate.

Electronic component.—The core of the shower appears to propagate in the direction of the initiating particle a and to fan out continuously from the origin. This may be due to the presence of penetrating particles or of several electron groups making small angles between themselves, or due to both causes. The maximum number of the shower particles occurs below the 6th plate and is about 50. The small group A contains about 10 particles.

Shower No. 14. (Fig. 14)

Origin.—The shower is produced in the 6th lead plate at the rear edge of the illuminated region and is inclined forwards. Hence the character of the initiating particle cannot be determined.

Heavily ionizing particles and penetrating particles.—The shower contains at least 3 penetrating particles, a, b, and d. They are heavily ionizing both above and below the 7th plate, though their tracks near the origin are rather faint because of the weak illumination in that region. Hence particles a, b, and d are probably protons. From the δ-ray on its track, the energy of particle d, assumed to be a proton, is estimated to be about 100 Mev below the 7th plate, or about 200 Mev as it leaves the 6th plate. There probably are other penetrating particles, but their identification is not very conclusive. Particle c is heavily ionizing, and cannot be traced beyond the 7th plate.

Electric component.—The shower contains two groups of electrons A and B, each containing about 5–10 particles. Because of a convection current at the left corner below the 8th plate, group B is somewhat displaced toward the right, and consequently it is impossible to determine its initiating particle. It is, however, certain that group B is not a continuation of group A, because the horizontal distance between the two groups as shown in the picture is greater than the possible displacement due to such a disturbance and, furthermore, group B appears to be nearer to the front than group A. Hence, group B is most likely produced in the 8th plate by a shower particle from the primary origin.

Group 3

Shower No. 15 (Fig. 15)

Origin.—There are two showers in this picture. The first shower is produced in the 3rd lead plate by the ionizing particle a. The second shower appears to be produced in the 7th plate by an ionizing particle which comes out of the center of the first shower exactly in the direction of particle a. It may be the same particle, or a secondary particle which takes most of the momentum of the primary particle. The accompanying track x is sharper than the shower tracks and is therefore not simultaneous with the two showers.

Heavily ionizing particles and penetrating particles.—The first shower contains only about 10 tracks. One track corresponds to a very penetrating particle b, making a small angle with particle a and traversing at least 4 lead plates. A second track corresponds to a penetrating particle c. This track becomes heavier each time the particle traverses a lead plate between the 3rd and the 6th. The increase of ionization is consistent with the assumption that the particle

is a proton. From the δ-ray on the track of particle *c*, the energy of this particle, if it is a proton, is estimated to be about 200 Mev below the 4th plate or about 250 Mev in leaving the 3rd plate. This is consistent with the range of the particle in lead.

The second shower has several particles going upwards. It contains about 9 heavily ionizing particles, of which particles *d*, *f*, *i*, *j*, and *k* are very prominent. Particles *i*, *k*, *l*, and *m* penetrate the 8th lead plate. It is possible that particle *k* gives a group of 3 particles below the 8th plate. Poor illumination makes it difficult to decide whether or not these particles are heavily ionizing.

Electronic component.—In the first shower there is no electron group which can be identified with certainty. In the second shower, group *A* may be composed of electrons. It contains 5 or more particles below the 8th plate, and its axis makes an angle of approximately 18° with the initiating particle of the second shower in the plane of the picture. There is another small group *B*, which may also consist of electrons belonging to the second shower.

Group 4

Shower No. 16 (Fig. 16)

This is a very penetrating shower, produced in the upper wall of the cloud chamber or somewhere above the chamber. The tracks below the 8th plate are displaced towards right by about one-third inch in a full size view by a convection current. The shower contains many penetrating particles. Some of them are individually identifiable, such as *a*, *b*, *c*, *d*, *f*, *g*, *h*, *i*, *j*, and *k* on the figure. Particle *k* is probably a proton as it gives heavy ionization both above and below the 4th lead plate. Particle *c* seems to be a meson because it is deflected through a large angle at the 2nd lead plate and stops in the 3rd plate without having very heavy ionization above that plate.

The electronic components in this shower are not very prominent.

Shower No. 17 (Fig. 17)

This is a group of showers produced in the lead plates by a number of high energy electrons and photons belonging to an air shower. These electrons and photons are inclined at approximately 15° toward the back of the chamber and 35° toward the left. The two largest showers contain several hundred electrons each, at the maximum, and thus indicate energies of the order of several tens of Bev. A number of stars are seen in the picture.

IV. SUMMARY OF RESULTS

From the foregoing analysis we can summarize the following conclusions: (a) Of the 15 mixed showers produced in the lead plates, all contain heavily ionizing particles. Fifteen of these particles are seen to penetrate one or more lead plates after they become heavily ionizing. They are identified as protons or particles still heavier than protons. In addition to these, there are 18 individually recognizable penetrating particles which are lightly ionizing. They may be fast mesons or fast particles heavier than mesons. One of them is identified as a meson by its large scattering in two lead plates (in Shower No. 9). There are two other penetrating particles which are scattered only once in lead through a large angle. They are probably also mesons.

(b) The electron component of the mixed showers consists sometimes of a single cascade shower and sometimes of several cascade showers. In cases where only a single cascade shower is present, its axis is found to be within an angle of 2 or 3 degrees from the direction of the primary particle when this is observable. In cases where several cascade showers appear, one of them often propagates nearly in the direction of the primary particle when this is observable.

(c) The simultaneous existence of several cascade showers with their axes diverging at fairly large angles indicates that several high energy electrons or photons are produced in the shower origin.

(d) In three cases, an electron group is produced below the shower origin by a non-ionizing particle which seems to originate from the primary nuclear event. (Shower Nos. 3, 8, and 9.) The energy required to produce these electron groups is of the order of 1 Bev. The particles which initiate these groups would not seem to be neutrons because neutrons would not be

likely to produce electron showers unaccompanied by heavy particles. If one assumes that the initiating particles are photons from the shower origin, one must consider two of the three cases, in which the particles traverse more than a half-inch of lead before giving rise to the electron groups. (Shower Nos. 3 and 9.) Since the probability that photons of 1 Bev will traverse so much lead without undergoing materialization is about 0.2, the photon hypothesis can account for the observations.

(e) In one case a penetrating particle produces a nuclear event in one lead plate, and one of the shower particles, which may be the primary particle itself, produces a mixed shower after traversing 60 g/cm² of lead.

(f) In one case a star is produced by a penetrating shower particle after traversing approximately 30 g/cm² of lead.

The foregoing results about the electron groups of the mixed showers comply with the assumption that these groups originate from photons or electrons produced either directly in the nuclear interactions or indirectly through the decay of short-lived mesons produced in these interactions.

ACKNOWLEDGMENTS

The author is grateful to Professor Bruno Rossi for his encouragement during the course of this experiment, and to Mr. H. Bridge and Mr. R. J. Davisson for their suggestions and help. He is also indebted to Professor G. E. Valley and Mr. A. L. Jerrems who designed and built the cloud chamber.

PHYSICAL REVIEW VOLUME 75, NUMBER 4 FEBRUARY 15, 1949

East-West Asymmetry and Latitude Effect of Cosmic Rays at Altitudes up to 33,000 Feet*

W. C. BARBER**
Department of Physics, University of California, Berkeley, California
(Received October 28, 1948)

By means of triple coincidence telescopes mounted in a B-29 airplane, the east-west asymmetry of cosmic rays has been measured at several geomagnetic latitudes from 0 degrees to 41 degrees north. The asymmetry was determined separately for the hard, soft, and shower producing components of the radiation. At a zenith angle of 45 degrees, the intensity of each of these components from the western direction exceeded that from the eastern direction by an amount which increased rapidly as the geomagnetic latitude was decreased. Comparison of the amount of asymmetry with the observed latitude effects permits the conclusion that all components arise from primary rays which in the range of energies explored by the experiment are all or nearly all positively charged.

During the course of the experiments, vertical intensities of the hard and soft components were also measured. Data on the variation of the vertical intensities with altitude and with geomagnetic latitude are presented.

I. INTRODUCTION

THE theory of the geomagnetic effects on charged particles has been worked out by Stoermer[1] and Lemaitre and Vallarta[2] and others so that quantitative conclusions about the primary cosmic rays can be drawn from observations of the cosmic-ray particles found in the earth's atmosphere. Measurements of the latitude effect give information about the momentum spectrum of the primary particles, and when the momentum spectrum is known, observations of the east-west asymmetry can be used to determine the sign of the charge of the primary particles.

Many ground level east-west asymmetry ex-

* This work was supported in part by the Atomic Energy Commission and the Office of Naval Research.
** Now at Stanford University.
[1] C. Stoermer, Vid. Selsk. Skr. Christiana (1904, 1913).
[2] G. Lemaitre and M. S. Vallarta, Phys. Rev. 50, 493 (1936).

periments[3] and recent measurements made in a B-29 airplane by Schein, Yngve, and Kraybill[4] give convincing evidence that the hard component of the cosmic rays arises from primary rays which are mostly positively charged.

The situation with regard to the soft component is not so clear. Ground level measurements do not yield information about the primaries of the soft component because this component is so rapidly absorbed in the atmosphere. An important experiment performed by Johnson and Barry[5] in 1939 to measure the east-west asymmetry at high altitudes indicated that the primary cosmic rays are a mixture of positive and negative particles. At atmospheric pressures less than 5 cm of Hg the east-west asymmetry of the total radiation was found to be about 7 percent, whereas an effect of 60 percent was expected if the primary rays were exclusively positive. However, the balloon experiments of Schein, Jesse, and Wollan[6] and of Hulsizer and Rossi[7] indicate that the primary radiation contains almost no shower producing particles such as electrons. Taken together the two lines of evidence appear to require the existence in the primary radiation of penetrating negative particles which do not excite mesotrons but go into the production of the soft component.[8]

The present latitude effect and east-west asymmetry experiments were undertaken in order to help clear up this question of the origin of the soft component. A B-29 aircraft was available for the experiments, and although these planes cannot reach altitudes where it would be most desirable to do the experiment, their ceiling of 35,000 feet or more is high enough that the magnetic field sensitive primaries of the soft component can make their effects felt.

II. EXPERIMENTAL APPARATUS

The apparatus for the experiment consisted of six triple coincidence telescopes which were operated simultaneously and which could be rotated and tilted into various positions. The telescopes were arranged in three pairs. One telescope of each pair contained 14 cm of lead absorber and thus measured only the hard component. The other telescope was without lead shielding and thus measured the total cosmic-ray intensity except for those low energy particles which could not penetrate the brass walls of the counters. The soft component intensity was obtained by subtracting the hard from the total intensity.

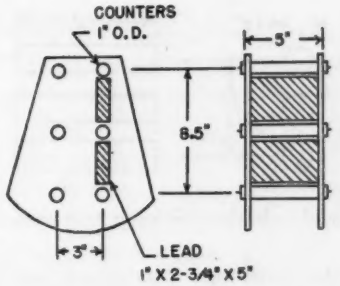

FIG. 1. Geometry of a counter telescope pair.

In the course of the experiments, telescopes of two different sizes were used. The geometrical arrangements of the two different telescopes are shown in Figs. 1 and 2. The small telescopes employed counters made of brass tubing with 0.030-inch walls. The tubing was one inch in outside diameter, and the exposed length of the central wire (0.003-inch diameter) was $3\frac{15}{16}$ inches. The extreme angular aperture of this unit was about ± 6 degrees by ± 24 degrees, but since the effective area of the telescope is smaller for the oblique angles, the average angle of the rays

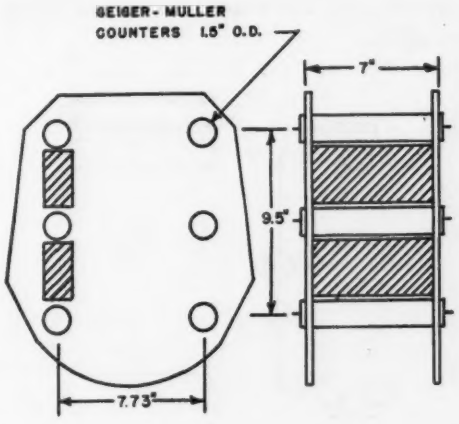

FIG. 2. Geometry of a large counter telescope pair.

[3] T. H. Johnson, Rev. Mod. Phys. 10, 193 (1938).
[4] M. Schein, V. H. Yngve, and H. L. Kraybill, Phys. Rev. 73, 928 (1948).
[5] T. H. Johnson and J. G. Barry, Phys. Rev. 56, 219 (1939).
[6] M. Schein, W. P. Jesse, and E. O. Wollan, Phys. Rev. 59, 615 (1941).
[7] R. I. Hulsizer and B. Rossi, Phys. Rev. 73, 1402 (1948).
[8] N. Arley, Phys. Rev. 70, 975 (1946).

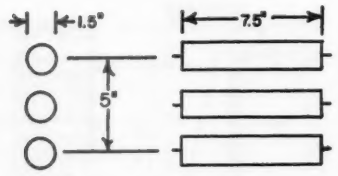

FIG. 3. Total radiation telescope with close geometry.

entering the telescope was much less than one-half of the values given. The counters of the larger telescopes were $1\frac{1}{2}$ inches in outside diameter with brass walls of 0.045-inch thickness. In this case the exposed length of the central wire was $5\frac{15}{16}$ inches so that the extreme angular aperture was about ± 9 degrees by ± 32 degrees. During the east-west experiments the telescopes were operated so that the best resolution was in the zenith angle.

For some of the latitude measurements on the vertical rays, the larger counters were used in a close geometry so that a larger solid angle was obtained. This geometry is shown in Fig. 3.

Experiments were also performed with a counter geometry which selected shower producing particles. For these experiments three of the larger size counters were placed in coincidence and arranged to form a triangle. In all of the shower measurements a $\frac{1}{2}$-inch layer of lead was placed above the top counter. The geometry of the shower arrangement is shown in Fig. 4.

The counters were filled with argon and a quenching vapor which in the small units was ethylene and in the large units was ethyl alcohol. The quenching gas was used in amounts of 10 to 15 percent, and the total pressure of filling was 10 cm of Hg.

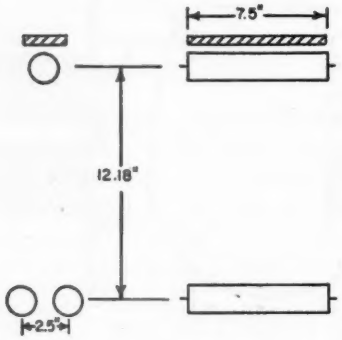

FIG. 4. Shower telescope.

Throughout most of the measurements the telescopes were used with an anticoincidence system in operation so that the background of coincidences due to showers was reduced. A coincidence of the three counters of the telescope measuring the hard intensity was not recorded if one or more counters of the associated telescope measuring the total intensity was discharged at the same time. Similarly, each one of the hard counters was in anticoincidence with the total telescope.

For some measurements the anticoincidence interconnection was removed. No anticoincidence was used with the telescope of Fig. 3 or the shower geometry of Fig. 4.

The resolving time of the coincidence circuits was about 7 microseconds, so that the rate of accidental triple coincidences was always less than 1 percent of the true rate and therefore negligible.

The calculated correction for loss in efficiency of a telescope due to the dead time of the individual counters was 4 percent in the case of the large telescopes at the highest altitude reached. This correction depends on the individual rates of the counters and therefore will not affect the measurement of the east-west asymmetry. The correction is most important in making measurements of intensity as a function of altitude. Some of these measurements were made with the present apparatus, but in this case the small telescope units were used and here the maximum correction is only about 2 percent.

The loss in coincidence counts due to the resetting time of the mechanical recorder was negligible in all cases except for the high altitude measurements made with the close geometry telescope of Fig. 3. In this case a correction was used which, at maximum, amounted to 3 percent.

III. MEASUREMENTS OF INTENSITY AS A FUNCTION OF ALTITUDE

The apparatus was operated successfully for 24 flights which were made during the period from February to July 1948. The total flying time was 160 hours, but the time spent at high altitudes in recording data was about 120 hours.

During the early flights, measurements of the vertical intensity of the hard and total components as a function of pressure altitude were

carried out. These measurements were intended chiefly as a test of the apparatus, and were therefore not exhaustive. However, the results are of some interest in their own right so they are given in Tables I and II. The results as given include a correction for counter dead time which at the maximum altitude amounted to 2 percent. The small telescopes were used exclusively for these measurements.

Table I gives the number of counts per minute when the anticoincidence protection against showers was employed. The column headed "W" gives the probable error based on the total number of counts recorded, while the column "W_0" gives the probable error as computed from the consistency of individual determinations. The general agreement between W and W_0 indicates the absence of gross experimental inconsistencies. At altitudes 25,000 and 36,000 feet measurements were also taken with 7 cm of lead absorber.

Table II gives the results obtained from one of the telescope pairs after the anticoincidence connection had been removed. The counting rates here are 5 to 10 percent higher than the corresponding rates in Table I.

In Fig. 5 the data of Table I are compared with results obtained by other investigators. The solid curves of Fig. 5 represent the absolute vertical intensity of the hard and total components as compiled by Rossi.[9] Table I and not Table II is used for the comparison because protection against showers was employed in most of the measurements presented by Rossi. The material of the total telescope was 5 g per cm² of brass for Rossi's case and also 5 g per cm² in the present experiments. The filters used for the hard component were 14.6 and 14 cm of lead for Rossi's curve and the present measurements respectively. No attempt at an absolute comparison of the intensities has been made. The hard component intensity of the present experiments has been fitted to Rossi's curve at an atmospheric depth of 955 g per cm², and all the other values of Table I have been plotted relative to this point. It is seen that at the higher altitudes the results of Table I lie below Rossi's curves. This difference can be accounted for in part by the

TABLE I. Vertical counter data with anticoincidence.

Geomagnetic latitude 41°N.							
Pressure altitude feet	Atmos. depth g/cm²	Total rate C/min.	W C/min.	W_0 C/min.	Hard rate 14-cm Pb C/min.	W C/min.	W_0 C/min.
2,200	955	0.79	±0.005	±0.01	0.57	±0.005	±0.008
15,000	583	3.20	±0.075	±0.035	1.27	±0.05	±0.055
20,000	475	5.13	±0.08	±0.035	1.72	±0.035	±0.03
25,000	383	8.50	±0.06	±0.07	2.18	±0.03	±0.03
29,000	321	10.55	±0.20	±0.20	2.68	±0.10	±0.11
33,000	266	14.20	±0.23	±0.22	3.01	±0.10	±0.07
36,000	231	16.3	±0.17	±0.22	3.24	±0.10	±0.14
25,000	383	——	——	——	7-cm Pb 2.69	±0.11	——
36,000	231	——	——	——	5.00	±0.16	——

TABLE II. Vertical counter data with no anticoincidence.

Geomagnetic latitude 41°N.					
Pressure altitude feet	Atmos. depth g/cm²	Total rate C/min.	W C/min.	Hard rate 14-cm Pb C/min.	W C/min.
2,200	955	0.84	±0.012	0.57	+0.01
20,000	475	5.95	±0.18	——	——
25,000	383	9.00	±0.09	2.35	±0.05
29,000	321	11.14	±0.20	2.72	±0.10
33,000	266	15.20	±0.15	3.41	±0.07
36,000	231	17.60	±0.24	3.85	±0.10

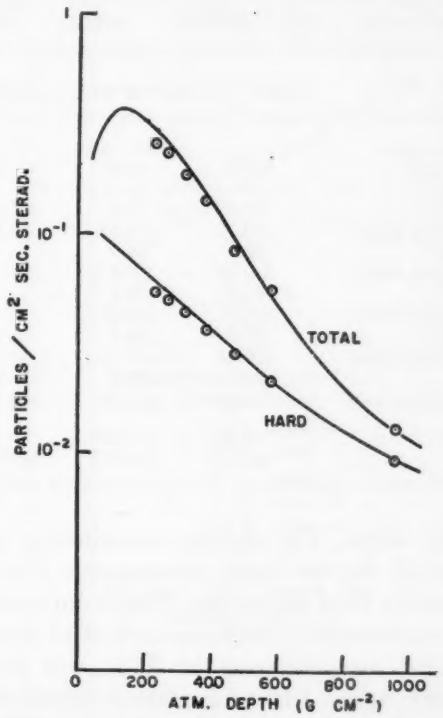

FIG. 5. Intensity of the total and hard radiation as a function of atmospheric depth. The solid curve represent the data compiled by Rossi (see reference 9). The points represent data taken with the telescopes of Fig. 1 where the hard component was filtered through 14 cm of lead and the absorber in the total telescope was 5 g per cm² of brass.

[9] B. Rossi, Rev. Mod. Phys. 20, 537 (1948).

TABLE III. Vertical intensity of showers, soft component, and total radiation at 2 different altitudes.

Pressure altitude feet	Atmos. depth	Geomagnetic latitude 41°N. Plus and minus (Figures are probable error) Shower rate geometry Fig. 4	Soft rate From Table I by subtraction	Total rate geometry Fig. 3	Total rate Table I
2,200	955	0.195±0.008	0.22±0.007	9.60±0.06	0.79±0.005
25,000	383	5.46 ±0.10	6.32±0.07	105.4 ±0.05	8.50±0.06
Factor of increase:		28.0 ±1.3	29.0 ±1.1	11.0 ±0.1	10.8 ±0.1

TABLE IV. Counting rates at 25,000 feet as a function of geomagnetic latitude.

Geomagnetic latitude	Total C/min. 45°E	45°W	Vertical	Hard C/min. 45°E	45°W	Vertical	Showers vertical C/min.
7° to 11°N	11.2	13.85	25.9	3.32	4.55	6.91	4.72
Probable error:	±0.30	±0.32	±0.30	±0.15	±0.18	±0.15	±0.10
24° to 30°N	14.05	15.70	——	3.93	5.15	——	5.21
Probable error:	±0.19	±0.21	——	±0.10	±0.12	——	±0.10
30° to 36°N	15.32	16.55	——	4.67	5.52	——	5.37
Probable error:	±0.19	±0.21	——	±0.11	±0.12	——	±0.10
41°N	16.35	17.30	33.0	4.93	5.37	9.21	5.46
Probable error:	±0.13	±0.13	±0.22	±0.07	±0.07	±0.12	±0.10
47° to 53°N	17.1	17.9	36.6	5.65	5.43	10.0	5.50
Probable error:	±0.44	±0.37	±0.20	±0.26	±0.21	±0.11	±0.10
$(I_{47}-I_9)/I_{47}=$	0.35	0.23	0.29	0.41	0.16	0.31	0.14
Probable error:	±0.032	±0.027	±0.010	±0.053	±0.05	±0.019	±0.026

TABLE V. Counting rates at 33,000 feet as a function of geomagnetic latitude.

Geomagnetic latitude	Total C/min. 45°E	45°W	Vertical	Hard C/min. 45°E	45°W	Vertical	Showers C/min. 45°E	45°W
1°S to 5°N	21.6	27.6	37.8	4.87	7.19	7.72	——	——
Probable error:	±0.30	±0.35	±0.8	±0.15	±0.18	±0.37	——	——
13° to 19°	22.7	28.6	——	4.72	7.69	——	5.46	6.40
Probable error:	±0.45	±0.4	——	±0.21	±0.21	——	±0.17	±0.17
20°	23.3	29.4	——	5.30	7.57	——	——	——
Probable error:	±0.21	±0.26	——	±0.11	±0.12	——	——	——
31° to 37°	28.6	32.4	——	6.70	7.93	——	6.22	6.45
Probable error:	±0.45	±0.51	——	±0.12	±0.14	——	±0.12	±0.13
41°	33.7	35.6	55.0	7.92	8.63	12.47	6.56	6.95
Probable error:	±0.25	±0.24	±0.9	±0.12	±0.12	±0.40	±0.12	±0.13
$(I_{41}-I_2)/I_{41}=$	0.36	0.225	0.31	0.385	0.17	0.38	——	——
	±0.012	±0.012	±0.022	±0.024	±0.025	±0.044	——	——

latitude effect. The present experiments were done at 41 degrees north geomagnetic latitude, whereas the data comprising Rossi's curves were taken at geomagnetic latitudes north of 45 degrees.

Vertical measurements at 2200 and 25,000 feet were taken with the shower telescope of Fig. 4 and the close geometry telescope of Fig. 3. A comparison of these measurements with the points of Table I, which correspond in altitude, is given in Table III. The total intensity as recorded by the geometry of Fig. 3 shows about the same increase in going from 2200 to 25,000 feet as does the intensity recorded by the total telescope of Fig. 1. The shower intensity, on the other hand, increases by about the same ratio as the soft component. This is to be expected, in that the showers are produced chiefly by electrons which also make up the bulk of the soft component.

IV. MEASUREMENTS OF THE EAST-WEST ASYMMETRY AND LATITUDE EFFECT

Measurements of the east-west asymmetry were carried out at several different geomagnetic

latitudes. Almost all of the measurements were made at pressure altitudes of either 25,000 or 33,000 feet and with the telescopes inclined at a zenith angle of 45 degrees.

It was unfortunately not possible to carry out the same type of flight plan in making all of the measurements. The plane was based at Inyokern, California, and by making flights from this base it was possible to make a series of measurements where the plane was flown back and forth (over a longitude range of 5 degrees) along the 41 parallel of geomagnetic latitude. Data about the point 34 degrees N geomagnetic latitude were obtained by making flights south from Inyokern along the coast of Lower California. In this case the results represent an average obtained over the range 31 to 37 degrees. Other measurements south of 34 degrees were made on a trip where the plane was flown to San Antonio, to Panama, and then south from Panama to the geomagnetic equator. The path was retraced for the return trip. Values of the east-west effect were measured enroute, but again the reported values represent averages over a range of latitudes. However, at Panama a flight was made under conditions similar to those which obtained at 41 degrees N. The plane was flown at 33,000 feet back and forth over a 5 degree range in longitude along the 20th parallel of geomagnetic latitude. Flights were also made north from Inyokern to the Canadian border in order to make more complete the range of latitudes covered by the experiment.

The geomagnetic positions have been obtained from the geographic positions by making use of the tables given by McNish.[10] The vertical and east and west counting rates as a function of geomagnetic latitude are given in Tables IV and V. The probable errors in each rate as determined from the number of counts recorded are also tabulated. At the bottom of each table the percent change of intensity over the range of latitudes is given. Because the measurements at 25,000 feet do not cover exactly the same range of latitudes as those at 33,000, care must be exercised in comparing the latitude changes at the different altitudes.

In making the measurements of Tables IV and V, the telescope pairs were always inclined in such a way that the hard telescope was underneath the total telescope. This precaution is necessary in order that showers produced by the vertical soft component in the lead absorbers are not likely to trip the total telescope. The large counter telescopes were used for most of these measurements, and consequently the rates in the tables are those recorded by the large units. In order to include in the tables the data recorded by the small telescopes, conversion factors between the large and small units were experimentally determined. At altitudes above 25,000 feet these factors were found to be 3.82 for the total telescopes and 4.08 for the hard telescopes. This difference in conversion factors for the total and hard telescopes is chiefly due to the fact that the counters of the large units have thicker walls than those of the small units so that the soft component is less able to penetrate the large telescopes.

Counting rates by the shower telescopes are also recorded in Tables IV and V. In taking the

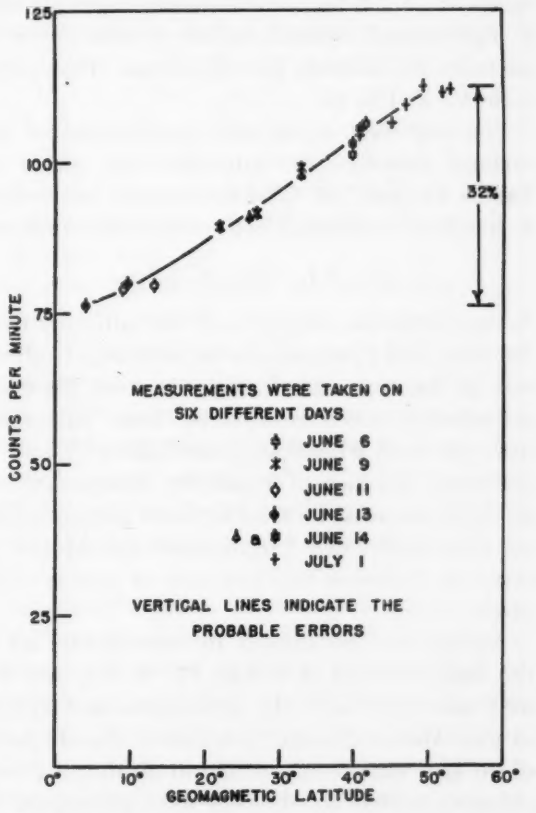

FIG. 6. Vertical total intensity as a function of geomagnetic latitude. The measurements were taken at 25,000-ft. pressure altitude with the telescope geometry shown in Fig. 3.

[10] A. G. McNish, Terr. Mag. 41, 37 (1936).

TABLE VI. East-west asymmetry at 25,000 feet, $A=2(I_W-I_E)/(I_W+I_E)$.

Zenith angle = 45°			
Geomagnetic latitude	Amount of Pb	A	Probable error
7° to 11°N	0	0.21	±0.036
av. 9°N	14 cm	0.31	±0.062
24° to 30°N	0	0.11	±0.020
av. 27°N	14 cm	0.27	±0.036
31° to 37°N	0	0.08	±0.020
av. 34°N	14 cm	0.12	±0.033
41°	0	0.055	±0.012
	14 cm	0.085	±0.028

The point at 34°N is not quite the same as the 33°N data in Table IV.

TABLE VII. East-west asymmetry at 33,000 feet, $A=2(I_W-I_E)/(I_W+I_E)$.

Zenith angle = 45°			
Geomagnetic latitude	Amount of Pb	A	Probable error
1°S to 5°N	0	0.24	±0.019
av. 2°N	14 cm	0.38	±0.040
	Soft (calc.)	0.20	±0.028
13° to 19°N	0	0.23	±0.024
av. 16°N	14 cm	0.48	±0.050
	Showers	0.16	±0.04
20°N	0	0.23	±0.013
	14	0.35	±0.026
	Soft (calc.)	0.19	±0.020
31° to 37°N	0	0.12	±0.018
av. 34°N	14	0.17	±0.024
	Soft (calc.)	0.11	±0.024
	Showers	0.035	±0.028
41°	0	0.055	±0.011
	14	0.085	±0.023
	Soft (calc.)	0.05	±0.016
	Showers	0.06	±0.027

shower rates no anticoincidence counters were used. For all the other data of Tables IV and V the anticoincidence system was in operation.

The statistical accuracy of the measurements given in Tables IV and V is not high enough to give the structure of the latitude effect in detail. The close geometry telescope of Fig. 3 was operated vertically during the latitude measurements at 25,000 feet, and here the counting rate is high enough that a rather precise curve of intensity *vs.* latitude can be drawn. This curve is shown in Fig. 6.

The east-west asymmetry coefficients for the various geomagnetic latitudes are given in Tables VI and VII. The asymmetry coefficient, A, has been calculated in the traditional manner,

$$A=2(I_w-I_e)/(I_w+I_e).$$

I_w represents the intensity of the radiation from the west, and I_e represents the intensity from the east at the same zenith angle. In most cases the asymmetry coefficients have been calculated from the data which comprise Tables IV and V. However, because of geometry differences, not all the data could be used for both purposes, and for this reason exact agreement should not be expected between the two sets of tables in all cases.

Except for the shower measurements, all of the data reported in Tables IV, V, VI, and VII were obtained with the anticoincidence system in use. Measurements to estimate the efficiency of the anticoincidence system in eliminating coincidences caused by showers were attempted by displacing one of the counters of a telescope so that at least two particles were required to produce a coincidence. With the anticoincidence system still in use, the counting rates with a counter thus displaced varied from four to ten percent of the count rate with a normal telescope. These measurements appeared to vary markedly with the distance that the out of line counter was removed from the telescope axis, and it was thought that knock-on particles rather than true showers were partially responsible for the residual counting rate with counters out of line. Because of this uncertainty, no shower correction beyond the use of the anticoincidence system has been employed in presenting the results. The asymmetry coefficients as reported in Tables VI and VII may be somewhat low on this account, but the error is probably less than 5 percent.

Some systematic errors which enter into the measurements have already been discussed. The most serious of these was the effect of counter dead time, and a calculated correction for this was applied before the results were tabulated.

Some of the more important of the non-systematic sources of error in the experiment are the following:

1. The altitude of the plane is not constant. The pilots were asked to maintain the altitude within ±100 feet while measurements were being taken, and except for a few occasions when the air was rough, this tolerance was held. The altimeter was always set to read zero feet at a pressure of 76 cm of Hg so that the flights were made at constant pressure with a probable error in pressure altitude of less than ±100 feet. This

corresponds to an error in cosmic-ray intensity of about 0.5 percent. In any asymmetry experiment, east and west intensities were measured simultaneously so that the altitude error should be expected to be of little importance.

2. The zenith angle of the telescopes varies as the plane tilts or changes its attitude. A sensitive level bubble was used to indicate the correct angle. During flight the zenith angle oscillated by about 1 degree. However, the average position was checked and adjusted from time to time and it is not likely that the average angle over a flight was in error by more than $\frac{1}{3}$ degree. With the telescopes at a 45 degree zenith angle, a $\frac{1}{3}$ degree error makes a difference in east and west intensity of about 2.3 percent. At the northern latitudes the east-west asymmetry is only a few times this difference, and the error is serious.

3. The efficiencies of similar telescope units may be different or may change with time. In order to minimize this effect, computation of the asymmetry, A, has been made individually for each telescope. The individual results were then averaged to give the results in the tables. Whenever possible the telescopes were changed from east to west by turning the plane through 180 degrees. The geometry of the telescope, relative to the airplane, is thus allowed to remain constant during a series of measurements. This is important because the metal structure of the plane varies from place to place and can influence the intensity of the soft component.

In addition to the errors discussed above there is the uncertainty in the counting rates due to statistical fluctuations. In any one flight the probable error due to this cause is usually larger than the other errors discussed above. For this reason and because the calculation is easy, the probable errors given in Tables I to VII are those computed on the basis of the statistical fluctuations alone. It is thus to be expected that the true errors are often larger than the $\pm$ range given.

DISCUSSION OF THE EAST-WEST ASYMMETRY AND LATITUDE EFFECT

The east-west asymmetry results of Tables VI and VII all show positive values for the coefficient A. Since positive values of A indicate positive primary rays, it is possible to make the qualitative conclusion that the primary particles for both hard and soft components are mostly positive.

The amount of asymmetry increases rapidly as the geomagnetic latitude is decreased. At 33,000 feet from 41 degrees N to 20 degrees N the asymmetry of both hard and soft component increases by a factor of about 4.

The data also indicate that the asymmetry is increasing with altitude. However, the probable errors in each determination of A are such that the small increase from 25,000 to 33,000 feet cannot be accurately determined. Perhaps the best quantitative measure of the altitude increase can be obtained by comparing sea level measurements as made by other experimenters with the present 33,000-ft. measurements. Johnson's measurements[3] at geomagnetic latitudes 0 and 20 degrees north are suitable for an altitude comparison. At 76 cm of Hg pressure and with counter telescopes at 45 degree zenith angle, Johnson found the asymmetry, A, of the total radiation to be 0.14 at 0 degrees north and 0.07 at 20 degrees north. He also reports that filtering with 14 cm of lead reduces the asymmetry by about 25 percent, so the sea level asymmetry of the hard component is about 0.10 at 0 degrees north and 0.05 at 20 degrees north. From Table VII the corresponding coefficients at 33,000 feet are 0.38 and 0.35.

Because the details of the transition from primaries to secondaries are unknown, and because the absorption of the secondaries in the atmosphere is a complex process, it is difficult to make a direct quantitative comparison of the results with the theory. However, it is possible to make a rough analysis of the east-west asymmetry by comparing the coefficient, A, with the change in intensity observed in the latitude effect.

The latitude effect on the vertical rays does not depend on whether the primary particles are positive or negative and can thus be used to determine an "effective" energy spectrum for the primaries. This will be done by making the assumption that the cosmic-ray intensity at a certain point and under a certain thickness of air is inversely proportional to a power of the magnetic field cut off energy. (A power law distribution is assumed because this type of dis-

tribution has been found to give a fairly good representation of the primary energy spectrum.) The observed latitude effect is used to evaluate the power coefficient from the relation

$$\frac{I_{47}}{I_9}=\frac{E_{47}^{-\gamma}}{E_9^{-\gamma}}=\left(\frac{E_{47}}{E_9}\right)^{-\gamma}.$$

I is the radiation intensity of a given cosmic-ray component, and E is the critical energy. The subscripts refer to the geomagnetic latitude where each is evaluated.

A different value of γ will be determined for each of the different cosmic-ray components. The value of γ together with the east and west cut-off energies can then be used to predict what east-west asymmetry should result if the primary particles are all positive. To make the comparison valid, the air absorption in the east-west experiments and the latitude measurements should be the same. This is approximately true if the vertical latitude effect at 25,000 feet is compared with the 45 degree east west effect at 33,000 feet.

TABLE VIII. Comparison of the observed east-west asymmetry with values predicted from the latitude effect under the assumption that all primaries are positive.

Component	Latitude ratio I_{47}/I_9	γ	Predic. A 0°N	Obs. A 2°N	Predic. A 20°N	Obs. A 20°N
Hard	1.43	0.265	0.21	0.38	0.21	0.35
Soft	1.40	0.250	0.19	0.20	0.19	0.20
Showers	1.165	0.114	0.09	—	0.09	0.16*

* Observed at 16°N.

The comparison is made in Table VIII. The cut-off energies for the positions in question were determined from the curves given by Lemaitre and Vallarta[2] under the assumption that the primary particles are protons. Lemaitre and Vallarta have not determined cut-off energies for east and west rays at all latitudes, but they give values at 0° and 20°N which are suitable for comparison with the measurements at 2° and 20°N.* The energies involved are 3.5 Bev and 13.5 Bev for vertical rays at 47 degrees N and 9 degrees N, respectively, 24 Bev and 11 Bev for east and west rays at the geomagnetic equator, and 20 Bev and 9 Bev, respectively, for east and west rays at 20 degrees N. The latitude ratios were calculated from the data in Table IV, and the observed values of the asymmetry were taken directly from Table VII.

The comparisons in Table VIII show that the observed values of the east-west asymmetry are larger than the values predicted from the "effective" energy spectrum as determined from the latitude measurements, The predicted values are for the case where the primary particles are all positive so the discrepancy is in the wrong direction to be explained by including negative particles in the primary spectrum. The trouble probably is due to the rough theoretical methods that have been used because experimental refinements would tend to increase the observed value of A. For example, the finite aperture of the telescope used in the present experiments reduces the asymmetry from that which would be recorded by a telescope of infinitesimal aperture. Also any background of air showers which was not eliminated by the anticoincidence would decrease the observed value of A.

With regard to the assumptions involved in the calculation, it is by no means certain that the "effective" energy spectrum can be represented by a power law. Furthermore, the coefficient γ, which is evaluated for the energy range 3.5 to 13.5 Bev by the latitude effect, may not be valid for the range 9 to 24 Bev of the east-west experiment.

The assumption of an "effective" spectrum of an exponential type, $N=\text{constant}\times e^{-aE}$, gives perhaps better agreement between the latitude effect and asymmetry measurements, but in view of the uncertainties mentioned above, this point should not be labored.

Fortunately, the experiment is quite sensitive to the number of negative particles in the primary radiation. If the number of negatives is $\frac{1}{4}$ of the total number, the east-west asymmetry is reduced by a factor of 2. In the case of the hard component and the showers, such a reduction would be completely out of line with experimental observations. The soft component, by the latitude effect comparison, has a relatively small asymmetry, so that the possibility of 25

* *Note added in proof:* Vallarta has recently published additional calculations suitable for the interpretation of the results of the present experiment [M. S. Vallarta, Phys. Rev. 74, 1837 (1948)].

percent negative primaries for this component cannot be immediately rejected. However, the showers and the soft component are closely related, and it is likely not fortuitous that the east-west asymmetries of these components are about the same.

What has been called the soft component includes those electrons which are recorded in the shower measurements as well as slow heavy particles such as protons and mesotrons. It has already been concluded that the shower particles and the fast heavy particles (hard component) arise from primaries which are nearly all positive, and since the soft component is so closely related to these components, it is rather unlikely that $\frac{1}{4}$ of its primaries are negative. The following mechanism would account for the high latitude effect and the small asymmetry of the soft component without requiring the introduction of negative primaries. Suppose the low energy particles in the soft component are produced from primaries which are sensitive to the earth's magnetic field, so that the low energy secondaries contribute heavily to the latitude effect. If these low energy particles result from processes where the direction of the primary ray is not preserved by the secondary rays, they will not contribute full measure to the east-west asymmetry. This explanation requires that a large number of slow heavy particles be present in the cosmic rays at high altitudes. That a considerable number of such particles are to be found at altitudes of about 30,000 feet is shown by the cloud-chamber investigations of Adams *et al.*[11]

CONCLUSION

The experiments show that the large majority of the primary cosmic rays in the energy range 5 to 25 Bev are positively charged. The evidence is that the primaries of the shower producing radiation as well as those of the hard component are probably all positive. It could perhaps be argued that the results in the case of the soft component leave room for as many as $\frac{1}{4}$ of the primaries of this component to be negative, but the results on the shower producing particles make this conclusion unlikely.

To put the argument the other way around, it can be said that the experiments give no evidence whatever for the existence of negative particles in the primary radiation. As far as these experiments are concerned, it is not necessary to postulate the existence of negative protons or negative nuclei, and it is possible that a single type of primary particle is responsible for all of the cosmic-ray particles observed in the atmosphere.

[11] Adams, Anderson, Lloyd, Rau, and Saxena, Rev. Mod. Phys. **20**, 334 (1948).

ACKNOWLEDGMENT

The work described in this report was carried out under Contract N6ori-111, Task Order II, with the Office of Naval Research. The B-29 used in the flight was supplied, maintained, and operated by the U. S. Air Force. The B-29 was based at the U. S. Naval Ordnance Test Station at Inyokern, California, and the facilities of this station were generously made available.

The experiment was made possible through the cooperation of all of the above organizations, and the author would like to take this opportunity to thank the many members of these organizations who contributed so greatly to the work.

Bruce Harris, M. L. MacKnight, and Andrew Yeiser were of assistance in constructing the experimental apparatus and in taking the measurements. Their help and cooperation is gratefully acknowledged.

The author is particularly indebted to Professor R. B. Brode for his support of the experiment, and for the many valuable suggestions which he made for carrying it out.

On the Magnetic Moments of C^{13}, F^{19}, Tl^{203}, and Tl^{205}*

H. L. Poss**
Massachusetts Institute of Technology, Cambridge, Massachusetts
(Received October 8, 1948)

The resonance absorption method has been applied to the measurement of the moments of C^{13}, F^{19}, Tl^{203}, and Tl^{205} in terms of the proton moment. The observed ratios of g-factor to that of the proton are as follows. C^{13}: 0.25143±0.00005; F^{19}: 0.94077±0.0001; Tl^{203}: 0.571499 ±0.00005; Tl^{205}: 0.577135±0.00005. By taking 5.5791±0.0016 for the proton gyromagnetic ratio, the values of the moments in nuclear magnetons are: $\mu(C^{13})=0.7016\pm0.0004$; $\mu(F^{19})=2.626\pm0.001$; $\mu(Tl^{203})=1.612$; $\mu(Tl^{205})=1.628$. For the thallium isotopes, $\mu_{205}/\mu_{203}=1.00986\pm0.00005$. The results for C^{13} and F^{19} are in close agreement with the molecular-beam values.

1. INTRODUCTION

SINCE the first successful observations of nuclear magnetic resonances in macroscopic aggregates of matter,[1] the method has been applied to the precise measurement of a number of magnetic moments.[2–12] The method is based upon the detection of nuclear spin reorientations in a magnetic field induced by an applied radiofrequency field. In the absence of perturbing fields, the probability for such transitions will be a maximum when the quantum of energy of the radiofrequency field is equal to the energy difference between the equally spaced energy levels that a nucleus can occupy in a magnetic field, H—that is, when

$$h\nu=g\mu_0 H, \tag{1}$$

where μ_0 is the nuclear magneton and g is the ratio of magnetic moment μ in units of μ_0 to angular momentum I in units of $\hbar$.

If no assemblance of nuclei in a magnetic field reaches the equilibrium Boltzmann distribution, transitions induced by an applied radiofrequency field will result in a net absorption of energy because the lower energy levels are more abundantly occupied. It is by this absorption of energy that the spin reorientations are detected.

2. METHOD AND APPARATUS

The sample containing the nuclei under investigation is placed in a uniform magnetic field. A small oscillating field perpendicular to the uniform field is supplied by a radiofrequency coil surrounding the sample. Under these conditions, a phenomenological theory developed by F. Bloch enables an explicit expression to be given for the r-f susceptibility of the coil when the passage through the resonance region, by varying the field or the frequency, is slow enough so that the rate of change of the component of nuclear magnetization in the field direction can be neglected.[13]

The susceptibility is complex, its real component representing a dispersion curve and its imaginary component, an absorption curve. If the amplitude of the oscillating field is sufficiently small, it does not contribute appreciably to the width of the resonance. Under these conditions, the maximum value of each component is of the order of $\chi_0(H/\Delta H)$ where ΔH is the separation in gauss of the half-amplitude points of the absorption component and χ_0 is the static sus-

* This work has been supported in part by the Signal Corps, the Air Materiel Command, and ONR.
** Research Laboratory of Electronics; now, Brookhaven National Laboratories, Upton, New York.
[1] E. M. Purcell, H. C. Torrey, and R. V. Pound, Phys. Rev. 69, 37 (1946); F. Bloch, W. W. Hansen, and M. Packard, Phys. Rev. 69, 127 (1946). A fuller account is given in references 13 and 14.
[2] H. L. Anderson and A. Novick, Phys. Rev. 71, 372 (1947).
[3] F. Bloch, A. C. Graves, M. Packard, and R. W. Spence, Phys. Rev. 71, 551 (1947).
[4] W. R. Arnold and A. Roberts, Phys. Rev. 71, 878 (1947).
[5] A. Roberts, Phys. Rev. 72, 979 (1947).
[6] F. Bloch, E. C. Levinthal, and M. E. Packard, Phys. Rev. 72, 1125 (1947).
[7] F. Bitter, N. L. Alpert, D. E. Nagle, and H. L. Poss, Phys. Rev. 72, 1271 (1947).
[8] H. L. Poss, Phys. Rev. 72, 637 (1947).
[9] R. V. Pound, Phys. Rev. 72, 1273 (1947).
[10] R. V. Pound, Phys. Rev. 73, 523 (1948).
[11] H. L. Anderson and A. Novick, Phys. Rev. 73, 919 (1948).
[12] R. V. Pound, Phys. Rev. 73, 1112 (1948).
[13] F. Bloch, Phys. Rev. 70, 460 (1946).

ceptibility of the nuclei given by the quantum generalization of Curie's law.†

Under experimental conditions, a half-width of about $\frac{1}{2}$ gauss in a field of 5000 gauss is achieved. The r-f susceptibility of the sample can then be greater than the static susceptibility by a factor of 10,000. It still, however, is only of the order of 10^{-5} at best. In order to keep ΔH small and, in fact, limited by inhomogeneities in the applied field, it is necessary in general to work with liquid samples. In solids, neighboring nuclei are likely to be more nearly fixed and their magnetic fields will serve to increase the resonance width. In addition, if the nucleus has a spin greater than $\frac{1}{2}$, there may be quadrupole interactions which will further broaden the resonance.

The use of a bridge circuit suggests itself in the detection of small changes in the circuit parameters of a coil. We have constructed bridge circuits for this purpose similar in design to the type introduced by Purcell and his co-workers and described by them in detail.[14] Such circuits are frequency sensitive, so that in searching for a resonance, it is the field which is varied rather than the frequency. Standard signal generators (General Radio Co. Types 805-C and 605-B) have been used to supply the bridge circuits. Communication receivers proved to have adequate sensitivity for use as detectors. The Hallicrafters SX-28 and the Signal Corps BC-348-N were employed.

A water-cooled electromagnet designed by F. Bitter has been used for most of the work. It has 8-inch diameter pole pieces and a $2\frac{1}{4}$-inch gap. It is energized by a bank of submarine storage batteries. As the current drawn from the batteries is considerably less than their rating, the field can be kept constant over long periods of time. Internal auxiliary coils are provided into which alternating current can be fed to modulate the field above and below its mean value.

The sample coils have for the most part been close wound with No. 33 enameled wire on hollow polystyrene forms $\frac{1}{16}$ inch in diameter. The volume occupied by such a coil for use in the range of 4.5 Mc/sec. is about $1\frac{1}{2}$ cc and is correspondingly less for higher frequency coils. The coils are mounted in a closed brass box which is attached to a positioning mechanism on the magnet so that it can be conveniently moved about in the field until the most homogeneous position is located.

A strong resonance may be observed directly on an oscilloscope connected to the audio output of the receiver. For this purpose, the magnetic field is modulated sinusoidally about the resonance value by applying 60-cycle current to the auxilliary coils of the magnet. A stationary pattern is observed when the oscilloscope sweep circuit is synchronized to this frequency. Two resonances are observed on the screen as the resonance field is passed through twice during each cycle. The general features of the oscillations associated with the resonances under these conditions have been explained by considering transient solutions of Bloch's equations.[15]

To observe weak resonances, the oscilloscope is replaced by a narrow-band 30-cycle amplifier, as has been done by other investigators in this field. The resonance region is slowly traversed and at the same time, a small 30-cycle current is applied to the auxilliary coils of the magnet. A 30-cycle modulation of the r-f susceptibility change results, the amplitude of which is proportional to the slope of the resonance curve if the 30-cycle current is sufficiently small. A recording meter connected to the amplifier output enables a graphical record to be made of the resonance. One or the other components of the susceptibility change will be accentuated, depending upon the type of bridge balance.

3. MEASUREMENTS

It is seen from Eq. (1) that the measurement of the resonant frequencies of two species of nuclei in the same magnetic field determines the ratio of their g-factors. In the experiments herein reported, the proton moment has been used as a reference moment. From its absolute value, one can then determine the absolute values of the moments measured in terms of it, taking into

† See, for example, Eq. (2) of reference 13.

[14] N. Bloembergen, E. M. Purcell, and R. V. Pound, Phys. Rev. **73**, 679 (1948).

[15] B. A. Jacobsohn and R. K. Wangsness, Phys. Rev. **73**, 942 (1948); M.I.T. Research Laboratory of Electronics, Quarterly Progress Report, July 15, 1947, p. 26.

account values of I obtained from other experiments.

The great accuracy inherent in the resonance absorption method arises from the sharpness of the resonance that can be achieved. Whether or not the full accuracy of the method can be utilized in the comparison of moments is determined by the extent to which the assumption of identical fields at both kinds of nuclei is valid.

Factors preventing the field from being the same at the two types of nuclei when their resonant frequencies are measured can arise from the experimental arrangement and from the diamagnetism of the atomic electrons surrounding the nucleus.

The effect of the latter is to make the field at a nucleus slightly less than the applied field so that the observed gyromagnetic ratio is less than the actual one. A calculation by Lamb[16] using the Fermi-Thomas model of the atom gives the expression

$$H'/H=3.19\times10^{-5}Z^{4/3} \qquad (2)$$

where H' is the reduction in field at the nucleus of an atom of atomic number Z in an applied field H. The dependency of the diamagnetic correction on Z as shown by Eq. (2) makes it of minor importance for the light nuclei. For the heavy nuclei, it becomes appreciable and in fact limits the accuracy with which values of their moments can be given.

The experimental arrangements for making these measurements have been of two types. Two coils can be placed in the magnetic field, each connected to a separate bridge circuit and containing one or the other of the two species of nuclei to be compared. An electronic switch permits the output of each radio receiver to be displayed as a separate trace on the oscilloscope. When the two sets of resonances are aligned, the frequencies are measured. If the coils are then interchanged and the measurements repeated, the effect of a possible difference in field at one coil as compared with the other can be eliminated by taking the geometric mean of the measurements.

An alternative procedure is to use one coil containing both types of nuclei. The frequency is varied so that first one resonance and then the other is obtained in the same field.

The next problem to consider is that of precisely locating the resonance. In the latter procedure outlined above, if the resonance is displayed on an oscilloscope, the amplitude of the modulating field is decreased while the resonance is kept centered on the trace by slight frequency readjustments. When the modulating field is reduced to the order of the resonance width, all that may be observed on the screen is a series of transient oscillations. By setting the frequency midway between the extreme points where the resonance appears, it is accurately located. The maximum possible error is limited to the amplitude of the modulating field which is but a few hundredths of a percent of the applied field. It will be recognized that provided the homogeneity in field can be maintained, the higher the applied field, the less the percentage error in locating the resonance.

If the resonance is too weak to be observed on the oscilloscope, a record of it can be made at a known frequency by using the narrow-band amplifier and recording meter. After it has been traced out, the reference proton resonance is obtained in the same magnet position. From a calibration of the sweep field, a correction can be made to take into account the small field differences separating the two resonances.

When the two sets of resonances are presented simultaneously on the oscilloscope, for a given amplitude of modulating field, it is again seen that the larger the applied field, the less consequential will be the error made in aligning the resonances. Ambiguity in telling when the both sets of resonances are aligned can come about from marked differences in their appearance resulting from differences in relaxation times and magnetic moments. Studies of transient effects have shown that the appearance of the resonance may be delayed until the resonant field has been passed through.[15] The delay may be sufficiently different for both sets of resonances so that if one aligns the right-hand resonances on each trace, the left-hand ones are distinctly misaligned. Such a case was encountered in the comparison of the proton and deuteron moments made in this laboratory and elsewhere.[5–7] In

[16] H. Schuler and J. E. Keyston, Zeits. f. Physik **70**, 1 (1931); H. Schuler and T. Schmidt, Zeits. f. Physik **104**, 468 (1937); H. Schuler and H. Korsching, Zeits. f. Physik **105**, 168 (1937).

these instances, use can be made of a symmetry property possessed by Bloch's equations which was pointed out by Jacobsohn and Wangsness.[15] They show that for a sinusoidal-field modulation and oscilloscope sweep centered at the resonance value, the observed trace resulting from the absorption component will be symmetrical about the center line while that from the dispersion component will be skew-symmetrical. Hence, if bridge balance and frequencies are adjusted so that two symmetrical patterns appear, we know that the resonances are "aligned" regardless of differences in appearance or separation.

Frequencies have been measured by means of crystal-calibrated frequency meters, General Radio Co. Type 620-A and the Signal Corps BC-221-T. The error in measurement is of the order of 0.005 percent to 0.01 percent depending upon the dial setting. A short antenna attached to the frequency meter radiates sufficient power to enable the beat frequency between the meter and signal generator to be observed directly on the oscilloscope connected to the receiver output.

The particular conditions applying to each of the nuclei measured will next be considered.

3.1. Measurements on the Thallium Isotopes, Tl^{203} and Tl^{205}

The following values for the spins and magnetic moments of the two stable thallium isotopes, mass numbers 203 and 205, have been determined spectroscopically.[16]

$$I=\tfrac{1}{2}$$
$$\mu=1.45 \quad \mu_{205}/\mu_{203}=1.00966.$$

The relatively high gyromagnetic ratio and abundance of these isotopes indicated that their resonances could be searched for on the oscilloscope. This was consequently done during a period of time when the M.I.T. cyclotron magnet was available to us for experiments in resonance absorption.

Saturated solutions of the soluble acetate and later the formate were placed in a glass coil form $\frac{7}{16}$ inch in diameter. Two coils, $\frac{1}{2}$-inch long and separated by $\frac{1}{2}$ inch were wound on the form and connected to separate bridge circuits. One coil was intended for the observation of proton resonances in the solution. The coils were contained within a 6-inch diameter coil through which 30-cycle current was sent to modulate the field.

Two resonances separated by a one percent field difference were observed for a field about 10 percent less than that expected on the basis of the spectroscopic results. The stronger resonance occurred at the lower field and was attributed to Tl^{205} since it is 2.5 times as abundant as Tl^{203}.

The proton and thallium resonances were then displayed simultaneously on an oscilloscope, the frequency of the former being 30.5 Mc/sec. and that of the latter in the vicinity of 17.5 Mc/sec. In this case, it was possible to line up the two resonances on one trace with the two on the other.

Measurements were first made on Tl^{205}, previously communicated,[8] and subsequently on Tl^{203}. Although the signal-to-noise ratio of the latter resonances was poor, the accuracy of the measurements is not appreciably lowered thereby. The resonances can be clearly distinguished from the noise by their characteristic motion across the oscilloscope as the field is varied. The applied field being about 7000 gauss and the modulating field 7 gauss, as long as both sets of resonances were visible on the oscilloscope together, an accuracy of one part in 1000 is achieved without attempting to align them. As the resonances had a width of less than $\frac{1}{2}$ gauss, errors in aligning them could be kept below those involved in the frequency measurements.

The cyclotron magnetic field was sufficiently uniform over the distance between coils so that it was not necessary to repeat the measurements with the coil positions interchanged. When the proton-deuteron magnetic moment ratio was measured with the use of this magnet,[7] no significant difference was noted when this interchange was made, even though an accuracy of almost one part in 100,000 was achieved.

Differences in phase shift in the audio stages of the two receivers were studied by observing the points on the oscilloscope trace where proton resonances entered and left as the field was varied so that the resonances occurred first in one coil and then the other. This error appeared to be under 0.01 percent.

Six independent determinations of the ratio of

TABLE I. Ratio of resonant frequency to that of the proton.

Tl^{205}	1	0.577129
	2	0.577150
	3	0.577111
	4	0.577152
	5	0.577112
	6	0.577155
	average:	0.577135
Tl^{203}	1	0.571468
	2	0.571526
	3	0.571500
	4	0.571503
	5	0.571498
	average:	0.571499
C^{13}	1	0.251402
	2	0.251423
	3	0.251414
	4	0.251443
	5	0.251419
	6	0.251467
	7	0.251459
	average:	0.251432
F^{19}	1	0.940775
	2	0.940767
	3	0.940745
	4	0.940785
	average:	0.940768

resonant frequencies of Tl^{205} to the proton were made and five for Tl^{203}. The individual results are given in Table I. To make an allowance for possible errors of the type mentioned above, 0.01 percent was taken for the probable error. The results are then

$$\nu_{Tl^{203}}/\nu_{H^1}=0.577135\pm0.00005,$$
$$\nu_{Tl^{205}}/\nu_{H^1}=0.571499\pm0.00005.$$

In considering the probable error to be associated with the ratio of the moments, possible systematic errors should cancel out and it would appear justifiable to add the probable errors obtained from the deviations in each set of measurements. Taking the ratio of the averages then gives

$$\mu_{205}/\mu_{203}=1.00986\pm0.00005.$$

Applying the diamagnetic correction as given by Eq. (2) and taking the proton gyromagnetic ratio to be 5.5791 ± 0.0016†† give for the moments, in nuclear magnetons,

$$\mu(Tl^{205})=1.628 \quad \mu(Tl^{203})=1.612.$$

It is difficult to list any probable error in the above results. The diamagnetic correction amounts to 1 percent of the values and there is no certain way of estimating the error in it.

The value of the ratio of the moments obtained in these measurements is 0.02 percent higher than the spectroscopic value. The discrepancy is within the limit of error of the spectroscopic work so that no significance can be attached to it.

It is of interest to note that on the basis of their spectroscopic measurements, Schuler and Korsching[16] concluded that the relation

$$\frac{M_{A+2}}{M_A}=\frac{\mu_{A+2}}{\mu_A}$$

appeared to hold for the isotopes of copper, rhenium, and thallium. M_A refers to the lighter isotope of mass number A and μ_A to its magnetic moment. The packing fraction of both the thallium isotopes is given to be $(2.9\pm0.5)\times10^{-4}$ mass unit.[17] Their mass ratio is then their mass number ratio and is

$$\frac{M_{A+2}}{M_A}=1.00985\pm0.0001.$$

The relation thus appears to hold very well for thallium. Pound[10] has measured the moment ratio of the copper isotopes by the resonance method and finds $\mu_{65}/\mu_{63}=1.0711\pm0.0002$, distinctly different from the mass ratio, 1.032. If the above relation represents a nuclear property which holds under certain conditions, possibly the higher spin of the copper isotopes (3/2) might prevent it from applying in their case.

The addition of copper sulfate solution to the thallium sample with the resulting concentration of about 10^{19} cupric ions per cc enhanced the proton resonance but almost obliterated the thallium resonance. The apparently stronger interaction between the copper and thallium ions would indicate that their average distance of separation is less than that of the copper ions and the protons.

†† This is the molecular beam value given in reference 20. It has not been corrected to take into account recent work on the g-factor of the electron.

[17] J. Mattauch and S. Fluegge, *Nuclear Physics Tables* (Interscience Publishers, Inc., New York, 1946), p. 119.

3.2. Measurements on C^{13}

The availability of a sample of methyl iodide enriched in C^{13} prompted measurements to be made on it. Its gyromagnetic ratio had been measured previously by the molecular-beam resonance method.[18] Its spin[19] is $\frac{1}{2}$. The molecular beam value of the moment is

$$\mu(C^{13}) = 0.701 \pm 0.002.$$

The methyl iodide, which is a liquid, was contained in a sealed-off glass tube $\frac{1}{2}$ inch in diameter. The liquid filled the tube to a depth of $\frac{3}{4}$ inch; 56.7 percent of the carbon atoms in the sample were stated to be C^{13}. The tube was fitted into a polystyrene coil form.

A search, with the use of the recording meter, revealed a weak resonance in the expected vicinity. The resonance was attributed to C^{13} since there were no other nuclei in the sample which would give resonances in this region. The frequency was 4.5 Mc/sec. A second coil mounted in the same box was used to obtain a reference proton resonance in oil at 18 Mc/sec.

The C^{13} resonance was recorded at a known frequency by using a motor-driven variable resistor to vary a small current through auxiliary coils on the magnet. This sweep field had been previously calibrated by measuring the change in frequency required by a change in current to keep a resonance at the same point on the oscilloscope trace. The proton resonance was obtained in the same magnet position and located in a manner previously described by displaying it on the oscilloscope and reducing the amplitude of the modulating field to a very small value. The main magnet current was monitored by using a potentiometer circuit with which a drift of a gauss could be easily detected. The field was corrected before each frequency measurement if a drift was noticeable.

The field difference separating the two resonances was about 10^{-3} of the applied field, so that an error of 10 percent in the calibration of the sweep field would affect the results by only 0.01 percent. The C^{13} resonance occupied about one gauss, while the applied field was 4200 gauss. The uncertainty in location of the exact resonance point is not believed to have exceeded 0.01 percent. The results of seven independent determinations are given in Table I. A probable error of 0.02 percent is considered to include the effects of possible errors. We then have for the ratio of resonant frequencies

$$\nu_{C^{13}}/\nu_{H^1} = 0.25143 \pm 0.00005.$$

The diamagnetic correction in this instance increases the observed gyromagnetic ratio by only 0.03 percent, and hence does not leave the accuracy of the final result uncertain as in the case of thallium. The magnetic moment in nuclear magnetons is then

$$\mu(C^{13}) = 0.7016 \pm 0.0004,$$

most of the error arising from that in the proton moment. The value obtained is seen to be well within the limit of error of the molecular-beam result.

3.3. Measurements on F^{19}

The resonance absorption method was applied to the measurement of the moment of fluorine to see how the results would compare with the observed molecular-beam value

$$g(F^{19}) = 5.250 \pm 0.005.$$

By taking into account its spin of $\frac{1}{2}$ and the diamagnetic correction of 0.06 percent, the molecular-beam value[20] of its moment is

$$\mu(F^{19}) = 2.627 \pm 0.003.$$

Hydrofluoric acid was used as a sample. It does not affect polystyrene and was poured directly into the coil forms. The addition of small concentrations of manganese chloride or ferric chloride solutions to the acid enhanced the proton resonance but obscured that of fluorine, a behavior similar to that found in the case of thallium. Here, the greater effect of the paramagnetic ions on the fluorine might be a result of their electrical attraction which would lower their average distance of separation.

Measurements on fluorine were first made by presenting both fluorine and proton resonances on an oscilloscope simultaneously as was done for thallium. The frequencies were in the vicinity

[18] R. H. Hay, Phys. Rev. 60, 75 (1941).
[19] F. A. Jenkins, Phys. Rev. 72, 169 (1947).
[20] S. Millman and P. Kusch, Phys. Rev. 60, 91 (1941).

of 4.5 Mc/sec., the field then being about 1000 gauss. As the modulating field was 10 gauss, the accuracy of the thallium measurements was not duplicated. The result obtained for the ratio of resonant frequencies was

$$\nu_{F^{19}}/\nu_{H^1}=0.9407\pm0.0003.$$

A subsequent series of measurements was made at a higher frequency, in the neighborhood of 19 Mc/sec. One sample coil was used. The field was kept constant and the frequency varied so that first one resonance was obtained and then the other. Slow field drifts, not exceeding one gauss, which sometimes occurred during the interval between measurements, were corrected. The resonances were displayed on the oscilloscope and located by reducing the modulating field until it was about 0.015 percent of the applied field, and keeping them centered on the trace. Four independent determinations were made, the results being given in Table I. A probable error of 0.01 percent is considered to include possible errors. The result is then

$$\nu_{F^{19}}/\nu_{H^1}=0.94077\pm0.0001.$$

Taking into account the diamagnetic correction gives for the moment, in nuclear magnetons,

$$\mu(F^{19})=2.626\pm0.001,$$

most of the error again arising from that in the proton moment. The value is in close agreement with the molecular-beam value.

ACKNOWLEDGMENT

The author is indebted to Professor F. Bitter for guiding the course of this research.

PHYSICAL REVIEW VOLUME 75, NUMBER 4 FEBRUARY 15, 1949

Magnetic Moments of Sunspots*

JAMES W. BROXON
Department of Physics, University of Colorado, Boulder, Colorado
(Received September 30, 1948)

Simple approximate representations of the magnetic fields of sunspots by dipoles or ring currents are considered, and expressions deduced for the magnetic moment of a sunspot in terms of its area and its maximum central magnetic field strength. These are extended to include sunspot groups, and a function (SS-MM) is defined as the arithmetical sum of the equivalent moments of all visible groups. Statistical treatment by Chree's method of superposed epochs provides some indication of a 27-day interval between recurrences of fluctuations in SS-MM.

IN an earlier paper[1] the writer provided an estimate of the magnetic moment of a sunspot. This was incidental to the discussion of the statistically determined recurrence of fluctuations in cosmic-ray intensity at 27- or 28-day intervals, and their relations to areas of sunspots and other variables. Because a new function has been devised which is based upon the earlier estimate of sunspot magnetic moment and which appears to be related to variations in cosmic-ray intensity, it is deemed worth while to provide further details regarding the manner in which that estimate was made.

How best to approach the representation of the magnetic properties of sunspots is not obvious. So far as the writer is aware, the only magnetic data regularly available in the literature are the values of H for individual sunspot groups determined at the Mt. Wilson Observatory by observation of the separation of the components of the Zeeman triplet λ6173.553 (Fe) in the second-order spectrum of their 75-foot spectrograph and published in the *Publications of the Astronomical Society of the Pacific*. Only one value of H is given for each group. This is the

* Presented at the meeting of the American Physical Society at Chicago, November 26–27, 1948.
[1] J. W. Broxon, Phys. Rev. **62**, 508 (1942).

maximum value of H ever observed at any point in that particular group while it remains visible. The unit employed is 100 gauss (or oersteds) which appears to serve as a practical limit of resolution since only integral values are listed. Because spot groups are likely to consist of anything from a single spot to several spots, sometimes with a single and sometimes with dual polarity and because the sizes and shapes as well as numbers and distributions of the spots in a group and their associated fields all vary with time, it appears to be impossible (with the limited data available) to devise any simple function to represent entirely satisfactorily the magnetic properties of a group. The complexity of the situation needs to be borne in mind when contemplating the adequacy of any function designed to represent even crudely the magnetic properties of a sunspot group.

In the case of a single sunspot of single polarity which may be regarded as approximately circular, something may be deduced regarding its magnetic state in terms of its size and the maximum magnetic field associated with it. On a statistical basis certain general statements may be made regarding the distribution of the field over the area of the sunspot. According to Chapman,[2] Nicholson has found the inclination of the magnetic field from the axis of a sunspot of radius a to vary with the distance r from its center in approximate accordance with the relation

$$\theta=(\pi/2)(r/a).$$

As was correctly surmised by Chapman, Dr. Seth B. Nicholson of Mt. Wilson observatory also informed the writer that H, the intensity of the field, may be regarded as varying over the area of the sunspot according to the relation

$$H=H_c(1-r^2/a^2),$$

where H_c is the intensity at the center.

With such a specification of the distribution of field over the area of a sunspot and with H_c and a given, one may, for instance, compute the total flux leaving or entering it and from this obtain the strength of the magnetic pole, assuming that the sunspot represents one pole of a pair. Chapman[2] has done this and in the case of the great bipolar group M.W. 6725, multiplied the pole strength computed for one of the two principal spots of the group by the distance between them to obtain the dipole moment of the pair, $5\times10^{16}\Gamma$ km^3 or 5×10^{31} e.m.u. He provided a close approximation to the appropriate distribution of H over the surfaces of the spots by imagining this to be due to a solenoidal distribution of electric current in a curved solenoid or vortex imbedded in the sun with its ends coinciding with the two spots. He found the appropriate current density in the interior of the solenoid to be

$$j=-2(H_c/\pi a)(r/a)(1-r^2/a^2),$$

where H_c is the magnetic intensity at the center of the sunspot, a its radius, and r the distance from the axis of the solenoid. The maximum value of j is given as $0.77\ H_c/\pi a$ at $r=a/\sqrt{3}=0.577a$.

One difficulty with the representation of sunspot moments in the manner outlined above is that some sunspot groups (about 9 percent[3]) are unipolar and some are irregular and there appears often to be no way to locate elsewhere the path of the flux associated with a particular sunspot. This was the chief consideration which led the writer in 1942 to attempt to represent the field of a unipolar spot approximately as that of a magnetic dipole with its axis coincident with that of the sunspot. As pointed out in the earlier paper,[1] if we imagine the dipole to be located along the solar radius through the center of a sunspot of radius a at a distance $a/\sqrt{2}$ nearer the center of the sun, then it would provide magnetic fields in the appropriate directions at the center and at the edge of the sunspot. To provide the field intensity H_c at the center of the sunspot, the moment of the dipole must be

$$M_d=\sqrt{2}a^3H_c/8=0.177a^3H_c.$$

The magnitude of its field would not vary over the area of the sunspot in close agreement with the empirical formula provided by Nicholson. Curve C in Fig. 1 shows how the intensity of the

[2] S. Chapman, Mon. Not. R. Astr. Soc. **103**, 117 (1943); see also Terr. Magn. Atmos. Elect. **49**, 37 (1944). K. O. Kiepenheuer (Zeits. f. Ap. **15**, 53 (1938)) has estimated that a sunspot has a magnetic moment $\geqq10^{30}$ oersted cm^3, but does not make clear his method of evaluation.

[3] R. S. Richardson, Astrophys. J. **107**, 78 (1948).

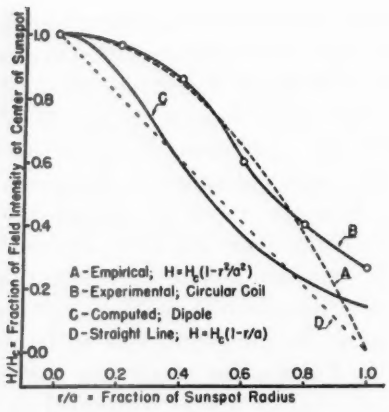

FIG. 1. Contemplated variations of H in a sunspot with distance from its center.

magnetic field produced by the dipole would vary with distance from the center of the sunspot in the plane of the sunspot. Except rather near the center and at the edge, it is seen to be much more closely represented by the linear relation

$$H=H_c(1-r/a),$$

curve D.

Before proposing this type of representation, the writer had a student (Mr. R. C. Allen) investigate experimentally the magnetic field in the neighborhood of a simple circular coil. With a current-bearing coil of mean radius 5.66 inches, he found that in a plane parallel to the coil and at a distance of 5.66 inches from it, the magnetic field was perpendicular to the axis at a distance of 10 inches from the axis. Hence this experiment indicates that if the magnetic field of a sunspot of radius a were supposed to be due to a current I flowing in a circle of radius $0.566a$ coaxial with the sunspot, and with its plane $0.566a$ beneath that of the sunspot, then this would also yield magnetic fields in the correct directions at the center and edge of the sunspot. To produce the field H_c at the center of the sunspot, we must have a current

$$I=\sqrt{2}RH_c/\pi \text{ e.m.u.}$$

where $R=0.566a$ is the radius of the circuit. (In this connection it is of interest to recall that Chapman found the maximum current density in his curved solenoid to occur at $r=0.577a$.) The magnetic moment of the magnetic shell equivalent to the circular current according to Ampere's theorem would be

$$M_c=\pi R^2I=\sqrt{2}R^3H_c=(0.566)^3\sqrt{2}a^3H_c$$
$$=0.256a^3H_c=1.45M_d.$$

Moreover, Mr. Allen's experimental observations of the magnetic field due to the circular current showed that the magnitude of H due to the current I located as specified would vary over the surface of the sunspot in accordance with curve B in Fig. 1. Curve B lies quite close to curve A which represents Nicholson's empirical relation, except near the edge of the sunspot where it is presumed that the empirical relation provides only a fair approximation. It is perhaps doubtful whether the accuracy of the empirical expressions for the magnitude and direction of H over the area of a sunspot would justify any closer approximations to either of these. Because it was considered that M_c provided quite a satisfactory representation of the magnetic moment to be associated with the sunspot and because M_d differed from this by only 45 percent while one can scarcely hope for much better than the proper order of magnitude under the circumstances, the simpler representation by the dipole was proposed in the earlier paper.

For the large unipolar sunspot group M.W. 6618 having a maximum area $A=1939$ (millionths of the Sun's visible hemisphere) and hence 44,000 km equivalent radius, and a maximum $H_c=36$ (hundred gauss), the maximum dipole moment was given as $M_d=5.2\times10^{31}$ e.m.u. Corresponding to this we have $M_c=7.5\times10^{31}$ e.m.u. representing a ring current of 4.0×10^{13} amperes with a radius of 25,000 km located 25,000 km closer to the center of the sun. It is perhaps of some interest to note that Chapman[2] found for the total flow of current across a radial half-plane through the axis of his curved solenoid $10^6H_c/2\pi$ amperes per km length. For the bipolar pair he considered, with a pole separation of 14° or 170,000 km and with $H_c=3900$ gauss, one obtains a total current of 1.7×10^{14} amperes if he supposes the solenoid to be semicircular, or 1.1×10^{14} amperes if he supposes it to extend almost straight from the one sunspot to the other.

If one desires to consider the magnetic properties of even a well-behaved sunspot throughout its history, he is confronted with further diffi-

culties. A sunspot is likely to begin as a rather small spot (its magnetic field can sometimes be detected before the spot is visible) which grows for several days and then decreases, perhaps breaking up into several parts meanwhile. While the sunspot varies in size, its central magnetic field varies somewhat correspondingly, but apparently not according to a well-defined law. Since we have available only one value of H for each group, namely, the maximum value ever observed for the group, it appears likely that this corresponds to the value of H at the center of the largest sunspot in the group when that sunspot is largest, though it appears that this is not necessarily the case. In order to make any estimate regarding the magnetic state of a group at any time other than that for which H is given, it appears necessary to make further rather bold assumptions which may be justified only partially on a statistical basis. Some information is available as a guide for such assumptions. On p. 55 of *Publications of the Astronomical Society of the Pacific* **39** (1927) we read:

> Up to a certain area, the field-strength is almost directly proportional to the diameter of the spot, with its maximum intensity near the middle of the umbra, decreasing to zero just beyond the outer edge of the penumbra. But when the spot is split into several members, the maximum field-strength in any one of them is much below that shown by an unbroken spot.

Dr. Nicholson has informed the writer that the phrase *up to a certain area* is important and that for greater areas the central field intensity is likely to be more nearly proportional to the square root of the diameter or the fourth root of the area.

If we make the simplifying assumption that the central field intensity in any sunspot is proportional to its radius and hence to the square root of its area, we have $H_c = H_m(A/A_m)^{\frac{1}{2}}$ where A is its area, A_m its maximum area, and H_m the maximum field intensity ever associated with it. Using the dipole representation, we might then assign to it the magnetic moment $M_d = \sqrt{2}a^3H_c/8 = \sqrt{2}/(8(\pi^3)^{\frac{1}{2}})(A^2H_m/(A_m)^{\frac{1}{2}}) = 0.0317A^2H_m/(A_m)^{\frac{1}{2}}$, or $M_c = 1.45M_d$ for the ring-current representation. This provides an expression presumably somewhat representative of the magnetic moment of the sunspot throughout its life. If H_m is expressed in gauss and A and A_m in cm², then M_d or M_c is expressed in e.m.u.

In order to obtain a function capable of evaluation and hence statistical investigation, further assumptions were made. Since only the H_m for a sunspot *group* is available, the entire area for the group was treated as if it were the area of a single circular sunspot, irrespective of the polarity of individual spots of the group. While this may appear to be an extraordinary procedure, an example indicates that it may not be so bad as it appears. If one applies this procedure to the great bipolar pair considered by Chapman,[2]

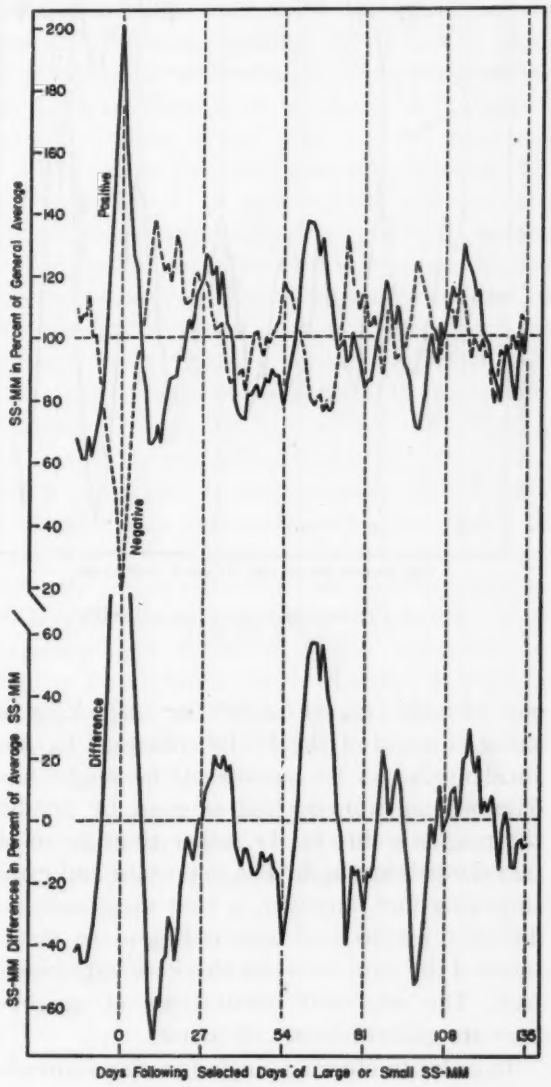

FIG. 2. Primary and subsequent subsidiary pulses in SS-MM.

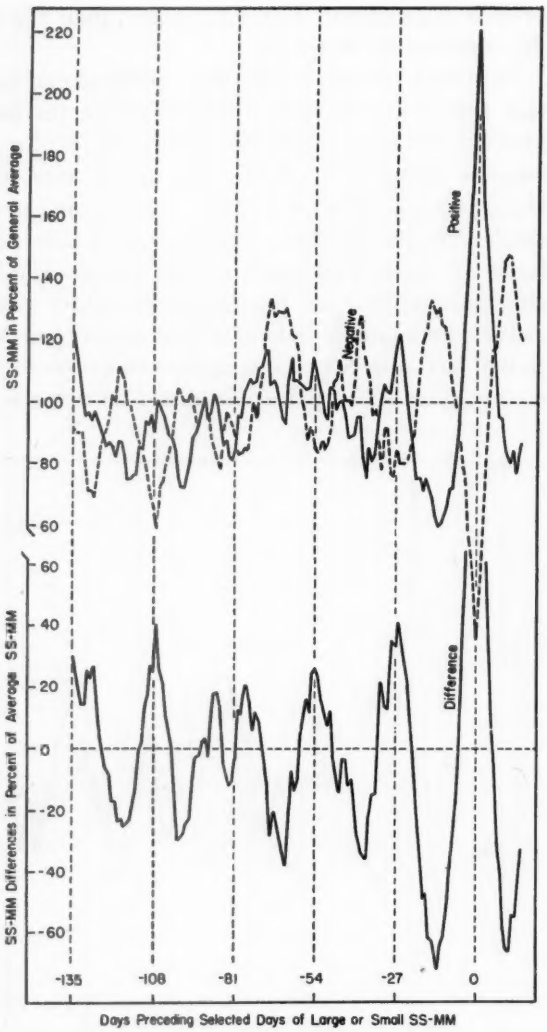

FIG. 3. Primary and preceding subsidiary pulses in SS-MM.

one obtains $M_d = 1.6 \times 10^{31}$ or $M_e = 2.3 \times 10^{31}$ e.m.u., instead of the 5×10^{31} obtained by him. Incidentally, as he mentioned, he might have obtained an estimate half as great by dividing the magnetic flux by 4π rather than 2π to obtain the pole strength. The important and rather surprising fact, however, is that these two very different methods of approach lead to magnitudes of the same order for this very large bipolar pair. The supposed orientations of magnetic axes are quite different, of course.

In order to obtain a single function somewhat representative of the state of magnetization of all the sunspots visible on the Sun, capable of evaluation, and not unwieldy, a further step was taken. The equivalent dipole (or ring-current) moment was computed as outlined above for each sunspot group for each day from daily values of their areas published in the *Monthly Weather Review*. (The writer corrected some obvious errors in tabulation.) These magnetic moments for all the sunspots visible on a particular day, irrespective of their locations, were then added together to provide a function which it was thought might prove to be of interest. This function, defined to be the arithmetic sum of the equivalent dipole or ring-current moments of all sunspot groups visible on a particular day, perhaps in some degree representative of all the sunspot magnetic moments on the nearer side of the Sun, will hereinafter be designated SS-MM. The possible usefulness of this function requires investigation, of course. It has been shown that terrestrial magnetic disturbances,[4] cosmic-ray intensity,[1] and frequency of small cosmic-ray bursts,[5] all bear some relation to the simple sum of the areas of the visible sunspots. Inasmuch as it provides some recognition of a physical property other than size, it occurred to the writer that a function such as the SS-MM might be found to be more closely related to such variables than is the total area. While application of Chree's method of analysis[4] showed recurrences of fluctuations of magnetic character, cosmic-ray intensity,[1] and burst frequency[6] at intervals of about 27 or 28 days, a casual investigation of sunspot areas by this method did not indicate such a recurrence interval.[7]

The SS-MM was subjected to Chree's superposed-epoch method of statistical analysis in the usual manner. Because the same period had been employed in the earlier work, the SS-MM was determined for each day with available data during the interval from May 25, 1938, to December 1, 1939, inclusive. For 13 of the days in this interval, data were not available; these were rather widely distributed, only two of them being consecutive.

Figures 2 and 3 show the results of the analysis. Figure 2 was obtained with zero-days se-

[4] C. Chree, Phil. Trans. Roy. Soc. **A212**, 75 (1913); **A213**, 245 (1914).
[5] J. W. Broxon, Phys. Rev. **72**, 1187 (1947).
[6] J. W. Broxon, Phys. Rev. **70**, 494 (1946).
[7] Note particularly Fig. 13 of reference 1.

lected from the first 15 months (June 1938–August 1939) and Fig. 3 with zero-days selected from the last 15 months (September 1938–November 1939). In each case the selected zero-days for the positive-pulse curve (marked Positive) were the five in each month with the largest values of SS-MM. For the negative-pulse curves (marked Negative) the selected zero-days were the five in each month with the smallest values of SS-MM. In each diagram the difference-pulse curve (marked Difference) was obtained by subtracting the ordinate for a particular day number on the negative curve from the ordinate for the same day number on the positive curve to provide the ordinate for that day number on the difference curve.

The positive and negative primary (zero-day) pulses in SS-MM are seen to represent variations of some 70 to 120 percent from the mean, with preceding and following secondary pulses representing variations of some 20 to 40 percent from the mean. The mean value of the SS-MM for all days in the period of investigation is 1.7×10^{31} or 2.5×10^{31} e.m.u. according to whether the dipole or ring-current representation is employed. This is only one-third as large as the value given above for the single great unipolar M.W. 6618 whose area attained its maximum on Sept. 23, 1939. Its maximum area also exceeded the mean value of the sum of the areas of all visible sunspots, but this excess amounted to less than 3 percent.

While the subsidiary pulses following the primary pulse in Fig. 2 are quite large, in general, there does not appear to be any good evidence of a constant period of recurrence. The four subsidiary positive pulses appear to be centered about day numbers 33, 65, 90, and 116. The three most definite subsidiary negative pulses appear to be centered about day numbers 34, 67, and 124. The four principal subsidiary pulses in the corresponding difference curve are rather well centered about day numbers 30, 65, 90, and 115. Among these it appears difficult to pick out any single period which would fit well into these groups. In each of the three curves the first two pulses follow at intervals of 30 to 35 days, while in the case of the difference curve, at any rate, the third and fourth pulses follow at intervals of 25 days. Comparison with Fig. 13 of reference 1 shows that the subsidiary pulses in SS-MM following the primary are generally larger and more clearly defined than are those in sunspot area. In the latter there is some evidence of a 34-day period for three pulses in the positive-pulse curve and for the first two pulses in the difference curve.

The subsidiary pulses preceding the primary in Fig. 3 provide rather good evidence for recurrence at intervals of 27 days. This is particularly true of the negative-pulse curve and is quite apparent in the difference curve. In the positive-pulse curve there is no evidence of a positive subsidiary pulse at day -81, and this produces a distortion in the third preceding pulse in the difference curve. In general, the positive subsidiary pulses preceding the primary are also rather smaller than the negative pulses. Taken together, however, this set of curves appears to provide rather good evidence of subsidiary pulses of some 12 to 20 percent amplitude preceding the primary pulses in SS-MM at intervals of about 27 days for four or five intervals. In the case of sunspot area no investigation of preceding pulses with zero-days selected on the basis of sunspot area was made, so we are unable to make a direct comparison. In the case of sunspot-area pulses obtained with days selected on the basis of cosmic-ray intensity, however, both preceding and following pulses combined to indicate a recurrence period of about 34 days in the fluctuations of total sunspot area.

Since there is some evidence of a 27-day interval between recurrences of fluctuations of the SS-MM, it appears that this function may be more closely associated than is the total sunspot area with other variables displaying this recurrence interval.

This research was supported in part by the Office of Naval Research.

Relation of the Cosmic Radiation to Sunspot Magnetic Moments*

JAMES W. BROXON
Department of Physics, University of Colorado, Boulder, Colorado
(Received September 30, 1948)

A function (SS-MM) designed to represent the arithmetical sum of the magnetic moments of all visible sunspots has been compared statistically with the intensity of the cosmic radiation (C-R). Large pulses (20 to 30 percent) in SS-MM were found to occur out of phase with primary pulses in C-R. SS-MM pulses of comparable magnitude bore different phase relations to subsidiary pulses in C-R. For subsidiary pulses preceding the primaries, the C-R was generally high when the SS-MM was increasing and low when it was decreasing. For subsidiary pulses following the primaries, the C-R was generally high when the SS-MM was decreasing and low when it was increasing. The analysis was carried out for intervals of 60 days preceding and following the selected days of high or low C-R. Some consideration was given to the e.m.f. generated in connection with an imaginary but in some respects representative sunspot by electromagnetic induction.

THE writer[1] has already introduced a function (SS-MM) designed to represent approximately the arithmetical sum of the magnitudes of the magnetic moments of all sunspots visible on a particular day, irrespective of polarity or location.

Analysis of the data for an eighteen-month period by Chree's method of superposed epochs provided evidence of recurrence of fluctuations in the magnitude of SS-MM at intervals of about 27 days, corresponding to recurrence phenomena displayed by intensity of the cosmic radiation[2] during the same period. Statistical treatment has also brought out a relation between primary pulses in cosmic-ray intensity and total sunspot area,[3] even though the latter did not display recurrence features at intervals approximating 27 days. These facts, combined with the further fact that the SS-MM includes recognition of a physical characteristic of sunspots which conceivably might affect the intensity of the cosmic radiation measured at a particular location on the Earth, led the writer to investigate the possibility that the SS-MM might display a closer relation to subsidiary pulses or minor fluctuations in cosmic-ray intensity than did total sunspot area.

The same period of investigation, May 25, 1938, to December 1, 1939, inclusive, and the same cosmic-ray data employed in the earlier investigations[2,3] were utilized again in this. As discussed more fully in the earlier papers, the cosmic-ray intensity was measured by means of a heavily shielded, high pressure ionization chamber and recording equipment, and was corrected for bursts and for variations in barometric pressure. Because, for purposes of comparison, the zero-days required for the Chree analysis were the identical days selected earlier on the basis of cosmic-ray intensity, the cosmic-ray curves appearing in this paper are the same (or sections of the same) cosmic-ray curves appearing in the earlier papers, with somewhat different scales. The SS-MM data were the same as heretofore employed,[1] of course.

The first step was to investigate what variations in SS-MM might be associated with the primary pulses in C-R. (C-R will be used hereinafter to designate cosmic-ray intensity.) Figures 1 and 2 show the results obtained. Figure 1 shows the primary positive pulse in C-R (dotted line) from day number -15 to $+15$ and the accompanying curve (solid line) for SS-MM. The ninety zero-days selected for this diagram were the five with highest C-R in each of the 18 months, June 1938 to November 1939, inclusive. Figure 2 shows the primary negative pulse in C-R with the corresponding curve for SS-MM.

* Presented at the meeting of the American Physical Society at Chicago, November 26–27, 1948.

[1] J. W. Broxon, Phys. Rev. **75**, 606 (1949).

[2] J. W. Broxon, Phys. Rev. **59**, 773 (1941). This paper provides details of the method of measurement of the cosmic-ray intensity at Boulder, Colorado (lat. 40° N; long. 105°16′ W; alt. 5440 ft.); its diagrams provide an indication of the statistical variations in the intensity, and the paper includes a brief description of Chree's method of analysis.

[3] J. W. Broxon, Phys. Rev. **62**, 508 (1942).

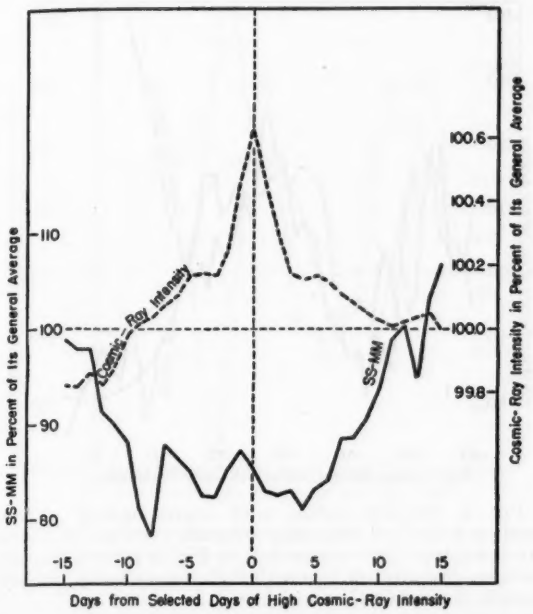
SS-MM in Percent of Its General Average
Cosmic-Ray Intensity in Percent of Its General Average
Cosmic-Ray Intensity
SS-MM
Days from Selected Days of High Cosmic-Ray Intensity

FIG. 1. The solid line represents SS-MM pulse corresponding to primary positive pulse in cosmic-ray intensity. The dotted line represents the cosmic-ray intensity. For both these curves the selected zero-days are the five days in each month with *highest* cosmic-ray intensity; included are all 90 zero-days for the 18 months.

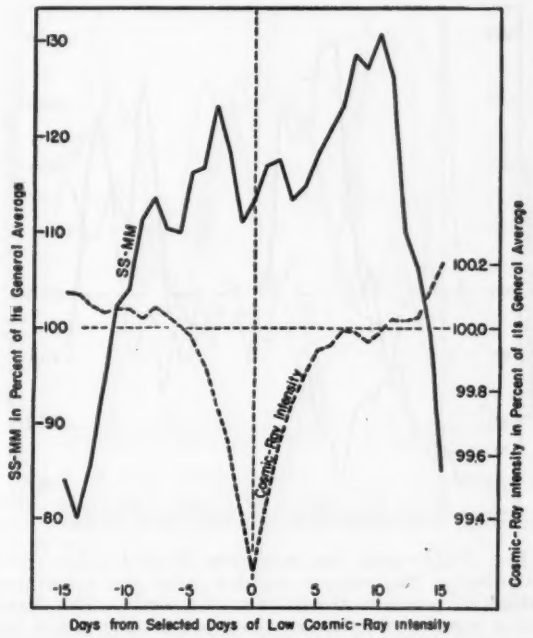
SS-MM in Percent of Its General Average
Cosmic-Ray Intensity in Percent of Its General Average
SS-MM
Cosmic-Ray Intensity
Days from Selected Days of Low Cosmic-Ray Intensity

FIG. 2. SS-MM pulse with corresponding primary negative pulse in cosmic-ray intensity. This corresponds to Fig. 1 except that here the selected zero-days are the five days with *lowest* cosmic-ray intensity in each month; again, 90 zero-days are employed.

For this diagram the selected zero-days were the five of lowest C-R in each of the 18 months.

The SS-MM resembles total sunspot area somewhat in that it displays large pulses in approximate phase opposition to the primary pulses in C-R. As is seen upon comparison of Figs. 1 and 2 with Figs. 6 and 7 of reference 3, however, the pulses in SS-MM and in sunspot area associated in the same way with the primary pulses in C-R are strikingly different in detail. (It should be recalled that the C-R curves of references 2 and 3 were drawn 0.09 percent too high.) The associated pulses in sunspot area have quite definite peaks opposed to the sharp peaks of the C-R primary pulses and preceding the latter by three or four days. The correspondingly associated pulses in SS-MM display no such definite peaks. With the exception of the rather unsymmetrically high portion of the curve of Fig. 2 in the region of day numbers 6 to 11, the SS-MM curves appear to have rather broad minimum and maximum, respectively, and to be rather well centered about day-number zero, indicating that they are almost exactly out of phase with the C-R primary pulses, or perhaps there is a lag in Fig. 2. In spite of the blunt form of the associated pulses in SS-MM, their bases (their widths in day numbers at the level where the average is attained) do not appear to be much broader than the bases of the pulses in sunspot area. The departures from the average are somewhat greater in the SS-MM pulses, extending to some 20 to 30 percent as compared with extreme variations of 14 to 21 percent in the case of the sunspot-area pulses. It seems really rather remarkable that such large variations in any variable should be disclosed in connection with the selection of days on the basis of variations in C-R whose primary peak values represent departures of less than 0.7 percent from the average C-R.

The next step was to investigate whether the SS-MM might also display any correlation with the minor variations or subsidiary pulses in C-R, such correlation not having been apparent in the other variables heretofore investigated. Accordingly, the Chree analysis was run from day number -5 (or -15 in some cases) to $+60$ for zero-days selected from the first 15 of the 18 months, and from -60 to $+5$ (or $+15$ in

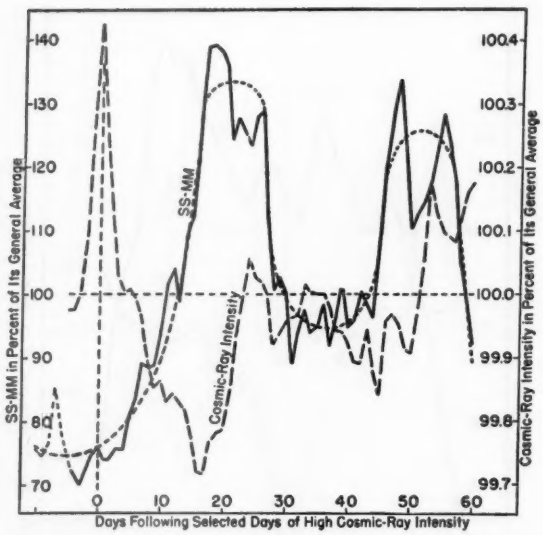
SS-MM in Percent of Its General Average
Cosmic-Ray Intensity in Percent of Its General Average
SS-MM
Cosmic-Ray Intensity
Days Following Selected Days of High Cosmic-Ray Intensity

FIG. 3. The solid line represents SS-MM pulses corresponding to the primary positive pulse and subsequent subsidiary pulses in the cosmic-ray intensity. The dotted line is one drawn arbitrarily to represent the salient features of the SS-MM pulses while minimizing irregularities of relatively short duration. The broken line represents cosmic-ray intensity. The 75 zero-days for these curves are the five with *highest* cosmic-ray intensity in each of the *first* 15 months.

some cases) for zero-days selected from the last 15 months of the period of the investigation.

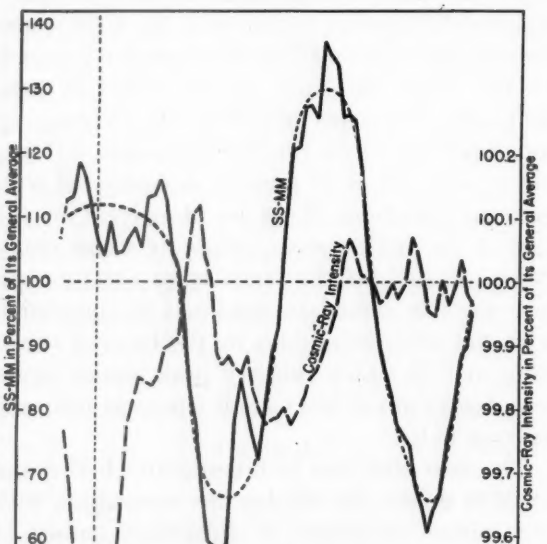
SS-MM in Percent of Its General Average
Cosmic-Ray Intensity in Percent of Its General Average
SS-MM
Cosmic-Ray Intensity
Days Following Selected Days of Low Cosmic-Ray Intensity

FIG. 4. SS-MM pulses with corresponding primary negative pulse and subsequent subsidiary pulses in cosmic-ray intensity. This corresponds to Fig. 3 except that here the selected zero-days are the five with *lowest* cosmic-ray intensity in each of the *first* 15 months.

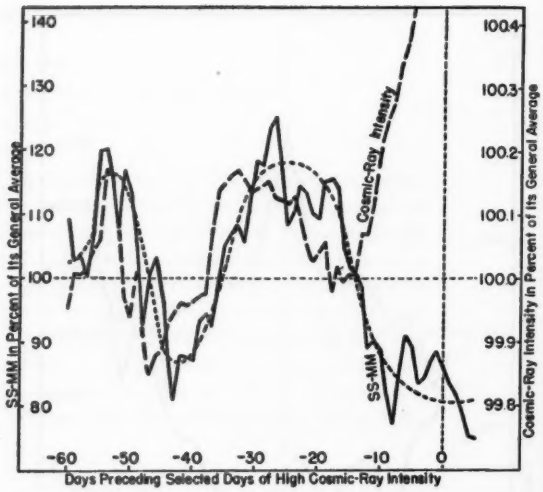
SS-MM in Percent of Its General Average
Cosmic-Ray Intensity in Percent of Its General Average
SS-MM
Cosmic-Ray Intensity
Days Preceding Selected Days of High Cosmic-Ray Intensity

FIG. 5. SS-MM pulses with corresponding primary positive pulse and preceding subsidiary pulses in cosmic-ray intensity. This corresponds to Fig. 3 except that here the zero-days are the five with *highest* cosmic-ray intensity in each of the *last* 15 months.

The results are shown in Figs. 3, 4, 5, and 6. In each of these (as well as in subsequent diagrams) the broken line represents the C-R pulses obtained earlier.[2] The solid lines represent the corresponding pulses in SS-MM obtained with the *identical* zero-days employed in obtaining the C-R curves. For Fig. 3 the selected zero-

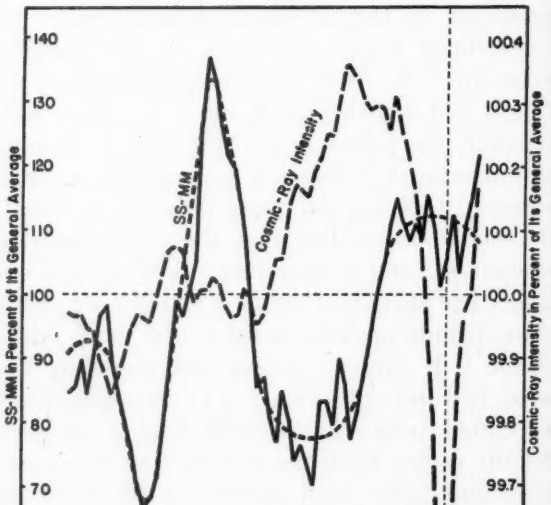
SS-MM in Percent of Its General Average
Cosmic-Ray Intensity in Percent of Its General Average
SS-MM
Cosmic-Ray Intensity
Days Preceding Selected Days of Low Cosmic Ray Intensity

FIG. 6. SS-MM pulses with corresponding primary negative pulse and preceding subsidiary pulses in cosmic-ray intensity. This corresponds to Fig. 3 except that here the zero-days are the five with *lowest* cosmic-ray intensity in each of the *last* 15 months.

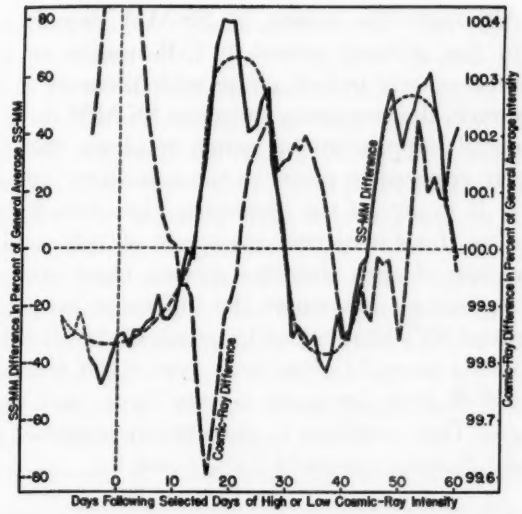
SS-MM Difference in Percent of General Average SS-MM
Cosmic-Ray Difference in Percent of General Average Intensity
SS-MM Difference
Cosmic-Ray Difference
Days Following Selected Days of High or Low Cosmic-Ray Intensity

FIG. 7. The solid line represents SS-MM primary and subsequent difference pulses obtained by subtracting the SS-MM values of Fig. 4 from the corresponding ones of Fig. 3. As in Figs. 3, 4, 5, and 6, the dotted line is drawn arbitrarily to represent the salient features of the SS-MM difference pulses while minimizing minor irregularities. The corresponding difference pulses in cosmic-ray intensity are shown by the broken line.

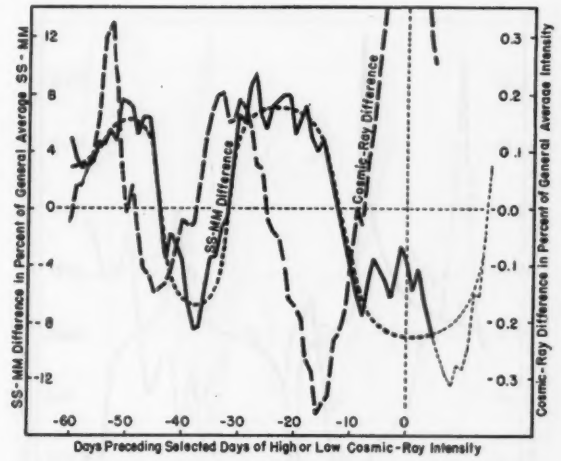
SS-MM Difference in Percent of General Average SS-MM
Cosmic-Ray Difference in Percent of General Average Intensity
SS-MM Difference
Cosmic-Ray Difference
Days Preceding Selected Days of High or Low Cosmic-Ray Intensity

FIG. 8. SS-MM and cosmic-ray primary and preceding difference pulses obtained by subtracting values in Fig. 6 from corresponding values in Fig. 5. Otherwise, this corresponds to Fig. 7.

days were the five with highest C-R in each of the months, June, 1938, to August, 1939, inclusive. For Fig. 4 the selected zero-days were the five of lowest C-R in each of these same months. For Fig. 5 the selected zero-days were the five with highest C-R in each of the months, September, 1938, to November, 1939, inclusive. For Fig. 6 the selected zero-days were the five of lowest C-R in these same months.

In each of these four diagrams the dotted line is drawn arbitrarily to represent what appears to the writer to be the principal features of the SS-MM pulses associated with the C-R pulses. While it appears that any attempt to represent these pulses by a smoothed-out curve must be rather arbitrary, it may be noted that the principal variations of SS-MM on either side of the mean, and the day numbers where the mean is attained, are quite well represented by the dotted lines. The smaller fluctuations near the troughs and crests of the pulses, presumably largely due to statistical variations and perhaps to inaccuracies in the data as well as in the mode of approximation in determining the SS-MM, were rather generally ignored in drawing the dotted curves. In considering irregularities it may be well to keep in mind not only the several approximations employed in obtaining the SS-MM, but also the facts that the date of determination of the maximum H for a particular sunspot group and the particular position in the group in which it was determined are not known, that this value is given only in integral multiples of 100 gauss, and that the sunspot areas are determined at widely different hours on different days.

In Figs. 7 and 8 are shown the difference pulses in SS-MM and C-R obtained in the usual way from the preceding four diagrams. The curves of Fig. 7 were obtained by subtracting ordinates of the curves of Fig. 4 from the corresponding ordinates of Fig. 3. The curves of Fig. 8 were obtained similarly by subtracting ordinates of Fig. 6 from the corresponding ones of Fig. 5. These difference curves in at least one respect are more satisfactory than the originals from which they were obtained, for the very considerable seasonal effect in C-R is largely eliminated in these. As in the preceding four diagrams, dotted lines have been drawn to represent the principal features of the SS-MM difference curves while smoothing out their minor fluctuations. The C-R difference curves are sections of those published earlier.[2]

Inspection of Figs. 3 to 6 shows that the secondary pulses in SS-MM are generally (though not always) quite as large or larger than those associated with the primary pulses in C-R, deviating in some cases by approximately 40

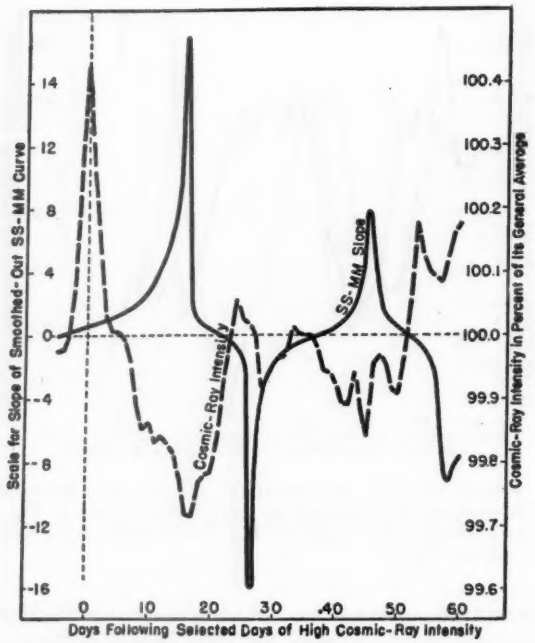
Scale for Slope of Smoothed-Out SS-MM Curve
Cosmic-Ray Intensity in Percent of its General Average
SS-MM Slope
Cosmic-Ray Intensity
Days Following Selected Days of High Cosmic-Ray Intensity

FIG. 9. The solid line represents the slope of the dotted line of Fig. 3. The broken line is the same as that in Fig. 3, and represents cosmic-ray intensity.

percent from the mean. They appear to be quite as large or rather larger than the secondary pulses obtained[1] with zero-days selected on the basis of large or small SS-MM. A similar statement holds for the SS-MM difference pulses in Figs. 7 and 8.

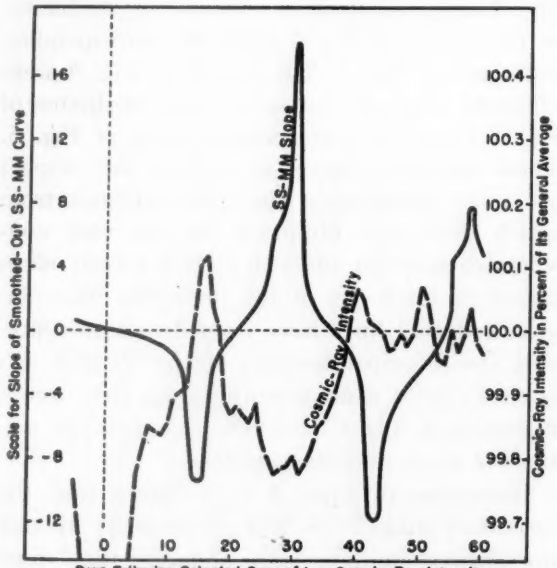
Scale for Slope of Smoothed-Out SS-MM Curve
Cosmic-Ray Intensity in Percent of its General Average
SS-MM Slope
Cosmic-Ray Intensity
Days Following Selected Days of Low Cosmic-Ray Intensity

FIG. 10. These curves bear the same relation to Fig. 4, as do those of Fig. 9 to Fig. 3.

Although the pulses in SS-MM associated with the primary pulses in C-R appear to be almost exactly out of phase with them in each instance, the remaining pulses in SS-MM do not generally appear to be either in phase nor directly opposed in phase to the subsidiary pulses in C-R in any of the diagrams, Figs. 3 to 8, inclusive. Insofar as one can speak of "phase" in the case of such irregular pulses, there appear to be many cases where the difference in phase is about 90°. That is, the departure of the SS-MM from its mean is often near zero when that of the C-R from its mean is very large, and vice versa. This condition is particularly apparent in the difference curves of Figs. 7 and 8.

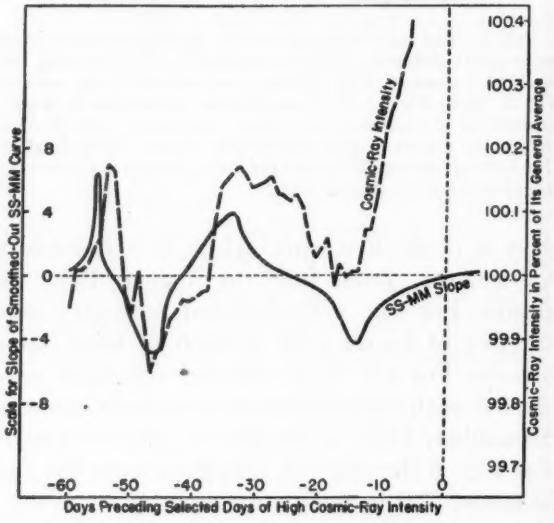
Scale for Slope of Smoothed-Out SS-MM Curve
Cosmic-Ray Intensity in Percent of its General Average
Cosmic-Ray Intensity
SS-MM Slope
Days Preceding Selected Days of High Cosmic-Ray Intensity

FIG. 11. These curves bear the same relation to Fig. 5, as do those of Fig. 9 to Fig. 3.

This situation suggests that there might be a close relation between the subsidiary pulses in C-R and the *rate of change* of SS-MM. It was this observation which led the writer to draw the smooth (dotted) curves to approximate the principal features of the SS-MM curves in Figs. 3 to 8, inclusive. In one instance the slopes of the jagged SS-MM curve were obtained directly and plotted against day numbers. As expected, the curve obtained was quite meaningless, because the slope is so highly susceptible to minor variations. Consequently, the smooth curves were drawn for all the SS-MM curves determined statistically, and the slope of the smooth curve was determined at each day number by a

tangent meter. These slopes were then plotted as ordinates with day numbers as abscissae. The curves so obtained are shown in Figs. 9 to 14, inclusive, which give the slopes of the smooth (dotted) curves for SS-MM in Figs. 3 to 8 in that order. In Figs. 9 to 14 are also included the identical C-R curves given in the corresponding diagrams of Figs. 3 to 8.

It is seen that the SS-MM slope curves do appear to bear a rather definite relation to the subsidiary pulses in C-R, at least for the first two subsidiary pulses on either side of the primary which have been investigated here. In all cases the SS-MM slopes appear to be almost directly out of phase with the subsidiary pulses

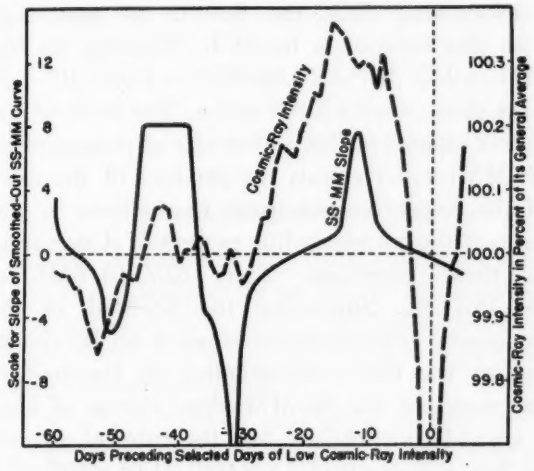
Scale for Slope of Smoothed-Out SS-MM Curve
Cosmic-Ray Intensity in Percent of its General Average
Cosmic-Ray Intensity
SS-MM Slope
Days Preceding Selected Days of Low Cosmic-Ray Intensity

FIG. 12. These curves bear the same relation to Fig. 6, as do those of Fig. 9 to Fig. 3.

in C-R following their primary pulses. On the other hand, the SS-MM slopes appear to be almost directly in phase with the subsidiary pulses in C-R preceding their primary pulses. That is, if we neglect the minor fluctuations in SS-MM but consider only the general trends represented by the smoothed-out SS-MM curves, then it appears that previous to the primary pulses, the C-R is generally high when the SS-MM is increasing and low when the SS-MM is decreasing; while subsequent to the primary pulses, the C-R is generally high when the SS-MM is decreasing and low when the SS-MM is increasing. As in the case of the primary pulses with zero-days selected from all 18 months, the SS-MM exhibits a pulse in approximate phase

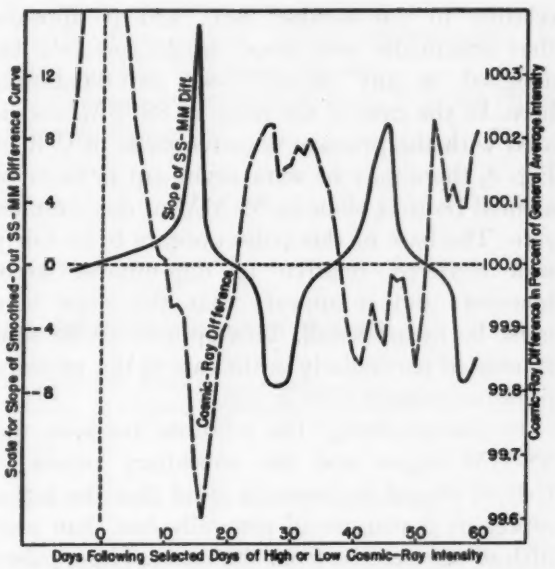
Scale for Slope of Smoothed-Out SS-MM Difference Curve
Cosmic-Ray Difference in Percent of General Average Intensity
Slope of SS-MM Diff.
Cosmic-Ray Difference
Days Following Selected Days of High or Low Cosmic-Ray Intensity

FIG. 13. These curves bear the same relation to Fig. 7, as do those of Fig. 9 to Fig. 3.

opposition to the primary pulse in C-R in every case, thus providing a slope of approximately zero at day number zero in each instance. It should be pointed out that the writer was influenced somewhat by the form of the eighteen-month curves in drawing the smooth curves for the several fifteen-month curves in the neighborhood of day-number zero. The pulse in SS-MM associated with the primary positive pulse in C-R in Fig. 1 is certainly quite symmetrical

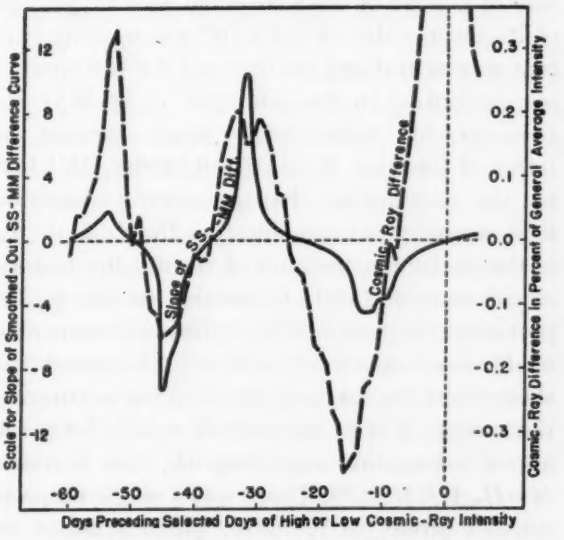
Scale for Slope of Smoothed-Out SS-MM Difference Curve
Cosmic-Ray Difference in Percent of General Average Intensity
Slope of SS-MM Diff.
Cosmic-Ray Difference
Days Preceding Selected Days of High or Low Cosmic-Ray Intensity

FIG. 14. These curves bear the same relation to Fig. 8, as do those of Fig. 9 to Fig. 3.

relative to day-number zero, and it appears that practically zero slope should certainly be assigned to any smoothed-out representation here. In the case of the pulse in SS-MM associated with the primary negative pulse in C-R in Fig. 2, there may be some argument in favor of a small positive slope in SS-MM at day-number zero. The base of this pulse appears to be fairly well centered relative to day-number zero, however, and it appears that the slope here must be rather small. This appears to be substantiated particularly in the case of the primary negative pulse in C-R in Fig. 4.

In contemplating the relations between the SS-MM slopes and the subsidiary pulses in C-R, it should be borne in mind that the latter represent deviations of generally less than one-fifth of one percent from the mean. These pulses are quite irregular, perhaps in part because there is a limit to the accuracy of measurement, and very likely because the C-R data have been corrected only for bursts and for variations in barometric pressure, while they are doubtless subject to variations associated with other phenomena. Moreover, they are brought out in each instance by statistical treatment of data extending over intervals of only 15 months. In view of these limitations, the relations indicated by the last six diagrams seem rather striking.

The unit of the scale for the SS-MM slope curves of Figs. 9 to 14, inclusive, represents a rate of change of SS-MM equal to 0.99 percent of its mean value of 2.5×10^{31} e.m.u. (ring-current representation) per day or 2.8×10^{24} e.m.u./sec. According to the definition[1] of SS-MM, its (ring-current) value for a single sunspot in terms of its area, A, is $M_c=0.0460H_mA^2/(A_m)^{\frac{1}{2}}$ on the assumption that its central magnetic field intensity is given by $H_c=H_m(A/A_m)^{\frac{1}{2}}$. A_m is the maximum value of A during the history of the sunspot (while it remains on the visible portion of the Sun) and H_m is the maximum value of H_c ever associated with it. Chapman[4] has shown that the magnetic flux leaving or entering the sunspot is approximately $N=AH_c/3$. On the above assumption regarding H_c, this becomes $N=H_mA^{\frac{1}{2}}/(3(A_m)^{\frac{1}{2}})$. There was a single unipolar sunspot group, M.W. 6618, which attained its maximum area during the period of this investigation (September 23, 1939), which was visible for thirteen days, whose maximum SS-MM was three times as great as the daily average for the total of all sunspots during the period, and whose maximum area was about three percent greater than the daily average value (1889 millionths of the Sun's visible hemisphere, or 5.82×10^{19} cm^2) of the total area of all sunspots observed during the period. Consequently, it may be of some interest to consider the magnetic flux that would be associated with a single sunspot with an area and corresponding SS-MM equal to the average values of these for all the sunspots for the whole period, according to the relations just stated.

Proceeding thus, the flux to be associated with the sunspot is found by dividing its SS-MM$(=M_c)$ by $3\times0.0460(A)^{\frac{1}{2}}=1.05\times10^9$ cm. This gives $N=2.4\times10^{22}$ e.m.u. The ratio of the rate of change of flux to the rate of change of its SS-MM$(=M_c)$ equals the product of the ratio of the respective functions, themselves, by the ratio of the corresponding powers of A occurring in these functions. Thus $(dN/dt)/(dM_c/dt)=0.75N/M_c$. Supposing the SS-MM of the imaginary representative sunspot to be changing at the rate corresponding to the unit of the scale for the SS-MM slope curves of Figs. 9 to 14, we obtain for its rate of change of flux, $dN/dt=0.75(2.8\times10^{24})/(1.05\times10^9)=2.0\times10^{15}$ e.m.u./sec. In Figs. 9 to 14, slopes of 8 units are not infrequently attained. On the basis of the foregoing assumptions, these would correspond to rates of change of flux associated with the representative sunspot which, according to Faraday's law, would produce an e.m.f. of 1.6×10^8 volts in a circuit linking the flux.

While these contemplations have dealt with a situation rather far removed from the actual physical situation, the magnitude of the e.m.f. obtained is at least interesting. It seems not unlikely that considerably larger e.m.f.'s may actually be produced in sunspots by electromagnetic induction. Several years ago Swann[5] deduced that stellar magnetic fields such as occur in sunspots can by electromagnetic induction

[4] S. Chapman, Mon. Not. R. Astr. Soc. **103**, 117 (1943).

[5] W. F. G. Swann, Phys. Rev. **43**, 217 (1933); J. Franklin Inst. **215**, 273 (1933).

impart to electrons energies corresponding to 10^{10} volts in a time interval of the order of one second without great magnetic field intensities, and that the rate of acquiring energy may reasonably be expected to be greater than the rate of loss by collision. He appears to have considered that 10^9 ev might approximate the upper limit in the case of the sun.

This work was supported in part by the Office of Naval Research.

PHYSICAL REVIEW VOLUME 75, NUMBER 4 FEBRUARY 15, 1949

The Radioactivities of Some High Mass Isotopes of Cobalt

THOMAS J. PARMLEY,* BURTON J. MOYER, AND ROBERT C. LILLY
Radiation Laboratory, Department of Physics, University of California, Berkeley, California

(Received October 28, 1948)

By neutron bombardments of samples of Ni enriched in isotopes 61, 62, and 64, respectively, the following radioactivities have been identified:

Co^{61}, β^- 1.3 Mev, no γ, half-life 1.75 hours,
Co^{62}, β^- 2.3 Mev, γ1.3 Mev, half-life 13.9 min.

Evidence is also presented for a 1.6-minute β- and γ-activity associated with Co^{62}, and for a 4- to 5-minute activity possibly of Co^{64}.

I. INTRODUCTION

THE availability of isotopically enriched nickel samples in milligram amounts has made possible the study of radiations from cobalt nuclei in the region of a few mass units above the well-known Co^{60}.

The nickel samples employed in this investigation were prepared by the calutron process here at the Radiation Laboratory. Only the sample enriched in Ni^{64} has been isotopically analyzed. The relative abundances for this sample were found to be:

Ni^{64}	Ni^{62}	Ni^{61}	Ni^{60}	Ni^{58}
61.6%	2.8%	1.0%	13.6%	21.0%

This article presents data on activities assigned to Co^{61} and Co^{62}, and also on an activity which is tentatively assigned to Co^{64}.

II. RADIOACTIVITY OF COBALT 61

In a letter to the editor of the Physical Review[1] a 1.75 ± 0.05-hour half-life, β-activity was reported as a result of Co^{61}. Here we wish to present more complete evidence of this assignment, and data on the energy of the β-particle.

To help determine the isotope responsible for this activity, samples of nickel 61, 62, and 64 were placed one in front of the other, separated by paper, within a 0.035-in. cadmium shield in the neutron beam produced by 22-Mev deuteron bombardment of beryllium in the Crocker Laboratory 60-inch cyclotron. In all neutron bombardments of the nickel isotopes, the cadmium covering was used to minimize the $Ni^{64}(n,\gamma)Ni^{65}$ reaction yielding the 2.64-hour activity. The 1.75-hour activity appeared in each sample but much more strongly in connection with the Ni^{61} isotope than in the others.

Chemical identification was made as follows: A small sample of approximately 2-mg weight enriched in the isotope 61 was bombarded with neutrons as described above. The activated metal was dissolved in HNO_3, the nitrates were converted to chlorides, and 2 mg of cobalt and 2 mg of iron as chlorides were added. An iron fraction was separated by precipitation with NH_4OH and purified by solution in HCl and additional NH_4OH precipitations. The filtrate was acidified slightly with HCl, saturated with NH_4SCN, and cobalt was extracted with an

* Department of Physics, University of Utah, Salt Lake City, Utah.

[1] T. J. Parmley and B. J. Moyer, Phys. Rev. **72**, 82 (1947).

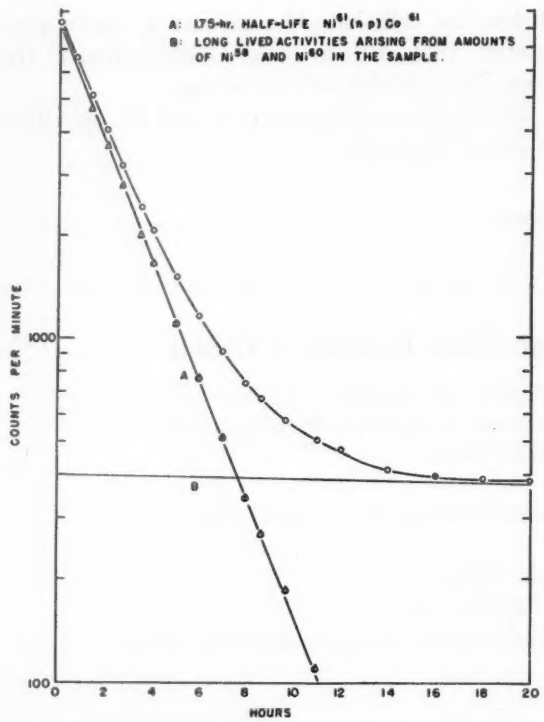
A: 1.75-hr. HALF-LIFE Ni⁶¹(n p) Co ⁶¹
B: LONG LIVED ACTIVITIES ARISING FROM AMOUNTS OF Ni⁵⁸ AND Ni⁶⁰ IN THE SAMPLE.
COUNTS PER MINUTE
1000
100
A
B
0 2 4 6 8 10 12 14 16 18 20
HOURS

FIG. 1. Decay curve for neutron activated Ni^{61}.

equal volume of amyl alcohol-ethyl ether (1:1). Cobalt was recovered from the organic layer with $6N$ NH_4OH, and after separation of this ammoniacal fraction and acidification with HCl, the above extraction procedure was repeated. Cobalt was precipitated with NH_4HS and mounted for counting as dried CoS or as CoO. The nickel fraction contained in the aqueous layer from the first extraction was further purified by again saturating it with NH_4SCN and reextracting with amyl alcohol-ethyl ether (1:1). The solution was boiled to expel ether, made ammoniacal; and nickel was precipitated with a 1 percent solution of dimethyl-glyoxime in alcohol. The 1.75-hour activity appeared in the cobalt fraction.

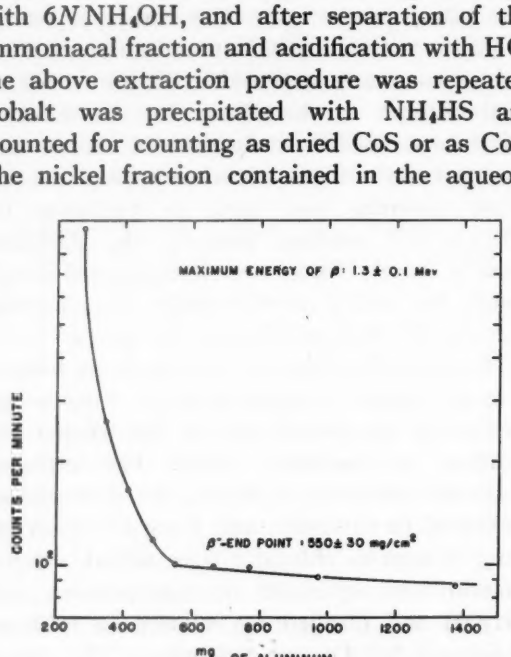

FIG. 2. Aluminum absorption curve for 1.75-hour half-life Co^{61}.

The mass assignment for this cobalt activity was made in the following way. A two-gram sample of isotopically normal nickel was given a 30-minute bombardment with approximately 22-Mev deuterons in the Crocker cyclotron. The activated metal was dissolved in HNO_3, the nitrates converted to chlorides, and 75 mg of copper and 50 mg of cobalt as chlorides were added. The copper was separated by reduction with SO_2 and precipitation with NH_4SCN. The filtrate was acidified with HCl and cobalt was precipitated with α-nitroso-β-naphthol in acetic acid. After being washed well with warm HCl (1:1) followed by H_2O, this precipitate was ignited to CoO. The CoO was converted to $CoCl_2$ by treating it with anhydrous Cl_2 at 650°C for 30 minutes. Calutron analysis of the $CoCl_2$ placed the 1.75-hour half-life in mass 61 position. We thus have both positive chemical and mass assignments for this activity.

As stated in reference 1, confirmatory evidence was obtained by neutron bombardment of electrolytic copper at the Crocker Laboratory 60-inch cyclotron, followed by calutron analysis, and by chemical analysis.

The chemical procedure was as follows: the copper metal, weighing 10 g, was dissolved in $6N$ HCl containing several milliliters of 30 percent H_2O_2. Excess H_2O_2 was boiled off, and 50 mg of cobalt as $CoCl_2$ were added. The copper was removed, and the cobalt separated and ignited to CoO as described in the previous chemical analysis.

The CoO was dissolved in HCl and 100 mg of copper and 25 mg of nickel as chlorides were added. Copper was removed a second time following the indicated procedure. A small part of the CoO was dissolved in HCl and mounted for counting on a platinum disk as CoO and the remainder was chlorinated as described above and used for the calutron analysis.

All beta-counting was done in the conven-

tional manner of placing the active sample at the proper distance from a thin mica window Geiger counter mounted within a thick-walled lead house. Corrections for coincidence count loss and for background were made in the usual way. Figure 1 displays a typical decay of the Co^{61} activity.

Measurement of the β-particle energy was done with Al absorbers. Figure 2 shows the curve of activity *vs.* absorber thickness, corrected of course for decay of the activity. The end point of the curve is taken to be 550 ± 30 mg/cm² of Al, yielding a maximum energy for the β-particles of 1.3 ± 0.1 Mev.

There was no indication of γ-radiation with this half-life.

In summary it may be stated that a 1.75-hour β-activity, with disintegration energy of 1.3 Mev, has been assigned through chemistry and mass analysis to Co^{61}. In all, this activity has been produced by each of the following reactions:

$Ni^{61}(n,p)Co^{61}$,
$Cu^{65}(n,\alpha n)Co^{61}$,
$Ni^{64}(p,\alpha)Co^{61}$(14-Mev protons),
$Ni^{64}(d,\alpha n)Co^{61}$ (22-Mev deuterons).

III. RADIOACTIVITY OF COBALT 62

Neutron bombardment of the nickel sample enriched in isotope 62 yielded activities with half-lives of 13.9 ± 0.2 min. and 1.6 ± 0.2 min. These activities did not appear in the neutron bombardment of Ni^{61} and only slightly in the sample enriched in Ni^{64}.

In isolating the 13.9-minute activity it would have been most desirable to have performed both mass and chemical analyses as in the case of Co^{61}. Because of the short half-life, the mass separation has not been successfully performed. Chemical identification was made by preparing counting samples of nickel and cobalt within a time of twelve minutes from the end of bombardment. The cobalt fraction was extracted by the process previously described, and the nickel was precipitated with NH_4HS in the aqueous layer after the cobalt extraction. It was mounted for counting as NiS.

This experiment was tried, using both nickel 62 and nickel 61 with the activity appearing in the cobalt fraction from the nickel 62, but not in

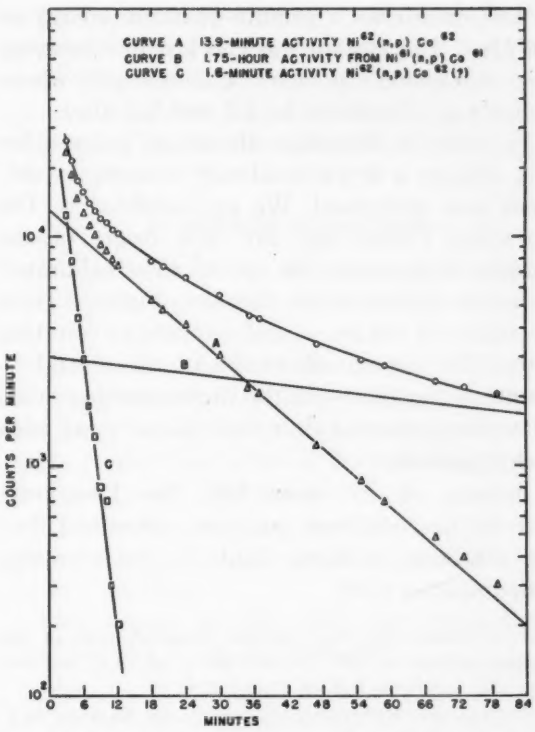
CURVE A 13.9-MINUTE ACTIVITY Ni⁶²(n,p) Co ⁶²
CURVE B 1.75-HOUR ACTIVITY FROM Ni⁶¹(n,p) Co ⁶¹
CURVE C 1.6-MINUTE ACTIVITY Ni⁶²(n,p) Co ⁶² (?)
COUNTS PER MINUTE
MINUTES
0 6 12 18 24 30 36 42 48 54 60 66 72 78 84

FIG. 3. Radioactive decay curve for 13.9-min. and 1.6-min. Co^{62}.

that from nickel 61. The activity did not appear in the residue in either case. The fact that nothing shorter than the 1.75-hour half-life appeared in the cobalt from nickel 61 is significant, since an (n,pn) reaction should yield cobalt 60 which has a 10.7-min. half-life activity. Inasmuch as this activity does not appear in the nickel 61 sample, it implies that the yield of (n,pn) reactions here is probably negligible. These facts make it apparent that the 13.9-minute decay is associated with an (n,p) reaction in Ni^{62} yielding radioactive Co^{62}. The decay curve in Fig. 3 shows the 13.9-minute and 1.6-minute lives in the Ni^{62} bombardment.

The 13.9-minute activity exhibits both β- and γ-radiation, the energies of which were measured by absorption in aluminum and lead in repeated runs with the Ni^{62} sample. The first 550 mg/cm² of aluminum eliminated the 1.75-hour β-particles, and the end point for β's with the 13.9-minute half-life came at 1100 ± 50 mg/cm². This denotes an energy of 2.3 ± 0.1 Mev.

Both β- and γ-absorption data are plotted in Fig. 4. The lead absorption half-value thickness

of 1.07 cm shows a gamma-quantum energy of 1.3 Mev. The system was checked by observing the absorption of Co^{60} gamma-rays whose energies are known to be 1.1 and 1.3 Mev.

In order to determine the decay pattern for this activity a β–γ-coincidence counting experiment was performed. We are indebted to Dr. Cornelius Tobias and Mr. Hal Anger of the Donner Laboratory for use of their calibrated counting equipment for this test. Figure 5 gives the decay of the β-, γ-, and coincidence counting rates. The known efficiencies of the β- and γ-counters, together with the three counting rates, allow the statement that there is one γ-ray with each β-particle.

Because of its short life, the 1.6-minute activity has not been positively identified, but the following evidence leads to its tentative assignment to Co^{62}.

(1) It arises from fast neutron bombardment of the sample enriched in Ni^{62}. It is not due to an (n,α) reaction, since this yields the known 47-day Fe^{59}.

(2) It is not Ni^{63}, for it does not arise from an (n,p) reaction on Cu^{63}, nor from a (d,α) reaction on Cu^{65} which was tried with 30-Mev deuterons at reduced radius on the 184-in. cyclotron. Also exposure of the Ni^{62} sample without Cd covering to slow neutrons by use of paraffin with neutrons from the 60-in. cyclotron did not augment the activity.

(3) It arises also from deuteron bombardment (30 Mev) of the sample enriched in Ni^{64}, presumably by the (d,α) reaction. It was not noted in bombardment of Ni^{64} with 14-Mev protons from the 37-in. frequency-modulated cyclotron though the Co^{61} 1.75-hour activity was produced by the (p,α) reaction.

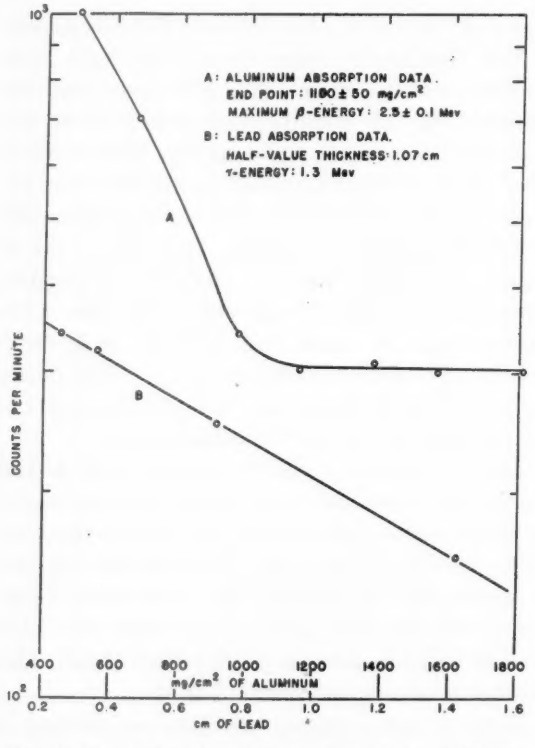

FIG. 4. Absorption data for 13.9-min. Co^{62} radiations.

Crude absorption experiments suggest the existence of γ-radiation since the activity has been observed through as much as 4 g/cm² of lead. Also the β–γ-coincidence data of Fig. 5 show both β- and γ-radiation with a short life of 1–2 minutes.

The best determination of the half-life of this activity was obtained from the $Ni^{64}(d,\alpha)Co^{62}$ bombardment. This is not displayed here, but leads to a value of 1.6±0.2 minutes. Both the 13.9-minute and the 1.6-minute lives appear with good yield in this bombardment.

IV. RESULT OF NEUTRON BOMARDMENT OF Ni^{64}

A 4- to 5-minute half-life activity was observed in a neutron bombardment of nickel 64 which did not appear in similar bombardments

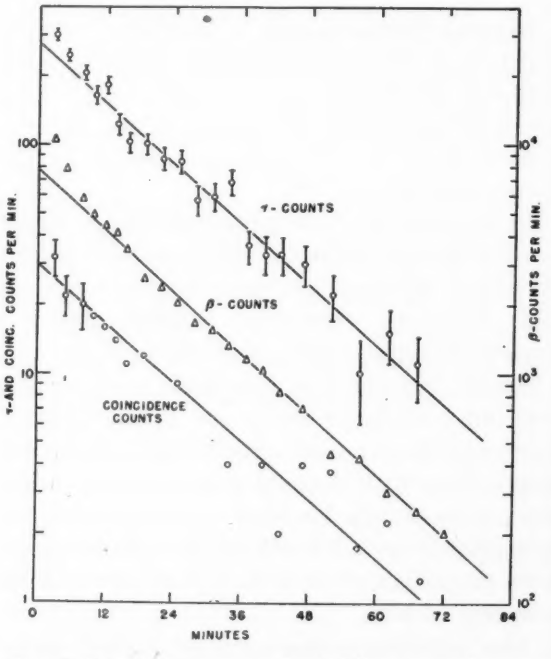

FIG. 5. Decay of β-, γ-, and coincidence counting rates for 13.9-minute Co^{62} (note evidence of the 1.6-minute decay in both β- and γ-radiation).

of nickel 61 or 62. Inasmuch as copper 66 exhibits an activity of 5 minutes, it was deemed advisable to free the nickel 64 isotope of any copper and zinc which might accidently be present. This chemical procedure was carefully done with the isotope appearing for bombardment as an oxide. In a subsequent neutron bombardment of the sample, the 4- to 5-minute activity persisted, suggesting that the activity is produced from a neutron bombardment of nickel 64. As an aid to the determination of this half-life, it was found useful to count the activity through sufficient absorber to eliminate the 1.75-hour half-life produced from the fraction of Ni^{61} existing in this sample. This left the 2.6-hour half-life as a good base line from which to proceed in the analysis of the decay curve. The activities remaining were the 13.9-minute Co^{62} from Ni^{62} in this sample, and the 4- to 5-minute period. The latter has been detected through as much as 1250 mg/cm² of aluminum.

Because of the shortness of the half-life involved and to the very small size of the sample of Ni^{64}, it has been difficult to establish certainly whether the source of the activity is in the cobalt or nickel group. Present chemical evidence points to cobalt with the suggestion that we are dealing with an n,p reaction on nickel 64 producing cobalt 64.

V. ACKNOWLEDGMENTS

The authors wish to acknowledge the cooperation of Messrs. Duane Sewell and James Vale of the 184-in. cyclotron staff, and Thomas Putnam and B. Rossi of the Crocker Laboratory 60-in. cyclotron group. Mr. Putnam contributed the use of special counting equipment for the study of short half-lives in the measurements of the 1.6-minute activity.

The metallic samples of isotopic nickel were prepared by J. Beaufait by an electroplating and stripping process.

The calutron analyses were carried out under the direction of Dr. Keith Pierce.

This problem was carried out under the auspices of the Atomic Energy Commission.

PHYSICAL REVIEW VOLUME 75, NUMBER 4 FEBRUARY 15, 1949

Quantitative Measurements with Scintillation Counters

HARTMUT KALLMANN
Kaiser-Wilhelm-Institute for Physical Chemistry, Berlin-Dahlem, Germany
(Received June 10, 1948)

The efficiency of a number of fluorescent materials used as scintillation counters for various materials has been measured. Two characteristics have been distinguished: (a) The physical light yield, i.e., the fraction of the absorbed energy transformed into light, and (b) the practical light yield, i.e., the amount of light obtained from a given intensity of radiation of a particular type, with the thickness of the phosphor adjusted for optimum results. Although the sulfide phosphors are high in physical yield, their practical yield is relatively lower because they are quite opaque to their fluorescent radiations. The organic phosphors, such as naphthalene and phenanthrene, and the potassium bromide phosphors are very much better in this respect.

THE counting of radioactive radiations by means of scintillations detected by photomultiplier tubes has recently received much interest.[1] We have performed a series of experiments with various fluorescent materials to investigate the applicability of this method to the determination of the intensity and energy of various radiations.[2] We characterize various phosphors by two main characteristics: (a) The physical light yield which is the fraction of the absorbed radiation energy transformed into

[1] See, e.g., F. Marshall and J. W. Coltman, Phys. Rev. 72, 528A (1947); R. J. Moon, Phys. Rev. 73, 1210 (1948); P. R. Bell, Phys. Rev. 73, 1405 (1948); G. B. Collins and R. C. Hoyt, Phys. Rev. 73, 1259 (1948).

[2] See also I. Broser and H. Kallmann, Zeits. f. Naturf. 2a, 439 (1947), Natur and Technik (July, 1947).

TABLE I. Light yields of various phosphors.

Phosphor	Wave-length A	Physical (relative to ZnS) α	β	γ	x-ray λ (A) 1.93	0.63	0.28	Technical (relative to ZnS) α	β	γ	x-ray λ (A) 1.93	0.63	0.28	Energy yield α
ZnS-Ag	4500	100	100	100	100	100	100	100	100	100	100	100	100	0.28
ZnS-Cu	5200	140	160	160			240	140		600			450	0.25
ZnS/CdS-Cu	5900	46						46						0.092
CdS-Ag	7600	78	~80	~80				78						0.23
Zn_2SiO_4-Mn	5250	13.5	81	80	40	50	52	13.5	130	130	40	50	60	0.027
ZnO	5500	7.0						7.0						0.014
$CaWO_4$	4300	6.3	49	60	18.5	23	30	6.3	52	72	25	33	36	0.013
$MgWO_4$	4900	6.4						6.4						0.013
KBr-Tl	3600	6	50.4	50.4				6		>1700				0.017
Naphthalene	3600	20	35	35	9	11		2.0	220	≧1000				0.004
Diphenyl	3600	6.0	52.5	525	25	22		6.0	220	580				0.012
Phenanthrene	4500	3.6	∞105	>61				3.6	198	241				0.007

light. (b) The technical light yield which gives the amount of light obtainable from a given intensity of radiation of particular type, choosing the optimum thickness of phosphor. The technical light yield depends on the physical light yield, the transparency of the phosphor for its own radiation, and the absorption for the primary radiation. It is desirable that a large fraction of the incident radiation be absorbed in a layer which is still transparent for the emitted light.

The physical light yield of the sulfide phosphors for α-particles approaches the maximum possible. E.g., for zinc sulfide it was found that for α-particles (independent of their energy) one light quantum is emitted for about 9 ev of kinetic energy expended in the phosphor, indicating a physical light yield of 27 percent.

It was found that with this phosphor an incident beam of 100 α-particles/sec. caused steady output current of about 10^{-9} amp. This current can be easily measured particularly when the tube is cooled to reduce the dark current. The multiplier has a gain of about 10^5, and the photo-cathode an efficiency of about 10^{-2} electron/photon. The physical light yield of ZnS for irradiation by β-particles is lower,[3] perhaps by a factor of two. In the third column of Table I the physical light yield of a variety of phosphors under alpha-bombardment is tabulated. The values should be accurate to about 15 percent. Because of the much greater uncertainty in the determination of the physical light yield under electron bombardment, the values for all phosphors have been referred arbitrarily to a value of 100 for ZnS-Ag, for each radiation considered. All values have been recalculated for uniform spectral response and refer to energy yield, not quantum yield. These values are tabulated in columns 3–8 in Table I. All values refer to steady currents, not pulses. Although the physical light yield of ZnS phosphors approaches perfection, the technical yield presents a very different picture. Most conventional phosphors are quite opaque to their fluorescent radiations. Thus only the light produced in about 50 mg/cm² nearest the photo-tube window is effective. In

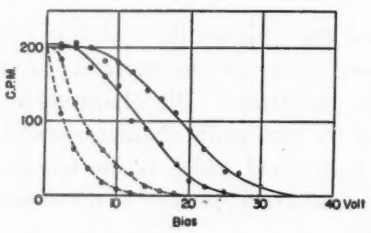

FIG. 1. Pulse height for Po α-particles after their passage through various absorbers. ZnS phosphor.

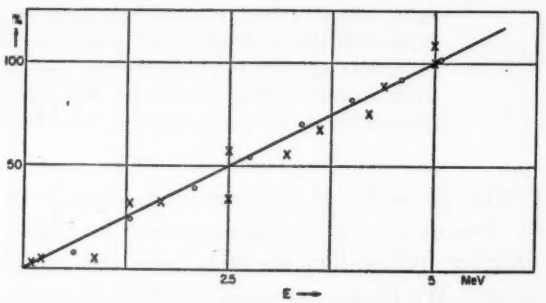

FIG. 2. Light output for α-particles of different energies. Circles: single pulses; crosses: steady current. ZnS phosphor.

[3] H. J. Born, N. Riehl, and K. G. Zimmer, Physik. Reichsber. 1, 153 (1944).

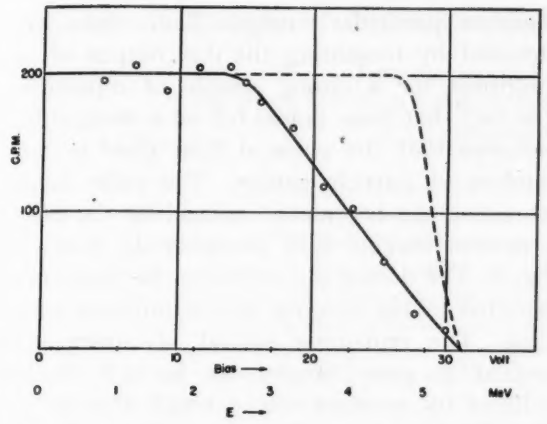

FIG. 3. Bias curve for Po α-particles using a single crystal CdS phosphor.

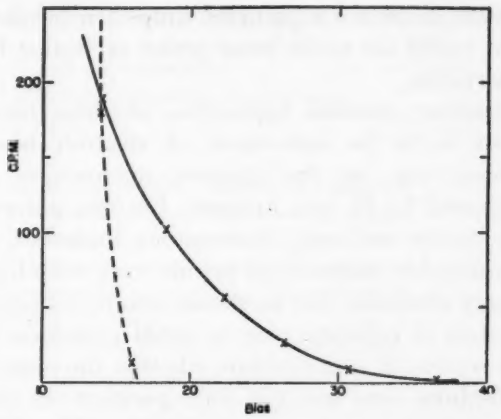

FIG. 4. Pulse height of uranium fission fragments (solid curve). Dotted line: uranium α-particles.

the case of α-particle bombardment this results in a drop in the output as the thickness is increased beyond about 50 mg/cm². For more penetrating radiations, particularly gamma-rays, it results in a "saturation" at about this thickness. We have investigated two other groups of phosphors which are more transparent to their fluorescent radiation. These are: (a) Organic phosphors, particularly those containing conjugate double bonds like naphthalene and phenanthrene,[4] and (b) potassium bromide[5] phosphors. The organic phosphors are characterized by their extreme transparency; e.g., sublimed, carefully purified naphthalene is still perfectly transparent for its own fluourescent light, in layers of 1-cm thickness. Diphenyl and phenanthrene, which have a greater physical light yield than naphthalene, show some absorption which can, however, be eliminated by producing transparent blocks by solidification from a melt. These blocks are perfectly clear and transparent to their fluorescent light but have a somewhat lower physical light yield than when the material is produced by other methods.[6] The great transparency of these organic phosphors makes them particularly suitable for the counting of energetic electrons and gamma-rays. Another advantage of the organic phosphors for the counting of individual scintillations is the short duration of the light flash—less than 10^{-6} second. In this respect they are much superior to the other phosphors. A more complete report on the investigations on the counting properties of the organic phosphors, particularly naphthalene, will appear soon in The Review of Scientific Instruments.

Professor Neuhaus (Marburg) has kindly prepared several large single crystals of potassium bromide phosphors. These also show a very high physical light yield for energetic electrons. However, the several large crystals showed varying light yields depending on the method of preparations. Our best crystal had an area of 3 cm² and depth of 1 cm, was perfectly transparent, and had a physical light yield of 0.5 compared with ZnS and 1.5 compared with naphthalene. Because of its relatively high density, it absorbs gamma-rays strongly, and its technical light yield for gamma-rays is therefore greatly superior even to the organic phosphors. An intensity of a few thousand gamma-quanta per second can still be detected by the *steady current* output of the photo-multiplier. Crystals of this general type may also prove very satisfactory as intensifying screens for the photographic recording of very hard x-rays. The particular crystal used by us emits light which is photographically not very effective since it is in the near ultraviolet. Other similar crystals can undoubtedly be prepared for greater photographic efficiency. On the other hand, the KBr phosphors are not suitable for the counting of single scintillation, since the duration of the flash is rather long according to our measurements.

Both the organic and the KBr phosphors are

[4] More extensive reports in press in Zeits. f. Naturf. and Rev. Sci. Inst.
[5] v. Meyeren, Zeits. f. Physik 61, 321 (1930).
[6] L. Herforth and H. Kallmann, Ann. d. Physik, in press.

less well suited for α-particles, since their physical light yields are much lower under excitation by α-particles.

Another possible application of these phosphors is to be conversion of electron beam images, e.g., in the electron microscope, as suggested by H. von Ardenne. For this purpose one wants not only transparent materials of considerable thickness to permit work with high energy electrons, but we should also prefer single crystals of sufficient size to avoid graininess of the screen. It is not certain whether the organic phosphors are suitable for operation in the vacuum of an electron microscope. The KBr phosphors would certainly be applicable and are available in large crystals. In the meantime we have also succeeded in preparing monocrystalline phosphors of ZnS and, particularly, CdS. The latter crystals were prepared by the methods of Frerichs[7] and then especially activated. ZnS crystals were prepared by W. Broser. CdS crystals can be prepared in thin pieces, several cm^2 in area and about 100 mg/cm^2 thick. The fluorescence, on proper activation, is an intense red, near the limit of the visible region. The physical light yield is as good as that of ZnS powder. The duration of the light flash is rather long—of the order of a tenth millisecond. The main difficulty lies in the high refractive index of the materials which causes most of the light to escape from the narrow edges because of total internal reflexion. The edges must therefore be masked.

We have investigated the pulse height distribution of the multiplier output when thin layers of ZnS and single crystals of CdS are bombarded with α particles. Figure 1 shows the (integral) bias curves for a ZnS screen for particles for various values of the residual range spent in the phosphors. Considerable pulse height straggling, which we believe to be due to the microcrystalline structure of the screen, appears in Fig. 2 the points marked by circles are obtained by integration of the curves in Fig. 1. These integrals should represent the average light output per particle of the particular residual range (and therefore particular energy). The crosses were obtained by measuring the d.c. output of the multiplier for a strong sample of α-particles. The fact that these points fall on a straight line indicates that the physical light yield is independent of particle energy. The pulse height straggling can be greatly reduced by the use of a monocrystalline CdS phosphor as shown in Fig. 3. The dotted line indicates the bias curve expected in the absence of instrumental straggling. The remaining spread of about ± 20 percent in pulse height can be still further reduced by masking out a small area of the phosphor.[8] One can clearly use this method to distinguish between particles of appreciably different energy down to 100 ev. We are using this method in our laboratory for the calibration of radioactive samples. This scintillation counter can also be used as a detector for range measurements. In this case the curves of Fig. 2 can be used to correct for counting losses near the end of the range. CdS gives consistently smaller pulses than ZnS, perhaps partly because of the greater duration of the pulses—about 10^{-4} sec. in CdS compared with less than 10^{-5} sec. in ZnS. Finally, we have investigated the pulses produced by fission fragments from a layer of uranium on the ZnS screen. Fissions were produced by a 10-mg Ra-Be source. Figure 4 shows the bias curve for the fission fragments. The fact that the pulses were really due to fission fragments was verified by the observation that a foil of 1.5 mg/cm^2 between the uranium and the ZnS screen completely suppressed the large pulses. It is noteworthy that the α-particle pulses from the uranium were completely unaffected by the gamma-rays from the Ra-Be source. Analogous experiments with gamma-rays, using naphthalene as phosphor, will be described in another publication.

Note added in proof: Since the writing of this paper we have developed better cadmium sulfide crystals giving curves which almost follow the dotted line of Fig. 3. These crystals give nearly homogeneous flashes for monoenergitic alpha-particles.

[7] R. Frerichs, Naturwiss. **33**, 381 (1946); Phys. Rev. **72**, 594 (1947).

[8] I. Broser and H. Kallmann, Ann. d. Phys. **3**, 281 (1948).

PHYSICAL REVIEW VOLUME 75, NUMBER 4 FEBRUARY 15, 1949

Change in Density of Potassium Chloride Crystals upon Irradiation with X-Rays*

I. ESTERMANN, W. J. LEIVO,** AND O. STERN***
Department of Physics, Carnegie Institute of Technology, Pittsburgh, Pennsylvania
(Received April 20, 1948)

Alkali halide crystals become colored when irradiated with x-rays. Theoretical considerations indicate that the coloration is due to absorption centers which consist of electrons trapped at negative ion vacancies. Precision measurements of the density of uncolored crystals, however, indicate that it is very unlikely that there is a sufficient number of vacancies present in well annealed crystals to account for the number of color centers, which may be determined optically, unless vacancies are formed as a result of the irradiation.

Potassium chloride crystals were irradiated with x-rays. Their change in density was measured by the "crystal suspension method." It was found that the crystals changed in density, and that the number of vacancies calculated from the decrease in density was in reasonable agreement with the number of color centers determined by optical measurement.

I. INTRODUCTION

CRYSTALS of alkali halides may be colored by irradiation with x-rays or cathode rays, as well as by several other methods.[1] Among the different theories proposed for this phenomenon, the theory that it is due to the trapping of electrons in negative ion vacancies (color centers or *F*-centers), seemed to be the most free from objections. An experimental test of it is the subject of this paper.

Experiments with single crystals of KCl have shown that darkening by cathode rays leads to concentrations of several times 10^{18}(*F*-centers/cm^3) as determined by optical measurements. However, an analysis of the precision density measurements of several different crystals indicates that the number of vacancies which may be present in well annealed crystals is not sufficient to permit *F*-center concentrations of several times 10^{18}/cm^3 to be formed by simple trapping of electrons in negative ion vacancies unless vacancies are formed during the process of irradiation.

As a result, it was concluded that an accurate measurement of the difference in density, if any, of a crystal due to the formation of *F*-centers would be a crucial experiment to determine whether vacancies were produced during irradiation, and that the measurement of the difference in density could probably be made with sufficient accuracy by the method of crystal suspension which had been used to make precision measurements of densities of crystals. If no change in density should occur, the entire vacancy theory of *F*-centers would have a serious objection. If a change did occur, the vacancy theory would be greatly strengthened.

In the determination of difference in density by the method of "crystal suspension in a liquid," use is made of the fact that the temperature coefficient of expansion of a solid crystal is generally much smaller than that of a liquid which has the same density at some particular temperature. The difference in density between two crystals can be obtained by placing the crystals in the liquid and then observing at what particular temperature each crystal will remain suspended in the liquid. From the difference in the suspension temperatures the difference in density can be computed. In making density measurements with crystals colored by cathode rays, a difficulty arose because the surface of the crystal became pitted to such an extent that density measurements were not reliable. Crystals colored by x-rays would have been satisfactory except that the highest concentrations of *F*-centers produced by x-rays in a single crystal were reported to be of the order of 10^{16}/cm^3. This concentration would not produce a

* This work was begun in September, 1943, by O. Stern and W. J. Leivo and was continued since June, 1945, by I. Estermann and W. J. Leivo.

** Abstract of Thesis submitted by W. J. Leivo in partial fulfillment of the requirements for the degree of Doctor of Science at Carnegie Institute of Technology.

*** Now at Berkeley, California.

[1] See, for example, R. W. Pohl, Physik. Zeits. **39**, 36 (1938); also Mott and Gurney, *Electronic Processes in Ionic Crystals* (Oxford University Press, London, 1940); F. Seitz, Rev. Mod. Phys. **18**, 384 (1946).

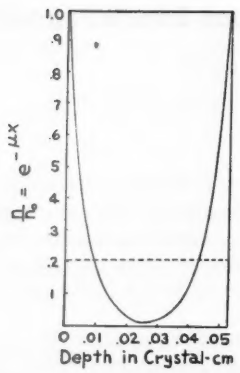

FIG. 1. Variation of the concentration of *F*-centers in a KCl crystal with the distance from the surface of the crystal.

sufficient change in density to be detectable. Higher concentrations than this had been produced on evaporated screens, but the screens undoubtedly do not compare with an annealed single crystal since the nature of production of evaporated screens would probably produce imperfections such as holes.

It was found, however, that crystals could be darkened to the point where they contained several times 10^{18} (*F*-centers/cm^3) by using soft x-rays from a tube with a beryllium window. This concentration of *F*-centers should produce a measurable difference in density. As a result of the experiments it was found that the crystals changed density upon irradiation with x-rays, and that this decrease in density was in reasonable agreement with that predicted from the concentration of *F*-centers as measured optically.

II. GENERAL PROCEDURE

As mentioned above, the change in density of the potassium chloride was obtained by determining the difference in suspension temperature between a colored and an uncolored crystal. The suspension liquid was 1,3-dibromopropane which has the same density as potassium chloride at a convenient temperature around 15°C. The method of "crystal suspension" has been developed by C. A. Hutchison, H. L. Johnston, D. A. Hutchison,[2] and others. After the change in density had been determined, the concentration of *F*-centers was determined by measuring the absorption coefficient of the crystal at the maximum of the *F* band for KCl. The measurement of the absorption coefficient and the calculation of the *F*-center concentration from this will be discussed later.

[2] D. A. Hutchison and H. L. Johnston, J. Am. Chem. Soc. 62, 3165 (1940); Phys. Rev. 62, 32 (1942); D. A. Hutchison, Phys. Rev. 66, 144 (1944); J. Chem. Phys. 10, 383 (1945); H. L. Johnston and C. A. Hutchison, J. Chem. Phys. 8, 869 (1940).

III. EXPERIMENTAL DETAILS

A. General Precautions

It was found in preliminary experiments that crystals which had been exposed to air during and after the cutting process did not yield reproducible density values. Consequently, great care had to be taken throughout the handling of the crystals in order to prevent them from being exposed to the atmosphere. Any moisture on the crystals or in the liquid would cause hydrolysis of the liquid. The resulting HBr acts as a catalytic agent causing an ion exchange between the KCl and the $BrCH_2CH_2CH_2Br$, the Cl^- ion being replaced by a Br^- ion with a resulting change in the density of the crystal. The 1,3-dibromo-propane also had to be free of HBr or Br_2 which might result from heating or decomposition due to light.

B. Preparation of Single Crystals of Potassium Chloride

A single crystal of potassium chloride, approximately three centimeters in diameter and five centimeters long, was grown from a melt of potassium chloride (C. P. Baker's Analyzed) by the method developed by Kyropolus.[3] The crystal was slowly cooled to room temperature.

Since the crystals could not be exposed to air while cutting them, the crystals were cut inside a box which could be filled with helium and was fitted with rubber gloves and a glass top. The crystals could be cut inside this box. The helium used was dried by passing it through a liquid nitrogen trap. In addition, the box contained phosphorus pentoxide as a drying agent to remove moisture entering through the rubber gloves.

The large crystal was cut into approximately one-centimeter cubes. These cubes were placed in a quartz tube containing helium, which was

[3] S. Kyropolus, Zeits. f. anorg. allgem. Chemie 154, 308 (1926).

then sealed. The tube with the crystals was placed in an annealing oven (Leeds and Northrup Micromax control). The rate of rise of the temperature was 4.2°C/min. The temperature was held constant at a point 56°C below the melting point for eight hours. The crystals were cooled at a rate of 3°C/min.

After removal from the annealing oven the tube with the crystals was again placed in the "glove box" containing helium. From a large crystal several small crystals were cleaved to a size of about 3×3×0.5 mm. One of the crystals was irradiated with x-rays while the rest were to serve as control specimens. At least one control crystal was cut from a place adjacent to the one to be darkened.

The penetration of the x-rays which are effective in coloring the crystal is of the order of 0.05 mm (see Fig. 1). This is computed from $I=I_0e^{-\mu x}$ where I is the intensity of the incident x-rays, μ is the absorption coefficient for x-rays of a wave-length believed effective for coloring the crystal, and x is the distance from the surface of the crystal. For $I/I_0=1/e$, and using $\mu=185/\text{cm}$, this gives $x=0.05$ mm. Crystals of this thickness could not be cleaved; it was therefore desirable to irradiate the crystal from both sides. Since the crystal could not be exposed to air, it was necessary to construct a radiation tube which would permit this and yet not reduce the intensity of the x-rays appreciably. In addition, the tube should be flat so that the crystal could be brought near the window of the x-ray tube where the intensity of the beam would be high. A satisfactory tube for holding the crystal while being irradiated was constructed by placing a piece of 9-mm Pyrex tubing over a copper strip 0.6 mm×7 mm×150 mm. The glass was heated and then pulled lengthwise, putting a skin of glass over the copper strip. The copper was dissolved with nitric acid, leaving a thin walled glass tube having a rectangular cross section. One end of the tube was sealed and to the other end was connnected a cap made from a "no lube" platinized tapered joint. A small arm was connected to the tube to hold the control crystals where they wouldn't be exposed to the x-rays. Also a small bulb was attached in which phosphorus pentoxide was placed as a drying agent.

After cleaving, the crystals were placed in the radiation tube which contained helium. The crystal to be colored was exposed to 50-kv x-rays with a beam current of 15 ma, the exposure time being a variable. The irradiation tube was placed directly in front of the beryllium window. After darkening the crystal, the tube was placed back in the "glove box" in which the crystals were transferred to the tube containing the suspension liquid, without exposure to the air.

C. Preparation of the Suspension Liquid

1,3-dibromo-propane, obtained from the Eastman-Kodak Company, was used for the suspension liquid. This liquid has a suitable density and temperature coefficient.[4] However, as mentioned above, care has to be taken to insure that the liquid is free of water, HBr, and Br_2, which may cause the crystal to react with the liquid.

The 1,3-dibromo-propane was treated with concentrated sulfuric acid in a separatory funnel. This process was repeated until the 1,3-dibromo-propane separated from the sulfuric acid as a clear liquid. The 1,3-dibromo-propane was then washed with a saturated solution of sodium bicarbonate, after which it was washed with distilled water and then dried over $CaSO_4$. The liquid was vacuum distilled and stored over $CaSO_4$ with a drop of mercury to precipitate any HBr or Br_2 formed.

D. Description of Vessel Containing Suspension Liquid and Crystals

The vessel containing the suspension liquid and the crystals was constructed so that the liquid could be distilled into it without exposure to air. The crystals also had to be transferred to the liquid without exposure to air. It was further

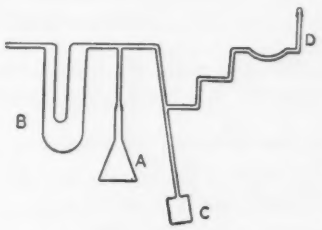

FIG. 2. Crystal suspension apparatus.

[4] Density KCl at 20°C=1.987 g/ml. Density 1,3-dibromo-propane at 20°C=1.979 g/ml.

TABLE I.

Thickness of crystal mm	Total radiation time hrs.	F-centers cm³ by optical measurement	F-centers cm³ from density measurement
0.518	17	5.94×10^{17}	12.3×10^{17}
0.420	17	6.40×10^{17}	11.6×10^{17}
0.543	17	5.27×10^{17}	10.2×10^{17}
0.417	8½	6.48×10^{17}	9.0×10^{17}
0.433	8½	7.62×10^{17}	10.1×10^{17}
0.388	8½	5.62×10^{17}	12.6×10^{17}
0.545	4¼	2.25×10^{17}	3.63×10^{17}
0.458	2⅛	1.25×10^{17}	—
0.528	2⅛	1.17×10^{17}	—

desirable to evacuate the crystals for about twenty minutes before immersing in the liquid so that any surface gases on the crystals would be removed. All this could be satisfactorily accomplished with the vessel shown in Fig. 2.

It was also found necessary to shield the crystals from electrostatic charges on the surface of the glass. The electrostatic forces caused by these charges were appreciable because of the small size of the crystals which had to be used. Shielding was obtained by lining the inside of the glass vessel with a platinum mesh through which the crystals could still be observed.

E. Procedure for Immersion of Crystals and the Distillation of the Liquid

The 1,3-dibromo-propane was placed in the distilling flask (*A*), Fig. 2, with some $CaSO_4$ ("Drierite" brand). The distillation was made at room temperature. Application of heat would cause decomposition of the liquid forming Br_2 which would produce the aforementioned reaction with KCl. The distillate was caught in the U tube (*B*) which was immersed in liquid nitrogen. After distillation the flask (*A*) was removed. The liquid from the U tube could then be poured into the vessel (*C*), which contained the crystals. A drop of mercury was also introduced to inhibit reaction. Helium was then let into the system through a liquid nitrogen trap. The tube (*D*) with the cap on it was projected into the "glove box" which contained the crystals in a helium atmosphere. The crystals were removed from the radiation tube and placed in the tube (*D*), after which the cap was replaced. The system was then evacuated for about twenty minutes, during which time the crystals were heated to 100°C to remove surface gases and moisture which might have been present. After the crystals were immersed in the liquid, the evacuation was continued for another ten minutes. Helium was finally introduced into the tube until atmospheric pressure was reached, and all connections were sealed. All the operations with the colored crystal were performed in the dark to prevent bleaching.

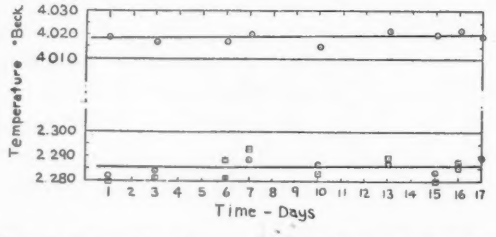

FIG. 3. Suspension temperatures of non-irradiated KCl crystals. Lower curve—comparison of suspension temperatures of thin plate of KCl (□) and cube of KCl (○). Upper curve—suspension temperatures of quartz float.

F. Determination of Suspension Temperatures

The temperature bath consisted of an insulated tank with windows for observing the crystals. Light entering the box was filtered with amber glass to prevent possible decomposition of the liquid. The temperature was manually controlled by allowing ice water to enter the tank. Temperatures were measured with a Beckmann thermometer. In spite of all precautions the 1,3-dibromo-propane was not quite homogenous. This caused the suspension temperature to vary with different trials, dependent mainly upon the length of time of evacuation of the crystals, since during this time the more volatile components (apparently isomers) of the liquid could escape. In order to have a correlation between the various trials a quartz float was made similar to the micro floats used in the determination of the concentration of heavy water.[5] The suspension temperature of the quartz float could be adjusted by altering the size of an air bubble in it so that it would be on the scale of the Beckmann thermometer in the neighborhood of the suspension temperature of the crystals. Corrections for slight changes in density of the liquid with time could be made by the use of the quartz float. The quartz float also proved valu-

[5] See, for instance, M. Randall and F. B. Longtin, Ind. Eng. Chem. 7, 44 (Jan. 15, 1939).

able in the work in case a reaction started to occur, since then it was possible to determine whether it was the liquid, the crystal, or both, which were changing. If a reaction did occur it would generally proceed quite rapidly, with the crystal getting more dense. However, if a reaction did not occur within a few days, the liquid and crystals remained stable as long as measurements were continued, in some cases for as long as one month.

IV. PRELIMINARY EXPERIMENTS

As was pointed out previously, crystals had to be cleaved to a thickness of about 0.4 mm in order that they could be colored throughout. This, however, brought up the question as to whether the density of the crystal might be changed by cleaving such a thin piece. Also the liquid might not completely penetrate holes in the surface of the crystal, or other surface effects might exist, in which case the density would depend upon the amount of surface area of the crystal. To test these possible effects, various size crystals were cleaved, some large cubes, others thin plates. It was found that to the degree of accuracy of the measurements no difference in density existed between a thin plate and a large cube (see Fig. 3).

V. RESULTS OF CHANGE IN DENSITY MEASUREMENTS

A number of crystals were irradiated for varying lengths of time. The change in suspension temperature for a crystal about 0.5 mm thick which had been exposed to x-rays for 8½ hours was about 0.09°C, which corresponds to a change in density of 1.4×10^{-4} g/cm³. Increasing the length of time that the crystal was irradiated above this did not change the density further, indicating that saturation had been attained in this time. Decreasing the time of irradiation decreased the change in density. The results obtained for different crystals for various radiation times are given in Table I. A typical experiment is represented in Fig. 4.

VI. OPTICAL DETERMINATION OF *F*-CENTER CONCENTRATION

The concentration of *F*-centers was computed from the absorption coefficient of each crystal

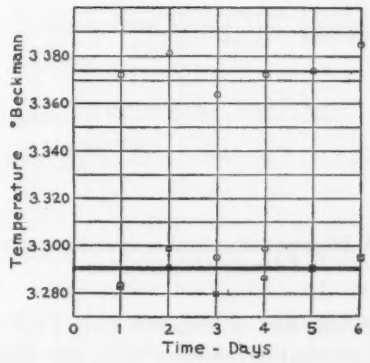

FIG. 4. Suspension temperatures of colored and uncolored KCl crystals. Upper curve—crystal irradiated 17½ hours with x-rays. Lower curve—(○) uncolored crystal No. 1; (□) uncolored crystal No. 2.

measured at the maximum of the *F*-band for KCl using the equation developed by Smakula.[6]

$$n_0 = 18mn'\alpha_m W/\pi e^2 h(n'+2)^2 f,$$

n_0 = number of *F*-centers per unit volume,
m = mass of electron,
e = charge of electron,
n' = index of refraction of crystal,
α_m = absorption coefficient at maximum of *F* band,
W = width at half-maximum of *F* band[1],
f = oscillator strength of absorbing center = 0.81 for KCl,
h = Planck's constant.

A diagram of the optical system used in the measurement of the absorption coefficient is shown in Fig. 5. The image of the filament of a lamp which was controlled by a voltage regulator was projected on the entrance slit of a prism monochromator after which it was focused on the crystal. The crystal was mounted so that it could be quickly moved in or out of the light beam. After passing through the crystal the light fell on a photo-cell. The photoelectric current was amplified by an FP54 tube used in a DuBridge and Brown[7] circuit. The dark current was compensated by a similar photo-cell in opposition to the other.

VII. COMPUTATION OF NUMBER OF *F*-CENTERS FROM CHANGE IN DENSITY MEASUREMENTS

The computation of the number of *F*-centers from the change in density was based on the assumption that there is one *F*-center for each pair of missing ions—a pair consisting of a

[6] A. Smakula, Zeits. f. Physik 59, 603 (1930).
[7] L. A. DuBridge and H. Brown, Rev. Sci. Inst. 4, 532 (1933).

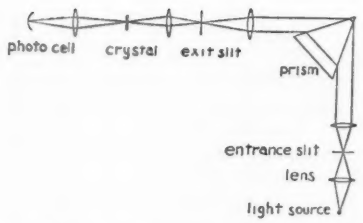

FIG. 5. Diagram of optical system for measuring *F*-center concentration.

potassium ion and a chlorine ion. This assumption is in general agreement with the behavior of crystals darkened by x-rays, in contrast to those subjected to additive coloring.[1] In addition, theoretical calculations[8] show that pairs are more mobile than isolated vacancies, and further, that the isolated vacancies would not have had sufficient time to migrate distances which have been observed in the length of time necessary to produce the coloration. On this basis the number of *F*-centers may be computed as follows:

$$\Delta\rho = -\rho\Delta v = -\rho n v_0,$$

where $\Delta\rho$ is the change in the density of KCl, Δv is the change in volume per unit volume of the crystal due to the migration of the ions from the interior to the surface of the crystal, n is the number of pairs of ions per cm³ which migrate to the surface, v_0 is the volume of a pair of ions. v_0 may be computed from the molecular weight M of KCl, the density of KCl, and Avogadro's number N:

$$v_0 = \frac{M}{\rho N}.$$

Now,

$$n = -\frac{\Delta\rho}{\rho v_0} = -\frac{N}{M}\Delta\rho.$$

Also,

$$-\Delta\rho = \rho(\alpha-\beta)\Delta t,$$

where α and β are the volume expansion coefficients of liquid and KCl, and ρ their common density at the suspension temperature, and Δt the change in suspension temperature due to the coloring of the crystal. Inserting this value for $\Delta\rho$, one obtains

$$n = \frac{N\rho}{M}(\alpha-\beta)\Delta t$$

Upon substituting the numerical values ($N = 6.02 \times 10^{23}$, $M = 74.6$, $\rho = 1.989$, $\alpha = 8.89 \times 10^{-4}$, and $\beta = 1.13 \times 10^{-4}$), we obtain $n = 1.24 \times 10^{19}\Delta t$(ion pairs/cm³) or *F*-centers/cm³.

This calculation does not allow for the possibility of a change in density resulting from an alteration of the lattice constants of the crystal caused by the missing ions. It is believed that this change is small; however, experiments to verify this are planned.

VIII. COMPARISON BETWEEN CHANGE IN DENSITY WITH THE *F*-CENTER CONCENTRATION

Table I gives a comparison of the number of *F*-centers per cm³ in the crystal, as computed from the change in suspension temperature, with the number of *F*-centers per cm³ as determined from the optical measurements. It can be seen that the *F*-center concentration reaches a saturation value after about 8½ hours of exposure to x-rays. The *F*-center concentration calculated from optical measurements is less than that obtained from the change in density. This is to be expected for several reasons. First, in the calculation of the absorption coefficient, monochromatic light is assumed. Secondly, since the amount of light transmitted through the crystal is of the order of 0.1 percent, a small amount of stray light can affect the results appreciably, reducing the computed number of *F*-centers. Thirdly, some bleaching will occur, since even to make a measurement of the absorption coefficient it is necessary to expose the crystal to light in the *F*-band. The significant fact, however, is that there is a correlation between the values in the two columns in Table I, giving strong support to the hypothesis that the *F*-centers are vacancies with trapped electrons which are responsible for the change in density.

It should be noted that the density measurements and also the optical measurements give the *average* number of *F*-centers per cm³ in the crystal. The maximum number of *F*-centers per cm³ may be considerably greater than this since the crystal is not uniformly colored. One may obtain a rough approximation, neglecting diffusion, for the number of *F*-centers per cm³ by assuming that the concentration falls of exponentially according to

$$n = n_0 e^{-\mu x},$$

[8] G. Dienes, thesis, Carnegie Institute of Technology.

where n is the concentration of F-centers, μ is the absorption coefficient of the x-rays, and x is the distance from the surface of the crystal. Figure 1 shows the concentration of F-centers calculated in this manner as a function of x for the first crystal appearing in Table I. The average ordinate in Fig. 1 (shown dashed) gives the experimentally measured concentration $\bar{n}$. The value of n_0 can be obtained from

$$2\int_0^d n_0 e^{-\mu x} dx = \bar{n}d,$$

where d is the thickness of the crystal. This gives

$$n_0 = \mu d/2(1-e^{-\mu d})\bar{n}.$$

For

$$\mu = 185 \text{ cm}^{-1}, \quad d = 0.0518 \text{ cm}, \quad n_0 = 4.8\bar{n}.$$

Thus the maximum concentration of F-centers may be around five times the value given in Table I.

IX. CONCLUDING REMARKS

F-centers were first observed about a half-century ago. Their nature has been seriously considered for over ten years. The exigencies of war particularly accelerated the study of the problem. Despite the enormous amount of experimental and theoretical work, their very nature still remained uncertain. As a result of these density measurements, the theory that the F-center is an electron occupying the position of a missing negative ion in the crystal lattice has been greatly strengthened. As a further result it has been found that the vacancies in which the electrons become trapped are largely produced during the process of irradiation.

PHYSICAL REVIEW VOLUME 75, NUMBER 4 FEBRUARY 15, 1949

A Study of the High Frequency Fundamental Bands in the Spectrum of AsH_3 and AsD_3

VIRGINIA MARIE MCCONAGHIE AND HARALD H. NIELSEN
Mendenhall Laboratory of Physics, Ohio State University, Columbus, Ohio

(Received October 21, 1948)

An analysis has been carried out on the fundamental bands ν_1 and ν_2 (Dennison's notation), in the infra-red spectrum of AsH_3. This analysis has made possible the evaluation of the reciprocals of inertia, B, and the Coriolis coupling coefficient, ζ_2. These are found to be $B''=3.723$ cm^{-1}, $B'(\nu_1)=3.682$ cm^{-1}, $B'(\nu_2)=3.69$ cm^{-1} and $\zeta_2=-0.0602$. The harmonic vibration frequencies have been computed after the method of Dennison. The values obtained are $\omega_1=2209.2$ cm^{-1}, $\omega_2=2225.8$ cm^{-1}, $\omega_3=973.3$ cm^{-1}, and $\omega_4=1012.1$ cm^{-1} for the AsH_3 molecule and $\omega_1=1571.2$ cm^{-1}, $\omega_2=1582.4$ cm^{-1}, $\omega_3=696$ cm^{-1}, and $\omega_4=718.6$ cm^{-1} for AsD_3. This information permits the calculation of ζ_2 for AsD_3. A value $\zeta_2=-0.0383$ is obtained which is in satisfactory agreement with experimental data. For AsD_3 the following B values prevail; $B''=1.896$ cm^{-1}, $B'(\nu_1)=1.883$ cm^{-1}, and $B'(\nu_2)=1.874$ cm^{-1}. The B'' values obtained enable one to estimate closely that the value of r(As-H) is equal to 1.513A and the H-As-H angle is equal to 89°50′.

I. INTRODUCTION

THE infra-red spectra of AsH_3, AsD_3, PH_3, and PD_3 have been investigated by a number of authors.[1] The only high dispersion measurements on the spectra of these molecules are those by Fung and Barker on PH_3 and those by Lee and Wu on AsH_3. From the foregoing works certain conclusions have been drawn concerning the size and the shape of these molecules by Sutherland, Lee, and Wu.[2] Recently a publication was made by us[3] on the preliminary results of our study of the spectra of AsH_3, AsD_3, and PH_3 under high dispersion, and in this paper we wish to discuss in somewhat greater detail our analysis of the high frequency funda-

[1] R. Robertson and J. J. Fox, Proc. Roy. Soc. **A120**, 128 (1928); L. W. Fung and E. F. Barker, Phys. Rev. **45**, 238 (1934); G. B. B. M. Sutherland and G. K. T. Conn, Nature **138**, 641 (1936); E. Lee and C. K. Wu, Trans. Faraday Soc. **35**, 1 (1939).

[2] G. B. B. M. Sutherland, E. Lee, and Cheng-Kai Wu, Trans. Faraday Soc. **35**, 1373 (1939).

[3] V. M. McConaghie and H. H. Nielsen, Proc. Nat. Acad. Sci. **34**, 455 (1948).

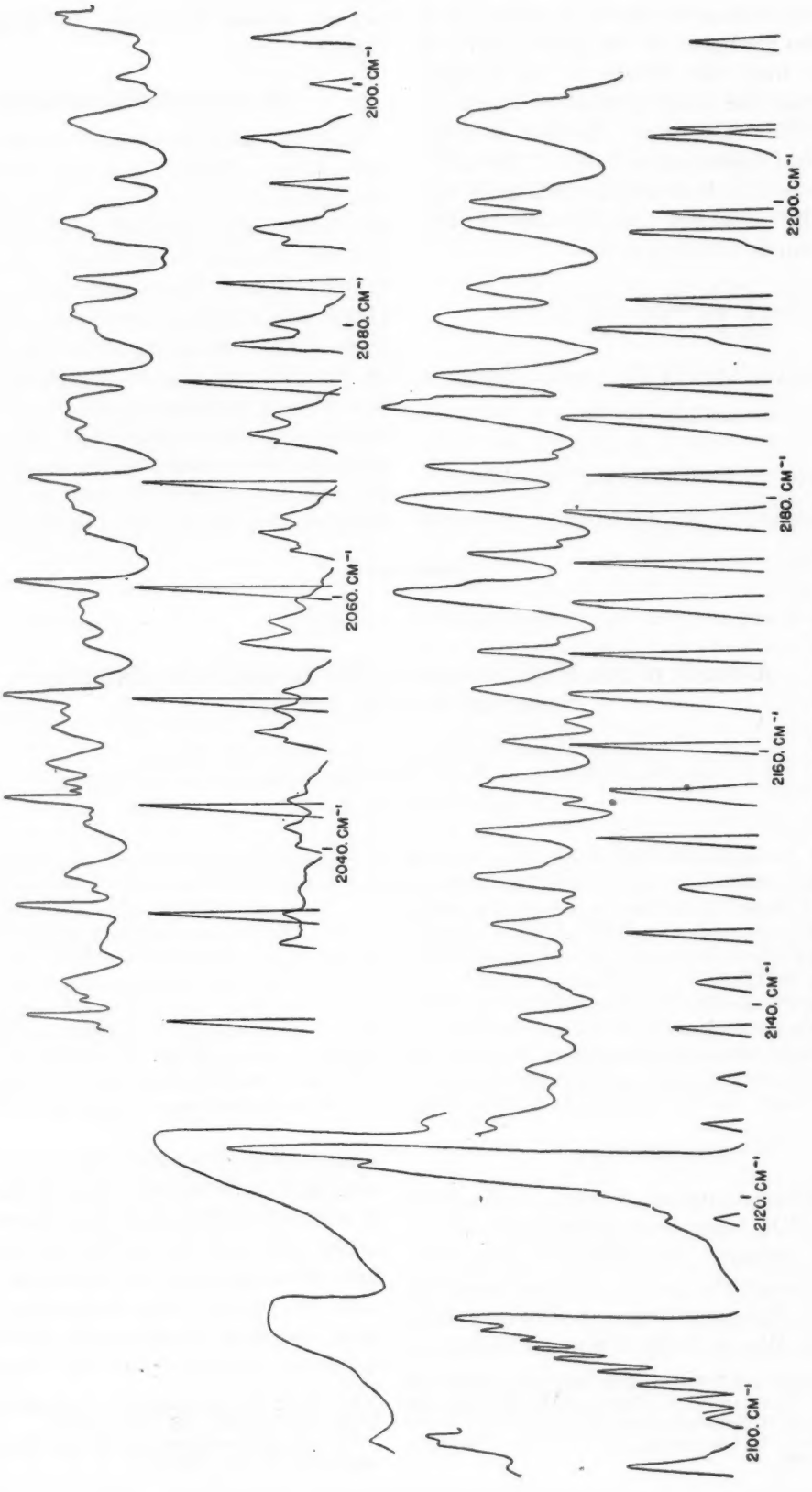

FIG. 1. Experimental and calculated absorption curves for AsH_3.

mental bands in the spectrum of AsH_3 and AsD_3 and the conclusions we have drawn from this analysis.

II. EXPERIMENTAL DETAILS

The two regions which we shall concern ourselves with here lie, respectively, near 2116 cm^{-1} and 1523 cm^{-1} for AsH_3 and AsD_3. The measurements were made with an absorption cell 24-cm long and a gas pressure of 30 mm Hg in both cases. The windows were of sodium chloride. The measurements were made using the vacuum prism-grating spectrograph described elsewhere,[4] which was equipped with a replica grating made by Wood with 7200 lines per inch. The data, recorded automatically, were taken with slit widths equivalent to a frequency interval of 0.3 cm^{-1}. The data have been redrawn and are shown as the upper curves in Figs. 1 and 2, respectively, for the two molecules AsH_3 and AsD_3. In Tables I and II are given the positions in cm^{-1} of the principal absorption lines in the two absorption regions.

III. DISCUSSION AND ANALYSIS OF THE BANDS

These bands have, in each case, been interpreted to comprise the fundamental bands ν_1 and ν_2, using the notation of Dennison.[5] The frequency ω_1 is a vibration where the electric moment oscillates along the axis of symmetry. The band is, therefore, a parallel band. The structure consists, for such a band, of a group of component bands (one for each value of K, $K \leqslant J$), each containing a Q branch and P and R branches. The former is a line at the center of the component band, the other two branches consisting of a set of nearly equally spaced lines on the low and high frequency sides, respectively, of the Q line. These component bands fall almost exactly on top of each other, so that the general appearance of the band is rather simple, i.e., a strong central Q branch and a group of nearly equally spaced P and R lines which lie on the low and high frequency sides of the Q branch.

The frequency ω_2 is a twofold degenerate oscillation where the electric moment alternates normally to the axis of symmetry. Such a band is known as a perpendicular band and consists also of a group of component bands (one on each side of the center for each value of K, $K \leqslant J$) each having P, Q, and R branches. The Q branches are, in this case, separated from each other by a frequency interval of about $2[(1-\zeta)\times C-B]$, where C and B are the reciprocals of inertia $h/8\pi^2cI_{zz}$ and $h/8\pi^2cI_{xx}$ and ζ is the Coriolis coupling coefficient. The perpendicular band is, therefore, likely to present a considerably more complicated appearance than the parallel type band.

In Fig. 1 we have, therefore, identified the sharp set of lines with the parallel band. Neglecting any splitting for different values of K, the combination relations

$$R(J-1)-P(J+1)=4B''(J+\tfrac{1}{2}), \tag{1a}$$

$$R(J)-P(J)=4B'(J+\tfrac{1}{2}), \tag{1b}$$

and

$$R(J-1)+P(J)=2\nu+2(B'-B'')J^2 \tag{1c}$$

have been applied to the lines in the band. When the values $R(J-1)-P(J+1)$ and $R(J)-P(J)$ are plotted against $4(J+\frac{1}{2})$, values for B in the initial and final states are obtained by determining the slopes of the resulting straight lines. The values obtained are $B''=3.723$ cm^{-1} and $B'=3.682$ cm^{-1}, respectively. When the values (1c) are plotted against $2J^2$, the value of the band center, ν_1, is obtained by reading the intercept, and the slope gives a value for $B'-B''$. For ν_1 we obtain 2116.1 cm^{-1} and the slope gives $B'-B''$ equal to $-0.04/cm^{-1}$. This value for $B'-B''$ is in satisfactory agreement with the value obtained by taking the difference between the magnitudes B' and B'' obtained above.

In Fig. 2, it will be seen that the two sets of lines appear almost equally sharp. By analogy, however, we assume that the band of lower frequency is ν_1, and we have identified the lines associated with it by means of asterisks. When the combination relations (1) are applied to these line positions, the following are obtained: $B''=1.896$ cm^{-1}, $B'=1.883$, $\nu_1=1523.1$ cm^{-1}, and $B''-B'=0.013$ cm^{-1}.

[4] E. E. Bell, R. H. Noble, and H. H. Nielsen, Rev. Sci. Inst. 18, 48 (1947).

[5] D. M. Dennison, Rev. Mod. Phys. 12, 175 (1940). In the notation of Gerhard Herzberg, *Infrared and Raman Spectra* (D. Van Nostrand Company, Inc., New York, 1945), these are the frequencies ν_1 and ν_2. We use the notation of Dennison because so much of the literature concerning the XY_3 molecular model is written in that notation.

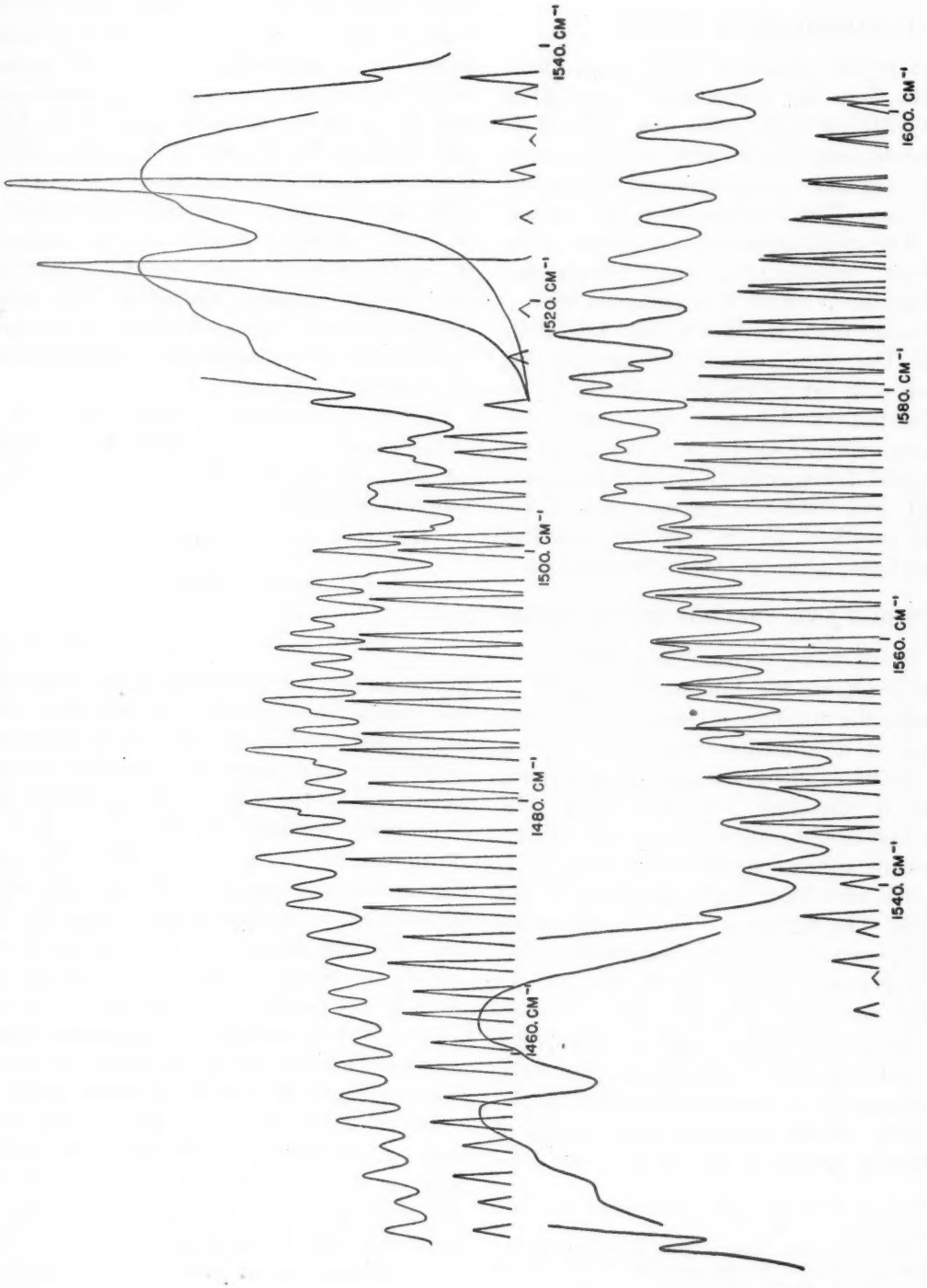

FIG. 2. Experimental absorption curves for AsD_3.

The values B'' obtained are, of course, those for B in the normal state of the molecule and not the quantities B_e obtained when the molecule is in equilibrium. The magnitudes of B'' will differ only very slightly from those of B_e, however, and we shall henceforth use the approximation $B_e=B''$ in our calculations. From the quantities B_e we may compute the values of the moments of inertia, $I_{zz}^{(e)}$, for the two molecules, $I_{zz}^{(e)}$ being one of the two equal moments of inertia. We obtain $I_{zz}^{(e)}=7.517\times10^{-40}$ g for AsH_3 and $I_{zz}^{(e)}=14.76\times10^{-40}$ g cm^2 for AsD_3. These are sufficient to determine the shape and size of the pyramid, since it may readily be shown that for the pyramidal XY_3 molecular model

$$I_{zz}^{(e)}=[3mr^2/2(1+3m/M)]\times\{2-[1-(3m/M)]\sin^2\beta\}, \quad (2)$$

in which m and M are the masses of the X and Y atoms, respectively, r is the $X-Y$ distance in the molecule, and β is the angle between the distance r and the axis of symmetry of the molecule. Using the two values $I_{zz}^{(e)}$ given above and assuming r and β to be the same for AsH_3 and AsD_3, we obtain $r=1.513$A and $\beta=54°39'$. We may now evaluate $I_{xx}^{(e)}$ and $C_e=(h/8\pi^2cI_{xx}^{(e)})$. For these we arrive at $I_{xx}^{(e)}=7.641\times10^{-40}$ g cm^2 for AsH_3 and $I_{xx}^{(e)}=15.282\times10^{-40}$ g cm^2 since $I_{xx}^{(e)}$ may be shown to be

$$I_{xx}^{(e)}=3mr^2\sin^2\beta. \quad (3)$$

These lead immediately to $C_e=3.663$ cm^{-1} and $C_e=1.831$ cm^{-1}, respectively.

We now turn our attention to the second set of lines in Fig. 1 which, we shall assume, must be ascribed to the band ν_2. It is convenient at this point to write down the relations which state the frequency positions of the lines we may expect to observe in a perpendicular band. When the transitions $\Delta J=0$, $\Delta K=\pm1$ are observed, we obtain the relation

$$\omega=\nu_2-(C''-B'')+J(J+1)(B'-B'')+K^2[C'-B'-C''+B'']\pm2K[(1-\zeta)C''-B''].^6 \quad (4)$$

When the transitions are $\Delta J=\pm1$, $\Delta K=\pm1$ one obtains

$$\omega=\nu_2-(C''-B'')+J^2(B'-B'')+K^2[C'-B'-C''+B'']\pm2K[(1-\zeta)C''-B'']\pm J(B'+B'').^6 \quad (5)$$

The transitions $\Delta J=\pm1$, $\Delta K=\mp1$ are less important and will not be considered here.

The data indicate that the perpendicular band ν_2 resembles much a parallel type band in appearance. The strong central line near 2123 cm^{-1} would then be the result of the Q branches of each component bands piling up at nearly the same frequency position. We take this to mean that the quantity $[(1-\zeta)C''-B'']$ in (4) and (5) is nearly equal to zero.

If this quantity is small, the lines on the high and low frequency sides of the center will group themselves in branches corresponding to a transition $J\rightarrow J\pm1$, each bunch consisting of J com-

TABLE I. Observed positions of lines of ν_1 for AsH_3 ν $VAC^{(cm^{-1})}$.

R_1	2130.7	P_2	2100.9
R_2	2138.1	P_3	2093.2
R_3	2145.1	P_4	2085.4
R_4	2152.2	P_5	2077.9
R_5	2159.3	P_6	2070.0
R_6	2166.3	P_7	2062.2
R_7	2172.9	P_8	2054.1
R_8	2179.4	P_9	2045.9
R_9	2186.1	P_{10}	2037.8
R_{10}	2192.5	P_{11}	2029.8
R_{11}	2198.8	P_{12}	2021.3
R_{12}	2204.6	P_{13}	2012.2
R_{13}	2210.5	P_{14}	2004.4
R_{14}	2216.8	P_{15}	1995.4
R_{15}	2223.1		
R_{16}	2229.7		
R_{17}	2237.9		

TABLE II. Observed positions of lines of ν_1 for AsD_3 ν $VAC^{(cm^{-1})}$.

R_3	1537.1	P_3	1511.9
R_4	1541.4	P_4	1507.7
R_5	1545.3	P_5	1503.7
R_6	1549.4	P_6	1499.7
R_7	1553.8	P_7	1496.0
R_8	1556.3	P_8	1492.0
R_9	1560.1	P_9	1488.0
R_{10}	1563.5	P_{10}	1483.7
R_{11}	1567.3	P_{11}	1479.6
R_{12}	1571.0	P_{12}	1475.4
R_{13}	1574.4	P_{13}	1471.5
R_{14}	1577.8	P_{14}	1467.0
R_{15}	1580.7	P_{15}	1463.2
R_{16}	1584.0	P_{16}	1459.0
R_{17}	1587.4	P_{17}	1454.7
R_{18}	1590.6	P_{18}	1450.4
R_{19}	1593.4	P_{19}	1446.1
R_{20}	1596.4		

[6] The centrifugal distortion terms have been omitted since the graphs resulting when $R(J-1)-P(J+1)$ and $R(J)-P(J)$ are plotted against $4(J+\frac{1}{2})$ are straight lines.

ponents. One sees from the data on the high frequency side that the component lines remain always very close together and give no indication of resolution. On the low frequency side this is not true. The component lines are spread out over a considerable distance giving a diffuse, partially resolved appearance. We interpret this to mean that neither of the two terms $-2K[(1-\zeta)C''-B'']$ nor $K^2[C''-B''-C'+B']$, though small, can be regarded as entirely negligible. It is assumed, moreover, that on the high frequency side the two terms have opposite signs, thereby tending to nullify their effect upon each other. Evidently, these terms will have the same sign on the low frequency side and their effects will be additive. A slight amount of trial and error will show that best agreement with experiment is obtained if the absolute values of the above terms are equal to each other for values of K equal approximately to $K=12$. From the fact that the effects of the two terms approximately nullify each other at this point on the high frequency side and from the magnitude of the spread of the components of the corresponding line on the low frequency side, we have estimated that $[(1-\zeta)C''-B'']\approx 0.16$ cm^{-1} and $[B''-C''-B'+C']\approx 0.02$ cm^{-1}. Evidently some latitude exists in the above choice, but the latitude is, nevertheless, surprisingly small. We estimate the above values to fit our data accurately to within 5 percent.

We must now decide on the sign to be attached to the terms $[(1-\zeta)C''-B'']$ and $[B''-C''-B'+C']$. This is not determined convincingly by the data of the high and low frequency sides of the band, since positive and negative values of the former quantity with corresponding values for the second term can be found which give satisfactory agreement with experiment. The choice is made, however, when we take into account that the Q branch converges on the high frequency side and diverges on the other side. This can be so only if both the above terms are positive, i.e., $[(1-\zeta)C''-B'']=0.16$ cm^{-1} and $[B''-C''-B'+C']=-0.02$ cm^{-1}. With the previously determined magnitudes for B'' and C'' we evaluate ζ to be equal to $\zeta=-0.0607$.

With these values it is found that rather satisfactory agreement with experiment is had if B' is taken to be 3.69 cm^{-1}. A plot of the band has been made by drawing each transition as a triangle of which the altitude is proportional to the calculated intensity of the line and of which the base is drawn about twice as wide as the equivalent slit width in wave numbers. The close-lying components are then added together to give a resultant absorption pattern. These composite "lines" have been drawn in the lower half of Fig. 1. To complete the picture, the intensities of the parallel transitions have also been calculated. Since it has been assumed that here the K splitting may be neglected, the components for a given line J have been added together and the resultant line is shown as a triangle proportional in height to the calculated intensity and with a base about twice as wide as the frequency interval subtended by the slit. To obtain the best agreement it is necessary to make the proportionality constant multiplying the intensities of ν_2 about 50 percent greater than the proportionality constant multiplying the intensities of ν_1. We believe the agreement between the computed absorption pattern and the measured pattern to be in reasonably good agreement.

It is desirable to have some verification that the analysis of this region is a reasonably accurate one. To make such a verification we shall test the data on ν_2 for the molecule AsD_3 and see if the structure of that band is consistent with our analysis of ν_2 for AsH_3. As we have noted, the lines on both sides of the center of ν_2 for the molecule AsD_3 remain quite sharp. This can be so only if the quantity $[(1-\zeta_2)C''-B'']$ for the AsD_3 molecule is much smaller than the same quantity for AsH_3 and provided the quantity $[B''-C''-B'+C']$ can be regarded as negligible. We have no way of estimating accurately what the value $B''-C''-B'+C'$ may be for AsD_3 but, since B'' and C'' have been determined, the magnitude $[(1-\zeta_2)C''-B'']$ may be estimated if it is possible to calculate ζ_2 for AsD_3. This is indeed possible,[7] but to arrive at an accurate estimate it is necessary to know the values of the harmonic frequencies ω_2 and ω_4 and not merely the band centers ν_2 and ν_4. Dennison[5] has shown how one may proceed to correct for the anharmonicity in such molecules as AsH_3 and AsD_3 where all the vibration frequencies transform with about the same factor. We shall not

[7] W. H. Shaffer, J. Chem. Phys. 9, 607 (1941).

here discuss his method except to say that it depends upon the observance of the Teller-Redlich product rule, $(4I_{zz}\mu'/I_{zz}'\mu)=(\omega_2\omega_4)^2/(\omega_2'\omega_4')^2$, and a second relation which is derived from a knowledge of how ζ_2 depends upon the potential energy constants α, β, and γ[8] in Dennison's notation. The primed quantities in the foregoing relate to the isotopic molecule and $\mu=3mM/(3m+M)$. Using the method of Dennison we obtain $\omega_2=2225.8$ cm^{-1}, $\omega_4=1012.1$ cm^{-1} for AsH_3, and $\omega_2'=1528.4$ cm^{-1} and $\omega_4'=718.6$ cm^{-1} for AsD_3. In making this determination we have made use of the value ν_4' for AsD_3 given in the work of Lee and Wu.[1] With these values for ω_2, ω_4, ω_2', and ω_4' it is possible to compute what will be the value of ζ_2 for the AsD_3 molecule by using Shaffer's relations[7] or by Dennison's[5] method. For ζ_2' we have calculated the value $\zeta_2'=-0.0270$. With this quantity we have determined $[(1-\zeta_2')C''-B'']$ to be 0.0053 cm^{-1} for the AsD_3 molecule, which is less than 1/30 the value for this quantity for the AsH_3 molecule. A hypothetical absorption pattern has been computed for AsD_3 in the same manner as for the AsH_3 molecule using the above determination for $[(1-\zeta_2')C''-B'']$ and regarding $[B''-C''-B'+C']$ to be entirely negligible. The pattern embracing ν_1 and ν_2 is shown in Fig. 2 below the experimental curve. The curve accounts for all the measured lines in a satisfactory manner except for three or four which we believe must be due to a weak superimposed band.

As one further verification that the model here proposed for the AsH_3 molecule is a satisfactory one, we have made the following calculation. It seems reasonable to assume that in this molecule the valence force field approximation is a rather satisfactory one. On the basis of the valence force field assumption, Lechner[9] has derived the relation

$$4\lambda_2\lambda_4=(f/m)(6d/m)[2/(1+3\cos^2\beta)]\times[p+(2-p)\cos^2\beta], \quad (6)$$

where $p=(3m+M)/M$ (M and m being the masses of the arsenic and hydrogen atoms, f and d the valence force constants) and where $\lambda_i=4\pi^2c^2\omega_i^2$ (ω_i being one of the normal frequencies). Since f, d, and β will be the same for AsH_3 and AsD_3, one quickly verifies that

$$(\lambda_2\lambda_4/4\lambda_2'\lambda_4')[p+(2-p)\cos^2\beta]/[p'+(2-p')\cos^2\beta]. \quad (7)$$

Using the ω_2 and ω_4 given above, one obtains for β the value $\beta=54°15'$.

We shall also make a calculation to determine values for the harmonic frequencies ω_1 and ω_3. We shall make up a method rather similar to that devised by Dennison[5] to determine ω_2 and ω_4 in NH_3. We shall assume, as did Dennison, that one may write $\nu_i=\omega_i(1+\alpha_i)$ for AsH_3 and $\nu_i'=\omega_i'(1+\omega_i'\alpha_i/\omega_i)\approx\omega_i'(1+\nu_i'\alpha_i/\nu_i)$. We have also the product relation $(\omega_1\omega_3/\omega_1'\omega_3')^2=(m'\mu'/m\mu)$. One more relation is required before the ω_i may be calculated. We obtain it in the following manner.

It is observed that for AsD_3 the convergence of the P and R lines in the band ν_1 is somewhat greater than for ν_2, i.e., $(B''-B')_{\nu_1}>(B''-B')_{\nu_2}$. It has been established[7] that a Coriolis interaction may exist between the two frequencies ω_1

TABLE III. Vibration frequencies and constants for the AsH_3 and AsD_3 molecules.

	AsH_3	AsD_3	
ν_1 (cm^{-1})	2116.1	1523.1	
ν_2	2123.0	1529.3	
ν_3	904.4–906.9	660.0	(1)
ν_4	1003.	714	(1)
ω_1	2209.2	1571.2	
ω_2	2225.8	1582.4	
ω_3	973.3	696.3	
ω_4	1012.1	718.6	
α (10^5 dynes/cm)	2.768	2.768	
β	1.665	1.665	
γ	1.204	1.204	
a	3.6221	3.6221	
b	2.2076	2.2076	
c	0.6851	0.6851	

TABLE IV. Rotational constants and dimensions of the AsH_3 and AsD_3 molecules.

	AsH_3	AsD_3
B'' (cm^{-1})	3.723	1.896
$B'(\nu_1)$	3.682	1.883
$B'(\nu_2)$	3.69	1.874
C''	3.663	1.831
	−0.0602	−0.0383
$I_{zz}^{2(e)}$(g-cm$^2\times10^{40}$)	7.517	14.760
$I_{xx}^{(e)}$	7.641	15.282
r_0 (A)	1.513	1.513
h_0	0.93	0.93
$\angle\beta$	54°39′(54°14′)	54°39′
$\angle\alpha$	89°50′	89°50′

[8] The constants α, β and γ are, respectively, equal to the constants $(I_{xx}^{(e)}/2I_{zz}^{(e)})^2n_1$, $(I_{xx}^{(e)}/2I_{zz}^{(e)})n_2$ and n_3 in Shaffer's notation.

[9] F. Lechner, Sitz. ber. Akad. Wiss. Wien 141, 633 (1932).

and ω_3. The effect of this interaction would be to decrease B' for ν_1 and to increase B' for ν_2. Since these frequencies are of about the same magnitude and the motions correspond to displacements along the AS−H bonds in both cases, but to no change in the bond angle we shall assume that the convergence in both instances is the same except for the Coriolis contribution. Inspection of the quantities α_1 and α_2 in reference 7 will then show that the Coriolis contribution $2\omega_2^2\xi_{12}^2/(\omega_2^2-\omega_1^2) \approx 2\omega_1^2\xi_{12}^2/(\omega_2^2-\omega_1^2) \approx 2\nu_1^2\xi_{12}^2/(\nu_2^2-\nu_1^2)=0.03$. In this relation ξ_{12} is the Coriolis coupling coefficient between ω_1 and ω_2. From this relation $|\xi_{12}|$ may be computed to be $\xi_{12}=0.01$. We shall make the approximation of setting ξ_{12} equal to zero. Shaffer's expression for ξ_{12} then makes it possible to derive the relation

$$\mu(\omega_1^2+\omega_3^2)-\mu'(\omega_1'^2+\omega_3'^2) = \left[\frac{(C-1)}{2C}\omega_1^2+\frac{(C+1)}{2C}\omega_3^2\right](\mu-\mu'/2), \quad (8)$$

where the primes refer to the isotopic molecule, $\mu=3mM/(3m+M)$ and $C=[(k_1/\mu)-(k_3/m)]$. Equation (8) supplies the additional relation required to evaluate ω_1 and ω_3. We have obtained the following values for these: $\omega_1=2209.2$ cm^{-1}, $\omega_3=973.3$ cm^{-1}, $\omega_1'=1571.2$ cm^{-1}, and $\omega_3'=696.3$ cm^{-1}. These values of ω_1 and ω_3 are probably less reliable than those obtained for ω_2 and ω_4, because the double minimum effect of the potential energy makes it more difficult to take the anharmonicity satisfactorily into account for ω_3. The separation of the components of ω_3 is only about 2.5 cm^{-1} and, since one may expect the doubling in the normal state to be quite negligible, the doubling of the first excited state must be about 2.5 cm^{-1}. Since this splitting is rather small (especially when compared to the splitting in the case of NH_3), this method of approximating to the frequencies ω_1 and ω_3 is, nevertheless, probably quite good.

The constants of the harmonic portion of the potential energy function have also been evaluated. They are $\alpha=2.768\times10^5$, $\beta=1.665\times10^5$, $\gamma=1.204\times10^5$ dynes/cm, and $a=3.622\times10^5$, $b=2.2076\times10^5$, $c=0.6851\times10^5$ in Dennison's notation. The last three of these are, respectively, equivalent to the constants k_1, k_3, and k_2 in Shaffer's notation. In Tables III and IV are summarized the information obtained concerning the size, shape, and structure of the AsH_3 molecule from a study of the fundamental bands ν_1 and ν_2. In a later paper we hope then to give a discussion of the structure of the bands ν_3 and ν_4 in the spectra of AsH_3 and AsD_3.

The authors gratefully acknowledge their indebtedness to the Research Corporation in New York City for a generous grant-in-aid. Acknowledgment is also made to the Cincinnati Chemical Works for a fellowship to one of us (V.M.M.).

PHYSICAL REVIEW VOLUME 75, NUMBER 4 FEBRUARY 15, 1949

Infra-Red Bands in the Spectrum of Difluoromethane

HUGH B. STEWART AND HARALD H. NIELSEN
Mendenhall Laboratory of Physics, Ohio State University, Columbus, Ohio

(Received November 12, 1948)

Eight absorption bands have been observed in the infra-red spectrum of CH_2F_2. Seven of these are believed to be fundamental bands and have been identified as follows; the symmetry species of the band being given in parentheses: $\omega_1(A_1)=2949$ cm^{-1}, $\omega_2(A_1)=1116$ cm^{-1}, $\omega_4(A_1)=528.6$ cm^{-1}, $\omega_6(B_1)=3015.2$, $\omega_7(B_1)=1176.1$ cm^{-1}, $\omega_8(B_2)=1089.7$ cm^{-1} and $\omega_9(B_2)=1435.4$ cm^2. A band of species B_1 is observed at 2945 cm^{-1}. It is identified as $\omega_5+\omega_9$ and from this it is inferred that $\omega_5(A_2)=1510.6$ cm^{-1}. Rotational constants for the normal state are found to be $B''=0.354$ cm^{-1} and $C''-B''=1.303$ cm^{-1}. From these values the values r_0(C−F) $=1.32$A and $\angle$(F−C−F)$=107°$ are obtained assuming that r_0(C−H)$=1.094$A and $\angle$(H−C−H)$=110°$.

I. INTRODUCTION

THE infra-red spectra of a considerable number of pentatomic molecules, in particular molecules of the type XY_4 (i.e., CH_4, SiH_4, GeH_4, etc.) and the XYZ_3 type (i.e., CH_3F, CH_3Cl, etc.), have been investigated under high dispersion. With the exception of the spectrum of CH_2D_2 which was resolved by

Ginsburg and Barker,[1] no spectra of molecules belonging to the XY_2Z_2 type have been studied under high dispersion. The difluoromethane molecule is a more general molecule of this type and is sufficiently light that one might expect to resolve most of the bands into rotational structure. This is particularly true since fluorine has no isotopes. Earlier work on this molecule confines itself to the Raman measurements by Glockler and Leader,[2] the electron diffraction measurements of Brockway[3] and the very recent work of Barker and Kao.[4] From the measurements of Brockway the C−F distance is determined to be $(1.36\pm0.02)\times10^{-8}$ cm, the F−F distance is found to be $(2.23\pm0.03)\times10^{-8}$ cm^{-1} and the F−CF angle, $110°\pm1°$. In this paper we wish to report on the high dispersion measurements made by us on the spectrum of this molecule and the information which may be inferred from them.

II. GENERAL CONSIDERATIONS

The XY_2Z_2 molecular model has been studied theoretically by several authors, but most completely by Shaffer and Herman[5] who have derived complete energy expressions for the rotation-vibration levels. The CH_2F_2 molecule has a twofold axis of rotation (the z axis) and two vertical reflection planes (the xz and yz planes which contain, respectively, the CH_2 and CF_2 triangles) and belongs to the symmetry point group C_{2v}. It has nine modes of vibration of which none are degenerate. The vibration may be divided into four symmetry species; namely, A_1 and A_2 which are symmetric to a rotation of the molecule about the z axis, through an angle π, but, respectively, symmetric and antisymmetric to a reflection of it in the xz plane; B_1 and B_2 which are antisymmetric to a rotation of the molecule about the z axis through an angle π, but respectively symmetric and antisymmetric to a reflection of it in the xz plane. The nature of the vibrations is illustrated in Fig. 1, where it may be seen that of species A_1 there are four, of the species A_2 there is only one, and of the species B_1 and B_2 there are, respectively, two. The dipole moment contains components A_1, B_1, and B_2. Consequently, eight of the fundamental frequencies and all overtone or combination frequencies belonging to these species might be

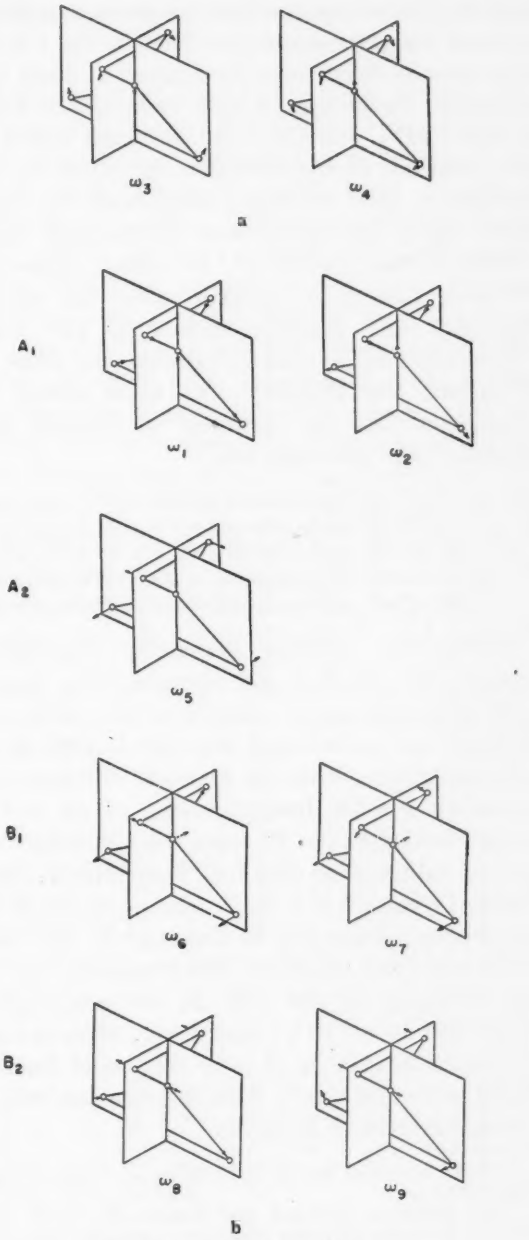

FIG. 1. Nature of vibrations.

[1] N. Ginsburg and E. F. Barker, J. Chem. Phys. **3**, 668 (1935).
[2] G. Glockler and G. R. Leader, J. Chem. Phys. **7**, 382 (1939).
[3] L. O. Brockway, J. Phys. Chem. **41**, 185 (1937).
[4] E. F. Barker and C. L. Kao (private communication).
[5] J. E. Rosenthal, Phys. Rev. **45**, 538 (1934); J. E. Rosenthal, Phys. Rev. **46**, 730 (1934); Ta-You Wu, *Vibrational Spectra and Structure of Molecules* (Prentice-Hall, Inc., New York, 1939), p. 224; Ta-You Wu, J. Chem. Phys. **10**, 116 (1942); W. H. Shaffer and R. C. Herman, J. Chem. Phys. **12**, 494 (1944); W. H. Shaffer and R. C. Herman, J. Chem. Phys. **13**, 83 (1945).

expected to be infra-red active. It may be shown, moreover, that all nine fundamental frequencies are Raman active.

As a guide to the subsequent attempt to identify the observed bands, it is convenient to make use of the formulation by Shaffer and Herman[5] of the vibration problem to estimate the positions in the spectrum of the fundamental bands. This may be accomplished in as much as the molecular shape and its dimensions are quite well-established and because the more important valence force constants involved in the CH_2F_2 vibration problem may be arrived at from the vibration frequencies of such molecules as CH_4, CH_3F, CHF_3, and CF_4. The predicted values of the positions of the vibration bands can be regarded as good estimates only, however, since these force constants were determined from bands in the spectra of the above molecules without having corrections made for anharmonicity and possible resonance. The force constants used in this calculation are those of Crawford and Brinkley[6] and those stated by Herzberg.[7] In the notation of Shaffer and Herman[5] the constants are

C_1(C−H bond constant)$=4.79\times10^5$ dynes/cm,
C_1'(C−F bond constant)$=5.96\times10^5$ dynes/cm,
C_2(H−C−H angle constant)$=0.46\times10^5$ dynes/cm,
C_2'(F−C−F angle constant)$=1.24\times10^5$ dynes/cm,
C_2''(H−C−F angle constant)$=0.62\times10^5$ dynes/cm.

Using the valence symmetry coordinates adopted by Shaffer and Herman,[5] the kinetic and potential energy constants have been calculated and substituted into the secular determinant which yields the classical vibration frequencies. For the frequencies ω_1, ω_2, ω_3, and ω_4 which belong to the A_1 type, the following computed values were obtained, respectively, 2930, 1064, 1406, and 575 cm^{-1}. For ω_5 which is the single band belonging to the type A_2 the value 1335 cm^{-1} was obtained. The frequencies ω_6 and ω_7 belonging to the type B_1 are predicted at 2994 and 1034 cm^{-1}, respectively, while the frequencies ω_8 and ω_9 of type B_2 should lie near 1090 and 1607 cm^{-1}. This information will be found restated in Table V.

[6] B. L. Crawford and S. R. Brinkley, J. Chem. Phys. 9, 69 (1941).
[7] G. Herzberg, *Infrared and Raman Spectra of Polyatomic Molecules* (D. Van Nostrand Company, Inc., New York, 1945), pp. 182 and 193.

With the aid of the molecular dimensions obtained by Brockway[3] and assuming the C−H distances and the H−C−H angle to be the same as in the methane molecule, the three principal moments of inertia for CH_2F_2 may be estimated to be about $I_{xx}=92.3\times10^{-40}$, $I_{zz}=81.0\times10^{-40}$, and $I_{yy}=16.7\times10^{-40}$ g cm^2. The molecule is therefore an asymmetric rotator where two of the moments of inertia are nearly alike. One should therefore expect the bands belonging to the three species types to be sufficiently different so that they may be readily identified. Vibrations of species A_1 induce electric moments along the axis z, vibrations belonging to species B_1 induce electric moments along the axis x, and the vibrations of species B_2 give rise to electric moments along the axis y. The first two types represent vibrations normal to the axis y which is the unique axis of the molecule considered as a rotator. To the extent that this molecule may be approximated as a symmetric rotator, these are, therefore, "perpendicular" bands, and the lines which will be prominent in these bands will be ${}^RQ$ and ${}^PQ$ branches arising from quantum transitions $\Delta J=0$, $\Delta K=\pm1$. Bands of species B_2 correspond to the "parallel" bands which occur in symmetric rotator molecules. They are characterized by a strong Q branch with P and R branches on the low and the high frequency sides.

The principal effect of the asymmetry in a molecule of the dimensions of CH_2F_2 is to split the rotation levels where $K\neq0$ into two components. This effect increases with J and is most prominent for small values of K. There will, therefore, be essential differences in the appearances of species A_1 and B_1 near the center of the bands. The selection rules for the asymmetric rotator show that for bands of species A_1 the components of the Q branches near the center spread away from the center for increasing values of J. This gives to these bands the appearance of having a region of small absorption near the center of the band. For bands of species B_1, however, the selection rules for the asymmetric rotator show that the components of the Q branches near the center crowd toward the center as the J value increases. This gives to these bands the appearance of a strong absorption peak at the center of the band which is sometimes referred to as a "gathered Q branch."

At some distance from the center the two types of bands will resemble each other, the frequency interval between two neighboring Q branches being about $\Delta\nu=2(C-B)$ where B is taken to mean

$$B=(h/8\pi^2c)\tfrac{1}{2}(1/I_{xx}+1/I_{zz}) \text{ and } C=(h/8\pi^2cI_{yy}).$$

The spacing between lines in a band type B_2 will be about $2B$.

In order to analyze the bands in the spectrum it is convenient to make use of certain combination relations analagous to those which have been so helpful in the analysis of the spectra of symmetric molecules. As we have seen, there is reason to believe that the CH_2F_2 molecule is rather nearly a symmetric rotator. Witmer[8] and Wang[9] have demonstrated that it is possible in such cases to calculate the energy levels by a perturbation method. The unperturbed energy levels are given by the energies of a symmetric rotator where the quantity $(1/I_{xx})$ is replaced by $\frac{1}{2}[(1/I_{xx})+(1/I_{zz})]$, and the perturbation corrections are functions of the asymmetry of the molecule, i.e., $(1/I_{xx})-(1/I_{zz})$. From the resulting energy relations and observing the fact that for our purpose the selection rules may be taken to be those for a symmetric rotator (i.e., $\Delta J=\pm1, 0$; $\Delta K=0$ for parallel (type B_2) bands and $\Delta J=\pm1, 0$; $\Delta K=\pm1$ for perpendicular (type A_1 and B_1) bands, we may arrive at combination relations which are applicable to our case.

In the case of the B_2 type bands (i.e., parallel) it will be seen that only the low frequency side of the band is resolved. It is, therefore, necessary to use a combination relation which involves only the $P(J)$ lines. Two useful relations are the following:

$$\nu_0-P(J)=(B'+B'')+(B''-B')J, \quad (1)$$

$$P(J)+P(J-1)-2J^2(B'-B'')=2\nu_0-(2J-1)B', \quad (2)$$

where the B's have already been defined. The primes and double primes refer, respectively, to the excited and normal states of the molecule. If the correct value of ν_0 is used, the left side of (1) plotted against J yields a straight line, where $(B''-B')$ is the slope and $(B''+B')$ is the intercept. If too small a value for ν_0 is used, the curve deviates from a straight line for small values of J, and if too large a value for ν_0 is used, the curve deviates from a straight line in the opposite direction. When the correct value for ν_0 has been determined, the values of $(B''-B')$ may be read from the graph and inserted in (2). The value $2\nu_0$ will then be the intercept, and $2B'$ will be the slope of the resulting straight line if the left side of (2) is plotted against $(2J-1)$.

Combination relations which are useful in dealing with the bands of type A_1 and type B_1

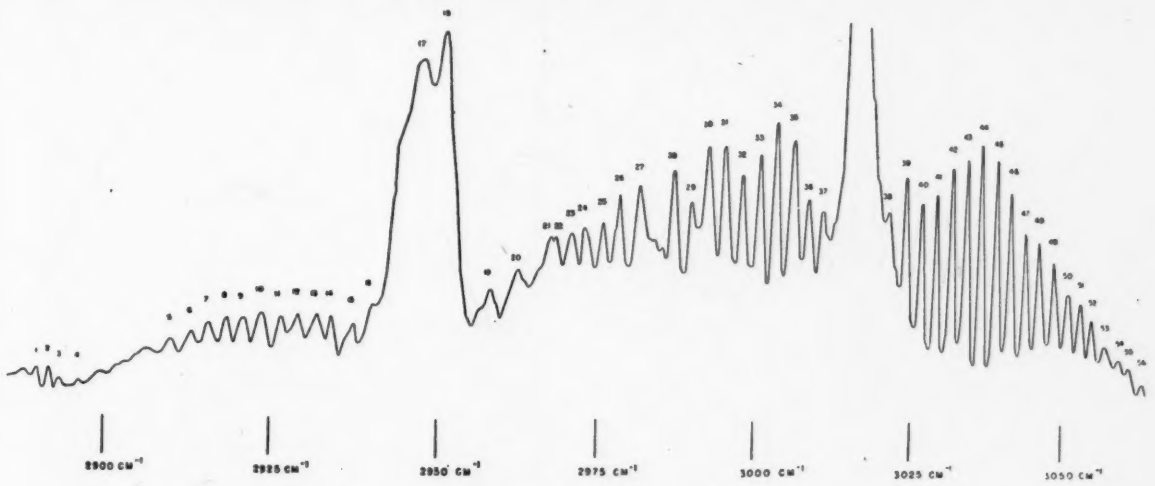

FIG. 2. Spectrum of CH_2F_2 in the 3.3-μ region.

[8] E. E. Witmer, Proc. Nat. Acad. Sci. 13, 60 (1927).
[9] S. C. Wang, Phys. Rev. 34, 243 (1929).

(i.e., the perpendicular bands) are

$$\tfrac{1}{2}({}^{R}Q_K+{}^{P}Q_K)=\nu_0+(C'-B') +K^2[(C'-B')-(C''-B'')], \quad (3)$$

$$({}^{R}Q_K-{}^{P}Q_K)=4K(C'-B'), \quad (4)$$

$$({}^{R}Q_{K-1}-{}^{P}Q_{K+1})=4K(C''-B''). \quad (5)$$

When the left side of (3) is plotted against K^2, the intercept will be $\nu_0+(C'-B')$. By plotting relations (4) and (5) against $4K$, the values $(C'-B')$ and $(C''-B'')$ may be determined, respectively. In this manner the band center ν_0 is determined. Relations (3), (4), and (5) will, as we have seen, be valid only for K values corresponding to lines at some distance from the band center.

III. EXPERIMENTAL DETAILS

The difluoromethane used in this investigation was obtained from the Jackson Laboratory of the E. I. duPont de Nemours Company, Wilmington, Delaware. The sample had been fractionated within 0.5°C of the actual boiling point of CH_2F_2 which is at −51.6°C. The only impurities present in the gas were probably air and traces of CH_2FCl which boils at −9°C.

A description of the spectrograph used in this investigation can be found elsewhere.[10] The instrument is an automatic recording prism grating spectrometer which is mounted in a tank that can be evacuated, thereby making it possible to remove the water vapor and carbon dioxide from the optical path. Three gratings were used, namely, a replica grating made by R. W. Wood with 7500 lines per inch and having its blaze near 3μ, a replica grating made by Wood with 3600 lines per inch and having its blaze near 6μ, and a grating ruled at the University of Michigan with its blaze near 16μ. The spectrometer was calibrated by determining the grating constants for the first two of the above gratings by measuring several infra-red lines of mercury in several orders. The grating constant of the third grating was obtained by measuring in several orders several lines in a band of the CH_2F_2 spectrum, used as substandards, which had been previously measured with the replica grating with 3600 lines per inch.

The absorption cell was a cylindrical glass tube, 2 inches in diameter and 5½ inches long, with a tube extending from the cell wall to the exterior of the spectrometer tank. This permitted chang-

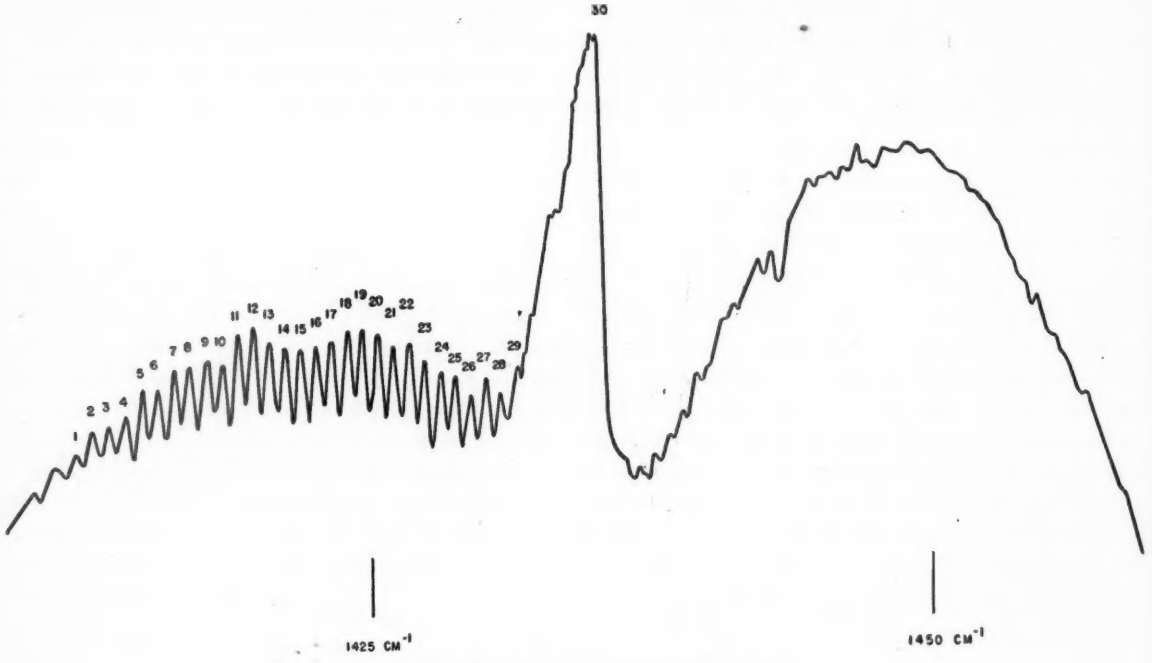

FIG. 3. Spectrum of CH_2F_2 in the 7.0-μ region.

[10] E. E. Bell, R. H. Noble, and H. H. Nielsen, Rev. Sci. Inst. 18, 48 (1947).

ing the gas pressure in the cell without opening up the spectrometer. The cell was closed at the ends by windows of potassium bromide to permit measurements to be made to 20μ.

It was found practicable to operate the spectrograph throughout the spectrum with slits subtending an angle equivalent to as little as 0.25 cm^{-1}.

IV. EXPERIMENTAL RESULTS

The spectrum has been scanned with the self-recording spectrometer from near 2.5μ to 20μ, and the four principal regions of absorption recorded. These regions were found to lie near the positions 3.3μ, 7.0μ, 9.0μ, and 19.0μ in the spectrum, respectively.

The 3.3-μ Region

Figure 2 is a reproduction of the recorded spectrum in the 3.3-μ region. The figure is simply a tracing of the record obtained automatically and is therefore not quite a linear representation of the frequency scale. This region appears to consist of three rather badly overlapping vibration bands of which the main lines are given in Table I.

The 7.0-μ Region

The spectrum obtained in the 7.0-μ region is shown in Fig. 3. The band structure and line spacing leaves no doubt that this is a parallel band. The line spacing in the P branch is practically the limit of the resolving power of the instrument, and as may be seen, the R branch is not resolved. As before, the frequency scale is not quite linear. The frequency positions of the main lines in this band are given in Table II.

The 9.0-μ Region

This region is shown in Figs. 4 and 5 which were recorded under different gas pressure conditions. The two records overlap slightly. The CH_2F_2 gas absorbs very strongly in this region from 1060 cm^{-1} to 1115 cm^{-1} (Fig. 4). With a gas pressure of 0.1 cm of Hg an absorption of over 50 percent was observed. The pressure maintained to obtain the record shown in Fig. 5 was about 1.0-cm Hg. The 9.0-μ region appears to consist of three bands, one near 1090 cm^{-1}, a second near 1115 cm^{-1}, and a third near 1175 cm^{-1}. The frequency positions of the principal lines in this region are given in Table III.

TABLE I. Frequencies and identifications of CH_2F_2 absorption lines in the 3.3-μ region.

Line number	Identification	Frequency
1		2889.8
2		2891.5
3		2892.9
4		2895.9
5		2909.8
6		2912.6
7		2915.1
8		2918.0
9		2920.5
10		2923.4
11		2926.2
12		2928.8
13		2931.7
14		2934.0
15		2937.3
16		2940.3
17		2947.1
18		2951.4
19		2957.8
20		2962.3
21		2967.4
22		2968.2
23	$^{P}Q(17)$	2970.7
24	$^{P}Q(16)$	2972.8
25	$^{P}Q(15)$	2975.9
26	$^{P}Q(14)$	2978.2
27	$^{P}Q(13)$	2981.3
28	$^{P}Q(11)$	2986.8
29	$^{P}Q(10)$	2989.6
30	$^{P}Q(9)$	2992.3
31	$^{P}Q(8)$	2994.8
32	$^{P}Q(7)$	2997.6
33	$^{P}Q(6)$	3000.4
34	$^{P}Q(5)$	3003.0
35	$^{P}Q(4)$	3005.7
36	$^{P}Q(3)$	3008.1
37	$^{P}Q(2)$	3010.3
38	$^{R}Q(2)$	3020.9
39	$^{R}Q(3)$	3023.8
40	$^{R}Q(4)$	3026.6
41	$^{R}Q(5)$	3028.9
42	$^{R}Q(6)$	3031.5
43	$^{R}Q(7)$	3034.0
44	$^{R}Q(8)$	3036.3
45	$^{R}Q(9)$	3038.8
46	$^{R}Q(10)$	3041.3
47	$^{R}Q(11)$	3043.6
48	$^{R}Q(12)$	3045.9
49	$^{R}Q(13)$	3048.4
50	$^{R}Q(14)$	3051.0
51	$^{R}Q(15)$	3052.9
52	$^{R}Q(16)$	3054.8
53	$^{R}Q(17)$	3056.5
54	$^{R}Q(18)$	3059.6
55	$^{R}Q(19)$	3061.4
56	$^{R}Q(20)$	3063.7

The 19.0-μ Region

This region consists of a single band which shows the structure characteristic of a band of

TABLE II. Frequencies and identifications of CH_2F_2 absorption lines in the 7.0-μ region.

Line number	Identification	Frequency
1	$P(33)$	1411.2
2	$P(32)$	1412.0
3	$P(31)$	1412.8
4	$P(30)$	1413.5
5	$P(29)$	1414.2
6	$P(28)$	1415.0
7	$P(27)$	1415.8
8	$P(26)$	1416.5
9	$P(25)$	1417.3
10	$P(24)$	1418.0
11	$P(23)$	1418.8
12	$P(22)$	1419.5
13	$P(21)$	1420.3
14	$P(20)$	1421.0
15	$P(19)$	1421.7
16	$P(18)$	1422.4
17	$P(17)$	1423.1
18	$P(16)$	1423.8
19	$P(15)$	1424.5
20	$P(14)$	1425.3
21	$P(13)$	1426.0
22	$P(12)$	1426.6
23	$P(11)$	1427.4
24	$P(10)$	1428.1
25	$P(9)$	1428.8
26	$P(8)$	1429.5
27	$P(7)$	1430.1
28	$P(6)$	1430.9
29	$P(5)$	1431.7
30	(Q)	1435.4

the type A_1. The energy is small in this region, and the record shows the principal lines (Q branches) plotted on a percentage absorption basis. The center is near 530 cm^{-1}. The frequency positions of the lines are given in Table IV.

V. DISCUSSION OF THE RESULTS

Only three of the four A_1 type fundamental bands which can occur have been observed, the two B_1 type fundamental bands and the two B_2 type fundamental bands have all been observed. The observed bands will be discussed in the following sections according to symmetry types.

Bands of Symmetry Type A_1

In general, the bands belonging to the symmetry type A_1 appear to be of low intensity. Of the four fundamental bands belonging to this type it was possible to determine the center of only one with great assurance.

The band ω_1 is predicted to fall near 2930 cm^{-1}. It is observed not only to be of low intensity, but to be badly overlapped by two bands of the symmetry type B_1. For this reason it is impossible to apply the combination relations to it to determine its center or the values of the rotational constants. The Raman value of 2963 cm^{-1} does, however, not seem inconsistent with the measurements reported here. A value which we might have chosen as the value of ω_1 is 2950 cm^{-1}. The correct value may, perhaps, best be obtained from Raman measurements on CH_2F_2 in the gas phase.

A band of the type A_1 is found in the region near 1120 cm^{-1}. It lies between two other intense bands, one on the low frequency side of type B_2 and one on the high frequency side of type B_1. The band of type B_2 has its center near 1090 cm^{-1} and is a region of intense absorption which obscures much of the type A_1 band. This band appears too intense to be regarded as an overtone ($2\omega_4$, for example) or a difference band, and since it lies in the region predicted for ω_2 and is of the right type, we have assigned it as the fundamental ω_2. Here again it is impossible to apply the combination relations to any advantage, but the center has been estimated to be 1116 cm^{-1}. The spacing between ${}^RQ$ branches appears to diverge rather rapidly from a value of about 2.5 cm^{-1} near the band center to 3.6 cm^{-1} at the edge of the band. For this effect we have no immediate explanations.

No absorption band was found in the region predicted for ω_3, i.e., near 1400 cm^{-1}, although the region was explored in an attempt to locate it. It is proposed that either the Raman frequency 1262 cm^{-1} or the Raman frequency 1508 cm^{-1} is the frequency ω_3. For reasons to be discussed at a later point we chose it to be the frequency 1262 cm^{-1}.

A band is found near 530 cm^{-1} which is the only band of the species A_1 which is entirely free from overlapping. It is the only one where the combination relations may be used with advantage, and the center determined with confidence. Applying the combination rule (3), the band center is found to be 528.5 cm^{-1}. Although the Q branches are not as sharp in this band as in others, a fairly accurate value of $C-B$ can be found. Using the combination relations (4) and (5) the following values are obtained

$$(C'-B')=1.315\pm0.007 \text{ cm}^{-1}$$

and

$$(C''-B'')=1.307\pm0.007 \text{ cm}^{-1}.$$

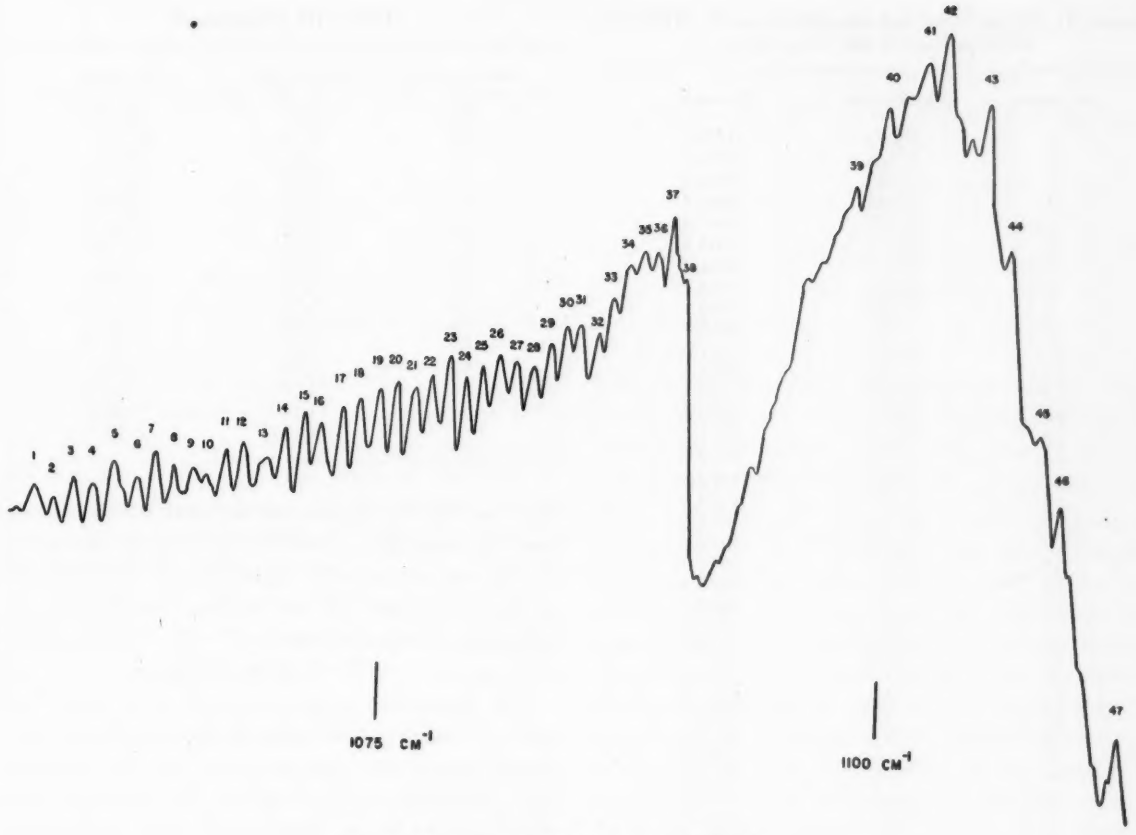

FIG. 4. Spectrum of CH_2F_2 in the 9.0-μ region.

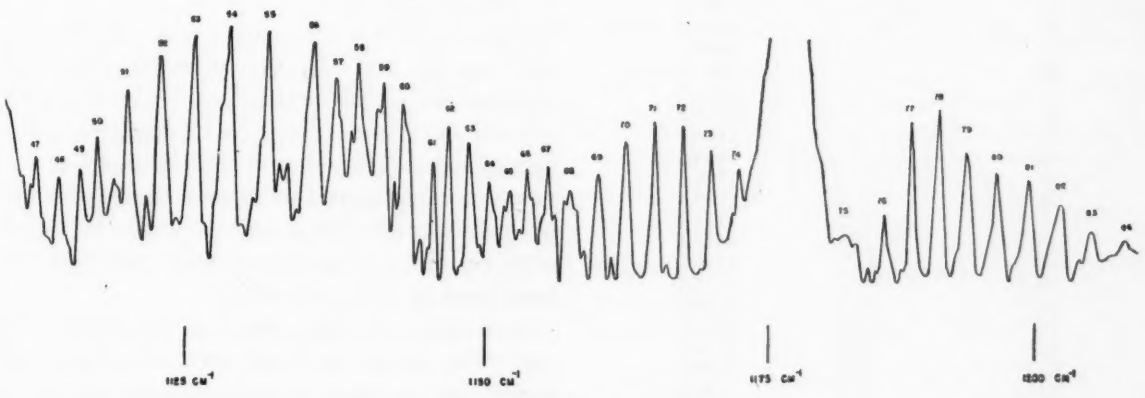

FIG. 5. Spectrum of CH_2F_2 in the 9.0-μ region.

Bands of Symmetry Type B_1

As was suggested earlier there are only two fundamental bands of the type B_1. Both of these have been observed experimentally and in addition a third band of this type has been observed.

The frequency ω_6 has been predicted to fall near 2994 cm^{-1}. It is observed actually to be near 3015 cm^{-1}. The central region of this band is quite free from overlapping by other bands so that use of the combination relations may here be made with profit. When the combination relation (3) is applied, the band center is found to be 3015.2 cm^{-1}. The individual ^PQ and ^RQ

TABLE III. Frequencies and identifications of CH_2F_2 absorption lines in the 9.0-μ region.

Line number	Identification	Frequency
1	$P(37)$	1058.6
2	$P(36)$	1059.5
3	$P(35)$	1060.4
4	$P(34)$	1061.4
5	$P(33)$	1062.3
6	$P(32)$	1063.4
7	$P(31)$	1064.3
8	$P(30)$	1065.2
9	$P(29)$	1066.1
10	$P(28)$	1066.7
11	$P(27)$	1067.6
12	$P(26)$	1068.3
13	$P(25)$	1069.5
14	$P(24)$	1070.3
15	$P(23)$	1071.2
16	$P(22)$	1072.0
17	$P(21)$	1073.0
18	$P(20)$	1073.9
19	$P(19)$	1074.8
20	$P(18)$	1075.6
21	$P(17)$	1076.5
22	$P(16)$	1077.3
23	$P(15)$	1078.2
24	$P(14)$	1079.0
25	$P(13)$	1079.8
26	$P(12)$	1080.6
27	$P(11)$	1081.4
28	$P(10)$	1082.3
29	$P(9)$	1083.0
30	$P(8)$	1083.8
31	$P(7)$	1084.4
32	$P(6)$	1085.3
33	$P(5)$	1086.0
34	$P(4)$	1086.8
35	$P(3)$	1087.5
36	$P(2)$	1088.2
37	$P(1)$	1089.0
38		1089.7
39		1098.2
40		1099.7
41		1101.8
42		1102.8
43		1105.8
44		1106.3
45		1108.3
46		1109.5
47		1113.2
48		1115.1
49		1116.8
50		1118.1
51		1120.5
52		1123.3
53		1126.1
54		1129.0
55		1132.1
56		1135.8
57		1137.5
58		1139.4
59		1141.5
60		1143.1
61		1145.6
62		1147.0
63		1148.6
64	$^PQ(12)$	1150.4
65	$^PQ(11)$	1152.2
66	$^PQ(10)$	1153.6
67	$^PQ(9)$	1155.3
68	$^PQ(8)$	1157.2
69	$^PQ(7)$	1159.9
70	$^PQ(6)$	1162.2
71	$^PQ(5)$	1164.7
72	$^PQ(4)$	1167.2
73	$^PQ(3)$	1169.8
74	$^PQ(2)$	1172.4
75	$^RQ(2)$	1182.2
76	$^RQ(3)$	1185.7
77	$^RQ(4)$	1188.2
78	$^RQ(5)$	1190.9
79	$^RQ(6)$	1193.8
80	$^RQ(7)$	1196.7
81	$^RQ(8)$	1199.7
82	$^RQ(9)$	1202.8
83	$^RQ(10)$	1205.8
84	$^RQ(11)$	1208.9

lines in the band are strong and well-resolved, thereby making it possible to measure the value $C-B$ very accurately. Applying the combination relations (4) and (5) to the lines in Table I the following values are found: $C'-B'=1.294\pm0.005$ cm^{-1} and $C''-B''=1.303\pm0.005$ cm^{-1}.

The frequency ω_7 is predicted to lie near 1034 cm^{-1}. A band of this type is found at 1176 cm^{-1} which seems too intense to be due to anything but a fundamental transition. We therefore take this band to be ω_7. Here again the combination rules may be used with advantage. With the aid of combination relation (3) the band center is located at 1176.1 cm^{-1}, and using combination relations (4) and (5), the following values are obtained for $C'-B'$ and $C''-B''$: $C'-B'=1.315\pm0.007$ cm^{-1} and $C''-B''=1.299\pm0.007$ cm^{-1}, using lines of K less than 8. The lines of larger K values are overlapped by lines of the band which we have identified as ω_2 and cannot be identified with certainty. These lines have therefore not been used in this analysis.

A third band of the type B_1 is found near 2945 cm^{-1}. The lines in the band, except for the central region, are too weak to make satisfactory use of the combination relations. This band has been observed by Barker and Kao[4] who have attributed it to the combination frequency $\omega_5+\omega_9$, where ω_5 is the torsional frequency of symmetry species A_2, and ω_9 is a frequency of symmetry species B_2. As Barker and Kao have pointed out, the combination frequency $\omega_5+\omega_9$ would be of the symmetry type B_1. It will be seen that if the value ω_9, which is later identified to lie at 1435

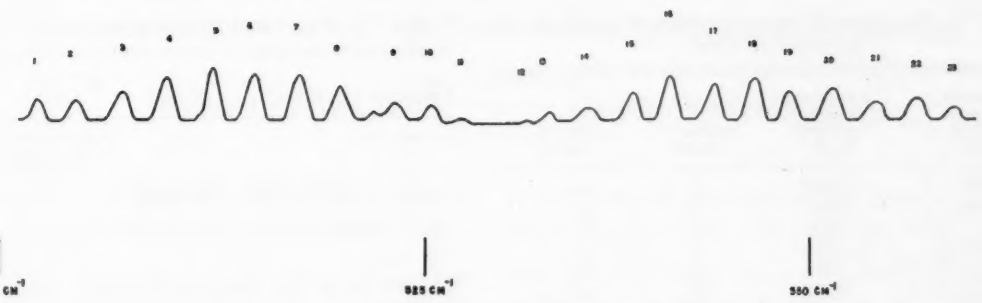

FIG. 6. Spectrum of CH_2F_2 in the 19.0-μ region.

cm^{-1}, is subtracted from 2945 cm^{-1}, the center of the band described here, a value $\omega_5=1510$ cm^{-1} is obtained. This is in good agreement with the Raman frequency observed at 1508 cm^{-1}. It is for this reason that ω_3 is identified with the Raman frequency at 1262 cm^{-1}. Barker and Kao[4] have explained the doubling of the central region as caused by the existence of the double minimum in the potential energy function associated with the torsional oscillation, ω_5.

Bands of Symmetry Type B_2

The two bands observed in the spectrum near 1090 cm^{-1} and 1435 cm^{-1} have a structure and line spacing which leaves no doubt that they are "parallel" bands and therefore must be identified as of the symmetry type B_2. Our earlier calculations indicated the fundamental frequencies of this symmetry species might be expected near 1090 cm^{-1} and 1600 cm^{-1}. We, therefore, identify these as ω_8 and ω_9, respectively.

It will be seen that in both of these bands only the P branches have been resolved. For this reason we are compelled to use the combination relations (1) and (2) which involve only the lines in the P branches. Applying the combination principle (1) to both bands, the band centers are determined to be $\omega_8=1089.7$ cm^{-1} and $\omega_9=1435.4$ cm^{-1}. For the band ω_8 the values $B''+B'=0.712\pm0.010$ cm^{-1} and $B''-B'=0.0039$ cm^{-1} and for ω_9 the values $B''+B'=0.708\pm0.010$ cm^{-1} and $B''-B'=0.0005$ cm^{-1} are obtained. The B values will then be for ω_8, $B''=0.358\pm0.005$ cm^{-1}, $B'=0.354\pm0.005$ cm^{-1}, and for ω_9, $B''=B'=0.354\pm0.005$ cm^{-1}.

It was indicated by our calculations in Section II that the frequency ω_2 should be lower than the frequency ω_8. This is equivalent to saying that the symmetric stretching frequency of the CF_2 group should be lower than the antisymmetric stretching frequency of the CF_2 group. Indeed, it is reported that the analagous frequencies in the CCl_2 group of the CH_2Cl_2 molecule fall in this order. It is, moreover, true here that the symmetric stretching frequency for the CH_2 group is lower than the antisymmetrical stretching frequency of the CH_2 group. Nevertheless, the frequency ω_2 is here found to be 1116 cm^{-1} while ω_8 falls near 1090 cm^{-1}. This effect is explained by supposing a strong Fermi-type resonance to occur between ω_2 and $2\omega_4$, which is permitted by the symmetry properties of the molecule. Since the CF bond constant is known quite accurately, and since the computed frequency for the CF_2 antisymmetric stretching frequency agreed so well with experiment, it

TABLE IV. Frequencies and identifications of CH_2F_2 absorption lines in the 19-μ region.

Line number	Identification	Frequency
1	$^PQ(11)$	502.0
2	$^PQ(10)$	504.3
3	$^PQ(9)$	506.9
4	$^PQ(8)$	509.4
5	$^PQ(7)$	512.1
6	$^PQ(6)$	514.6
7	$^PQ(5)$	517.2
8	$^PQ(4)$	519.6
9	$^PQ(3)$	522.9
10	$^PQ(2)$	525.4
11	$^PQ(1)$	527.5
12	$^RQ(0)$	530.9
13	$^RQ(1)$	532.5
14	$^RQ(2)$	535.1
15	$^RQ(3)$	538.1
16	$^RQ(4)$	540.5
17	$^RQ(5)$	543.3
18	$^RQ(6)$	546.2
19	$^RQ(7)$	548.4
20	$^RQ(8)$	551.6
21	$^RQ(9)$	554.6
22	$^RQ(10)$	557.5
23	$^RQ(11)$	560.3

TABLE V. The identification of observed bands in the spectrum of CH_2F_2.

Observed frequency position in cm^{-1}	Calculated frequency position in cm^{-1}	Symmetry species	Identification
2949	2930	A_1	ω_1
1116	1064	A_1	ω_2
	1406	A_1	ω_3
528.5	575	A_1	ω_4
1510.6*	1335	A_2	ω_5
3015.2	2994	B_1	ω_6
2945		B_1	$\omega_8+\omega_9$
1176.1	1034	B_1	ω_7
1089.7	1090	B_2	ω_8
1435.4	1607	B_2	ω_9

* Arrived at from the combination band $\omega_8+\omega_9=2945$ cm^{-1}.

seems reasonable to expect the computed frequency $\omega_2=1064$ cm^{-1} to be fairly accurate. The overtone, $2\omega_4$, should be very close to $2\omega_4=1057$ cm^{-1}. A Fermi resonance would cause ω_2 to appear at a higher frequency in the spectrum and $2\omega_4$ at a lower frequency. The region below 1057 cm^{-1} was investigated to try to locate the band $2\omega_4$, but it was not found probably because ω_8 was too intense to allow a good inspection.

CONCLUSION

As a conclusion we shall summarize briefly the results we have obtained. In all, eight bands have been observed. Of these seven are believed to be fundamental bands, three of which are of symmetry type A_1, two are of symmetry type B_1 and two of species B_2. The eighth band observed is believed to be a combination band. Our identifications of the observed bands are stated in Table V.

It has been practicable to evaluate the rotational constant B for the upper and lower states for the frequencies ω_8 and ω_9 and the rotational constant $(B-C)$ for the upper and lower states for the frequencies ω_4, ω_6, and ω_7. Their values are stated in Table VI.

These values are, of course, not the equilibrium values of B and $C-B$. In fact, enough data are not available to evaluate the equilibrium values. The values of these constants must, however, be rather close to the equilibrium values since it will be seen that the values change only very slightly from one vibration state to another. Even if the values B'' and C'' be taken to represent the equilibrium values of B and C quite accurately, these two rotational constants are not sufficient to evaluate all of the dimensions of the molecule. Nevertheless, an estimate of these may be made by assuming that the C−H distance is the same here as in other hydrocarbon molecules and that the H−C−H angle remains here also a tetrahedral angle. If we take then $r_0(C-H)=1.094\times10^{-8}$ cm and $\angle(H-C-H)=110°$ we may determine the value of $r_0(C-F)$ and $\angle(F-C-F)$. The values obtained here are the following:

TABLE VI. Rotational constants of the CH_2F_2 molecule.

Frequency	B'' cm^{-1}	B' cm^{-1}	$(C''-B'')$ cm^{-1}	$(C'-B')$ cm^{-1}
ω_4			1.307 ± 0.007	1.315 ± 0.007
ω_6			1.303 ± 0.005	1.294 ± 0.005
ω_7			1.299 ± 0.007	1.315 ± 0.007
ω_8	0.358 ± 0.005	0.354 ± 0.005		
ω_9	0.354 ± 0.005	0.354 ± 0.005		

$$r_0(C-F)=1.32\pm0.01A$$

and

$$\angle(F-C-F)=107°0'\pm30'.$$

It will be seen that the dimensions obtained from the infra-red data for the C−F distance and the F−C−F angle are somewhat smaller than those obtained by Brockway from electron diffraction measurements. It is also interesting to note that the C−F distance in CH_2F_2 is considerably smaller than the C−F distance in CH_3F, the latter being 1.398×10^{-8} cm. We feel, nevertheless, that the accuracies for the quantities from which our values of $r_0(C-F)$ and $\angle(F-C-F)$ have been determined are conservatively estimated.

The authors wish to acknowledge their gratefulness to the Research Corporation of New York for a grant-in-aid which has made this work possible.

PHYSICAL REVIEW VOLUME 75, NUMBER 4 FEBRUARY 15, 1949

Quantum Electrodynamics. II. Vacuum Polarization and Self-Energy

JULIAN SCHWINGER
Department of Physics, Harvard University, Cambridge, Massachusetts
(Received November 1, 1948)

The covariant formulation of quantum electrodynamics, developed in a previous paper, is here applied to two elementary problems—the polarization of the vacuum and the self-energies of the electron and photon. In the first section the vacuum of the non-interacting electromagnetic and matter fields is covariantly defined as that state for which the eigenvalue of an arbitrary time-like component of the energy-momentum four-vector is an absolute minimum. It is remarked that this definition must be compatible with the requirement that the vacuum expectation values of a physical quantity in various coordinate systems should be, not only covariantly related, but identical, since the vacuum has a significance that is independent of the coordinate system. In order to construct a suitable characterization of the vacuum state vector, a covariant decomposition of the field operators into positive and negative frequency components is introduced, and the properties of these associated fields developed. It is shown that the state vector for the electromagnetic vacuum is annihilated by the positive frequency part of the transverse four-vector potential, while that for the matter vacuum is annihilated by the positive frequency part of the Dirac spinor and of its charge conjugate. These defining properties of the vacuum state vector are employed in the calculation of the vacuum expectation values of quadratic field quantities, specifically the energy-momentum tensors of the independent electromagnetic and matter fields, and the current four-vector. It is inferred that the electromagnetic energy-momentum tensor, and the current vector must vanish in the vacuum, while the matter field energy-momentum tensor vanishes in the vacuum only by the addition of a suitable multiple of the unit tensor. The second section treats the induction of a current in the vacuum by an external electromagnetic field. It is supposed that the latter does not produce actual electron-positron pairs; that is, we consider only the phenomenon of virtual pair creation. This restriction is introduced by requiring that the establishment and subsequent removal of the external field produce no net change in state for the matter field. It is demonstrated, in a general manner, that the induced current at a given space-time point involves the external current in the vicinity of that point, and not the electromagnetic potentials. This gauge invariant result shows that a light wave, propagating at remote distances from its source, induces no current in the vacuum and is therefore undisturbed in its passage through space. The absence of a light quantum self-energy effect is thus indicated. The current induced at a point consists, more precisely, of two parts: a logarithmically divergent multiple of the external current at that point, which produces an unobservable renormalization of charge, and a more involved finite contribution, which is the physically significant induced current. The latter agrees with the results of previous investigations. The modification of the matter field properties arising from interaction with the vacuum fluctuations of the electromagnetic field is considered in the third section. The analysis is carried out with two alternative formulations, one employing the complete electromagnetic potential together with a supplementary condition, the other using the transverse potential, with the variables of the supplementary condition eliminated. It is noted that no real processes are produced by the first order coupling between the fields. Accordingly, alternative equations of motion for the state vector are constructed, from which the first order interaction term has been eliminated and replaced by the second order coupling which it generates. The latter includes the self action of individual particles and light quanta, the interaction of different particles, and a coupling between particles and light quanta which produces such effects as Compton scattering and two quantum pair annihilation. It is concluded from a comparison of the alternative procedures that, for the treatment of virtual light quantum processes, the separate consideration of longitudinal and transverse fields is an inadvisable complication. The light quantum self-energy term is shown to vanish, while that for a particle has the anticipated form for a change in proper mass, although the latter is logarithmically divergent, in agreement with previous calculations. To confirm the identification of the self-energy effect with a change in proper mass, it is shown that the result of removing this term from the state vector equation of motion is to alter the matter field equations of motion in the expected manner. It is verified, finally, that the energy and momentum modifications produced by self-interaction effects are entirely accounted for by the addition of the electromagnetic proper mass to the mechanical proper mass—an unobservable mass renormalization. An appendix is devoted to the construction of several invariant functions associated with the electromagnetic and matter fields.

THE first article of this series[1] was concerned with a formulation of quantum electrodynamics that has the following essential features—explicit covariance with respect to Lorentz transformations, and a natural division between the properties of independent fields and the effects of field interactions. As the simplest

[1] Quantum electrodynamics. I. A covariant formulation, Phys. Rev. **74**, 1439 (1948), hereinafter referred to as I. References to equations in the work will be written in the typical form (I, 2.3).

example of the latter, we consider, in this second paper, the phenomena of vacuum polarization and the self energies of photon and electron, which arise from the coupling between the matter and electromagnetic fields and their vacuum fluctuations. It will first be necessary to construct a suitable covariant definition for the vacuum of the independent matter and electromagnetic fields.

1. DEFINITION OF THE VACUUM

In order to define the vacuum of the electromagnetic fields, it is convenient to introduce two auxiliary four-vector fields that obey the same differential equation as $A_\mu(x)$

$$A_\mu^{(+)}(x)=\frac{1}{2\pi i}\int_{C_+}A_\mu(x-\epsilon\tau)\frac{d\tau}{\tau}, \quad (1.1a)$$

$$A_\mu^{(-)}(x)=\frac{1}{2\pi i}\int_{C_+}A_\mu(x+\epsilon\tau)\frac{d\tau}{\tau}, \quad (1.1b)$$

in which the contour C_+ is extended from $-\infty$ to $+\infty$, deformed below the singularity at $\tau=0$. It is intended that ϵ_μ be a time-like vector, $\epsilon_\mu^2<0$, with $\epsilon_0=(1/i)\epsilon_4>0$, which are covariant requirements. The fields $A_\mu^{(+)}(x)$ and $A_\mu^{(-)}(x)$ are then independent of the special choice of ϵ_μ. A simple connection between the three fields is obtained by rewriting (1.1b) as

$$A_\mu^{(-)}(x)=\frac{1}{2\pi i}\int_{C_-}A_\mu(x-\epsilon\tau)\frac{d\tau}{\tau}, \quad (1.2)$$

where C_- is extended from $+\infty$ to $-\infty$, deformed above the singularity at $\tau=0$. Evidently the sum of the contours C_+ and C_- is a closed contour drawn about the singularity at the origin, whence

$$A_\mu^{(+)}(x)+A_\mu^{(-)}(x)=\frac{1}{2\pi i}\oint A_\mu(x-\epsilon\tau)\frac{d\tau}{\tau}=A_\mu(x). \quad (1.3)$$

On choosing the contours C_+ and C_- to coincide with the real axis, save for appropriate semicircles of negligible radius drawn about the origin, one obtains from (1.1a) and (1.2) the forms

$$\begin{aligned}A_\mu^{(+)}(x)&=\tfrac{1}{2}[A_\mu(x)-iA_\mu^{(1)}(x)],\\ A_\mu^{(-)}(x)&=\tfrac{1}{2}[A_\mu(x)+iA_\mu^{(1)}(x)],\end{aligned} \quad (1.4)$$

where

$$\begin{aligned}A_\mu^{(1)}(x)&=i[A_\mu^{(+)}(x)-A_\mu^{(-)}(x)],\\ &=-\frac{1}{\pi}P\int_{-\infty}^{\infty}A_\mu(x-\epsilon\tau)\frac{d\tau}{\tau},\end{aligned} \quad (1.5)$$

and P symbolizes the principal part of the integral. It will be noted that $A_1^{(1)}$, $A_2^{(1)}$, $A_3^{(1)}$, and $A_0^{(1)}=(1/i)A_4^{(1)}$ are Hermitian operators, in view of the Hermitian character of the corresponding components of $A_\mu(x)$. Accordingly, $A_\mu^{(-)}$ is the Hermitian conjugate of $A_\mu^{(+)}$, where $\mu=0, 1, 2, 3$.

The significance of the associated fields $A_\mu^{(+)}(x)$, $A_\mu^{(-)}(x)$, and $A_\mu^{(1)}(x)$ can best be appreciated in terms of a Fourier representation of $A_\mu(x)$,

$$A_\mu(x)=\int A_\mu(k)\delta(k_\lambda^2)\exp(ik_\mu x_\mu)(dk), \quad (1.6)$$

where $(dk)=dk_0dk_1dk_2dk_3$ is the four-dimensional volume element in wave number, or k space. The delta function, $\delta(k_\lambda^2)$, ensures that the individual terms of the expansion obey the wave Eq. (I, 2.11), leaving the Fourier amplitudes, $A_\mu(k)$, quite arbitrary. According to the definition (1.1a) and (1.1b),

$$A_\mu^{(+)}(x)=\int A_\mu(k)\delta(k_\lambda^2)\exp(ik_\mu x_\mu)(dk)\frac{1}{2\pi i}\times\int_{C_+}\exp(-ik_\lambda\epsilon_\lambda\tau)\frac{d\tau}{\tau}, \quad (1.7)$$

$$A_\mu^{(-)}(x)=\int A_\mu(k)\delta(k_\lambda^2)\exp(ik_\mu x_\mu)(dk)\frac{1}{2\pi i}\times\int_{C_+}\exp(ik_\lambda\epsilon_\lambda\tau)\frac{d\tau}{\tau}.$$

But

$$\frac{1}{2\pi i}\int_{C_+}\exp(-ik_\lambda\epsilon_\lambda\tau)\frac{d\tau}{\tau}=\begin{cases}1, & -k_\lambda\epsilon_\lambda>0\\ 0, & -k_\lambda\epsilon_\lambda<0,\end{cases} \quad (1.8)$$

whence

$$A_\mu^{(+)}(x)=\int_{-k_\lambda\epsilon_\lambda>0}A_\mu(k)\delta(k_\lambda^2)\times\exp(ik_\mu x_\mu)(dk), \quad (1.9)$$

and

$$A_\mu^{(-)}(x)=\int_{-k_\lambda\epsilon_\lambda<0} A_\mu(k)\delta(k_\lambda^2)\times\exp(ik_\mu x_\mu)(dk). \quad (1.10)$$

The two domains in wave number space characterized by the sign of $-k_\mu\epsilon_\mu$ are actually independent of ϵ_μ, provided the latter is a time-like vector with a definite sign for ϵ_0. It is sufficient to observe that

$$-k_\mu\epsilon_\mu=k_0\epsilon_0\left(1-\frac{\mathbf{k}\cdot\boldsymbol{\varepsilon}}{k_0\epsilon_0}\right), \quad (1.11)$$

and

$$\left|\frac{\mathbf{k}\cdot\boldsymbol{\varepsilon}}{k_0\epsilon_0}\right|<\frac{|\mathbf{k}|}{|k_0|}\frac{|\boldsymbol{\varepsilon}|}{|\epsilon_0|}<1, \quad (1.12)$$

in which the last inequality presupposes that ϵ_μ is time-like and k_μ either a null vector or a time-like vector. Accordingly, the sign of $-k_\mu\epsilon_\mu$ is determined by that of $k_0\epsilon_0$, and if ϵ_0 is restricted to be positive, itself an invariant requirement, it is inferred that $-k_\mu\epsilon_\mu$ possesses the algebraic sign of k_0. It is now clear that if $A_\mu(x)$ is constructed as an arbitrary superposition of plane waves,

$$\exp(ik_\mu x_\mu)=\exp[i(\mathbf{k}\cdot\mathbf{r}-k_0x_0)],$$

the functions $A_\mu^{(+)}(x)$ and $A_\mu^{(-)}(x)$ consist of the positive and negative frequency parts, respectively, which is an invariant decomposition. The function $A_\mu^{(1)}(x)$ contains both the positive and negative frequency parts of $A_\mu(x)$, but with the factors i and $-i$, respectively.

The commutation properties of the auxiliary fields with $A_\mu(x)$ are easily constructed. According to the definitions and Eq. (I, 2.28),

$$\begin{aligned}[A_\mu^{(+)}(x),A_\nu(x')]&=ihc\delta_{\mu\nu}D^{(+)}(x-x'),\\ [A_\mu^{(-)}(x),A_\nu(x')]&=ihc\delta_{\mu\nu}D^{(-)}(x-x'),\\ [A_\mu^{(1)}(x),A_\nu(x')]&=ihc\delta_{\mu\nu}D^{(1)}(x-x'),\end{aligned} \quad (1.13)$$

where

$$\begin{aligned}D^{(+)}(x)&=\frac{1}{2\pi i}\int_{C_+}D(x-\epsilon\tau)\frac{d\tau}{\tau},\\ D^{(-)}(x)&=\frac{1}{2\pi i}\int_{C_-}D(x-\epsilon\tau)\frac{d\tau}{\tau},\\ D^{(1)}(x)&=\frac{1}{\pi}P\int_{-\infty}^{\infty}D(x-\epsilon\tau)\frac{d\tau}{\tau}.\end{aligned} \quad (1.14)$$

Relations analogous to (1.3) and (1.4) are valid, of course, for the various D functions:

$$\begin{aligned}D^{(+)}(x)+D^{(-)}(x)&=D(x),\\ D^{(+)}(x)&=\tfrac{1}{2}[D(x)-iD^{(1)}(x)],\\ D^{(-)}(x)&=\tfrac{1}{2}[D(x)+iD^{(1)}(x)].\end{aligned} \quad (1.15)$$

In addition, $D^{(1)}(x)$ shares the reality property of $D(x)$, and $D^{(-)}(x)$ is the complex conjugate of $D^{(+)}(x)$. Further, the odd nature of $D(x)$, as a function of the coordinates, implies that $D^{(1)}(x)$ is an even function

$$D^{(1)}(-x)=D^{(1)}(x), \quad (1.16)$$

which has as a consequence that

$$D^{(-)}(x)=-D^{(+)}(-x). \quad (1.17)$$

Finally, the validity of the differential equations

$$\Box^2D^{(+)}(x)=\Box^2D^{(-)}(x)=\Box^2D^{(1)}(x)=0 \quad (1.18)$$

will be evident.

The essential commutation properties of the auxiliary fields are contained in the statements

$$[A_\mu^{(+)}(x),A_\nu^{(+)}(x')]=[A_\mu^{(-)}(x),A_\nu^{(-)}(x')]=0. \quad (1.19)$$

It follows by direct calculation that

$$\begin{aligned}&[A_\mu^{(+)}(x),A_\nu^{(+)}(x')]\\ &=ihc\delta_{\mu\nu}\frac{1}{(2\pi i)^2}\int_{C_+}D(x-x'-\epsilon(\tau-\tau'))\frac{d\tau}{\tau}\frac{d\tau'}{\tau'}\\ &=ihc\delta_{\mu\nu}\frac{1}{2\pi}\int_{-\infty}^{\infty}d\alpha e^{i\alpha\lambda}D(x-x'-\epsilon\lambda)\frac{1}{2\pi i}\\ &\quad\times\int_{C_+}e^{i\alpha\tau}\frac{d\tau}{\tau}\frac{1}{2\pi i}\int_{C_+}e^{-i\alpha\tau'}\frac{d\tau'}{\tau'}=0,\end{aligned} \quad (1.20)$$

in which the decisive steps are the introduction of a Fourier integral representation for the τ dependence of $D(x-\epsilon\tau)$, and the observation (see Eq. (1.8)) that the two resulting contour integrals are never simultaneously different from zero (except for the isolated point $\alpha=0$). Alternatively, we can remark that the positive frequency character of $A_\mu^{(+)}(x)$ is incompatible with the physical requirement that the commutator involve only $x_\mu-x_\mu'$, the interval be-

tween the two points x and x', unless the commutator vanishes. The proof for $A_\mu^{(-)}$ is identical. The commutator of $A_\mu^{(+)}(x)$ with $A_\nu^{(-)}(x')$ can also be directly evaluated along the lines of (1.20), but it is sufficient to combine (1.19) with (1.13) to obtain

$$[A_\mu^{(+)}(x), A_\nu^{(-)}(x')]=ihc\delta_{\mu\nu}D^{(+)}(x-x'), \quad (1.21)$$

or

$$[A_\mu^{(-)}(x), A_\nu^{(+)}(x')]=ihc\delta_{\mu\nu}D^{(-)}(x-x'). \quad (1.22)$$

It should also be noted that, in view of the identity

$$\begin{aligned}[A_\mu^{(1)}(x), A_\nu^{(1)}(x')]-[A_\mu(x), A_\nu(x')]\\ =-2[A_\mu^{(+)}(x), A_\nu^{(+)}(x')]\\ -2[A_\mu^{(-)}(x), A_\nu^{(-)}(x')],\end{aligned} \quad (1.23)$$

the commutation relations (1.19) imply that

$$\begin{aligned}[A_\mu^{(1)}(x), A_\nu^{(1)}(x')]&=[A_\mu(x), A_\nu(x')]\\ &=ihc\delta_{\mu\nu}D(x-x').\end{aligned} \quad (1.24)$$

In a manner quite analogous to that presented for $A_\mu(x)$, various associated functions can be defined for $\mathfrak{A}_\mu(x)$, $\Lambda(x)$, and $\Lambda'(x)$. Without entering into repetitious detail, let us merely record the definitions

$$\begin{aligned}\mathfrak{A}_\mu^{(+)}(x)&=\tfrac{1}{2}[\mathfrak{A}_\mu(x)-i\mathfrak{A}_\mu^{(1)}(x)],\\ \mathfrak{A}_\mu^{(-)}(x)&=\tfrac{1}{2}[\mathfrak{A}_\mu(x)+i\mathfrak{A}_\mu^{(1)}(x)],\end{aligned} \quad (1.25)$$

and the commutation relations

$$[\mathfrak{A}_\mu^{(+)}(x), \mathfrak{A}_\nu^{(+)}(x')]=[\mathfrak{A}_\mu^{(-)}(x), \mathfrak{A}_\nu^{(-)}(x')]=0, \quad (1.26)$$

$$\begin{aligned}[\mathfrak{A}_\mu^{(1)}(x), \mathfrak{A}_\nu(x')]&=ihc\delta_{\mu\nu}D^{(1)}(x-x')\\ &-ihc\left[\frac{\partial}{\partial x_\mu}\frac{\partial}{\partial x_\nu}+\left(n_\mu\frac{\partial}{\partial x_\nu}+n_\nu\frac{\partial}{\partial x_\mu}\right)n_\lambda\frac{\partial}{\partial x_\lambda}\right]\\ &\times\mathfrak{D}^{(1)}(x-x').\end{aligned} \quad (1.27)$$

We shall consider the vacuum of the isolated electromagnetic field to be that state for which the eigenvalue of the energy, or better, an arbitrary time-like component of the energy-momentum four-vector, is an absolute minimum. This definition must also be compatible with the evident requirement that the vacuum expectation values of a physical quantity in various coordinate systems should be, not only covariantly related, but identical; the properties of the vacuum are independent of the coordinate system. In order to utilize the minimum energy definition, we apply (I, 1.38) to the positive frequency part of the physically significant electromagnetic field vector $\mathfrak{A}_\mu(x)$,

$$\mathfrak{A}_\mu^{(+)}(x)P_\nu-P_\nu\mathfrak{A}_\mu^{(+)}(x)=\frac{\hbar}{i}\frac{\partial}{\partial x_\nu}\mathfrak{A}_\mu^{(+)}(x). \quad (1.28)$$

On considering a particular Fourier component of $\mathfrak{A}_\mu^{(+)}(x)$, the latter equation becomes

$$\mathfrak{A}_\mu^{(+)}(k)P_\nu-P_\nu\mathfrak{A}_\mu^{(+)}(k)=\hbar k_\nu\mathfrak{A}_\mu^{(+)}(k), \quad (1.29)$$

which further reduces to

$$\mathfrak{A}_\mu^{(+)}(k)W-W\mathfrak{A}_\mu^{(+)}(k)=\hbar\omega\mathfrak{A}_\mu^{(+)}(k) \quad (1.30)$$

on multiplication with a unit time-like vector ϵ_ν such that $\epsilon_0>0$.

Here

$$W=-\epsilon_\nu P_\nu c, \quad \omega=-\epsilon_\nu k_\nu c \quad (1.31)$$

represent invariant expressions for energy and frequency in an arbitrary coordinate system specified by ϵ_ν. We may now apply both sides of (1.30) to the state vector Ψ_0 representing the vacuum of the electromagnetic field and obtain

$$W[\mathfrak{A}_\mu^{(+)}(k)\Psi_0]=(W_0-\hbar\omega)[\mathfrak{A}_\mu^{(+)}(k)\Psi_0], \quad (1.32)$$

where W_0 is the eigenvalue of W in the state described by Ψ_0. This result implies that in the state described by $\mathfrak{A}_\mu^{(+)}(k)\Psi_0$, W has the eigenvalue $W_0-\hbar\omega$. Inasmuch as the defining property of $\mathfrak{A}_\mu^{(+)}(k)$ guarantees that ω is positive, we are confronted with a state of lower energy than that in the vacuum. This contradiction can be resolved only if

$$\mathfrak{A}_\mu^{(+)}(k)\Psi_0=0, \quad (1.33)$$

which serves to specify Ψ_0. Since (1.33) is valid for all k, we may write

$$\mathfrak{A}_\mu^{(+)}(x)\Psi_0=0, \quad (1.34)$$

which is self-consistent, in view of the commutation properties of $\mathfrak{A}_\mu^{(+)}$.

The definition of the vacuum thus obtained can be used to evaluate vacuum expectation values of quadratic field quantities, of which

the basic form is

$$\{\mathfrak{A}_\mu(x),\ \mathfrak{A}_\nu(x')\}=\mathfrak{A}_\mu(x)\,\mathfrak{A}_\nu(x')+\mathfrak{A}_\nu(x')\,\mathfrak{A}_\mu(x).$$

Now

$$\begin{aligned}&\{\mathfrak{A}_\mu(x),\ \mathfrak{A}_\nu(x')\}\\&=(2\mathfrak{A}_\mu^{(-)}(x)-i\mathfrak{A}_\mu^{(1)}(x))\,\mathfrak{A}_\nu(x')\\&\qquad+\mathfrak{A}_\nu(x')(2\mathfrak{A}_\mu^{(+)}(x)+i\mathfrak{A}_\mu^{(1)}(x))\\&=-i[\mathfrak{A}_\mu^{(1)}(x),\ \mathfrak{A}_\nu(x')]\\&\quad+2(\mathfrak{A}_\mu^{(-)}(x)\,\mathfrak{A}_\nu(x')+\mathfrak{A}_\nu(x')\,\mathfrak{A}_\mu^{(+)}(x)),\end{aligned}\tag{1.35}$$

where the first term is a known commutator and the second has a vanishing vacuum expectation value. Thus

$$\begin{aligned}&\langle\mathfrak{A}_\mu^{(-)}(x)\,\mathfrak{A}_\nu(x')+\mathfrak{A}_\nu(x')\,\mathfrak{A}_\mu^{(+)}(x)\rangle_0\\&=(\Psi_0,\ (\mathfrak{A}_\mu^{(-)}(x)\,\mathfrak{A}_\nu(x')+\mathfrak{A}_\nu(x')\,\mathfrak{A}_\nu^{(+)}(x))\Psi_0)\\&=\pm(\mathfrak{A}_\mu^{(+)}(x)\Psi_0,\ \mathfrak{A}_\nu(x')\Psi_0)\\&\qquad+(\Psi_0,\ \mathfrak{A}_\nu(x')\,\mathfrak{A}_\mu^{(+)}(x)\Psi_0)=0,\end{aligned}\tag{1.36}$$

which involves the fact that, to within a minus sign for $\mu=4$, the Hermitian conjugate of $\mathfrak{A}_\mu^{(-)}$ is $\mathfrak{A}_\mu^{(+)}$. Hence,

$$\begin{aligned}&\langle\{\mathfrak{A}_\mu(x),\ \mathfrak{A}_\nu(x')\}\rangle_0=\hbar c\delta_{\mu\nu}D^{(1)}(x-x')\\&\quad-\hbar c\left[\frac{\partial}{\partial x_\mu}\frac{\partial}{\partial x_\nu}+\left(n_\mu\frac{\partial}{\partial x_\nu}+n_\nu\frac{\partial}{\partial x_\mu}\right)n_\lambda\frac{\partial}{\partial x_\lambda}\right]\\&\qquad\times\mathfrak{D}^{(1)}(x-x').\end{aligned}\tag{1.37}$$

From this result, one can compute that

$$\begin{aligned}&\langle\{\mathfrak{F}_{\mu\lambda}(x),\ \mathfrak{F}_{\nu\sigma}(x')\}\rangle_0\\&=\hbar c\left(\delta_{\lambda\nu}\frac{\partial}{\partial x_\mu}\frac{\partial}{\partial x_\sigma}+\delta_{\mu\sigma}\frac{\partial}{\partial x_\lambda}\frac{\partial}{\partial x_\nu}-\delta_{\lambda\sigma}\frac{\partial}{\partial x_\mu}\frac{\partial}{\partial x_\nu}\right.\\&\qquad\left.-\delta_{\mu\nu}\frac{\partial}{\partial x_\lambda}\frac{\partial}{\partial x_\sigma}\right)D^{(1)}(x-x'),\end{aligned}\tag{1.38}$$

of which two successive specializations are

$$\begin{aligned}&\langle\{\mathfrak{F}_{\mu\lambda}(x),\ \mathfrak{F}_{\nu\lambda}(x')\}\rangle_0\\&=-\hbar c\left(2\frac{\partial}{\partial x_\mu}\frac{\partial}{\partial x_\nu}+\delta_{\mu\nu}\Box^2\right)D^{(1)}(x-x')\\&=-2\hbar c\frac{\partial}{\partial x_\mu}\frac{\partial}{\partial x_\nu}D^{(1)}(x-x'),\end{aligned}\tag{1.39}$$

and

$$\begin{aligned}\langle\{\mathfrak{F}_{\lambda\sigma}(x),\ \mathfrak{F}_{\lambda\sigma}(x')\}\rangle_0&=-2\hbar c\Box^2D^{(1)}(x-x')\\&=0.\end{aligned}\tag{1.40}$$

As an elementary application of these vacuum expectation values, one may consider the computation of the vacuum average value of the mechanical quantities comprised in the electromagnetic energy-momentum tensor

$$\Theta_{\mu\nu}=\tfrac{1}{2}\{\mathfrak{F}_{\mu\lambda}(x),\ \mathfrak{F}_{\nu\lambda}(x)\}-\tfrac{1}{8}\delta_{\mu\nu}\{\mathfrak{F}_{\lambda\sigma}(x),\ \mathfrak{F}_{\lambda\sigma}(x)\},\tag{1.41}$$

which has the important property of being trace-less,

$$\Theta_{\mu\mu}=0.\tag{1.42}$$

Evidently,

$$\langle\Theta_{\mu\nu}\rangle_0=-\hbar c\frac{\partial}{\partial\xi_\mu}\frac{\partial}{\partial\xi_\nu}D^{(1)}(\xi)\Big]_{\xi=0},\tag{1.43}$$

which is indeterminate in view of the singularity of $D^{(1)}(\xi)$ as $\xi_\mu^2\to0$. However, the form of (1.43) can be inferred from quite general requirements. Since $D^{(1)}(\xi)$ is a function only of ξ_μ^2, the tensor resulting from the indicated process can only be a multiple of $\delta_{\mu\nu}$,

$$\frac{\partial}{\partial\xi_\mu}\frac{\partial}{\partial\xi_\nu}D^{(1)}(\xi)\Big]_{\xi=0}=K\delta_{\mu\nu},\tag{1.44}$$

and, on placing $\mu=\nu$, with the implied summation, we learn that

$$4K=\Box^2D^{(1)}(\xi)\Big]_{\xi=0}=0,\tag{1.45}$$

whence

$$\langle\Theta_{\mu\nu}\rangle_0=0.\tag{1.46}$$

This, indeed, is the only result compatible with the requirement that the properties of the vacuum be independent of the coordinate system. The values ascribed to the symmetrical tensor $\langle\Theta_{\mu\nu}\rangle_0$ can be identical in all coordinate systems only if the tensor is a multiple of $\delta_{\mu\nu}$. If, in addition, it is restricted to be trace-less, the tensor must vanish. Thus, a non-vanishing electromagnetic vacuum fluctuation energy is incompatible with relativistic requirements.

The process of defining the vacuum of the matter field follows the pattern that has been

presented for the electromagnetic field, with appropriate modifications. The spinors

$$\psi^{(+)}(x)=\frac{1}{2\pi i}\int_{C_+}\psi(x-\epsilon\tau)\frac{d\tau}{\tau} \tag{1.47}$$

and

$$\psi^{(-)}(x)=\frac{1}{2\pi i}\int_{C_+}\psi(x+\epsilon\tau)\frac{d\tau}{\tau} \tag{1.48}$$

are the positive and negative frequency (or energy) parts of $\psi(x)$. They may be written

$$\begin{aligned}\psi^{(+)}(x)&=\tfrac{1}{2}[\psi(x)-i\psi^{(1)}(x)],\\ \psi^{(-)}(x)&=\tfrac{1}{2}[\psi(x)+i\psi^{(1)}(x)],\end{aligned} \tag{1.49}$$

where

$$\psi^{(1)}(x)=\frac{1}{\pi}P\int_{-\infty}^{\infty}\psi(x-\epsilon\tau)\frac{d\tau}{\tau}. \tag{1.50}$$

The same operations can be applied to the adjoint spinor $\bar{\psi}(x)$. In particular,

$$\bar{\psi}^{(1)}(x)=\frac{1}{\pi}P\int_{-\infty}^{\infty}\bar{\psi}(x-\epsilon\tau)\frac{d\tau}{\tau}, \tag{1.51}$$

which makes it evident that

$$\bar{\psi}^{(1)}(x)=\overline{\psi^{(1)}}(x). \tag{1.52}$$

This, in turn, implies the relations

$$\bar{\psi}^{(+)}(x)=\overline{\psi^{(-)}}(x),\quad \bar{\psi}^{(-)}(x)=\overline{\psi^{(+)}}(x), \tag{1.53}$$

replacing the simpler reality properties of the functions associated with the electromagnetic four-vector potential. The decomposition of the charge conjugate spinors follows directly from the definitions (I, 1.3). Thus,

$$\psi'^{(+)}=C\bar{\psi}^{(+)}=C\overline{\psi^{(-)}},\quad \psi'^{(-)}=C\bar{\psi}^{(-)}=C\overline{\psi^{(+)}}, \tag{1.54}$$

and

$$\begin{aligned}\bar{\psi}'^{(+)}&=\overline{\psi'^{(-)}}=C^{-1}\psi^{(+)},\\ \bar{\psi}'^{(-)}&=\overline{\psi'^{(+)}}=C^{-1}\psi^{(-)}.\end{aligned} \tag{1.55}$$

The commutation relations of ψ with the various associated fields can be constructed immediately. In particular,

$$\begin{aligned}\{\psi_\alpha^{(1)}(x),\bar{\psi}_\beta(x')\}&=-\{\psi_\alpha(x),\overline{\psi_\beta^{(1)}}(x')\}\\ &=\frac{1}{i}S_{\alpha\beta}^{(1)}(x-x')\\ &=\frac{1}{i}\left(\gamma_\mu\frac{\partial}{\partial x_\mu}-\kappa_0\right)_{\alpha\beta}\Delta^{(1)}(x-x')\end{aligned} \tag{1.56}$$

where

$$\Delta^{(1)}(x)=\frac{1}{\pi}P\int_{-\infty}^{\infty}\Delta(x-\epsilon\tau)\frac{d\tau}{\tau} \tag{1.57}$$

is an even function of x obeying the differential equation

$$(\Box^2-\kappa_0^2)\Delta^{(1)}(x)=0. \tag{1.58}$$

The explicit construction of this and the other functions that have been introduced is performed in the Appendix. The elementary arguments used to prove (1.19) will also serve to demonstrate that

$$\begin{aligned}\{\psi_\alpha^{(+)}(x),\bar{\psi}_\beta^{(+)}(x')\}&=\{\psi_\alpha^{(+)}(x),\overline{\psi_\beta^{(-)}}(x')\}=0,\\ \{\psi_\alpha^{(-)}(x),\bar{\psi}_\beta^{(-)}(x')\}&=\{\psi_\alpha^{(-)}(x),\overline{\psi_\beta^{(+)}}(x')\}=0,\end{aligned} \tag{1.59}$$

whence

$$\begin{aligned}\{\psi_\alpha^{(+)}(x),\overline{\bar{\psi}_\beta^{(+)}(x')}\}&=\frac{1}{i}S_{\alpha\beta}^{(+)}(x-x'),\\ \{\psi_\alpha^{(-)}(x),\overline{\bar{\psi}_\beta^{(-)}(x')}\}&=\frac{1}{i}S_{\alpha\beta}^{(-)}(x-x').\end{aligned} \tag{1.60}$$

It can also be shown, analogously to (1.23), that

$$\begin{aligned}\{\psi_\alpha^{(1)}(x),\overline{\bar{\psi}_\beta^{(1)}(x')}\}&=\{\psi_\alpha(x),\bar{\psi}_\beta(x')\}\\ &=\frac{1}{i}S_{\alpha\beta}(x-x').\end{aligned} \tag{1.61}$$

All such commutation relations are invariant with respect to charge conjugation. As an example,

$$\begin{aligned}&\{\psi_\alpha'^{(1)}(x),\bar{\psi}_\beta'(x')\}\\ &\quad=\{(C\bar{\psi}^{(1)}(x))_\alpha,(C^{-1}\psi(x'))_\beta\}\\ &\quad=-C_{\alpha\gamma}\{\psi_\delta(x'),\bar{\psi}_\gamma^{(1)}(x)\}C_{\delta\beta}^{-1}\\ &\quad=\frac{1}{i}\left(C\gamma_\mu{}^TC^{-1}\frac{\partial}{\partial x_\mu'}-\kappa_0\right)_{\alpha\beta}\Delta^{(1)}(x'-x)\\ &\quad=\frac{1}{i}\left(\gamma_\mu\frac{\partial}{\partial x_\mu}-\kappa_0\right)_{\alpha\beta}\Delta^{(1)}(x-x')\\ &\quad=\frac{1}{i}S_{\alpha\beta}^{(1)}(x-x').\end{aligned} \tag{1.62}$$

The characterization of the matter field vacuum as the state of minimum energy can be

exploited, in complete analogy with the procedure for the electromagnetic field, to yield the following defining equations for the vacuum state vector Ψ_0

$$\psi^{(+)}(x)\Psi_0=0, \tag{1.63}$$

and

$$\bar{\psi}^{(+)}(x)\Psi_0=\overline{\psi^{(-)}}(x)\Psi_0=0. \tag{1.64}$$

The latter equation can also be written as the charge conjugate form of (1.63)

$$\psi'^{(+)}(x)\Psi_0=0. \tag{1.65}$$

In order to evaluate the vacuum expectation value of the typical bilinear expression

$$[\psi_\alpha(x), \bar{\psi}_\beta(x')]=\psi_\alpha(x)\bar{\psi}_\beta(x')-\bar{\psi}_\beta(x')\psi_\alpha(x),$$

we write

$$\begin{aligned}&[\psi_\alpha(x), \bar{\psi}_\beta(x')]\\&=(2\psi_\alpha^{(-)}(x)-i\psi_\alpha^{(1)}(x))\bar{\psi}_\beta(x')\\&\qquad-\bar{\psi}_\beta(x')(2\psi_\alpha^{(+)}(x)+i\psi_\alpha^{(1)}(x))\\&=-i\{\psi_\alpha^{(1)}(x), \bar{\psi}_\beta(x')\}\\&\qquad+2(\psi_\alpha^{(-)}(x)\bar{\psi}_\beta(x')-\bar{\psi}_\beta(x')\psi_\alpha^{(+)}(x)),\end{aligned} \tag{1.66}$$

and observe that the vacuum expectation value of the second term is zero.

$$\begin{aligned}&(\Psi_0, (\psi_\alpha^{(-)}(x)\bar{\psi}_\beta(x')-\bar{\psi}_\beta(x')\psi_\alpha^{(+)}(x))\Psi_0)\\&\qquad=(\psi_\alpha^{(-)\dagger}(x)\Psi_0, \bar{\psi}_\beta(x')\Psi_0)\\&\qquad-(\Psi_0, \bar{\psi}_\beta(x')\psi_\alpha^{(+)}(x)\Psi_0)=0,\end{aligned} \tag{1.67}$$

since the Hermitian conjugate and adjoint spinors are linearly related. Hence

$$\begin{aligned}\langle[\psi_\alpha(x), \bar{\psi}_\beta(x')]\rangle_0&=\langle[\psi_\alpha'(x), \bar{\psi}_\beta'(x')]\rangle_0\\&=-S_{\alpha\beta}^{(1)}(x-x').\end{aligned} \tag{1.68}$$

We may apply this result to the evaluation of the expectation values of the current four-vector,

$$\begin{aligned}j_\mu&=-\frac{iec}{2}[\psi_\alpha(x), \bar{\psi}_\beta(x)](\gamma_\mu)_{\beta\alpha}\\&=\frac{iec}{2}[\psi_\alpha'(x), \bar{\psi}_\beta'(x)](\gamma_\mu)_{\beta\alpha},\end{aligned} \tag{1.69}$$

and the symmetrical energy-momentum tensor of the matter field (see (I, 1.29)),

$$\begin{aligned}\Theta_{\mu\nu}=-\frac{\hbar c}{4}\Big[&(\gamma_\mu)_{\beta\alpha}\frac{\partial}{\partial\xi_\nu}[\psi_\alpha(x+\tfrac{1}{2}\xi), \bar{\psi}_\beta(x-\tfrac{1}{2}\xi)]\\&+(\gamma_\nu)_{\beta\alpha}\frac{\partial}{\partial\xi_\mu}[\psi_\alpha(x+\tfrac{1}{2}\xi), \bar{\psi}_\beta(x-\tfrac{1}{2}\xi]\Big]_{\xi=0},\end{aligned} \tag{1.70}$$

the trace of which is (see (I, 1.34))

$$\Theta_{\mu\mu}=m_0c^2\tfrac{1}{2}[\psi_\alpha(x), \bar{\psi}_\alpha(x)]. \tag{1.71}$$

On adding the two equivalent, charge conjugate, expressions for the current vector we find, according to (1.68), that

$$\begin{aligned}\langle j_\mu\rangle_0=\frac{iec}{4}(\gamma_\mu)_{\beta\alpha}(&\langle[\psi_\alpha'(x), \bar{\psi}_\beta'(x)]\rangle_0\\&-\langle[\psi_\alpha(x), \bar{\psi}_\beta(x)]\rangle_0)=0,\end{aligned} \tag{1.72}$$

which is a simple expression of the charge symmetry of the theory. Alternatively, direct calculation yields

$$\begin{aligned}\langle j_\mu\rangle_0&=-\frac{iec}{2}\langle[\psi_\alpha(x), \bar{\psi}_\beta(x)]\rangle_0(\gamma_\mu)_{\beta\alpha}\\&=\frac{iec}{2}TrS^{(1)}(\xi)\gamma_\mu\Big]_{\xi=0}\\&=2iec\frac{\partial}{\partial\xi_\mu}\Delta^{(1)}(\xi)\Big]_{\xi=0}=0,\end{aligned} \tag{1.73}$$

since $\Delta^{(1)}(\xi)$ is an even function. In (1.73) the symbol Tr indicates the trace, or diagonal sum, of the Dirac matrices. The following trace evaluations have been used:

$$Tr\gamma_\mu\gamma_\nu=4\delta_{\mu\nu}, \quad Tr\gamma_\mu=0, \tag{1.74}$$

the proofs of which involve only the anti-commutation properties of the γ_μ, and elementary theorems concerning traces. Thus,

$$Tr\gamma_\mu\gamma_\nu=Tr\tfrac{1}{2}(\gamma_\mu\gamma_\nu+\gamma_\nu\gamma_\mu)=4\delta_{\mu\nu}$$

and

$$Tr\gamma_\mu=Tr\tfrac{1}{2}\gamma_\mu(\gamma_5\gamma_5+\gamma_5\gamma_5)=Tr\tfrac{1}{2}(\gamma_\mu\gamma_5+\gamma_5\gamma_\mu)\gamma_5=0.$$

In the latter proof, $\gamma_5=\gamma_1\gamma_2\gamma_3\gamma_4$ forms the fifth Dirac matrix, completing the set obeying the anti-commutation relations (I, 1.1).

The vacuum expectation value of the energy-

momentum tensor is

$$\langle\Theta_{\mu\nu}\rangle_0=\frac{\hbar c}{4}Tr\left(\gamma_\mu\frac{\partial}{\partial\xi_\nu}+\gamma_\nu\frac{\partial}{\partial\xi_\mu}\right)S^{(1)}(\xi)\Big]_{\xi=0}$$
$$=2\hbar c\frac{\partial}{\partial\xi_\mu}\frac{\partial}{\partial\xi_\nu}\Delta^{(1)}(\xi)\Big]_{\xi=0}. \tag{1.75}$$

The trace of $\langle\Theta_{\mu\nu}\rangle_0$ can be computed directly from (1.71),

$$\langle\Theta_{\mu\mu}\rangle_0=-m_0c^2\tfrac{1}{2}TrS^{(1)}(\xi)]_{\xi=0}$$
$$=2\hbar c\kappa_0{}^2\Delta^{(1)}(\xi)]_{\xi=0}, \tag{1.76}$$

which result also follows from (1.75). According to the general arguments presented in connection with the electromagnetic energy-momentum tensor, $\langle\Theta_{\mu\nu}\rangle_0$ must be a multiple of $\delta_{\mu\nu}$:

$$\langle\Theta_{\mu\nu}\rangle_0=K\delta_{\mu\nu}, \tag{1.77}$$

with

$$K=\tfrac{1}{4}\langle\Theta_{\mu\mu}\rangle_0=\tfrac{1}{2}\hbar c\kappa_0{}^2\Delta^{(1)}(0). \tag{1.78}$$

Unlike the electromagnetic field situation, the trace of the matter energy-momentum tensor does not vanish and, indeed, is divergent. There can be no objection, however, to altering the definition of the energy-momentum tensor by the addition of a suitable multiple of $\delta_{\mu\nu}$, which is so chosen that the vacuum expectation value of $\Theta_{\mu\nu}$ is zero.

2. THE POLARIZATION OF THE VACUUM

The first problem to which we turn our attention is the induction of a current in the matter field vacuum by an electromagnetic field—the polarization of the vacuum. It is supposed that the matter field, initially in its vacuum state, is perturbed by the establishment of an externally generated electromagnetic field, described by the potential $A_\mu(x)$. It will be convenient to assume that the potential vanishes prior to the creation of the field, as well as after the eventual removal of the field, which restricts the otherwise unlimited group of gauge transformations associated with an external electromagnetic field. Indeed, according to this specialization, the function $\Lambda(x)$ that generates a gauge transformation must be constant before the establishment of the field. In placing this constant equal to zero, no further assumption is introduced. We may then characterize the initial matter vacuum state by a unique state vector Ψ_0, without the inconsequential ambiguity associated with gauge transformations. The alteration of the state vector, produced by the external field, is described by

$$i\hbar c\frac{\delta\Psi[\sigma]}{\delta\sigma(x)}=-\frac{1}{c}j_\mu(x)A_\mu(x)\Psi[\sigma]. \tag{2.1}$$

Following the program of I, Section 4, we replace (2.1) by the functional integral equation

$$\Psi[\sigma]=\Psi_0+\frac{i}{\hbar c^2}\int_{-\infty}^{\sigma}j_\mu(x')A_\mu(x')\Psi[\sigma']d\omega', \tag{2.2}$$

which includes the initial condition

$$\Psi[\sigma]\rightarrow\Psi_0,\quad \sigma\rightarrow-\infty, \tag{2.3}$$

and can be solved by successive substitution. We shall be content with the first approximation, which regards the disturbance of the vacuum as small.

$$\Psi[\sigma]=\left(1+\frac{i}{\hbar c^2}\int_{-\infty}^{\sigma}j_\mu(x')A_\mu(x')d\omega'\right)\Psi_0$$
$$=U[\sigma,-\infty]\Psi_0. \tag{2.4}$$

The operator $U[\sigma,-\infty]$ is unitary, to the order of approximation considered. The expectation value of $j_\mu(x)$, computed for the state of the system as modified by the external electromagnetic field, is

$$\langle j_\mu(x)\rangle=(\Psi[\sigma],\, j_\mu(x)\Psi[\sigma])$$
$$=(\Psi_0,\, U^{-1}[\sigma,-\infty]j_\mu(x)U[\sigma,-\infty]\Psi_0)$$
$$=\langle U^{-1}[\sigma,-\infty]j_\mu(x)U[\sigma,-\infty]\rangle_0. \tag{2.5}$$

To the required order of approximation,

$$U^{-1}[\sigma,-\infty]j_\mu(x)U[\sigma,-\infty]$$
$$=j_\mu(x)+\frac{i}{\hbar c^2}\int_{-\infty}^{\sigma}[j_\mu(x),\, j_\nu(x')]A_\nu(x')d\omega', \tag{2.6}$$

whence

$$\langle j_\mu(x)\rangle=\frac{i}{\hbar c^2}\int_{-\infty}^{\sigma}\langle[j_\mu(x),\, j_\nu(x')]\rangle_0A_\nu(x')d\omega'. \tag{2.7}$$

An important test to which this expression should be subjected is that of gauge invariance.

We must require that, in the absence of a real electromagnetic field, no current be induced in the vacuum; that is, $A_\mu(x)=-\partial\Lambda(x)/\partial x_\mu$ must imply $\langle j_\mu(x)\rangle=0$. On introducing this form for $A_\mu(x)$, we find that

$$\begin{aligned}\langle j_\mu(x)\rangle&=-\frac{i}{\hbar c^2}\int_{-\infty}^{\sigma}d\omega'\frac{\partial}{\partial x_\nu'}\\&\qquad\times\{\langle[j_\mu(x),\,j_\nu(x')]\rangle_0\Lambda(x')\}\\&=-\frac{i}{\hbar c^2}\int_\sigma d\sigma_\nu'\langle[j_\mu(x),\,j_\nu(x')]\rangle_0\Lambda(x')\\&=-\frac{i}{\hbar c^2}\Lambda(x)\int_\sigma\langle[j_\mu(x),\,j_\nu(x')]\rangle_0 d\sigma_\nu'\\&=0,\end{aligned}\tag{2.8}$$

as required. In the course of this proof we have employed the commutability of all components of the current at two distinct points of a space-like surface, and of a time-like component of the current with j_μ at the same point, as contained in (I, 2.34). The previously discussed requirement that Λ vanish in the remote past is also involved.

In order to construct the vacuum expectation value of the commutator contained in (2.7), we write (see (I, 2.33)):

$$\begin{aligned}&[j_\mu(x),\,j_\nu(x')]\\&=\frac{ie^2c^2}{2}\{[\psi_\alpha(x),\bar\psi_\beta(x')](\gamma_\nu S(x'-x)\gamma_\mu)_{\beta\alpha}\\&\qquad-[\psi_\alpha(x'),\bar\psi_\beta(x)](\gamma_\mu S(x-x')\gamma_\nu)_{\beta\alpha}\},\end{aligned}\tag{2.9}$$

whence

$$\begin{aligned}&\langle[j_\mu(x),\,j_\nu(x')]\rangle_0\\&=\frac{ie^2c^2}{2}Tr[S^{(1)}(x'-x)\gamma_\mu S(x-x')\gamma_\nu\\&\qquad-S^{(1)}(x-x')\gamma_\nu S(x'-x)\gamma_\mu].\end{aligned}\tag{2.10}$$

To evaluate this trace, we first remark that the product of any three γ's (more generally, an odd number) has a vanishing trace:

$$Tr\gamma_\mu\gamma_\nu\gamma_\lambda=0.\tag{2.11}$$

Indeed,

$$\begin{aligned}Tr\gamma_\mu\gamma_\nu\gamma_\lambda&=Tr\tfrac{1}{2}\gamma_\mu\gamma_\nu\gamma_\lambda(\gamma_5\gamma_5+\gamma_5\gamma_5)\\&=Tr\tfrac{1}{2}(\gamma_\mu\gamma_\nu\gamma_\lambda\gamma_5+\gamma_5\gamma_\mu\gamma_\nu\gamma_\lambda)\gamma_5=0,\end{aligned}$$

since γ_5 anti-commutes with all components of γ_μ. Therefore,

$$\begin{aligned}&Tr[S^{(1)}(x'-x)\gamma_\mu S(x-x')\gamma_\nu\\&\qquad-S^{(1)}(x-x')\gamma_\nu S(x'-x)\gamma_\mu]\\&=-\frac{\partial\Delta^{(1)}(x-x')}{\partial x_\lambda}\frac{\partial\Delta(x-x')}{\partial x_\sigma}\\&\qquad\times Tr(\gamma_\lambda\gamma_\mu\gamma_\sigma\gamma_\nu+\gamma_\lambda\gamma_\nu\gamma_\sigma\gamma_\mu)\\&\quad+\kappa_0^2\Delta^{(1)}(x-x')\Delta(x-x')Tr(\gamma_\mu\gamma_\nu+\gamma_\nu\gamma_\mu)\end{aligned}\tag{2.12}$$

in which the even and odd natures of $\Delta^{(1)}$ and Δ have been employed. Now

$$\begin{aligned}\gamma_\lambda\gamma_\mu\gamma_\sigma\gamma_\nu+\gamma_\lambda\gamma_\nu\gamma_\sigma\gamma_\mu&=2\delta_{\mu\sigma}\gamma_\lambda\gamma_\nu\\&\quad+2\delta_{\nu\sigma}\gamma_\lambda\gamma_\mu-2\delta_{\mu\nu}\gamma_\lambda\gamma_\sigma,\end{aligned}\tag{2.13}$$

so that

$$\begin{aligned}&Tr(\gamma_\lambda\gamma_\mu\gamma_\sigma\gamma_\nu+\gamma_\lambda\gamma_\nu\gamma_\sigma\gamma_\mu)\\&\qquad=8(\delta_{\mu\sigma}\delta_{\lambda\nu}+\delta_{\nu\sigma}\delta_{\lambda\mu}-\delta_{\mu\nu}\delta_{\lambda\sigma}),\end{aligned}\tag{2.14}$$

and, finally

$$\begin{aligned}&\langle[j_\mu(x),\,j_\nu(x')]\rangle_0\\&=-4ie^2c^2\Big[\frac{\partial\Delta(x-x')}{\partial x_\mu}\frac{\partial\Delta^{(1)}(x-x')}{\partial x_\nu}\\&\quad+\frac{\partial\Delta(x-x')}{\partial x_\nu}\frac{\partial\Delta^{(1)}(x-x')}{\partial x_\mu}\\&\quad-\delta_{\mu\nu}\Big(\frac{\partial\Delta(x-x')}{\partial x_\lambda}\frac{\partial\Delta^{(1)}(x-x')}{\partial x_\lambda}\\&\qquad+\kappa_0^2\Delta(x-x')\Delta^{(1)}(x-x')\Big)\Big].\end{aligned}\tag{2.15}$$

In order to simplify further discussion, we shall suppose that the electromagnetic field under consideration does not produce actual electron-positron pairs in the vacuum; that is, we treat only the phenomenon of virtual pair creation. The restriction thereby imposed can be obtained from (2.4). The final state of the matter field, resulting from the establishment and subsequent removal of an electromagnetic field in the vacuum, is given by

$$\Psi[\infty]=\Big(1+\frac{i}{\hbar c^2}\int_{-\infty}^{\infty}j_\mu(x')A_\mu(x')d\omega'\Big)\Psi_0,\tag{2.16}$$

which must be simply Ψ_0 if no real pair creation has occurred. Hence,

$$\left[\int_{-\infty}^{\infty} j_\mu(x)A_\mu(x)d\omega\right]\Psi_0=0 \qquad (2.17)$$

is the condition describing the absence of real pair creation events. According to the discussion in I, Section 4, (2.17) will indeed result if the energy and momentum conservation laws cannot be simultaneously obeyed in the course of the pair producing interaction between the electromagnetic field and the fluctuating current in the vacuum. To exploit this limitation, we may rewrite (2.7) as

$$\langle j_\mu(x)\rangle=\frac{i}{\hbar c^2}\int_{-\infty}^{\infty}\langle[j_\mu(x),\, j_\nu(x')]\rangle_0 \times\tfrac{1}{2}(1+\epsilon(x-x'))A_\nu(x')d\omega', \qquad (2.18)$$

where $\epsilon(x)$ is $+1$ or -1 according as x_0 is positive or negative, which is effectively invariant since only time-like intervals $x_\mu-x_\mu'$ occur in (2.18). The condition (2.17) now enables us to replace (2.18) with

$$\langle j_\mu(x)\rangle=\frac{i}{2\hbar c^2}\int_{-\infty}^{\infty}\langle[j_\mu(x),\, j_\nu(x')]\rangle_0 \times\epsilon(x-x')A_\nu(x')d\omega'. \qquad (2.19)$$

The advantage of this form is the possibility of writing

$$\langle[j_\mu(x),\, j_\nu(x')]\rangle_0\epsilon(x-x') =8ie^2c^2\left[\frac{\partial\bar\Delta(x-x')}{\partial x_\mu}\frac{\partial\Delta^{(1)}(x-x')}{\partial x_\nu} +\frac{\partial\bar\Delta(x-x')}{\partial x_\nu}\frac{\partial\Delta^{(1)}(x-x')}{\partial x_\mu} -\delta_{\mu\nu}\left(\frac{\partial\bar\Delta(x-x')}{\partial x_\lambda}\frac{\partial\Delta^{(1)}(x-x')}{\partial x_\lambda} +\kappa_0{}^2\bar\Delta(x-x')\Delta^{(1)}(x-x')\right)\right], \qquad (2.20)$$

where

$$\bar\Delta(x)=-\tfrac{1}{2}\Delta(x)\epsilon(x) \qquad (2.21)$$

shares with $\Delta^{(1)}(x)$ the property of being a function only of $\lambda=-x_\mu{}^2$. Involved in the relation (2.20) is the fact that

$$\Delta(x)(\partial\epsilon(x)/\partial x_\mu)=0, \qquad (2.22)$$

which is demonstrated by remarking that $\epsilon(x)$ varies only by crossing a space-like surface through the origin, on which $\Delta(x)$ vanishes.

It will now be shown that

$$\langle[j_\mu(x),\, j_\nu(x')]\rangle_0\epsilon(x-x') =8ie^2c^2\left[\frac{\partial}{\partial x_\mu}\frac{\partial}{\partial x_\nu}G(\lambda)-\delta_{\mu\nu}\Box^2G(\lambda)\right], \qquad (2.23)$$

where

$$2\frac{\partial\bar\Delta(\lambda)}{\partial\lambda}\frac{\partial\Delta^{(1)}(\lambda)}{\partial\lambda}=\frac{\partial^2G(\lambda)}{\partial\lambda^2}, \qquad (2.24)$$

and $\lambda=-(x_\mu-x_\mu')^2$. The function $G(\lambda)$ is made precise by requiring that it vanish at infinity. Let it first be noted that

$$\frac{\partial\bar\Delta(x)}{\partial x_\mu}\frac{\partial\Delta^{(1)}(x)}{\partial x_\nu}+\frac{\partial\bar\Delta(x)}{\partial x_\nu}\frac{\partial\Delta^{(1)}(x)}{\partial x_\mu}=4x_\mu x_\nu\frac{\partial^2G(\lambda)}{\partial\lambda^2} =\frac{\partial}{\partial x_\mu}\frac{\partial}{\partial x_\nu}G(\lambda)+2\delta_{\mu\nu}\frac{\partial G(\lambda)}{\partial\lambda}, \qquad (2.25)$$

so that

$$\langle[j_\mu(x),\, j_\nu(x')]\rangle_0\epsilon(x-x') =8ie^2c^2\left[\frac{\partial}{\partial x_\mu}\frac{\partial}{\partial x_\nu}G(\lambda)-\delta_{\mu\nu}H(\lambda)\right], \qquad (2.26)$$

where

$$H(\lambda)=\tfrac{1}{2}\Box^2G(\lambda)+2\frac{\partial G(\lambda)}{\partial\lambda}+\kappa_0{}^2\bar\Delta(\lambda)\Delta^{(1)}(\lambda) =-2\lambda\frac{\partial^2G}{\partial\lambda^2}-2\frac{\partial G(\lambda)}{\partial\lambda}+\kappa_0{}^2\bar\Delta(\lambda)\Delta^{(1)}(\lambda). \qquad (2.27)$$

The stated simplification of $H(\lambda)$, namely

$$H(\lambda)=\Box^2G(\lambda), \qquad (2.28)$$

can be proven with the aid of the theorem

$$\frac{\partial}{\partial x_\mu}(\langle[j_\mu(x),\, j_\nu(x')]\rangle_0\epsilon(x-x'))=0 \qquad (2.29)$$

since the indicated differentiation, applied to (2.26), yields

$$0=\frac{\partial}{\partial x_\nu}[\Box^2G(\lambda)-H(\lambda)], \qquad (2.30)$$

from which (2.28) follows. To verify (2.29), observe that the left side reduces to

$$\langle[j_\mu(x),\, j_\nu(x')]\rangle_0 \frac{\partial\epsilon(x-x')}{\partial x_\mu}.$$

Now $\partial\epsilon(x-x')/\partial x_\mu$ is a non-vanishing time-like vector only if x and x' lie on a space-like surface, and, since a time-like component of the current commutes with j_ν at all points on a space-like surface, the validity of (2.29) becomes evident.

The introduction of the relation (2.23) into the formula (2.19) for the induced current gives, after an integration by parts that employs the vanishing of the external potential in the remote past and future,

$$\begin{aligned}\langle j_\mu(x)\rangle &= 4\frac{e^2}{\hbar}\int_{-\infty}^{\infty} G(\lambda)\\ &\quad\times\left(\Box'^2 A_\mu(x') - \frac{\partial}{\partial x_\mu'}\frac{\partial A_\nu(x')}{\partial x_\nu'}\right)d\omega'\\ &= -4\frac{e^2}{\hbar}\int_{-\infty}^{\infty} G(\lambda)\frac{\partial}{\partial x_\nu'}F_{\mu\nu}(x')d\omega' \qquad (2.31)\\ &= -4\frac{e^2}{hc}\int_{-\infty}^{\infty} G(\lambda)J_\mu(x')d\omega',\end{aligned}$$

where $J_\mu(x)$ is the external current generating the electromagnetic field. In this form, the gauge invariance of the theory is made explicit. The induced current depends, not upon the electromagnetic potentials, but rather the field strengths. Our result goes further, however, and states that the induced current at a given space-time point involves only the external current in the vicinity of that point. This has the important consequence that a light wave, propagating at remote distances from its source, induces no current in the vacuum and therefore is undisturbed in its passage through space. There is no light quantum self energy phenomenon akin to that for electrons, as we shall further discuss.

Our last task is the explicit construction of the function $G(\lambda)$. On inserting the integral representations for $\bar{\Delta}(\lambda)$ and $\Delta^{(1)}(\lambda)$ (Eqs. (A.15) and (A.33)):

$$\begin{aligned}\bar{\Delta}(\lambda) &= \frac{1}{8\pi^2}\int_{-\infty}^{\infty}\exp\left(i\lambda\alpha + i\frac{\kappa_0^2}{4\alpha}\right)d\alpha,\\ \Delta^{(1)}(\lambda) &= \frac{i}{4\pi^2}\int_{-\infty}^{\infty}\exp\left(i\lambda\beta + i\frac{\kappa_0^2}{4\beta}\right)\frac{\beta}{|\beta|}d\beta\end{aligned} \qquad (2.32)$$

into (2.24), we obtain

$$\begin{aligned}\frac{\partial^2 G(\lambda)}{\partial\lambda^2} &= -\frac{i}{(2\pi)^4}\int_{-\infty}^{\infty}\\ &\quad\times\exp\left[i\lambda(\alpha+\beta)+\frac{i\kappa_0^2}{4}\left(\frac{1}{\alpha}+\frac{1}{\beta}\right)\right]\alpha\beta\frac{\beta}{|\beta|}d\alpha d\beta,\end{aligned}$$

whence

$$\begin{aligned}G(\lambda) &= \frac{i}{(2\pi)^4}\int_{-\infty}^{\infty}\exp\left[i\lambda(\alpha+\beta)+\frac{i\kappa_0^2}{4}\left(\frac{1}{\alpha}+\frac{1}{\beta}\right)\right]\\ &\quad\times\frac{\alpha\beta}{(\alpha+\beta)^2}\frac{1}{2}\left(\frac{\alpha}{|\alpha|}+\frac{\beta}{|\beta|}\right)d\alpha d\beta \qquad (2.33)\end{aligned}$$

in which a symmetrization with respect to α and β has been performed. It will now be useful to introduce new variables, v and w, defined by

$$\alpha = \frac{\kappa_0^2}{2w}\frac{1}{1-v}, \quad \beta = \frac{\kappa_0^2}{2w}\frac{1}{1+v}, \qquad (2.34)$$

which are such that

$$\begin{aligned}G(\lambda) &= \frac{2i}{(4\pi)^4}\kappa_0^4\int_{-\infty}^{\infty}\exp\left(iw+i\frac{\kappa_0^2\lambda}{w(1-v^2)}\right)\\ &\quad\times\frac{1}{2}\left(\frac{1+v}{|1+v|}+\frac{1-v}{|1-v|}\right)\frac{dv}{1-v^2}\frac{dw}{w^3}\\ &= \frac{2i}{(4\pi)^4}\kappa_0^4\int_{-1}^{1}\frac{dv}{1-v^2}\int_{-\infty}^{\infty}\frac{dw}{w^3}\\ &\quad\times\exp\left(iw+i\frac{\kappa_0^2\lambda}{w(1-v^2)}\right). \qquad (2.35)\end{aligned}$$

The integral representation

$$\begin{aligned}&\int(dk)\exp(ik_\mu(x_\mu-x_\mu'))\exp\left(i\frac{k_\mu^2}{4\kappa_0^2}w(1-v^2)\right)\\ &\qquad\exp\left(i\frac{\kappa_0^2\lambda}{w(1-v^2)}\right)\\ &= i(4\pi)^2\kappa_0^4\frac{}{w|w|(1-v^2)^2} \qquad (2.36)\end{aligned}$$

then transforms (2.35) into

$$G(\lambda)=\frac{8}{(4\pi)^6}\int(dk)\exp(ik_\mu(x_\mu-x_\mu'))\times\int_0^1(1-v^2)dv\int_0^\infty\frac{dw}{w}\times\cos\left(1+\frac{k_\mu^2}{4\kappa_0^2}(1-v^2)\right)w, \quad (2.37)$$

which can be followed by an integration by parts with respect to v, according to

$$\int_0 d\left(v-\frac{v^3}{3}\right)\int_0^\infty\frac{dw}{w}\cos\left(1+\frac{k_\mu^2}{4\kappa_0^2}(1-v^2)\right)w=\frac{2}{3}\int_0^\infty\frac{\cos w}{w}dw-\frac{k_\mu^2}{2\kappa_0^2}\int_0^1\left(1-\frac{v^2}{3}\right)v^2dv\times\int_0^\infty dw\sin\left(1+\frac{k_\mu^2}{4\kappa_0^2}(1-v^2)\right)w. \quad (2.38)$$

The first w integral is logarithmically divergent at the origin. On introducing a lower limit, w_0, we obtain

$$\frac{2}{3}\log\frac{1}{\gamma w_0}-\frac{k_\mu^2}{2\kappa_0^2}P\int_0^1\frac{1-(v^2/3)}{1+(k_\mu^2/4\kappa_0^2)(1-v^2)}v^2dv$$

as the value of the integral (2.38), where $\gamma=1.781$. The insertion of this result into (2.37) yields

$$G(\lambda)=\frac{1}{48\pi^2}\log\frac{1}{\gamma w_0}\delta(x-x')+\frac{4}{(4\pi)^6}\frac{1}{\kappa_0^2}\Box^2\int_0^1\left(1-\frac{v^2}{3}\right)v^2dvP\times\int(dk)\frac{\exp(ik_\mu(x_\mu-x_\mu'))}{1+(k_\mu^2/4\kappa_0^2)(1-v^2)} \quad (2.39)$$

in which it has been noticed that the operator $\Box^2$ is equivalent to multiplication by $-k_\mu^2$ in its effect on $\exp(ik_\mu x_\mu)$, and that

$$\frac{1}{(2\pi)^4}\int\exp(ik_\mu x_\mu)(dk)=\delta(x)=\delta(x_0)\delta(x_1)\delta(x_2)\delta(x_3). \quad (2.40)$$

The Fourier integral contained in the second term of (2.39) can be recognized as related to that of the function $\bar{\Delta}(x)$ (Eq. (A.10)):

$$\bar{\Delta}(x)=\frac{1}{(2\pi)^4}P\int\frac{\exp(ik_\mu x_\mu)}{k_\mu^2+\kappa_0^2}(dk). \quad (2.41)$$

Indeed,

$$\frac{1}{(2\pi)^4}P\int\frac{\exp(ik_\mu x_\mu)}{1+(k_\mu^2/4\kappa_0^2)(1-v^2)}(dk)=\frac{16\kappa_0^2}{(1-v^2)^2}\bar{\Delta}\left(\frac{2}{(1-v^2)^{\frac{1}{2}}}x\right), \quad (2.42)$$

so that

$$G(\lambda)=\frac{1}{48\pi^2}\log\frac{1}{\gamma w_0}\delta(x-x')+\frac{1}{4\pi^2}\Box^2\int_0^1\bar{\Delta}\left(\frac{2}{(1-v^2)^{\frac{1}{2}}}(x-x')\right)\times\frac{1-\frac{1}{3}v^2}{(1-v^2)^2}v^2dv. \quad (2.43)$$

The expression for the induced current that is obtained from this form for $G(\lambda)$ is

$$\langle j_\mu(x)\rangle=-\frac{\alpha}{3\pi}\log\frac{1}{\gamma\omega_0}J_\mu(x)-\frac{4}{\pi}\alpha\int d\omega'\Box^2\times\int_0^1\bar{\Delta}\left(\frac{2}{(1-v^2)^{\frac{1}{2}}}(x-x')\right)\times\frac{1-\frac{1}{3}v^2}{(1-v^2)^2}v^2dvJ_\mu(x'), \quad (2.44)$$

where $\alpha=e^2/4\pi\hbar c$ is the fine structure constant. The current induced at a given point is thus exhibited in two parts: a logarithmically divergent multiple of the external current at that point, and a finite contribution involving the external current in the vicinity of the given point. The first part reduces the strength of the external current by a constant factor and hence produces an unobservable charge renormalization, as discussed in I. The second part of (2.44) is therefore the physically significant induced current.

An alternative form for the latter is[2]

$$\langle j_\mu(x)\rangle = -\frac{4}{\pi}\alpha\int d\omega'\int_0^1 \bar{\Delta}\left(\frac{2}{(1-v^2)^{\frac{1}{2}}}(x-x')\right) \times\frac{1-\frac{1}{3}v^2}{(1-v^2)^2}v^2dv\Box'^2 J_\mu(x'). \quad (2.45)$$

If the external current varies sufficiently slowly, the relevant unit of length being $1/\kappa_0=\hbar/m_0c$, one can obtain a series in ascending powers of $\Box^2$ applied to $J_\mu(x)$. This may be done by continued application of the relation:

$$\bar{\Delta}\left(\frac{2}{(1-v^2)^{\frac{1}{2}}}x\right)=\frac{(1-v^2)^2}{16\kappa_0^2}\delta(x) +\frac{1-v^2}{4\kappa_0^2}\Box^2\bar{\Delta}\left(\frac{2}{(1-v^2)^{\frac{1}{2}}}x\right). \quad (2.46)$$

Thus

$$\begin{aligned}\langle j_\mu(x)\rangle &= -\frac{\alpha}{15\pi}\frac{1}{\kappa_0^2}\Box^2 J_\mu(x)-\frac{\alpha}{\pi}\frac{1}{\kappa_0^2}\int d\omega' \times\int_0^1 \bar{\Delta}\left(\frac{2}{(1-v^2)^{\frac{1}{2}}}(x-x')\right) \times\frac{1-\frac{1}{3}v^2}{1-v^2}v^2dv\Box'^2\Box'^2 J_\mu(x') \\ &= -\frac{\alpha}{15\pi}\frac{1}{\kappa_0^2}\Box^2 J_\mu(x) -\frac{\alpha}{140\pi}\left(\frac{1}{\kappa_0^2}\Box^2\right)^2 J_\mu(x)-\cdots.\end{aligned} \quad (2.47)$$

If, however, the first term[3] is not an adequate approximation, the series will usually be inconvenient and recourse must be had to the original integral expression.

A particular case of importance is that of a time independent external charge or current distribution. In this situation, (2.45) can be specialized to

$$\langle j_\mu(x)\rangle = -\frac{4}{\pi}\alpha\int d\tau'\int_{-\infty}^{\infty}dx_0'\int_0^1 \times\bar{\Delta}\left(\frac{2}{(1-v^2)^{\frac{1}{2}}}(\mathbf{r}-\mathbf{r}'),\frac{2}{(1-v^2)^{\frac{1}{2}}}(x_0-x_0')\right) \times\frac{1-\frac{1}{3}v^2}{(1-v^2)^2}v^2dv\nabla'^2 J_\mu(\mathbf{r}'), \quad (2.48)$$

where $d\tau'$ here denotes a three-dimensional volume element. Now

$$G(\mathbf{r})=\int_{-\infty}^{\infty}\bar{\Delta}(\mathbf{r},x_0)dx_0 \quad (2.49)$$

obeys the differential equation

$$(\nabla^2-\kappa_0^2)G(\mathbf{r})=-\delta(\mathbf{r}) \quad (2.50)$$

and is therefore the three-dimensional Green's function:

$$G(\mathbf{r})=\frac{e^{-\kappa_0 r}}{4\pi r}. \quad (2.51)$$

Accordingly,[4]

$$\begin{aligned}\langle j_\mu(x)\rangle &= -\frac{\alpha}{4\pi^2}\int d\tau'\int_0^1 \frac{\exp\left(\frac{2\kappa_0}{(1-v^2)^{\frac{1}{2}}}|\mathbf{r}-\mathbf{r}'|\right)}{|\mathbf{r}-\mathbf{r}'|} \times\frac{1-\frac{1}{3}v^2}{1-v^2}v^2dv\nabla'^2 J_\mu(\mathbf{r}') \\ &= -\frac{\alpha}{6\pi^2}\int K(\mathbf{r}-\mathbf{r}')\nabla'^2 J_\mu(\mathbf{r}')d\tau',\end{aligned} \quad (2.52)$$

with

$$K(\mathbf{r})=\int_1^\infty \frac{e^{-2\kappa_0 r\xi}}{r}\left(1+\frac{1}{2\xi^2}\right)\frac{(\xi^2-1)^{\frac{1}{2}}}{\xi^2}d\xi. \quad (2.53)$$

We shall be content to record the asymptotic forms of $K(r)$, which can be expressed in terms of the Hankel function of imaginary argument, $K_0(2\kappa_0 r)$, and associated functions:[5]

$$\begin{aligned}K(\mathbf{r}) &= \frac{1}{r}\left(\log\frac{1}{\gamma\kappa_0 r}-\frac{5}{6}\right), \quad \kappa_0 r\ll 1 \\ K(\mathbf{r}) &= \frac{3\pi^{\frac{1}{2}}}{8}\frac{e^{-2\kappa_0 r}}{(\kappa_0 r)^{\frac{1}{2}}}, \quad \kappa_0 r\gg 1.\end{aligned} \quad (2.54)$$

[2] Formulae equivalent to (2.45) have been given by R. Serber, Phys. Rev. **48**, 49 (1935).

[3] The original discussion of the polarization of the vacuum were confined to this term. P. A. M. Dirac, 7e Conseil Solvay, 203 (1934); W. Heisenberg, Zeits. f. Physik 90, 209 (1934).

[4] An equivalent result has been derived by E. A. Uehling, Phys. Rev. **48**, 55 (1935).

[5] W. Pauli and M. E. Rose, Phys. Rev. **49**, 462 (1936).

3. THE SELF-ENERGY OF THE ELECTRON

The second problem to be treated is the modification of the matter field properties arising from its interaction with the vacuum fluctuations of the electromagnetic field. The coupling between the fields can be described in two equivalent ways; either employing the complete electromagnetic four-vector potential, together with a supplementary condition

$$i\hbar c\frac{\delta\Psi[\sigma]}{\delta\sigma(x)}=-\frac{1}{c}j_\mu(x)A_\mu(x)\Psi[\sigma], \quad (3.1a)$$

$$\left(\frac{\partial A_\mu(x)}{\partial x_\mu}-\int_\sigma D(x-x')\frac{1}{c}j_\mu(x')d\sigma_\mu'\right)\Psi[\sigma]=0, \quad (3.1b)$$

or using the transverse four-vector potential, which requires no explicit use of the supplementary condition

$$i\hbar c\frac{\delta\Psi[\sigma]}{\delta\sigma(x)}=\Bigg[-\frac{1}{c}j_\mu(x)\,\mathfrak{A}_\mu(x)-\frac{1}{c^2}\int_\sigma\left(\frac{1}{2}\frac{\partial\mathfrak{D}(x-x')}{\partial x_\mu}+n_\mu n_\nu\frac{\partial\mathfrak{D}(x-x')}{\partial x_\nu}\right)\times j_\mu(x)j_\lambda(x')d\sigma_\lambda'\Bigg]\Psi[\sigma], \quad (3.2)$$

In discussing either of these equations of motion for $\Psi[\sigma]$, we shall employ a perturbation method based on the weakness of the coupling between the two fields, as measured by the smallness of $\alpha=e^2/4\pi\hbar c=1/137$. Physical quantities will accordingly be classified as to order of magnitude, depending upon the power of e, or better $\alpha^{\frac{1}{2}}$, which they involve.

To zero order, there is no interaction between the fields, and the state vector $\Psi[\sigma]$ is constant. The first-order coupling between the two fields corresponds to the emission or absorption of a light quantum by a free electron, or in the course of creation or annihilation of a pair. It is important that all such processes are virtual; that is, in consequence of the impossibility of simultaneously satisfying energy and momentum conservation laws, a free electron cannot emit or absorb a light quantum, nor can a light quantum create a pair, or a pair annihilate with the emission of a single quantum. Hence first-order interaction effects have no direct physical significance, but only exhibit themselves to the second order in such processes as the virtual emission and subsequent absorption of a light quantum by the matter field, thus producing the interaction between different particles and the self-energy of a single particle. We shall therefore attempt to construct an equation of motion for $\Psi[\sigma]$ from which the first order interaction term has been eliminated and replaced by the second order couplings which it generates.

In order to carry out this program, we must exhibit the first-order solution of the equation of motion for $\Psi[\sigma]$. As in the discussion of vacuum polarization, the required solution, of (3.2) say, is given by

$$\Psi[\sigma]\cong\left(1+\frac{i}{\hbar c^2}\int_{-\infty}^{\sigma}j_\mu(x')\,\mathfrak{A}_\mu(x')d\omega'\right)\Psi, \quad (3.3)$$

where Ψ is the state vector in the absence of interaction. Although this solution has been chosen to fit a boundary condition as $\sigma\rightarrow-\infty$, the absence of any real first-order effect, as expressed by

$$\int_{-\infty}^{\infty}j_\mu(x)\,\mathfrak{A}_\mu(x)d\omega=0, \quad (3.4)$$

enables (3.3) to be rewritten:

$$\Psi[\sigma]\cong(1-iS[\sigma])\Psi \quad (3.5)$$
$$S[\sigma]=-\frac{1}{2\hbar c^2}\int_{-\infty}^{\infty}j_\mu(x')\,\mathfrak{A}_\mu(x')\epsilon[\sigma,\sigma']d\omega',$$

in which form there is no distinction between past and future.

The operator $1-iS[\sigma]$ is unitary only to first order. In order that the unitary property be valid to the second order, the operator can be extended to

$$1-iS[\sigma]-\tfrac{1}{2}(S[\sigma])^2, \quad (3.6)$$

which in turn may be replaced by any rigorous unitary operator that agrees with (3.6) to the desired degree of approximation. The simplest choice of such an operator is $e^{-iS[\sigma]}$. Accordingly, we introduce the state vector transformation

$$\Psi[\sigma]\rightarrow e^{-iS[\sigma]}\Psi[\sigma] \quad (3.7)$$

in which the new state vector varies only in response to second-order interactions. The new equation of motion, replacing (3.2), is

$$ihc\frac{\delta\Psi[\sigma]}{\delta\sigma(x)}+ihce^{iS[\sigma]}\frac{\delta e^{-iS[\sigma]}}{\delta\sigma(x)}\Psi[\sigma]$$
$$=\Big[-e^{iS[\sigma]}\frac{1}{c}j_\mu(x)\,\mathfrak{A}_\mu(x)e^{-iS[\sigma]}$$
$$-\frac{1}{c^2}\int_\sigma\Big(\frac{1}{2}\frac{\partial\mathfrak{D}(x-x')}{\partial x_\mu}+n_\mu n_\nu\frac{\partial\mathfrak{D}(x-x')}{\partial x_\nu}\Big)$$
$$\times j_\mu(x)j_\lambda(x')d\sigma_\lambda'\Big]\Psi[\sigma],\quad(3.8)$$

in which corrections to the generalized Coulomb term have been discarded, since we shall consistently retain only second-order terms. We are required to evaluate

$$e^{iS[\sigma]}\frac{\delta e^{-iS[\sigma]}}{\delta\sigma(x)}=-i\frac{\delta S[\sigma]}{\delta\sigma(x)}$$
$$+\frac{1}{2}\Big[S[\sigma],\frac{\delta S[\sigma]}{\delta\sigma(x)}\Big]+\cdots\quad(3.9)$$

and

$$e^{iS[\sigma]}j_\mu(x)\,\mathfrak{A}_\mu(x)e^{-iS[\sigma]}=j_\mu(x)\,\mathfrak{A}_\mu(x)$$
$$+i[S[\sigma],j_\mu(x)\,\mathfrak{A}_\mu(x)]+\cdots.\quad(3.10)$$

Now $S[\sigma]$, as defined in (3.5), satisfies the equation of motion

$$\hbar c\frac{\delta S[\sigma]}{\delta\sigma(x)}=-\frac{1}{c}j_\mu(x)\,\mathfrak{A}_\mu(x),\quad(3.11)$$

whence

$$ihce^{iS[\sigma]}\frac{\delta e^{-iS[\sigma]}}{\delta\sigma(x)}+e^{iS[\sigma]}\frac{1}{c}j_\mu(x)\,\mathfrak{A}_\mu(x)e^{-iS[\sigma]}$$
$$=\frac{i}{2}\Big[S[\sigma]\frac{1}{c}j_\mu(x)\,\mathfrak{A}_\mu(x)\Big]$$
$$=\frac{i}{4\hbar c^3}\int_{-\infty}^{\infty}[j_\mu(x)\,\mathfrak{A}_\mu(x),j_\nu(x')\,\mathfrak{A}_\nu(x')]$$
$$\times\epsilon[\sigma,\sigma']d\omega',\quad(3.12)$$

and

$$ihc\frac{\delta\Psi[\sigma]}{\delta\sigma(x)}=\Big[-\frac{i}{4\hbar c^3}\int[j_\mu(x)\,\mathfrak{A}_\mu(x),$$
$$j_\nu(x')\,\mathfrak{A}_\nu(x')]\epsilon[\sigma,\sigma']d\omega'$$
$$-\frac{1}{c^2}\int_\sigma\Big(\frac{1}{2}\frac{\partial\mathfrak{D}(x-x')}{\partial x_\mu}+n_\mu n_\nu\frac{\partial\mathfrak{D}(x-x')}{\partial x_\nu}\Big)$$
$$\times j_\mu(x)j_\lambda(x')d\sigma_\lambda'\Big]\Psi[\sigma].\quad(3.13)$$

The same operations can be carried out with Eq. (3.1a); in particular, the functional $S[\sigma]$ occurring in the unitary transformation (3.7) has the same form as in (3.5), but with $A_\mu(x)$ replacing $\mathfrak{A}_\mu(x)$. The result of the transformation is, evidently,

$$ihc\frac{\delta\Psi[\sigma]}{\delta\sigma(x)}=\Big[-\frac{i}{4\hbar c^3}\int[j_\mu(x)A_\mu(x),j_\nu(x')A_\nu(x')]$$
$$\times\epsilon(x-x')d\omega'\Big]\Psi[\sigma].\quad(3.14)$$

However, we must also consider the supplementary condition (3.1b), which becomes:

$$\Big[e^{iS[\sigma]}\frac{\partial A_\mu(x)}{\partial x_\mu}e^{-iS[\sigma]}-\frac{1}{c}\int_\sigma D(x-x')e^{iS[\sigma]}$$
$$\times j_\mu(x')e^{-iS[\sigma]}d\sigma_\mu'\Big]\Psi[\sigma]=0.\quad(3.15)$$

In order to simplify

$$e^{iS[\sigma]}\frac{\partial A_\mu(x)}{\partial x_\mu}e^{-iS[\sigma]}=\frac{\partial A_\mu(x)}{\partial x_\mu}+i\Big[S[\sigma],\frac{\partial A_\mu(x)}{\partial x_\mu}\Big]$$
$$-\frac{1}{2}\Big[S[\sigma],\Big[S[\sigma],\frac{\partial A_\mu(x)}{\partial x_\mu}\Big]\Big]+\cdots,$$

observe that

$$i\Big[S[\sigma],\frac{\partial A_\mu(x)}{\partial x_\mu}\Big]$$
$$=\frac{i}{2\hbar c^2}\int\Big[\frac{\partial A_\mu(x)}{\partial x_\mu},A_\nu(x')\Big]j_\nu(x')\epsilon(x-x')d\omega'$$
$$=\frac{1}{2c}\int\frac{\partial}{\partial x_\nu'}(D(x-x')j_\nu(x'))\epsilon(x-x')d\omega'$$
$$=\frac{1}{c}\int_\sigma D(x-x')j_\nu(x')d\sigma_\nu'.\quad(3.16)$$

The first-order terms are thereby removed from the supplementary condition, which now reads

$$\left[\frac{\partial A_\mu(x)}{\partial x_\mu}-\frac{i}{4\hbar c^3}\int_\sigma d\sigma_\mu'\int d\omega'' D(x-x')\right.$$
$$\left.\times[j_\mu(x'),j_\nu(x'')]A_\nu(x'')\epsilon[\sigma,\sigma'']\right]\Psi[\sigma]=0. \quad (3.17)$$

The commutator contained in (3.14) can be simplified in the following manner:

$$\begin{aligned}&[j_\mu(x)A_\mu(x),\ j_\nu(x')A_\nu(x')]\\&=\tfrac{1}{2}[A_\mu(x),\ A_\nu(x')]\{j_\mu(x),\ j_\nu(x')\}\\&\quad+\tfrac{1}{2}[j_\mu(x),\ j_\nu(x')]\{A_\mu(x),\ A_\nu(x')\}\\&=\frac{ihc}{2}\delta_{\mu\nu}D(x-x')\{j_\mu(x),\ j_\nu(x')\}\\&\quad+\tfrac{1}{2}[j_\mu(x),\ j_\nu(x')]\{A_\mu(x),\ A_\nu(x')\},\end{aligned} \quad (3.18)$$

which brings the equation of motion into the form

$$\begin{aligned}ihc\frac{\delta\Psi[\sigma]}{\delta\sigma(x)}=\Big[&-\frac{1}{4c^2}\int\{j_\mu(x),\ j_\mu(x')\}\bar{D}(x-x')d\omega'\\&-\frac{i}{8\hbar c^3}\int[j_\mu(x),\ j_\nu(x')]\{A_\mu(x),\ A_\nu(x')\}\\&\times\epsilon(x-x')d\omega'\Big]\Psi[\sigma].\end{aligned} \quad (3.19)$$

Both terms have an elementary interpretation, describing the self-action of each field through the intermediary of the other field. First note that the operator replacing $A_\mu(x)$, in consequence of the state vector transformation, is

$$\begin{aligned}&e^{iS[\sigma]}A_\mu(x)e^{-iS[\sigma]}\\&=A_\mu(x)+i[S[\sigma],\ A_\mu(x)]+\cdots\\&=A_\mu(x)+\frac{1}{c}\int\bar{D}(x-x')j_\mu(x')d\omega'+\cdots.\end{aligned} \quad (3.20)$$

The additional term thus produced,

$$\delta A_\mu(x)=\frac{1}{c}\int\bar{D}(x-x')j_\mu(x')d\omega', \quad (3.21)$$

represents the electromagnetic field induced by the current in virtue of the first-order coupling. This potential satisfies

$$\begin{aligned}&\Box^2\delta A_\mu(x)=-\frac{1}{c}j_\mu(x),\\&\frac{\partial}{\partial x_\mu}\delta A_\mu(x)=0,\end{aligned} \quad (3.22)$$

and is simply half the sum of advanced and retarded potentials classically ascribed to the current distribution $j_\mu(x)$. Similarly,

$$\begin{aligned}e^{iS[\sigma]}j_\mu(x)e^{-iS[\sigma]}&=j_\mu(x)+i[S[\sigma],\ j_\mu(x)]+\cdots\\&=j_\mu(x)+\delta j_\mu(x)\end{aligned} \quad (3.23)$$

where

$$\delta j_\mu(x)=\frac{i}{2\hbar c^2}\int[j_\mu(x),\ j_\nu(x')]A_\nu(x')\times\epsilon(x-x')d\omega' \quad (3.24)$$

is the current induced by the electromagnetic field. It is the vacuum expectation value of this current that was considered in the previous section. We now observe that (3.19) may be written

$$\begin{aligned}ihc\frac{\delta\Psi[\sigma]}{\delta\sigma(x)}=\Big[&-\frac{1}{4c}\{j_\mu(x),\ \delta A_\mu(x)\}\\&-\frac{1}{4c}\{\delta j_\mu(x),\ A_\mu(x)\}\Big]\Psi[\sigma],\end{aligned} \quad (3.25)$$

in which the two terms evidently represent the interaction of the current with the electromagnetic field generated by the current, and of the electromagnetic field with the current induced by the field. The factor of $\frac{1}{2}$ (other than the $\frac{1}{2}$ accompanying the symmetrization of the products) is that inevitably associated with the self-action of a system.

The equation of motion (3.13) can be given an analogous interpretation except that the interaction between the current and the field generated by the current occurs in two parts, associated with the transverse and longitudinal potentials of the current distribution. However, this more involved representation of the field differs from (3.21) only by a gauge transformation. The transverse potential induced by the

current is

$$\delta\mathfrak{A}_\mu(x)=\frac{i}{2\hbar c^2}\int[\mathfrak{A}_\mu(x),\ \mathfrak{A}_\nu(x')]j_\nu(x')\epsilon[\sigma,\sigma']d\omega'$$

$$=\frac{1}{c}\int\bar{D}(x-x')j_\mu(x')d\omega'$$

$$+\frac{1}{2c}\int\left[\frac{\partial}{\partial x_\mu}\frac{\partial}{\partial x_\nu}+\left(n_\mu\frac{\partial}{\partial x_\nu}\right.\right.$$

$$\left.\left.+n_\nu\frac{\partial}{\partial x_\mu}\right)n_\lambda\frac{\partial}{\partial x_\lambda}\right]\mathfrak{D}(x-x')$$

$$\times j_\nu(x')\epsilon[\sigma,\sigma']d\omega'. \quad (3.26)$$

Now

$$\frac{1}{2}\int\left[\frac{\partial}{\partial x_\mu}\frac{\partial}{\partial x_\nu}+n_\mu\frac{\partial}{\partial x_\nu}n_\lambda\frac{\partial}{\partial x_\lambda}\right]$$

$$\times\mathfrak{D}(x-x')j_\nu(x')\epsilon[\sigma,\sigma']d\omega'$$

$$=-\frac{1}{2}\int\frac{\partial}{\partial x_\nu'}\left[\left(\frac{\partial}{\partial x_\mu}+n_\mu n_\lambda\frac{\partial}{\partial x_\lambda}\right)\right.$$

$$\left.\times\mathfrak{D}(x-x')j_\nu(x')\right]\epsilon[\sigma,\sigma']d\omega' \quad (3.27)$$

$$=-\int_\sigma\left(\frac{\partial}{\partial x_\mu}+n_\mu n_\nu\frac{\partial}{\partial x_\nu}\right)\mathfrak{D}(x-x')j_\lambda(x')d\sigma_\lambda',$$

and

$$\frac{1}{2}\int n_\nu\frac{\partial}{\partial x_\mu}n_\lambda\frac{\partial}{\partial x_\lambda}\mathfrak{D}(x-x')j_\nu(x')\epsilon[\sigma,\sigma']d\omega'$$

$$=\frac{\partial}{\partial x_\mu}\left[\frac{1}{2}\int n_\lambda\frac{\partial}{\partial x_\lambda}\mathfrak{D}(x-x')n_\nu j_\nu(x')\epsilon[\sigma,\sigma']d\omega'\right]$$

$$+\frac{1}{2}\int n_\lambda\frac{\partial}{\partial x_\lambda}\mathfrak{D}(x-x')j_\nu(x')n_\nu\frac{\partial}{\partial x_\mu'}$$

$$\times\epsilon[\sigma,\sigma']d\omega'. \quad (3.28)$$

It is a consequence of the time-like nature of the gradient of $\epsilon[\sigma,\sigma']$ that

$$n_\nu\frac{\partial}{\partial x_\mu'}\epsilon[\sigma,\sigma']=n_\mu\frac{\partial}{\partial x_\nu'}\epsilon[\sigma,\sigma'],$$

whence the second term of the right side of (3.28) becomes

$$-\int_\sigma n_\mu n_\nu\frac{\partial}{\partial x_\nu}\mathfrak{D}(x-x')j_\lambda(x')d\sigma_\lambda'.$$

Hence,

$$\delta\mathfrak{A}_\mu(x)=\delta A_\mu(x)-\frac{1}{c}\int_\sigma\left(\frac{\partial}{\partial x_\mu}+n_\mu n_\nu\frac{\partial}{\partial x_\nu}\right)$$

$$\times\mathfrak{D}(x-x')j_\lambda(x')d\sigma_\lambda'$$

$$+\frac{\partial}{\partial x_\mu}\left[\frac{1}{2}\int n_\lambda\frac{\partial}{\partial x_\lambda}\mathfrak{D}(x-x')\right.$$

$$\left.\times n_\nu j_\nu(x')\epsilon[\sigma,\sigma']d\omega'\right]. \quad (3.29)$$

The gradient term can be completely eliminated, in the approximation of retaining only second order quantities, by a suitable gauge transformation on the state vector. The second term of $\delta\mathfrak{A}_\mu(x)$ exactly cancels the Coulomb coupling expression, and we are left with

$$i\hbar c\frac{\delta\Psi[\sigma]}{\delta\sigma(x)}=\left[-\frac{1}{4c}\{j_\mu(x),\ \delta A_\mu(x)\}\right.$$

$$\left.-\frac{1}{4c}\{\delta j_\mu(x),\ \mathfrak{A}_\mu(x)\}\right]\Psi[\sigma] \quad (3.30)$$

as the simplified form of (3.13). Here $\delta j_\mu(x)$ is given by (3.24) but with $\mathfrak{A}_\mu(x)$ replacing $A_\mu(x)$. It will be evident from this discussion that the separate consideration of longitudinal and transverse fields is an inadvisable complication in the treatment of virtual light quantum processes.

The current induced by the electromagnetic field is naturally divided into two parts, that existing in the absence of any charged particles,

$$(\delta j_\mu(x))_0=\frac{i}{2\hbar c^2}\int\langle[j_\mu(x),\ j_\nu(x')]\rangle_0$$

$$\times\mathfrak{A}_\nu(x')\epsilon[\sigma,\sigma']d\omega', \quad (3.31)$$

and that specifically associated with the presence of matter,

$$(\delta j_\mu(x))_1=\frac{i}{2\hbar c^2}\int\{[j_\mu(x),\ j_\nu(x')]$$

$$-\langle[j_\mu(x),\ j_\nu(x')]\rangle_0\}\mathfrak{A}_\nu(x')\epsilon[\sigma,\sigma']d\omega'. \quad (3.32)$$

Were the vacuum induced current different from zero, Eq. (3.30) would contain a term

describing modifications in the properties of the electromagnetic field, without the presence of charged particles.[6] Such a light quantum self-energy effect does not in fact exist, since no current is induced in the vacuum by a light wave, as we have shown in the previous section. However, note that while

$$\Box^2 \mathfrak{A}_\mu(x) - \frac{\partial}{\partial x_\mu}\left(\frac{\partial \mathfrak{A}_\nu(x)}{\partial x_\nu}\right) = 0,$$

as required in the proof, further discussion is required for $A_\mu(x)$, since the supplementary condition is involved in the treatment of $\partial A_\mu(x)/\partial x_\mu$. Now

$$\begin{aligned}
&\{(\delta j_\mu(x))_0, A_\mu(x)\}\Psi[\sigma] \\
&= \frac{i}{2\hbar c^2}\int \langle [j_\mu(x), j_\nu(x')]\rangle_0 [A_\mu(x)A_\nu(x') \\
&\qquad + A_\nu(x')A_\mu(x)]\epsilon(x-x')d\omega'\Psi[\sigma] \\
&= \frac{i}{\hbar c^2}A_\mu(x)\int \langle [j_\mu(x), j_\nu(x')]\rangle_0 \\
&\qquad \times A_\nu(x')\epsilon(x-x')d\omega'\Psi[\sigma] \\
&\quad + \frac{1}{2c}\int \langle [j_\mu(x), j_\mu(x')]\rangle_0 \epsilon(x-x') \\
&\qquad \times D(x-x')d\omega'\Psi[\sigma]. \qquad (3.33)
\end{aligned}$$

In the first term on the right side of Eq. (3.33), $\partial A_\nu(x')/\partial x_\nu'$ operates directly on $\Psi[\sigma]$, permitting the supplementary condition (3.17) to be invoked and is effectively equal to zero since a fourth order quantity is to be neglected. The second term of (3.33) also vanishes since $\langle [j_\mu(x), j_\mu(x')]\rangle_0 \epsilon(x-x')$ is an even function, while $D(x-x')$ is an odd function of $x-x'$. Therefore,

$$\{(\delta j_\mu(x))_0, A_\mu(x)\}\Psi[\sigma] = 0. \qquad (3.34)$$

It is convenient to divide the interaction of the electromagnetic field with the current that it induces,

$$\begin{aligned}
-\frac{1}{4c}\{(\delta j_\mu(x))_1, \mathfrak{A}_\mu(x)\} &= -\frac{i}{8\hbar c^3}\int [j_\mu(x), j_\nu(x')]_1 \\
&\times \{\mathfrak{A}_\mu(x), \mathfrak{A}_\nu(x')\}\epsilon(x-x')d\omega', \qquad (3.35)
\end{aligned}$$

into two parts, of which one is associated with the vacuum fluctuations of the electromagnetic field,

$$\begin{aligned}
-\frac{1}{4c}\{(\delta j_\mu(x))_1, \mathfrak{A}_\mu(x)\}_0 &= -\frac{i}{8\hbar c^3}\int [j_\mu(x), j_\nu(x')]_1 \\
&\times \langle\{\mathfrak{A}_\mu(x), \mathfrak{A}_\nu(x')\}\rangle_0 \epsilon(x-x')d\omega', \qquad (3.36)
\end{aligned}$$

and the other exists only in the presence of actual light quanta:

$$\begin{aligned}
-\frac{1}{4c}\{(\delta j_\mu(x))_1, \mathfrak{A}_\mu(x)\}_1 &= -\frac{i}{8\hbar c^3}\int [j_\mu(x), j_\nu(x')]_1 \\
&\times \{\mathfrak{A}_\mu(x), \mathfrak{A}_\nu(x')\}_1 \epsilon(x-x')d\omega'. \qquad (3.37)
\end{aligned}$$

In these formulae, the subscript one indicates the difference between the quantity and its vacuum expectation value. The second part of the interaction, Eq. (3.37), describes the real coupling between matter and radiation, as exhibited in such processes as the scattering of a light quantum by an electron, and the two quantum annihilation of an electron-position pair. The first part, Eq. (3.36), contains only the dynamical variables of the matter field and constitutes a portion of the electron self-energy.

A similar decomposition can be performed with

$$\begin{aligned}
-\frac{1}{4c}\{(\delta j_\mu(x))_1, A_\mu(x)\} &= -\frac{i}{8\hbar c^2}\int [j_\mu(x), j_\nu(x')]_1 \\
&\times \{A_\mu(x), A_\nu(x')\}\epsilon(x-x')d\omega' \qquad (3.38)
\end{aligned}$$

except that the definition of the vacuum for the field described by $A_\mu(x)$ requires a slight discussion. Evidently a statement concerning the vacuum state of the longitudinal fields is meaningless since these fields are completely eliminated by the supplementary condition. However, it is certainly permissible to adopt a conventional definition that unifies the treatment of the longitudinal and transverse fields, with the full knowledge that the eventual elimination of the longitudinal fields will deprive the particular convention of any physical content. For this reason, the definition of the vacuum (1.34) may be extended by the conventions

$$\Lambda^{(+)}(x)\Psi_0 = 0, \quad \Lambda'^{(+)}(x)\Psi_0 = 0, \qquad (3.39)$$

thus yielding

$$A_\mu{}^{(+)}(x)\Psi_0 = 0 \qquad (3.40)$$

[6] A logarithmically divergent term of this type was obtained by W. Heisenberg (see reference 3).

as the natural definition of the vacuum in a treatment that employs the complete four-vector potential. Expectation values of quadratic forms can be computed as before:

$$\begin{aligned}\langle A_\mu(x)A_\nu(x')+A_\nu(x')A_\mu(x)\rangle_0 &\\ =-i[A_\mu^{(1)}(x),\, A_\nu(x')] &\\ =\hbar c\delta_{\mu\nu}D^{(1)}(x-x').&\end{aligned} \tag{3.41}$$

In particular,

$$-\frac{1}{4c}\{(\delta j_\mu(x))_1,\, A_\mu(x)\}_0=-\frac{i}{8c^2}\int[j_\mu(x),\, j_\mu(x')]_1 \times\epsilon(x-x')D^{(1)}(x-x')d\omega'. \tag{3.42}$$

That nothing of a physical nature has been added by adopting the vacuum definition (3.40) can be made more convincing by proving the equivalence, to within a gauge transformation, of the two expressions (3.36) and (3.42), involving their respective definitions of the vacuum. Now

$$\begin{aligned}-\frac{1}{4c}\{(\delta j_\mu(x))_1,\, \mathfrak{A}_\mu(x)\}_0&=-\frac{1}{4c}\{(\delta j_\mu(x))_1,\, A_\mu(x)\}_0\\ &+\frac{i}{8c^2}\int[j_\mu(x),\, j_\nu(x')]_1\left(\frac{\partial}{\partial x_\mu}\frac{\partial}{\partial x_\nu}\right.\\ &\left.+\left(n_\mu\frac{\partial}{\partial x_\nu}+n_\nu\frac{\partial}{\partial x_\mu}\right)n_\lambda\frac{\partial}{\partial x_\lambda}\right)\\ &\times\mathfrak{D}^{(1)}(x-x')\epsilon(x-x')d\omega',\end{aligned} \tag{3.43}$$

and

$$\begin{aligned}&\frac{1}{2}\int[j_\mu(x),\, j_\nu(x')]_1\left(\frac{\partial}{\partial x_\mu}\frac{\partial}{\partial x_\nu}+n_\mu\frac{\partial}{\partial x_\nu}n_\lambda\frac{\partial}{\partial x_\lambda}\right)\\ &\qquad\times\mathfrak{D}^{(1)}(x-x')\epsilon(x-x')d\omega'\\ &=-\frac{1}{2}\int\frac{\partial}{\partial x_\nu'}\left\{[j_\mu(x),\, j_\nu(x')]_1\left(\frac{\partial}{\partial x_\mu}+n_\mu n_\lambda\frac{\partial}{\partial x_\lambda}\right)\right.\\ &\qquad\left.\times\mathfrak{D}^{(1)}(x-x')\right\}\epsilon(x-x')d\omega'\\ &=-\int_\sigma\left(\frac{\partial}{\partial x_\mu}+n_\mu n_\lambda\frac{\partial}{\partial x_\lambda}\right)\mathfrak{D}^{(1)}(x-x')\\ &\qquad\times[j_\mu(x),\, j_\nu(x')]_1d\sigma_\nu'=0,\end{aligned}$$

while

$$\begin{aligned}&\frac{1}{2}\int[j_\mu(x),\, j_\nu(x')]_1\left(n_\nu\frac{\partial}{\partial x_\mu}n_\lambda\frac{\partial}{\partial x_\lambda}\right)\\ &\qquad\times\mathfrak{D}^{(1)}(x-x')\epsilon(x-x')d\omega'\\ &=\frac{\partial}{\partial x_\mu}\left[\frac{1}{2}\int[j_\mu(x),\, j_\nu(x')]_1n_\nu n_\lambda\frac{\partial}{\partial x_\lambda}\right.\\ &\qquad\left.\times\mathfrak{D}^{(1)}(x-x')\epsilon(x-x')d\omega'\right],\end{aligned} \tag{3.44}$$

since

$$\begin{aligned}&\frac{1}{2}\int[j_\mu(x),\, j_\nu(x')]_1n_\lambda\frac{\partial}{\partial x_\lambda}\\ &\qquad\times\mathfrak{D}^{(1)}(x-x')n_\nu\frac{\partial}{\partial x_\mu'}\epsilon(x-x')d\omega'\\ &=\frac{1}{2}\int[j_\mu(x),\, j_\nu(x')]_1n_\lambda\frac{\partial}{\partial x_\lambda}\\ &\qquad\times\mathfrak{D}^{(1)}(x-x')n_\mu\frac{\partial}{\partial x_\nu'}\epsilon(x-x')d\omega'\\ &=-\int_\sigma n_\lambda\frac{\partial}{\partial x_\lambda}\mathfrak{D}^{(1)}(x-x')n_\mu[j_\mu(x),\, j_\nu(x')]_1d\sigma_\nu'\\ &=0.\end{aligned} \tag{3.45}$$

Therefore,

$$\begin{aligned}-\frac{1}{4c}\{(\delta j_\mu(x))_1,\, \mathfrak{A}_\mu(x)\}_0&\\ =-\frac{1}{4c}\{(\delta j_\mu(x))_1,\, A_\mu(x)\}_0&\\ +\frac{\partial}{\partial x_\mu}\left[\frac{i}{8c^2}\int[j_\mu(x),\, j_\nu(x')]_1n_\nu n_\lambda\frac{\partial}{\partial x_\lambda}\right.&\\ \left.\times\mathfrak{D}^{(1)}(x-x')\epsilon(x-x')d\omega'\right],&\end{aligned} \tag{3.46}$$

which establishes the stated equivalence.

The elimination of the first-order terms in (3.1) and (3.2) has thus resulted in the following

equations for the new state vectors:

$$i\hbar c\frac{\delta\Psi[\sigma]}{\delta\sigma(x)}=\Big[-\frac{1}{4c}\{j_\mu(x),\,\delta A_\mu(x)\}$$
$$-\frac{1}{4c}\{(\delta j_\mu(x))_1,\,A_\mu(x)\}_0$$
$$-\frac{1}{4c}\{(\delta j_\mu(x))_1,\,A_\mu(x)\}_1\Big]\Psi[\sigma],\quad(3.47a)$$

$$\Big[\frac{\partial A_\mu(x)}{\partial x_\mu}-\frac{1}{2c}\int_\sigma D(x-x')(\delta j_\mu(x'))_1 d\sigma_\mu'\Big]$$
$$\times\Psi[\sigma]=0,\quad(3.47b)$$

and

$$i\hbar c\frac{\delta\Psi[\sigma]}{\delta\sigma(x)}=\Big[-\frac{1}{4c}\{j_\mu(x),\,\delta A_\mu(x)\}$$
$$-\frac{1}{4c}\{(\delta j_\mu(x))_1,\,A_\mu(x)\}_0$$
$$-\frac{1}{4c}\{(\delta j_\mu(x))_1,\,\mathcal{A}_\mu(x)\}_1\Big]\Psi[\sigma].\quad(3.48)$$

The matter interaction terms in (3.47a) have been obtained in a natural and direct manner, while the same quantities in (3.48) have resulted from rather elaborate operations designed to unite the longitudinal and transverse field contributions. On the other hand, the elimination of the longitudinal fields has yet to be performed in (3.47a), while the term describing radiation processes in (3.48) requires no further manipulation. To complete the picture of these alternative procedures for dealing with second-order effects, we shall carry out the elimination of the longitudinal field in (3.47a), thus finally performing the process that has already been incorporated in (3.2) and its successor, (3.48).

We first observe that

$$-\frac{1}{4c}\{(\delta j_\mu(x))_1,\,A_\mu(x)\}=-\frac{1}{4c}\{(\delta j_\mu(x))_1,\,\mathcal{A}_\mu(x)\}$$
$$-\frac{1}{4c}n_\mu\Big\{(\delta j_\mu(x))_1,\,n_\nu\frac{\partial}{\partial x_\nu}(\Lambda(x)-\Lambda'(x))\Big\}$$
$$+\frac{\partial}{\partial x_\mu}\frac{1}{4c}\{(\delta j_\mu(x))_1,\,\Lambda'(x)\},\quad(3.49)$$

of which the last term can be eliminated by the canonical transformation

$$\Psi[\sigma]\rightarrow e^{-iG'[\sigma]}\Psi[\sigma],$$
$$G'[\sigma]=\frac{1}{4\hbar c^2}\int_\sigma\{(\delta j_\mu(x))_1,\,\Lambda'(x)\}d\sigma_\mu\quad(3.50)$$

in analogy with (I, 3.19, 3.20). However, the elimination is only to the required second order since the commutation properties of $\delta j_\mu(x)$ are unlike those of $j_\mu(x)$ in the situation cited. The new supplementary condition, correct to the second order, is

$$\Big[\Lambda(x)-\Lambda'(x)+i[G'[\sigma],\,(\Lambda(x)-\Lambda'(x))]$$
$$-\frac{1}{2c}\int_\sigma\mathfrak{D}(x-x')(\delta j_\mu(x'))_1 d\sigma_\mu'\Big]\Psi[\sigma]=0.\quad(3.51)$$

Happily, $\delta j_\mu(x)$ does commute with $\Lambda(x)-\Lambda'(x)$, which is all that is required in order that the new supplementary condition be simply:

$$[\Lambda(x)-\Lambda'(x)]\Psi[\sigma]=0,\quad(3.52)$$

as in (I, 3.26). To verify the stated commutation law, note that

$$\delta j_\mu(x)=\frac{i}{2\hbar c^2}\int[j_\mu(x),\,j_\nu(x')]\epsilon(x-x')$$
$$\times\Big\{\mathcal{A}_\nu(x')+n_\nu n_\lambda\frac{\partial}{\partial x_\lambda'}(\Lambda(x')-\Lambda'(x'))\Big\},\quad(3.53)$$

in which the omitted $\partial\Lambda'(x')/\partial x_\nu'$ term is easily shown to give no contribution. The proof is completed by remarking that there is a vanishing commutator for $\Lambda(x)-\Lambda'(x)$ at two different points. The new form of the supplementary condition ensures that the second term on the right side of (3.49) does not contribute to the state vector equation of motion. Furthermore, the supplementary condition reduces the expression for the current induced by $A_\mu(x)$, (3.53), to that induced by $\mathcal{A}_\mu(x)$. We have thereby demonstrated that the elimination of the longitudinal fields in (3.47a) yields (3.48).

The coupling of the matter field with itself includes both the interaction of different par-

ticles and the self-action of individual particles. Our next task is the separation of the matter interaction terms into these component parts. The basis for such a decomposition in to what may be called one particle and two particle terms lies in the interpretation of the spinors describing the matter field as particle creation and annihilation operators. The operator commutation law

$$[\psi(x), Q] = ie\int_\sigma [\psi(x), (\bar{\psi}(x')\gamma_\mu)_\alpha]\psi_\alpha(x')d\sigma_\mu' \quad (3.54)$$
$$= e\psi(x),$$

when applied to an eigenstate of total charge, $\Psi(Q')$, states that

$$Q\psi(x)\Psi(Q') = (Q'-e)\psi(x)\Psi(Q'). \quad (3.55)$$

Evidently $\psi(x)$ acts as an operator decreasing the charge of the system by e and therefore either annihilates a particle of charge e, or creates a particle of charge $-e$. Similarly, $\psi'(x)$ or $\bar{\psi}(x)$ either creates a particle of charge e or destroys a particle of charge $-e$. Quantities of the typical form $\bar{\psi}\psi$ consequently induce such effects as the annihilation of a particle in one state and the creation of a similar particle in another state, which can be viewed as the transition of particle between the two states. Such quantities may be called one particle operators, although the nomenclature is only strictly accurate when the vacuum expectation value of $\bar{\psi}\psi$ is subtracted. The latter arises from the creation and subsequent annihilation of particles of charge $-e$, occurring in the absence of matter as a vacuum fluctuation. The more complicated operators of the type $\bar{\psi}\psi\bar{\psi}\psi$ induce a variety of effects including the annihilation of two particles and creation of two others in different states, which is to be regarded as the transition of a pair of particles from one set of states to another. Such two-particle effects are to be distinguished from phenomena in which one particle makes a transition while another is created and then destroyed. This one-particle transition coupled with a vacuum fluctuation is observationally indistinguishable from the simple one particle effects previously mentioned. Of course, $\bar{\psi}\psi\bar{\psi}\psi$ also produces phenomena in the vacuum, in which both transitions are vacuum fluctuations. It is in this way, by successively restricting the possible transitions to be vacuum fluctuations, that $\bar{\psi}\psi\bar{\psi}\psi$, and more general expressions, can be decomposed into operators associated with various numbers of particles.

The operator to which we shall apply this decomposition is

$$\{j_\mu(x), j_\nu(x')\} = -e^2c^2\{\tfrac{1}{2}[\bar{\psi}(x)\gamma_\mu, \psi(x)], \times\tfrac{1}{2}[\bar{\psi}(x')\gamma_\nu, \psi(x')]\}. \quad (3.56)$$

In order to evaluate its vacuum expectation value, it is merely necessary to replace the bilinear products $\bar{\psi}\psi$ and $\psi\bar{\psi}$, in all possible combinations, by their vacuum expectation values. However, since $j_\mu(x)$ and $j_\nu(x')$ have a vanishing vacuum expectation value, it is only products of the type $\bar{\psi}(x)\psi(x')$, $\bar{\psi}(x')\psi(x)$, $\psi(x)\bar{\psi}(x')$ and $\psi(x')\bar{\psi}(x)$ that need be included. To discuss one term in detail, consider

$$(\gamma_\mu)_{\alpha\beta}(\gamma_\nu)_{\gamma\delta}\bar{\psi}_\alpha(x)\psi_\beta(x)\bar{\psi}_\gamma(x')\psi_\delta(x'). \quad (3.57)$$

The operator $\psi_\delta(x')$, acting on the vacuum state vector, produces a particle of charge $-e$ (an electron, say). The effect of $\bar{\psi}_\gamma(x')$ can be to immediately annihilate this particle, but, for the reason mentioned above, such a term would be cancelled on considering the second part of the expression for $j_\nu(x')$. Thus, the essential result produced by $\bar{\psi}_\gamma(x')$ will be the creation of a particle with charge e (positron). The remaining two operators must destroy the electron and positron that have been created in order that we deal with a vacuum effect. Hence $\psi_\beta(x)$ must annihilate the particle generated by $\bar{\psi}_\gamma(x')$, which effectively replaces $\psi_\beta(x)\bar{\psi}_\gamma(x')$ by its vacuum expectation value. Finally, $\bar{\psi}_\alpha(x)$ must destroy the electron created by $\psi_\delta(x')$, thus replacing the product $\bar{\psi}_\alpha(x)\psi_\delta(x')$ by its vacuum expectation value. There is no difficulty in associating $\bar{\psi}_\alpha(x)$ with $\psi_\delta(x')$, despite the two intervening operators, since $\bar{\psi}_\alpha(x)$ effectively anticommutes with both operators, acting as it does on a different particle from those affected by the operator product $\psi_\beta(x)\bar{\psi}_\gamma(x')$. Therefore, the vacuum expectation value of (3.57) is

$$(\gamma_\mu)_{\alpha\beta}(\gamma_\nu)_{\gamma\delta}\langle\bar{\psi}_\alpha(x)\psi_\delta(x')\rangle_0\langle\psi_\beta(x)\bar{\psi}_\gamma(x')\rangle_0. \quad (3.58)$$

But

$$\langle\psi_\beta(x)\bar{\psi}_\gamma(x')\rangle_0=\tfrac{1}{2}\{\psi_\beta(x),\bar{\psi}_\gamma(x')\}+\tfrac{1}{2}\langle[\psi_\beta(x),\bar{\psi}_\gamma(x')]\rangle_0$$
$$=-\frac{i}{2}S_{\beta\gamma}(x-x')-\tfrac{1}{2}S_{\beta\gamma}{}^{(1)}(x-x')$$
$$=-iS_{\beta\gamma}{}^{(+)}(x-x'), \tag{3.59}$$

and

$$\langle\bar{\psi}_\alpha(x)\psi_\delta(x')\rangle_0=-iS_{\delta\alpha}(x'-x)-\langle\psi_\delta(x'),\bar{\psi}_\alpha(x)\rangle_0$$
$$=-iS_{\delta\alpha}(x'-x)+iS_{\delta\alpha}{}^{(+)}(x'-x)$$
$$=-iS_{\delta\alpha}{}^{(-)}(x'-x), \tag{3.60}$$

whence (3.58) becomes

$$-Tr[\gamma_\mu S^{(+)}(x-x')\gamma_\nu S^{(-)}(x'-x)]. \tag{3.61}$$

Continuing in this manner, we find that

$$\{j_\mu(x),j_\nu(x')\}_0$$
$$=e^2c^2Tr[\gamma_\mu S^{(+)}(x-x')\gamma_\nu S^{(-)}(x'-x)+\gamma_\mu S^{(-)}(x-x')\gamma_\nu S^{(+)}(x'-x)]$$
$$=\frac{e^2c^2}{2}Tr[\gamma_\mu S(x-x')\gamma_\nu S(x'-x)+\gamma_\mu S^{(1)}(x-x')\gamma_\nu S^{(1)}(x'-x)]. \tag{3.62}$$

An evaluation of this trace, employing the same method used to derive (2.15), yields

$$\{j_\mu(x),j_\nu(x')\}_0$$
$$=2e^2c^2\Big\{2\frac{\partial\Delta(x-x')}{\partial x_\mu}\frac{\partial\Delta(x-x')}{\partial x_\nu}-\delta_{\mu\nu}\Big[\Big(\frac{\partial\Delta(x-x')}{\partial x_\lambda}\Big)^2+\kappa_0{}^2(\Delta(x-x'))^2\Big]$$
$$-2\frac{\partial\Delta^{(1)}(x-x')}{\partial x_\mu}\frac{\partial\Delta^{(1)}(x-x')}{\partial x_\nu}+\delta_{\mu\nu}\Big[\Big(\frac{\partial\Delta^{(1)}(x-x')}{\partial x_\lambda}\Big)^2+\kappa_0{}^2(\Delta^{(1)}(x-x'))^2\Big]\Big\}. \tag{3.63}$$

This, in turn, can be replaced by a form analogous to (2.23):

$$\{j_\mu(x),j_\nu(x')\}_0=4e^2c^2\Big(\frac{\partial}{\partial x_\mu}\frac{\partial}{\partial x_\nu}-\delta_{\mu\nu}\Box^2\Big)\times(\bar{L}(\lambda)-L^{(1)}(\lambda)), \tag{3.64}$$

where

$$4\Big(\frac{\partial\bar{\Delta}(\lambda)}{\partial\lambda}\Big)^2=\frac{\partial^2\bar{L}(\lambda)}{\partial\lambda^2},$$
$$\Big(\frac{\partial\Delta^{(1)}(\lambda)}{\partial\lambda}\Big)^2=\frac{\partial^2L^{(1)}(\lambda)}{\partial\lambda^2}. \tag{3.65}$$

In particular,

$$\{j_\mu(x),j_\mu(x')\}_0=-12e^2c^2\Box^2(\bar{L}(\lambda)-L^{(1)}(\lambda)). \tag{3.66}$$

To find the one particle component of (3.56), we shall isolate that part of the operator that induces the transition of a positron, say, from one state to another with no other observable change in the matter field. We may again consider the typical term (3.57). The operator $\psi_\delta(x')$ either annihilates the single positron present or creates an electron. If it is the destruction of the original positron that occurs, the second operator $\bar{\psi}_\gamma(x')$ can only re-create a positron, in what is generally another state. The third operator can annihilate the previously generated positron, thus forming the vacuum expectation value of $\psi_\beta(x)\bar{\psi}_\gamma(x')$, or create an electron. However, if the latter occurs, $\bar{\psi}_\alpha(x)$ must annihilate that electron, in order that only a one-particle transition occur. But this would form the vacuum expectation value of $\bar{\psi}_\alpha(x)\psi_\beta(x)$, which, as we know, is effectively cancelled by the second term of $j_\mu(x)$. Thus, if the original positron is first annihilated, the only event that can ensue is a vacuum fluctuation, followed by the creation of the positron in its final state. If, on the other hand, the first process to occur is the creation of an electron, this must be followed by the creation of a positron in what will turn out to be the final state; the immediate annihilation of the electron need not be considered, for previously stated reasons. The third operator $\psi_\beta(x)$ can now only annihilate the original positron, and $\bar{\psi}_\alpha(x)$ destroys the electron. The two sets of transitions

that have thus been described in detail are those induced by the operator

$$(\gamma_\mu)_{\alpha\beta}(\gamma_\nu)_{\gamma\delta}\{[\bar\psi_\alpha(x)\psi_\delta(x')]_1\langle\psi_\beta(x)\bar\psi_\gamma(x')\rangle_0 + [\psi_\beta(x)\bar\psi_\gamma(x')]_1\langle\bar\psi_\alpha(x)\psi_\delta(x')\rangle_0\}, \quad (3.67)$$

which, indeed, is the one-particle part of (3.57) since it has a vanishing vacuum expectation value.

It is now only a short step to the one-particle part of (3.56):

$$\{j_\mu(x), j_\nu(x')\}_1$$
$$= -\frac{e^2c^2}{2}(\gamma_\mu)_{\alpha\beta}(\gamma_\nu)_{\gamma\delta}\{[\bar\psi_\alpha(x), \psi_\delta(x')]_1 \times\langle[\psi_\beta(x), \bar\psi_\gamma(x')]\rangle_0+[\psi_\beta(x), \bar\psi_\gamma(x')]_1 \times\langle[\bar\psi_\alpha(x), \psi_\delta(x')]\rangle_0\}$$
$$=\frac{e^2c^2}{2}\{[\bar\psi(x), \gamma_\mu S^{(1)}(x-x')\gamma_\nu\psi(x')]_1 + [\bar\psi(x')\gamma_\nu S^{(1)}(x'-x)\gamma_\mu, \psi(x)]_1\}, \quad (3.68)$$

and the actual quantity of interest

$$\{j_\mu(x), j_\mu(x')\}_1$$
$$=\frac{e^2c^2}{2}\{[\bar\psi(x), \gamma_\mu S^{(1)}(x-x')\gamma_\mu\psi(x')]_1 + [\bar\psi(x')\gamma_\mu S^{(1)}(x'-x)\gamma_\mu, \psi(x)]_1\}. \quad (3.69)$$

Of course, the two particle part of (3.56) is simply

$$\{j_\mu(x), j_\nu(x')\}_2=\{j_\mu(x), j_\nu(x')\} - \{j_\mu(x), j_\nu(x')\}_1-\{j_\mu(x), j_\nu(x')\}_0, \quad (3.70)$$

and we shall have no occasion to further simplify it.

It is now possible to write the second-order state vector equation in the detailed form

$$ihc\frac{\delta\Psi[\sigma]}{\delta\sigma(x)}=\{\mathcal{H}_{0,0}+\mathcal{H}_{1,0}(x)+\mathcal{H}_{2,0}(x) +\mathcal{H}_{1,1}(x)\}\Psi[\sigma], \quad (3.71)$$

where

$$\mathcal{H}_{0,0}=-\frac{1}{4c}\{j_\mu(x), \delta A_\mu(x)\}_0 =-\frac{1}{4c^2}\int\{j_\mu(x), j_\mu(x')\}_0 \times\bar D(x-x')d\omega', \quad (3.72)$$

$$\mathcal{H}_{1,0}(x)=-\frac{1}{4c}\{j_\mu(x), \delta A_\mu(x)\}_1 -\frac{1}{4c}\{(\delta j_\mu(x))_1, A_\mu(x)\}_0$$
$$=-\frac{1}{4c^2}\int\{j_\mu(x), j_\mu(x')\}_1\bar D(x-x')d\omega' -\frac{i}{8c^2}\int[j_\mu(x), j_\mu(x')]_1 \times\epsilon(x-x')D^{(1)}(x-x')d\omega', \quad (3.73)$$

$$\mathcal{H}_{2,0}(x)=-\frac{1}{4c}\{j_\mu(x), \delta A_\mu(x)\}_2 =-\frac{1}{4c^2}\int\{j_\mu(x), j_\mu(x')\}_2 \times\bar D(x-x')d\omega', \quad (3.74)$$

and

$$\mathcal{H}_{1,1}(x)=-\frac{1}{4c}\{(\delta j_\mu(x))_1, \mathfrak{A}_\mu(x)\}_1 =-\frac{i}{8\hbar c^2}\int[j_\mu(x), j_\nu(x')]_1\epsilon(x-x') \times\{\mathfrak{A}_\mu(x), \mathfrak{A}_\mu(x')\}_1d\omega'. \quad (3.75)$$

In these quantities the subscripts refer to the number of particles and light quanta whose transitions are described by the term in question. The change in the properties of the vacuum arising from the coupling between matter and radiation is produced by

$$\mathcal{H}_{0,0}=3e^2\int\Box'^2(\bar L(\lambda)-L^{(1)}(\lambda))\bar D(x-x')d\omega' =-3e^2(\bar L(0)-L^{(1)}(0)), \quad (3.76)$$

which implies nothing of physical interest, however. We turn, at last, to the quantity describing the altered properties of individual particles:

$$\mathcal{H}_{1,0}(x)$$
$$=-\frac{e^2}{8}\int\{[\bar\psi(x), \gamma_\mu S^{(1)}(x-x')\gamma_\mu\psi(x')]_1\bar D(x-x') +[\bar\psi(x), \gamma_\mu\bar S(x-x')\gamma_\mu\psi(x')]_1D^{(1)}(x-x') +[\bar\psi(x')\gamma_\mu S^{(1)}(x'-x)\gamma_\mu, \psi(x)]_1\bar D(x-x') +[\bar\psi(x')\gamma_\mu\bar S(x'-x)\gamma_\mu, \psi(x)]_1D^{(1)}(x-x')\}d\omega'$$
$$=\tfrac{1}{4}[\bar\psi(x), \phi(x)]_1+\tfrac{1}{4}[\bar\phi(x), \psi(x)]_1, \quad (3.77)$$

where

$$\phi(x)=-\frac{e^2}{2}\int\gamma_\mu[\bar{D}(x-x')S^{(1)}(x-x')$$
$$+D^{(1)}(x-x')\bar{S}(x-x')]\gamma_\mu\psi(x')d\omega'. \quad (3.78)$$

We shall prove that $\phi(x)$ is simply a multiple of $\psi(x)$,

$$\phi(x)=\delta mc^2\psi(x), \quad (3.79)$$

whence

$$\mathcal{H}_{1,0}(x)=\delta mc^2\tfrac{1}{2}[\bar{\psi}(x),\psi(x)]_1$$
$$=\delta mc^2\tfrac{1}{2}[\bar{\psi}(x)\psi(x)+\bar{\psi}'(x)\psi'(x)]_1. \quad (3.80)$$

It will be evident that δm is the electromagnetic mass of the electron.

The identity

$$\gamma_\mu\left(\gamma_\lambda\frac{\partial}{\partial x_\lambda}-\kappa_0\right)\gamma_\mu=-2\left(\gamma_\lambda\frac{\partial}{\partial x_\lambda}+2\kappa_0\right) \quad (3.81)$$

enables $\phi(x)$ to be written:

$$\phi(x)=e^2\int\left\{\gamma_\lambda\left[\bar{D}(x-x')\frac{\partial}{\partial x_\lambda}\Delta^{(1)}(x-x')\right.\right.$$
$$\left.+D^{(1)}(x-x')\frac{\partial}{\partial x_\lambda}\bar{\Delta}(x-x')\right]$$
$$+2\kappa_0[\bar{D}(x-x')\Delta^{(1)}(x-x')$$
$$\left.+D^{(1)}(x-x')\bar{\Delta}(x-x')]\right\}\psi(x')d\omega'. \quad (3.82)$$

We now define $P(\lambda)$, a function of $\lambda=-(x_\mu-x_\mu')^2$ according to

$$\frac{\partial P(\lambda)}{\partial\lambda}=\bar{D}(\lambda)\frac{\partial\Delta^{(1)}(\lambda)}{\partial\lambda}+D^{(1)}(\lambda)\frac{\partial\bar{\Delta}(\lambda)}{\partial\lambda}. \quad (3.83)$$

The utility of this quantity stems from the relation

$$\bar{D}(x)\frac{\partial\Delta^{(1)}(x)}{\partial x_\mu}+D^{(1)}(x)\frac{\partial\bar{\Delta}(x)}{\partial x_\mu}$$
$$=-2x_\mu\frac{\partial P(\lambda)}{\partial\lambda}=\frac{\partial P(\lambda)}{\partial x_\mu}, \quad (3.84)$$

which permits the first term of (3.82) to be simplified,

$$e^2\int\gamma_\mu\frac{\partial P(\lambda)}{\partial x_\mu}\psi(x')d\omega'$$
$$=e^2\int P(\lambda)\gamma_\mu\frac{\partial}{\partial x_\mu'}\psi(x')d\omega'$$
$$=-e^2\kappa_0\int P(\lambda)\psi(x')d\omega'. \quad (3.85)$$

Hence,

$$\phi(x)=e^2\kappa_0\int Q(\lambda)\psi(x')d\omega', \quad (3.86)$$

where

$$Q(\lambda)=2[\bar{D}(\lambda)\Delta^{(1)}(\lambda)+D^{(1)}(\lambda)\bar{\Delta}(\lambda)]-P(\lambda). \quad (3.87)$$

The explicit construction of $P(\lambda)$ and $Q(\lambda)$ proceeds analogously to that of $G(\lambda)$ in the second section. We first note that

$$\frac{\partial P(\lambda)}{\partial\lambda}=-\frac{1}{(2\pi)^4}\int\exp\left(i\lambda(\alpha+\beta)+i\frac{\kappa_0^2}{4\alpha}\right)$$
$$\times\alpha\frac{1}{2}\left(\frac{\alpha}{|\alpha|}+\frac{\beta}{|\beta|}\right)d\alpha d\beta,$$

and

$$P(\lambda)=\frac{i}{(2\pi)^4}\int\exp\left(i\lambda(\alpha+\beta)+i\frac{\kappa_0^2}{4\alpha}\right)$$
$$\times\frac{\alpha}{\alpha+\beta}\frac{1}{2}\left(\frac{\alpha}{|\alpha|}+\frac{\beta}{|\beta|}\right)d\alpha d\beta. \quad (3.38)$$

Hence,

$$Q(\lambda)=\frac{i}{(2\pi)^4}\int\exp\left(i\lambda(\alpha+\beta)+i\frac{\kappa_0^2}{4\alpha}\right)$$
$$\times\left(2-\frac{\alpha}{\alpha+\beta}\right)\frac{1}{2}\left(\frac{\alpha}{|\alpha|}+\frac{\beta}{|\beta|}\right)d\alpha d\beta. \quad (3.89)$$

In terms of the variables v and w, defined by (2.34), this reads

$$Q=\frac{i}{4(2\pi)^4}\kappa_0^4\int_{-1}^{1}\frac{3-v}{(1-v^2)^2}dv\int_{-\infty}^{\infty}\frac{dw}{w^3}$$
$$\times\exp\left[iw\frac{1-v}{2}+i\frac{\lambda\kappa_0^2}{w(1-v^2)}\right], \quad (3.90)$$

which in turn becomes

$$Q=\frac{1}{16(2\pi)^6}\int(dk)\exp(ik_\mu(x_\mu-x_\mu'))\times\int_{-1}^{1}(3-v)dv\int_{-\infty}^{\infty}\frac{dw}{|w|}\times\exp\left(i\left[\frac{1-v}{2}+\frac{k_\mu^2}{4\kappa_0^2}(1-v^2)\right]w\right),\quad(3.91)$$

on using the integral representation (2.36).

We now remark that $\psi(x)$ satisfies the second order differential equation

$$(\Box^2-\kappa_0^2)\psi(x)=0,\quad(3.92)$$

which implies that a Fourier decomposition of $\psi(x)$ into plane waves of the form $e^{ik_\mu x_\mu}$ involves only such propagation vectors that obey

$$k_\mu^2=-\kappa_0^2.\quad(3.93)$$

Therefore, in evaluating the integral

$$\int Q(\lambda)\psi(x')d\omega',$$

with $Q(\lambda)$ expressed as a Fourier integral involving $e^{ik_\mu(x_\mu-x_\mu')}$, multiplied by a function of k_μ^2:

$$Q(\lambda)=\frac{1}{(2\pi)^4}\int\exp(ik_\mu(x_\mu-x_\mu'))F(k_\mu^2)(dk),\quad(3.94)$$

the latter quantity may be replaced by $-\kappa_0^2$. Thus

$$\int Q(\lambda)\psi(x')d\omega'=\frac{1}{(2\pi)^4}\int(dk)\int d\omega'\times\exp(ik_\mu(x_\mu-x_\mu'))F(-\kappa_0^2)\psi(x')=F(-\kappa_0^2)\psi(x),\quad(3.95)$$

which confirms the statement that $\phi(x)$ is proportioned to $\psi(x)$, and yields as the value of the constant:

$$\delta mc^2=\frac{\alpha}{8\pi}m_0c^2\int_{-1}^{1}(3-v)dv\times\int_0^\infty\frac{dw}{w}\cos\left(\frac{1-v}{2}\right)^2w.\quad(3.96)$$

To complete the evaluation, it is convenient to integrate by parts, according to

$$\frac{\delta m}{m_0}=\frac{\alpha}{16\pi}\int_{-1}^{1}d[(v-5)(1-v)]\times\int_0^\infty\frac{dw}{w}\cos\left(\frac{1-v}{2}\right)^2w=\frac{\alpha}{8\pi}\left[6\int_0^\infty\frac{\cos w}{w}dw+\int_{-1}^{1}(5-v)\left(\frac{1-v}{2}\right)^2dv\times\int_0^\infty\sin\left(\frac{1-v}{2}\right)^2wdw\right]=\frac{3\alpha}{2\pi}\left[\frac{1}{2}\log\frac{1}{\gamma w_0}+\frac{5}{6}\right],\quad(3.97)$$

whereby we obtain a logarithmically divergent result for the electromagnetic mass of the electron or positron. An alternative evaluation can be given, which permits comparison with previous treatments,[7] by employing directly the Fourier integral representations for the functions $D(x)$, $\Delta(x)$, $D^{(1)}(x)$ and $\Delta^{(1)}(x)$, in (3.82). One thus obtains the electromagnetic mass as an integral over the momenta of the virtual quanta involved in the self energy process, with the result

$$\frac{\delta m}{m_0}=\frac{3\alpha}{2\pi}\left[\log\frac{K+K_0}{\kappa_0}-\frac{1}{6}\right]_{K=\infty},\quad(3.98)$$

where $K_0=(K^2+\kappa_0^2)^{\frac{1}{2}}$. Evidently $1/w_0\sim(K/\kappa_0)^2$.

To justify the identification of δm with the electromagnetic mass, we must show that it is possible to remove the term $\mathfrak{IC}_{1,0}(x)$ from (3.71) and thereby alter the equation of motion for the matter field into that of a particle of mass $m=m_0+\delta m$, thus demonstrating the unity of the two contributions to the actual electron mass. Accordingly, we introduce the state vector transformation

$$\Psi[\sigma]=U[\sigma]\Psi[\sigma],\quad(3.99)$$

where $U[\sigma]$ is designed to remove the variation associated with $\mathfrak{IC}_{1,0}(x)$ from $\Psi[\sigma]$ and therefore

[7] V. Weisskopf. Zeits. f. Physik 89, 27 (1934); 90, 817 (1934), and Phys. Rev. 56, 72 (1939).

is subject to the equation of motion

$$i\hbar c\frac{\delta U[\sigma]}{\delta\sigma(x)}=\mathcal{H}_{1,0}(x)\,U[\sigma]. \tag{3.100}$$

Thus, we return to a Heisenberg representation for the description of self-energy effects. The transformation (3.99) induces a concomitant change in the matter field operators,

$$\psi(x)=U^{-1}[\sigma]\psi(x)\,U[\sigma], \tag{3.101}$$

in which we use bold face letters to designate the new operators as well as the new state vector. To construct the equation of motion satisfied by $\psi(x)$, we require an equation analogous to (I, 2.9). Since the roles of interaction and Heisenberg representations have been interchanged, we find that

$$\frac{\partial\psi(x)}{\partial x_\mu}=U^{-1}[\sigma]\frac{\partial\psi(x)}{\partial x_\mu}U[\sigma]$$

$$-\frac{i}{\hbar c}\int_\sigma[\psi(x'),\,\boldsymbol{H}_{1,0}(x)]d\sigma_\mu', \tag{3.102}$$

whence

$$\left(\gamma_\mu\frac{\partial}{\partial x_\mu}+\kappa_0\right)\psi(x)$$

$$=-\frac{i}{\hbar c}\int_\sigma[\gamma_\mu\psi(x'),\,\boldsymbol{H}_{1,0}(x)]d\sigma_\mu'$$

$$=-\frac{\delta mc}{\hbar}i\int_\sigma[\gamma_\mu\psi(x'),\,\bar{\psi}_\alpha(x)]d\sigma_\mu'\psi_\alpha(x)$$

$$=-\delta\kappa\psi(x), \tag{3.103}$$

where

$$\delta\kappa=\delta mc/\hbar. \tag{3.104}$$

Finally, then

$$\left(\gamma_\mu\frac{\partial}{\partial x_\mu}+\kappa\right)\psi(x)=0 \tag{3.105}$$

with

$$\kappa=mc/\hbar,\quad m=m_0+\delta m, \tag{3.106}$$

which is the desired result. The σ-variation of the state vector that remains after removal of $\mathcal{H}_{1,0}(x)$, and $\mathcal{H}_{0,0}$ (which we may include, without altering the previous considerations) is described, correct to the second order, by the equation of motion

$$i\hbar c\frac{\delta\Psi[\sigma]}{\delta\sigma(x)}=\{\boldsymbol{H}_{2,0}(x)+\boldsymbol{H}_{1,1}(x)\}\,\Psi[\sigma], \tag{3.107}$$

which governs the second order interaction of a particle with a light quantum or another particle.

It will be our final task to examine the form which the energy-momentum quantities assume as a result of the succession of transformations which have culminated in (3.107). In particular, we shall again confirm the complete amalgamation of the mechanical and electromagnetic mass of the electron. We may first remark on the generality of the arguments that led to the expression for the energy-momentum four-vector in the interaction representation (I, 2.52):

$$P_\mu[\sigma]=P_\mu{}^{(0)}-\frac{1}{c}\int_\sigma\mathcal{H}(x)d\sigma_\mu \tag{3.108a}$$

$$\mathcal{H}(x)=-\frac{1}{c}j_\mu(x)A_\mu(x). \tag{3.108b}$$

This form must be preserved on subjecting the state vector to a transformation, provided one employs the appropriately transformed $\mathcal{H}(x)$. We shall prove this by direct calculation, however. The energy-momentum operator associated with the new state vector in the transformation (3.7) is, to second order,

$$P_\mu[\sigma]=e^{iS[\sigma]}\left[P_\mu{}^{(0)}+\frac{1}{c^2}\int_\sigma j_\nu(x)A_\nu(x)d\sigma_\mu\right]e^{-iS[\sigma]}$$

$$=P_\mu{}^{(0)}+i[S[\sigma],\,P_\mu{}^{(0)}]$$

$$-\tfrac{1}{2}[S[\sigma],\,[S[\sigma],\,P_\mu{}^{(0)}]]$$

$$+\frac{1}{c^2}\int_\sigma j_\nu(x)A_\nu(x)d\sigma_\mu$$

$$+i\left[S[\sigma],\,\frac{1}{c^2}\int_\sigma j_\nu(x)A_\nu(x)d\sigma_\mu\right]. \tag{3.109}$$

The interpretation of $P_\mu{}^{(0)}$ as the displacement operator for the independent fields, when applied to the displacement of a functional, leads to

$$\frac{i}{\hbar}[S[\sigma],\,P_\mu{}^{(0)}]=\int_\sigma\frac{\delta S[\sigma]}{\delta\sigma(x)}d\sigma_\mu, \tag{3.110}$$

whence

$$i[S[\sigma], P_\mu^{(0)}]+\frac{1}{c^2}\int_\sigma j_\nu(x)A_\nu(x)d\sigma_\mu=0, \quad (3.111)$$

and

$$P_\mu[\sigma]=P_\mu^{(0)}-\frac{1}{c}\int_\sigma d\sigma_\mu\frac{i}{2}[j_\nu(x)A_\nu(x), S[\sigma]]. \quad (3.112)$$

This indeed is still of the form (3.108a), with $\mathcal{H}(x)$ the quantity occurring in (3.14). There is no difficulty in proceeding to the form

$$P_\mu[\sigma]=P_\mu^{(0)}-\frac{1}{c}\int_\sigma[\mathcal{H}_{0,0}+\mathcal{H}_{1,0}(x)+\mathcal{H}_{2,0}(x)+\mathcal{H}_{1,1}(x)]d\sigma_\mu, \quad (3.113)$$

associated with the state vector equation (3.71). The last transformation to be considered is (3.99), which provides us with the energy-momentum four vector:

$$\mathbf{P}_\mu[\sigma]=U^{-1}[\sigma]P_\mu^{(0)}U[\sigma]-\frac{1}{c}\int_\sigma[\mathcal{H}_{0,0}+\boldsymbol{H}_{1,0}(x)+\boldsymbol{H}_{2,0}(x)+\boldsymbol{H}_{1,1}(x)]d\sigma_\mu. \quad (3.114)$$

Now, according to (I, 1.64) and (3.102),

$$U^{-1}[\sigma]P_\mu^{(0)}U[\sigma]=\mathbf{P}_\mu^{(0)}+\frac{i}{2c}\int_\sigma d\sigma_\mu\times[\bar{\psi}(x), [\gamma_\mu\psi(x'), \boldsymbol{H}_{1,0}(x)]]_1 d\sigma_\nu', \quad (3.115)$$

in which the subscript one indicates that $P_\mu^{(0)}$, or $\mathbf{P}_\mu^{(0)}$, is constructed to have a vanishing vacuum expectation value. On evaluating the second term of (3.115) as:

$$\frac{1}{c}\int_\sigma d\sigma_\mu i\{\gamma_\mu\psi(x'), \bar{\psi}_\alpha(x)\}\delta mc^2\tfrac{1}{2}[\bar{\psi}(x), \psi_\alpha(x)]_1 d\sigma_\nu'$$

$$=-\frac{1}{c}\int_\sigma\delta mc^2\tfrac{1}{2}[\bar{\psi}(x), \psi(x)]d\sigma_\nu=-\frac{1}{c}\int_\sigma\boldsymbol{H}_{1,0}(x)d\sigma_\nu,$$

we find

$$\mathbf{P}_\mu[\sigma]=\mathbf{P}_\mu^{(0)}-\frac{1}{c}\int_\sigma[\boldsymbol{H}_{2,0}(x)+\boldsymbol{H}_{1,1}(x)]d\sigma_\mu \quad (3.116)$$

from which the vacuum term $\mathcal{H}_{0,0}$ has been removed, in accordance with the trivial possibility of adding a multiple of $\delta_{\mu\nu}$ to the energy-momentum tensor of the system. With this result, we have confirmed that, for an individual particle, the energy and momentum modifications produced by self-interaction effects are entirely accounted for by the addition of the electromagnetic proper mass δm to the mechanical proper mass m_0—an unobservable mass renormalization.

APPENDIX

In the course of this development of quantum electrodynamics, various functions associated with the electromagnetic and matter fields have been defined, notably $D(x)$, $D^{(1)}(x)$, $\Delta(x)$ and $\Delta^{(1)}(x)$. It is now our task to construct these functions explicitly. We begin with the invariant function associated with the matter field, $\Delta(x)$ (from which $D(x)$ can be obtained by placing $\kappa_0=0$). Its construction is facilitated by considering the associated function

$$\bar{\Delta}(x)=-\tfrac{1}{2}\Delta(x)\epsilon(x)=\tfrac{1}{2}\Delta(x)\frac{\epsilon_\mu x_\mu}{|\epsilon_\mu x_\mu|}, \quad (A.1)$$

where $\epsilon(x)$ is $+1$ or -1 according as x_0 is positive or negative. This sign factor is effectively an invariant since only time-like vectors x_μ need be considered in (A.1). This is emphasized by the invariant representation of $\epsilon(x)$:

$$\epsilon(x)=-\frac{\epsilon_\mu x_\mu}{|\epsilon_\mu x_\mu|} \quad (A.2)$$

where ϵ_μ is an arbitrary time-like vector with $\epsilon_0>0$. It will first be noted that

$$(\Box^2-\kappa_0^2)\bar{\Delta}(x)=0, \quad x_\mu\neq 0 \quad (A.3)$$

since only at the time-like neighborhood of the origin is a sign change of $\epsilon(x)$ combined with a non-vanishing value of $\Delta(x)$. To evaluate the left side of (A.3) at the origin, we consider

$$\mathrm{Lim}\int_{\delta\omega}d\omega(\Box^2-\kappa_0^2)\bar{\Delta}(x)=\mathrm{Lim}\left[\int_{\sigma_+}d\sigma_\mu\frac{\partial\bar{\Delta}(x)}{\partial x_\mu}-\int_{\sigma_-}d\sigma_\mu\frac{\partial\bar{\Delta}(x)}{\partial x_\mu}\right], \quad (A.4)$$

in which the region of integration $\delta\omega$ is extended between two space-like surfaces σ_+ and σ_-, which lie in the future and past, respectively, relative to the origin, and coincide in the limit with the space-like surface σ through the origin. Thus

$$\mathrm{Lim}\int_{\delta\omega}d\omega(\Box^2-\kappa_0^2)\bar{\Delta}(x)=-\int_\sigma\frac{\partial\Delta(x)}{\partial x_\mu}d\sigma_\mu=-1, \quad (A.5)$$

which shows that

$$(\Box^2-\kappa_0^2)\bar{\Delta}(x)=-\delta(x), \quad (A.6)$$

where

$$\delta(x)=\delta(x_0)\delta(x_1)\delta(x_2)\delta(x_3) \quad (A.7)$$

is the four-dimensional delta-function. Evidently $\bar{\Delta}(x)$

plays the role of a four-dimensional Green's function. In terms of the integral representation

$$\delta(x)=\frac{1}{(2\pi)^4}\int \exp(ik_\mu x_\mu)(dk), \tag{A.8}$$

where

$$(dk)=dk_0dk_1dk_2dk_3, \tag{A.9}$$

we obtain as a particular solution of (A.6),

$$\bar{\Delta}(x)=\frac{1}{(2\pi)^4}P\int\frac{\exp(ik_\mu x_\mu)}{k_\lambda^2+\kappa_0^2}(dk) \tag{A.10}$$

which, as will be shown, provides a function $\Delta(x)$ that satisfies the equations of definition (I, 2.18).

The integral representation

$$P\frac{1}{\tau}=-\frac{i}{2}\int_{-\infty}^{\infty}e^{ia\tau}\frac{a}{|a|}da \tag{A.11}$$

with $\tau=k_\lambda^2+\kappa_0^2$, enables the integration over k space to be effected:

$$\begin{aligned}\bar{\Delta}(x)&=-\frac{i}{2(2\pi)^4}\int_{-\infty}^{\infty}\frac{a}{|a|}da\int(dk)\\&\qquad\times\exp(iak_\mu^2+ik_\mu x_\mu)\exp(ia\kappa_0^2)\\&=\frac{1}{32\pi^2}\int_{-\infty}^{\infty}\frac{da}{a^2}\exp\left(-i\frac{x_\mu^2}{4a}+ia\kappa_0^2\right)\end{aligned} \tag{A.12}$$

with the aid of the formula

$$\begin{aligned}&\int(dk)\exp(iak_\mu^2+ik_\mu x_\mu)\\&\qquad=\int(dk)\exp(iak_\mu^2)\exp-\left(i\frac{x_\mu^2}{4a}\right)\\&\qquad=i\frac{\pi^2}{a|a|}\exp\left(-i\frac{x_\mu^2}{4a}\right).\end{aligned} \tag{A.13}$$

The introduction of the new variable,

$$\alpha=1/4a, \tag{A.14}$$

brings (A.12) into the form

$$\bar{\Delta}(x)=\frac{1}{8\pi^2}\int_{-\infty}^{\infty}\exp\left(i\lambda\alpha+i\frac{\kappa_0^2}{4\alpha}\right)d\alpha, \tag{A.15}$$

where

$$\lambda=-x_\mu^2. \tag{A.16}$$

Equivalent forms of (A.15) are:

$$\begin{aligned}\bar{\Delta}(x)=\bar{\Delta}(\lambda)&=\frac{1}{4\pi^2}\int_0^{\infty}\cos\left(\lambda\alpha+\frac{\kappa_0^2}{4\alpha}\right)d\alpha\\&=\frac{1}{4\pi^2}\frac{\partial}{\partial\lambda}\int_0^{\infty}\sin\left(\lambda\alpha+\frac{\kappa_0^2}{4\alpha}\right)d\alpha.\end{aligned} \tag{A.17}$$

In order to evaluate the last integral, we define a new variable of integration, according to

$$\alpha=\frac{\kappa_0}{2|\lambda|^{\frac{1}{2}}}e^{\vartheta}, \tag{A.18}$$

whence

$$\begin{aligned}\int_0^{\infty}\sin\left(\lambda\alpha+\frac{\kappa_0^2}{4\alpha}\right)\frac{d\alpha}{\alpha}&=\int_{-\infty}^{\infty}\sin\left[\frac{\kappa_0|\lambda|^{\frac{1}{2}}}{2}\left(\frac{\lambda}{|\lambda|}e^{\vartheta}+e^{-\vartheta}\right)\right]d\vartheta\\&=\begin{cases}\int_{-\infty}^{\infty}\sin(\kappa_0\lambda^{\frac{1}{2}}\cosh\vartheta)d\vartheta, & \lambda>0\\-\int_{-\infty}^{\infty}\sin(\kappa_0(-\lambda)^{\frac{1}{2}}\sinh\vartheta)d\vartheta, & \lambda<0\end{cases}\\&=\begin{cases}\pi J_0(\kappa_0\lambda^{\frac{1}{2}}), & \lambda>0\\0, & 0<\lambda.\end{cases}\end{aligned} \tag{A.19}$$

This discontinuous value can be compactly represented by

$$\int_0^{\infty}\sin\left(\lambda\alpha+\frac{\kappa_0^2}{4\alpha}\right)\frac{d\alpha}{\alpha}=\pi Re H_0^{(1)}(\kappa_0\lambda^{\frac{1}{2}}) \tag{A.20}$$

provided $\lambda^{\frac{1}{2}}$, with λ negative, is interpreted as $i|\lambda|^{\frac{1}{2}}$. Finally,

$$\bar{\Delta}(x)=\frac{1}{4\pi}\delta(\lambda)-\frac{\kappa_0^2}{8\pi}Re\frac{H_1^{(1)}(\kappa_0\lambda^{\frac{1}{2}})}{\kappa_0\lambda^{\frac{1}{2}}} \tag{A.21}$$

where

$$Re\frac{H_1^{(1)}(\kappa_0\lambda^{\frac{1}{2}})}{\kappa_0\lambda^{\frac{1}{2}}}=\begin{cases}\dfrac{J_1(\kappa_0\lambda^{\frac{1}{2}})}{\kappa_0\lambda^{\frac{1}{2}}}, & \lambda>0\\0, & 0<\lambda,\end{cases} \tag{A.22}$$

and the delta-function of λ arises from the discontinuity of (A.20) at $\lambda=0$. Clearly $\bar{\Delta}(x)$, and therefore $\Delta(x)$, vanishes if $x_\mu^2>0$ which is one of the defining properties of the latter function. On placing $\kappa_0=0$, we obtain

$$\begin{aligned}\bar{D}(x)=-\tfrac{1}{2}D(x)\epsilon(x)&=\frac{1}{4\pi}\delta(\lambda)\\&=\frac{1}{4\pi}\delta(x_\mu^2),\end{aligned} \tag{A.23}$$

which evidently corresponds to the propagation properties of electromagnetic pulses.

An integral representation for $\Delta(x)$ itself can be constructed with the aid of the Fourier inversion of (A.11):

$$\frac{a}{|a|}=-\frac{i}{\pi}P\int_{-\infty}^{\infty}e^{ia\tau}\frac{d\tau}{\tau}, \tag{A.24}$$

in the form

$$\epsilon(x)=-\frac{\epsilon_\mu x_\mu}{|\epsilon_\mu x_\mu|}=\frac{i}{\pi}P\int_{-\infty}^{\infty}\exp(i\epsilon x_\mu\tau)\frac{d\tau}{\tau}. \tag{A.25}$$

On employing the first expression of (A.12) for $\bar{\Delta}(x)$, we obtain

$$\begin{aligned}\Delta(x)=-\frac{2}{(2\pi)^5}\int(dk)\int_{-\infty}^{\infty}\frac{a}{|a|}daP\int_{-\infty}^{\infty}\frac{d\tau}{\tau}\\\times\exp(i(k_\mu+\epsilon_\mu\tau)x_\mu)\exp(ia(k_\mu^2+\kappa_0^2))\end{aligned} \tag{A.26}$$

which becomes

$$\begin{aligned}\Delta(x)=-\frac{2}{(2\pi)^5}\int(dk)\int_{-\infty}^{\infty}\frac{a}{|a|}daP\int_{-\infty}^{\infty}\frac{d\tau}{\tau}\\\times\exp(-2ia\epsilon_\mu k_\mu\tau)\exp(ia\epsilon_\mu^2\tau^2)\\\times\exp(ik_\mu x_\mu)\exp(ia(k_\mu^2+\kappa_0^2))\end{aligned} \tag{A.27}$$

on introducing the transformation $k_\mu\rightarrow k_\mu-\epsilon_\mu\tau$. It may now be argued that (A.27) is independent of ϵ_μ, provided only that it is a time-like vector with positive ϵ_0. However, these essential characteristics can be maintained with $-\epsilon_\mu^2$ an arbitrarily small positive number. It is, therefore, permissible to evaluate (A.27) in the limit $\epsilon_\mu^2\rightarrow 0$, which, in view of the formula

$$\begin{aligned}P\int_{-\infty}^{\infty}\exp(-2ia\epsilon_\mu k_\mu\tau)\frac{d\tau}{\tau}&=-\pi i\frac{a}{|a|}\frac{\epsilon_\mu k_\mu}{|\epsilon_\mu k_\mu|}\\&=\pi i\frac{a}{|a|}\epsilon(k),\end{aligned} \tag{A.28}$$

yields

$$\begin{aligned}\Delta(x)=-\frac{i}{(2\pi)^4}\int(dk)\int_{-\infty}^{\infty}da\exp(ia(k_\mu^2+\kappa_0^2))\\\times\exp(ik_\mu x_\mu)\epsilon(k)\\=-\frac{i}{(2\pi)^3}\int\exp(ik_\mu x_\mu)\delta(k_\mu^2+\kappa_0^2)\epsilon(k)(dk).\end{aligned} \tag{A.29}$$

This result makes it evident that $\Delta(x)$, as constructed, satisfies the proper differential equation

$$(\Box^2-\kappa_0^2)\Delta(x)=\frac{i}{(2\pi)^3}\int \exp(ik_\mu x_\mu)(k_\lambda{}^2+\kappa_0{}^2)\times\delta(k_\lambda{}^2+\kappa_0{}^2)\epsilon(k)(dk)=0, \tag{A.30}$$

since $x\delta(x)=0$. We have thereby completed the proof of the integral representation (A.10) since the three equations of definition for $\Delta(x)$ have been verified, the integral condition being equivalent, according to (A.5), to the differential equation defining $\bar{\Delta}(x)$.

An integral representation for $\Delta^{(1)}(x)$ can be obtained immediately from that of $\Delta(x)$. According to the equation of definition (1.57), and (A.29):

$$\begin{aligned}\Delta^{(1)}(x)&=\frac{1}{\pi}P\int_{-\infty}^{\infty}\Delta(x-\epsilon\tau)\frac{d\tau}{\tau}\\&=-\frac{i}{\pi}\frac{1}{(2\pi)^3}\int(dk)\epsilon(k)P\int_{-\infty}^{\infty}\frac{d\tau}{\tau}\times\exp(-ik_\mu\epsilon_\mu\tau)\exp(ik_\mu x_\mu)\delta(k_\mu{}^2+\kappa_0{}^2)\\&=\frac{1}{(2\pi)^3}\int\exp(ik_\mu x_\mu)\delta(k_\mu{}^2+\kappa_0{}^2)(dk),\end{aligned} \tag{A.31}$$

which is also easily derived, in a less formal manner, by means of the decomposition into positive and negative k_0. In order to evaluate $\Delta^{(1)}(x)$ in a manner similar to $\bar{\Delta}(x)$, we employ the integral representation

$$\delta(\tau)=\frac{1}{2\pi}\int_{-\infty}^{\infty}e^{ia\tau}da \tag{A.32}$$

with $\tau=k_\mu{}^2+\kappa_0{}^2$, and perform the integration over k space

$$\begin{aligned}\Delta^{(1)}(x)&=\frac{1}{(2\pi)^4}\int_{-\infty}^{\infty}da\int(dk)\exp(iak_\mu{}^2+ik_\mu x_\mu)\times\exp(ia\kappa_0{}^2)\\&=\frac{i}{16\pi^2}\int_{-\infty}^{\infty}\exp\left(-i\frac{x_\mu{}^2}{4a}+ia\kappa_0{}^2\right)\frac{a}{|a|}\frac{da}{a^2}\\&=\frac{i}{4\pi^2}\int_{-\infty}^{\infty}\exp\left(i\lambda\alpha+i\frac{\kappa_0{}^2}{4\alpha}\right)\frac{\alpha}{|\alpha|}d\alpha.\end{aligned} \tag{A.33}$$

Further rearrangements of (A.33) yield

$$\begin{aligned}\Delta^{(1)}(x)=\Delta^{(1)}(\lambda)&=-\frac{1}{2\pi^2}\int_0^{\infty}\sin\left(\lambda\alpha+\frac{\kappa_0{}^2}{4\alpha}\right)d\alpha\\&=\frac{1}{2\pi^2}\frac{\partial}{\partial\lambda}\int_0^{\infty}\cos\left(\lambda\alpha+\frac{\kappa_0{}^2}{4\alpha}\right)\frac{d\alpha}{\alpha}.\end{aligned} \tag{A.34}$$

Again utilizing the transformation (A.18), we now find

$$\begin{aligned}\int_0^{\infty}\cos\left(\lambda\alpha+\frac{\kappa_0{}^2}{4\alpha}\right)\frac{d\alpha}{\alpha}&=\begin{cases}\int_{-\infty}^{\infty}\cos(\kappa_0\lambda^{\frac{1}{2}}\cosh\vartheta)d\vartheta, & \lambda>0\\ \int_{-\infty}^{\infty}\cos(\kappa_0(-\lambda)^{\frac{1}{2}}\sinh\vartheta)d\vartheta, & \lambda<0\end{cases}\\&=\begin{cases}-\pi N_0(\kappa_0\lambda^{\frac{1}{2}}), & \lambda>0\\ 2K_0(\kappa_0(-\lambda)^{\frac{1}{2}}), & \lambda<0,\end{cases}\end{aligned} \tag{A.35}$$

which is summarized in

$$\int_0^{\infty}\cos\left(\lambda\alpha+\frac{\kappa_0{}^2}{4\alpha}\right)\frac{d\alpha}{\alpha}=-\pi ImH_0{}^{(1)}(\kappa_0\lambda^{\frac{1}{2}}). \tag{A.36}$$

Unlike the situation in (A.19), there is no discontinuity at $\lambda=0$. Therefore

$$\Delta^{(1)}(x)=\frac{\kappa_0{}^2}{4\pi}Im\frac{H_1{}^{(1)}(\kappa_0\lambda^{\frac{1}{2}})}{\kappa_0\lambda^{\frac{1}{2}}}=\begin{cases}\frac{\kappa_0{}^2}{4\pi}\frac{N_1(\kappa_0\lambda^{\frac{1}{2}})}{\kappa_0\lambda^{\frac{1}{2}}}, & \lambda>0\\ \frac{\kappa_0{}^2}{2\pi^2}\frac{K_1(\kappa_0(-\lambda)^{\frac{1}{2}})}{\kappa_0(-\lambda)^{\frac{1}{2}}}, & \lambda<0.\end{cases} \tag{A.37}$$

The singularity of $\Delta^{(1)}(x)$ at $\lambda=0$ can be exhibited by writing

$$\Delta^{(1)}(x)=-\frac{1}{2\pi^2\lambda}+\frac{\kappa_0{}^2}{4\pi}Im\left[\frac{H_1{}^{(1)}(\kappa_0\lambda^{\frac{1}{2}})}{\kappa_0\lambda^{\frac{1}{2}}}+\frac{2i}{\pi}\frac{1}{\kappa_0{}^2\lambda}\right] \tag{A.38}$$

since

$$Im\left[\frac{H_1{}^{(1)}(\kappa_0\lambda^{\frac{1}{2}})}{\kappa_0\lambda^{\frac{1}{2}}}+\frac{2i}{\pi}\frac{1}{\kappa_0{}^2\lambda}\right]\sim\frac{1}{\pi}\left[\log\frac{\gamma\kappa_0|\lambda|^{\frac{1}{2}}}{2}-\frac{1}{2}\right],\quad \kappa_0|\lambda|^{\frac{1}{2}}\ll 1 \tag{A.39}$$

where $\gamma=1.781$. On letting $\kappa_0\to 0$, we obtain

$$D^{(1)}(x)=-\frac{1}{2\pi^2\lambda}=\frac{1}{2\pi^2}\frac{1}{x_\mu{}^2}. \tag{A.40}$$

PHYSICAL REVIEW VOLUME 75, NUMBER 4 FEBRUARY 15, 1949

Non-Linear Field Theories

PETER G. BERGMANN
Department of Physics, Syracuse University, Syracuse, New York
(Received June 8, 1948)

This is the first paper in a program concerned with the quantization of field theories which are covariant with respect to general coordinate transformations, like the general theory of relativity. All these theories share the property that the existence and form of the equations of motion is a direct consequence of the covariant character of the equations. It is hoped that in the quantization of theories of this type some of the divergences which are ordinarily encountered in quantum field theories can be avoided. The present paper lays the classical foundation for this program: It examines the formal properties of covariant field equations, derives the form of the conservation laws, the form of the equations of motion, and the properties of the canonical momentum components which can be introduced.

I. INTRODUCTION

AT the present time, two great theoretical structures in physics can lay claim to containing significant parts of the "truth" which to unearth must remain the principal aim of both the experimental and the theoretical physicist. One of these structures is modern quantum physics as applied to both mechanical and field theoretical problems; the other is the general theory of relativity, which in the author's opinion represents the least imperfect "classical" (i.e., non-quantized) field theory. It is well known that at this time each one of these structures suffers from serious and apparently inherent weaknesses; Quantum physics in most of its realizations still requires a two-stage development, an underlying classical theory (a mechanical system or a set of field equations together with equations of motion) followed by a process of quantization. The result of this quantization process, when applied to a combination of fields and particles, usually leads to characteristic divergences. The general theory of relativity, on the other hand, has so far not successfully absorbed the existence of quantities possessing half-odd spin, nor can it be quantized in a satisfactory manner; as a result, the theory has been completely useless in atomic and nuclear physics.

Neither theory has as yet made any significant contribution to the problem of the constitution of the elementary particles. Moreover, while each structure undeniably contains elements of truth, their combination has so far proved unsuccessful.

The purpose of the present program is to analyze each of the two theories for its essential and, presumably, relatively permanent contributions to our present knowledge and, thus, to construct what might be called skeletonized theories. An attempt will be made to see whether such a covariant theory is at all susceptible to quantization and whether the result will be an improved theory.

Specifically, it is believed that the theory of relativity contains two great permanent achievements: (a) it is the only theory of gravitation which explains reasonably the equality of inertial and gravitational mass (the so-called principle of equivalence); (b) it is the only classical field theory in which the equations of motion of particles in the field are contained in the field equations, instead of being logical juxtapositions. That is why it is possible, in the general theory of relativity, to treat the motion of field singularities (which are used to represent particles) without having to deal with infinite interaction terms of one kind or another. It is possible that this accomplishment will also lead to a more satisfactory quantized theory, although the author has little hope that such a theory would be sufficiently powerful to attack the problem of the constitution of elementary particles.

On the other hand, there is probably no particular reason why the theory of relativity must appear in the form of Riemannian geometry, i.e., using primarily the differential covariants of a symmetric tensor of rank 2. The first step in the program sketched above consists therefore, in the setting up of a generalized classical theory

and the examination of its properties. This is the scope of the present paper.

The theory to be developed is essentially non-linear, and its Hamiltonian non-quadratic. It is impossible to envisage a set of differential equations which is covariant with respect to general coordinate transformations, yet linear. While this might appear to be merely an annoying complication, the non-linear character of the general theory of relativity is crucial for the possibility of interaction between different particles. It is possible to set up linear, Lorentz-covariant field equations for a field similar to gravitational potentials, which contain equations of motion; but these turn out to represent simply Newton's first law: Each singularity is tied inexorably to a straight-line uniform motion, without any interaction between pairs of particles. It is the non-linear terms in the field equations which provide for forces, gravitational and otherwise.[1-3]

II. THE FIELD VARIABLES AND THE LAGRANGIAN

Instead of introducing a metric tensor, as is done in the general theory of relativity, we shall leave the exact nature of the field variables unspecified, denoting them merely by the symbol y_A $(A=1, \cdots, N)$, where N is the number of algebraically independent components. It will be assumed that the field equations can be derived from a variational principle of the form

$$\delta I=0, \quad I=\int_V L(y_A, y_{A,\mu})d^4x. \tag{2.1}$$

In other words, the field equations will determine values of the integral I which are stationary with respect to infinitesimal changes in the field variables; these changes are arbitrary, except that they must remain confined to the interior of the chosen four-dimensional volume V. The Lagrangian L is assumed to be an algebraic function of the field variables themselves and their first partial derivatives with respect to the coordinates. As is customary, $y_{A,\mu}$ is short for $\partial y_A/\partial x^\mu$.

The field equations which result from the variation of the field variables in the interior shall be designated by L^A,

$$L^A \equiv (\partial L/\partial y_A)-(\partial L/\partial y_{A,\rho}),_\rho=0. \tag{2.2}$$

More precisely, the symbol L^A will be used for the left-hand side of these equations, no matter whether they are satisfied or not.

In this paper it will be assumed that the transformation law of the field variables is linear and homogeneous in the field variables themselves and that it depends algebraically on the first derivatives of the new coordinates with respect to the old ones. With respect to *infinitesimal* coordinate transformations, the field variables will transform according to a law having the form

$$\bar{\delta} y_A = F_{A\mu}{}^{B\nu}\xi^\mu,_\nu y_B - y_{A,\mu}\xi^\mu. \tag{2.3}$$

The four functions ξ^μ represent the infinitesimal changes of the coordinate values of a fixed world point. The $F_{A\mu}{}^{B\nu}$ are numbers, independent of both the choice of coordinate system and the coordinate values themselves, but characteristic for the type of field variables representing the field. Finally, the $\bar{\delta} y_A$ are the changes produced in the field variables y_A *as functions of their arguments* because of the infinitesimal coordinate transformations. Because the transformed y_A are not compared with the original values at the same world point, but with the original values at that world point which possesses the same coordinate values prior to the transformation, Eq. (2.3) contains a "transport" term, the second term on the right-hand side. Incidentally, in this equation, as well as throughout the paper, the summation convention is being applied both to the Greek indices which are associated with the coordinates and run from 1 to 4 and to the capital indices which run from 1 to N.

The transformation law (2.3) is, of course, not the most general law which may be encountered in geometrical objects, but it does include all types of tensors and tensor densities and also spinors. Being an infinitesimal transformation law, it is subject to the requirement that the commutator should again be an operator of the same type. This condition is represented by the

[1] Einstein, Infeld, and Hoffman, Annals of Mathematics **39**, 65 (1938).
[2] A. Einstein and L. Infeld, Annals of Mathematics **41**, 455 (1940).
[3] L. Infeld and P. R. Wallace, Phys. Rev. **57**, 797 (1940).

identity

$$F_{A\mu}{}^{C\nu}F_{C\rho}{}^{B\sigma}-F_{A\rho}{}^{C\sigma}F_{C\mu}{}^{B\nu}$$
$$\equiv\delta_\rho{}^\nu F_{A\mu}{}^{B\sigma}-\delta_\mu{}^\sigma F_{A\rho}{}^{B\nu}. \quad (2.4)$$

The field equations (2.2) must be covariant, i.e., if they are satisfied in one coordinate system, they must also be satisfied automatically in any other coordinate system. They would certainly be covariant if the integral I were an invariant, for in that case its extremization would also be an invariant operation. However, this condition is too strong, as it cannot even be satisfied in the general theory of relativity. There it is possible to introduce either a Lagrangian of which the integral is an invariant but which contains explicitly second derivatives of the field variables, or one which contains only first derivatives but which has no invariant integral. If the Lagrangian, in the face of an infinitesimal coordinate transformation, adds a divergence, then that condition is sufficient (though possibly not necessary) to assure covariant field equations. We shall, therefore, require that

$$\bar{\delta}L=Q^\mu{}_{,\mu}, \quad (2.5)$$

where the four expressions Q^μ are some functions of the ξ^μ and their derivatives (including those of higher order). In other words, it will be assumed that the infinitesimal change in the integral I can be expressed by means of a surface integral

$$\bar{\delta}I=\oint_S Q^\mu n_\mu dS, \quad (2.6)$$

without being affected by the values of the ξ^μ in the interior. The four quantities n_μ represent the components of a "unit normal vector" which is introduced so that Gauss' theorem can be formulated. This is possible even without the introduction of a metric.

By considering the transformation of a variation of the Lagrangian, $\bar{\delta}(\delta L)$, it can easily be shown that the field equations, because of Eq. (2.5) or its equivalent (2.6), satisfy the transformation law

$$\bar{\delta}L^B=-F_{A\mu}{}^{B\nu}\xi^\mu{}_{,\nu}L^A-(L^B\xi^\mu)_{,\mu}, \quad (2.7)$$

where the constants $F_{A\mu}{}^{B\nu}$ are identical with those introduced in Eq. (2.3).

III. IDENTITIES

Consider again the transformation law (2.5), which specifies that in the event of an infinitesimal coordinate transformation the change in the Lagrangian is a divergence. That change can also be represented in the form of a *variation* induced by the infinitesimal transformation:

$$\bar{\delta}L=L^A\bar{\delta}y_A+((\partial L/\partial y_{A,\rho})\bar{\delta}y_A)_{,\rho}. \quad (3.1)$$

Substitution of Eqs. (2.3) and (2.5) results in

$$(Q^\rho-(\partial L/\partial y_{A,\rho})\bar{\delta}y_A)_{,\rho}$$
$$=L^A(F_{A\mu}{}^{B\nu}\xi^\mu{}_{,\nu}y_B-y_{A,\mu}\xi^\mu). \quad (3.2)$$

The right-hand side will be a divergence only if the left-hand sides of the field equations satisfy the four identities

$$(F_{A\mu}{}^{B\nu}y_BL^A)_{,\nu}+y_{A,\mu}L^A\equiv 0. \quad (3.3)$$

In the general theory of relativity these identities are known as the contracted Bianchi identities. They hold no matter whether the field equations are satisfied or not.

The expressions L^A contain the field variables themselves and also their first and second derivatives. The second derivatives occur only linearly, and their coefficients can be represented in the form

$$L^A=L^{AB\rho\sigma}y_{B,\rho\sigma}+\cdots,$$
$$L^{AB\rho\sigma}=-\tfrac{1}{2}[(\partial^2L/\partial y_{A,\rho}\partial y_{B,\sigma})+(\partial^2L/\partial y_{A,\sigma}\partial y_{B,\rho})]. \quad (3.4)$$

When the L^A are substituted into the identities (3.3), the terms containing second derivatives will, in turn, lead to terms containing third derivatives, and those must cancel each other, irrespective of other terms,

$$F_{A\mu}{}^{B\rho}y_BL^{AC\sigma\tau}y_{C,\rho\sigma\tau}\equiv 0. \quad (3.5)$$

It follows that the coefficients $L^{AB\sigma\tau}$ must satisfy the identities

$$(F_{A\mu}{}^{B\rho}L^{AC\sigma\tau}+F_{A\mu}{}^{B\sigma}L^{AC\tau\rho}+F_{A\mu}{}^{B\tau}L^{AC\rho\sigma})y_B\equiv 0. \quad (3.6)$$

For what follows, $4N$ of these identities are of special interest, those in which ρ, σ, and τ all

equal 4,

$$F_{A\mu}{}^{B4}\Lambda^{AC}y_B \equiv 0,$$
$$\Lambda^{AC} = L^{AC44} = -\partial^2 L/\partial y_{A,4}\partial y_{C,4}. \tag{3.7}$$

Before concluding this section, it will be well also to formulate the conservation laws which are satisfied in a covariant theory. It is well known that in the presence of a Lagrangian, and provided the field equations are satisfied, there exist 16 quantities $t_\iota{}^\kappa$, functions of the field variables and their first derivatives only, which satisfy four divergence relationships:

$$t_\iota{}^\rho{}_{,\rho} = 0,$$
$$t_\iota{}^\kappa = \delta_\iota{}^\kappa L - y_{A,\iota}(\delta L/\delta y_{A,\kappa}). \tag{3.8}$$

If now the presence of matter in the field is represented by continuous and differentiable right-hand sides of the field equations,

$$L^A = P^A, \tag{3.9}$$

then the right-hand side of Eq. (3.8) no longer vanishes, but one obtains instead

$$t_\iota{}^\rho{}_{,\rho} = y_{A,\iota}P^A. \tag{3.10}$$

Because of the existence of the differential identities (3.3), this right-hand side can also be given the form of a divergence. Naturally, the field equations (3.9) can be satisfied only if the right-hand sides satisfy the same relationships which are satisfied identically by the left-hand sides. Therefore, Eq. (3.10) may be written in the form

$$T_\iota{}^\rho{}_{,\rho} = 0,$$
$$T_\iota{}^\kappa = \delta_\iota{}^\kappa L - y_{A,\iota}(\partial L/\partial y_{A,\kappa}) + F_{A\iota}{}^{B\kappa}P^A y_B. \tag{3.11}$$

Only in this "strong" form are the conservation laws useful in the consideration of situations in which matter is represented by continuous expressions P^A, or else by discrete singularities of the field variables.

IV. EQUATIONS OF MOTION

The equations of motion are obtained by the method initiated by Einstein and collaborators.[1,2] Because of the identities derived in Section III, any singularities present in the field are subject to certain restrictions which represent both the conservation of mass (or its equivalent) and the equations of motion. Just as in those papers, it is impossible to formulate these conditions precisely without taking recourse to an *approximation method*. This is because the motions of the singularities cannot be completely determined unless such effects as spontaneous polarization and spontaneous emission of radiation by the singularities are specifically excluded. This exclusion is accomplished by assuming that all motions are "slow" in the sense that differentiation of a field variable with respect to x^4 (the time) reduces the order of magnitude at every stage of the approximation method.

It shall be assumed that solutions of the field equations are to be obtained in the form of a power series expansion with respect to some parameter ϵ, which might, for instance, represent the order of magnitude of the material velocities involved, (v/c):

$$y_A = \overset{0}{y}_A + \epsilon\overset{1}{y}_A + \epsilon^2\overset{2}{y}_A + \cdots. \tag{4.1}$$

Moreover, the zeroth approximation shall be the "trivial" solution, a rigorous solution of the field equations in which all field variables are constants. (In the theory of relativity, this trivial solution is represented by the flat Minkowski metric.) The first approximation must then satisfy the following linear, homogeneous equations:

$$\overset{0}{L}{}^{ABrs}\overset{1}{y}_{B,rs} = 0. \tag{4.2}$$

In this approximation, there appear no time derivatives, because of the assumption that these are of a higher order of magnitude. The $\overset{0}{L}{}^{ABrs}$ are the coefficients (3.4), and the indices r and s are coordinate indices running from 1 to 3, in accordance with the usual notation in the literature. Because of the condition of "slow motion," this approximation will not contain radiation, but rather solutions corresponding to material particles, with as yet undetermined motions.

Generally, these solutions will not be defined throughout space. There will be singularities, probably of the $(1/r)$ type; more precisely, at each instant of time (x^4) there will be certain three-dimensional domains in which the field equations have no bounded solutions. However, only such solutions will be considered in which each one of these singular regions can be surrounded by a closed surface S (in three-dimensional space, S is two dimensional) on which the

field equations are satisfied. It is this condition of separateness of the singular regions which makes possible the formulation of additional requirements on the solutions outside.

If we proceed to the next approximation, the equations will have the form

$$\overset{0}{L}{}^{ABrs}\overset{2}{y}_{B,rs}=-\overset{2}{L}{}^{A}(\overset{0}{y}+\epsilon\overset{1}{y}). \tag{4.3}$$

The right-hand sides will be the L^A of the second order, formed from the first-order solutions (the $\overset{1}{L}{}^A$ vanish, of course). They will contain terms which are linear in the first and second time derivatives of the first approximation, and quadratic in the purely spatial derivatives of the first approximation.

Because of Eqs. (3.6), the left-hand sides of the second-order equations (4.3) satisfy identically the four relationships

$$F_{A\mu}{}^{Ct}\overset{0}{y}_{C}(\overset{0}{L}{}^{ABrs}\overset{2}{y}_{B,rs})_{,t}\equiv 0, \tag{4.4}$$

irrespective of the choice of the second-order field variables. In particular, it is possible to satisfy the field equations outside the singular regions and to continue the second-order variables throughout the interior of the singular regions with arbitrary continuous and three times differentiable functions. Then the conditions (4.4) will be satisfied throughout (three-dimensional) space and will permit the application of Gauss' theorem to a three-dimensional domain which includes a singular region but which is bounded by a closed surface on which the field equations are satisfied. On that surface, on which Eqs. (4.3) are to be satisfied, we have then

$$\begin{aligned} 0&\equiv \oint_S F_{A\mu}{}^{Ct}\overset{0}{y}_{C}\overset{0}{L}{}^{ABrs}\overset{2}{y}_{B,rs}n_t dS \\ &=-\oint_S F_{A\mu}{}^{Ct}\overset{0}{y}_{C}\overset{2}{L}{}^{A}(\overset{0}{y}+\epsilon\overset{1}{y})n_t dS, \end{aligned} \tag{4.5}$$

which represent for that singularity inside S the three equations of motion and the law of the conservation of mass (μ takes all four values $1\cdots 4$). It can be shown easily that these conditions for the first approximation are empty unless S encloses a singular region. The number of conditions which can be obtained equals, therefore, four times the number of separate singular regions.

V. UNIQUENESS OF SOLUTIONS, MOMENTA

In this section it will be shown first that if the field variables and their first derivatives are given on a three-dimensional hypersurface in space-time (e.g., throughout three-space at a specified time), the continuation of the solution beyond that initial hypersurface is not unique. As a corollary, it will then be shown that if canonical momenta are introduced in that formalism, not all the time derivatives of the field variables can be expressed in terms of these momenta. Both of these results can be predicted qualitatively from the covariance of the field equations. Suppose that one solution were known which satisfies the initial conditions on the hypersurface. Then one could always carry out a coordinate transformation such that the new coordinates coincide on the surface with the old ones, up to second derivatives, but not elsewhere. Then the solutions would be transformed into *formally* different solutions satisfying the same initial conditions. *Physically*, one would be inclined to call such equivalent solutions "the same solution;" in that sense, the solutions are presumably uniquely determined by the initial conditions.

It was pointed out previously that the field equations are linear with respect to the second derivatives of the field variables. If we choose as the hypersurface one with x^4 constant, then the y_A as well as the $y_{A,4}$ are given on that hypersurface. The continuation would be unique if the field equations could be solved with respect to the terms containing $y_{A,44}$. This, however, is not possible. Consider the coefficients of these second time derivatives. They are the quantities L^{AB44}. If the matrix

$$\|\Lambda^{AB}\|=\|L^{AB44}\| \tag{5.1}$$

were regular, then this solution could be accomplished. Actually, there are four different sets of N quantities which are zero eigenvectors of that matrix, as shown in Eq. (3.7). Conversely, there exist four linear combinations of field equations which are free of second time derivatives and which, therefore, represent restrictions on the choice of initial conditions on the hypersurface. They are

$$y_B F_{A\mu}{}^{B4}L^A=0. \tag{5.2}$$

It follows that four linear combinations of the

second time derivatives remain completely arbitrary on each space-like hypersurface. Naturally, the singling out of some particular coordinate as the "time" is completely arbitrary, and the term "time" was used only to conform to physical intuition.

The ambiguous character of the continuation of the solution with given initial conditions leads to pecularities of the canonical momenta which are analogous to those encountered in quantum electrodynamics. As is customary, the derivatives of L with respect to $y_{A,4}$ are designated as the momenta,

$$\partial L/\partial y_{A,4}=\pi^A. \tag{5.3}$$

These N equations cannot be solved with respect to the $y_{A,4}$, but, on the contrary, there exist four relationships between the π^A and y_A, $y_{A,s}$. First, Eqs. (5.3) can be solved with respect to $y_{A,4}$ only if the determinant of the partial derivatives

$$(\partial\pi^A(y_B, y_{B,s}, y_{B,4})/\partial y_{C,4})$$
$$=(\partial^2 L/\partial y_{A,4}\partial y_{C,4})=-\Lambda^{AC} \tag{5.4}$$

does not vanish. But Λ^{AC} is a singular matrix, and its determinant is zero. It follows that an attempt to solve with respect to the $y_{A,4}$ will result in the establishment of four relationships which do not contain any (first-order) time derivatives. In view of the $4N$ identities

$$y_B F_{A\mu}{}^{B4}(\partial\pi^A/\partial y_{C,4})\equiv 0, \tag{5.5}$$

these four relationships can be obtained by straightforward integration. They are

$$y_B F_{A\mu}{}^{B4}\pi^A - K_\mu(y_C, y_{C,s})\equiv 0, \tag{5.6}$$

where the K_μ are functions introduced by the integration, but actually determined in any theory.

VII. CONCLUSION

The relationships set up in the last Section will give rise to the usual difficulties in quantization, since the N momenta are not algebraically independent of each other. Four of the Hamiltonian equations will turn out to be empty, as a result. When the field variables y_A and π^A are reinterpreted as operators, it will not be possible to interpret Eqs. (5.6) as linear relationships satisfied by the operators π^A; such an assumption would be incompatible with the commutation relations. Rather, they will have to be interpreted as initial conditions which are imposed on the state vector and which are preserved automatically in the course of time. At each instant, the infinitesimal contact transformation leading from the state at t to the state at $(t+dt)$ will contain four arbitrary functions of the spatial coordinates. These arbitrary functions are usually eliminated by the setting up of so-called coordinate conditions, analogous to the gauge condition of electrodynamics; but it is also possible to retain this arbitrariness in the formalism and set up a quantized theory in which the Hamiltonian is determined only up to four arbitrary functions. It is proposed to examine these problems in a future paper.

Letters to the Editor

PUBLICATION of brief reports of important discoveries in physics may be secured by addressing them to this department. The closing date for this department is five weeks prior to the date of issue. No proof will be sent to the authors. The Board of Editors does not hold itself responsible for the opinions expressed by the correspondents. Communications should not exceed 600 words in length.

Emissions of Mesons in Cosmic Stars in Photographic Emulsions

ERIC PICKUP AND ADAIR MORRISON
Physics Division, National Research Council, Ottawa, Canada
January 3, 1949

ILFORD C2, boron, lithium, and deuterium loaded emulsions have been exposed to cosmic rays on transatlantic flights at an average height of 12,000–15,000 feet.[1] Meson tracks have been recorded in all these emulsions and one such event was previously reported.[2] Out of 1700 cosmic stars recorded with two or more prongs, including 600 with five or more prongs, there were 15 definite σ-mesons entering the emulsion, one $\pi-\mu$-event, where the μ-meson was entirely in the emulsion, two stars emitting σ-mesons, one star with a star producing fragment which is probably an α-particle, one or two stars emitting a particle which appears to be a meson ending without producing any visible disintegration, and 7 stars in which Li^8 nuclei are ejected[3] showing the characteristic hammer tracks. The numbers of these particular events produced within the emulsion relative to the total number of stars agrees fairly well, so far as we can judge with such small numbers, with the observations of the Bristol group[4] whose emulsions were exposed at about the same altitude, except that the number of π- and σ-mesons entering seems to be lower. Thus, in boron loaded emulsions, their estimated number of $(\pi+\sigma)$ mesons is about 17 percent of the number of stars with 5 prongs or more. Their observed number is less than this, but will be, however, greater than the observed 3 percent we get using varied emulsions as stated, but mainly boron loaded. The difference may be due to the smaller amount of extraneous material in the vicinity of the plates in the aircraft as compared with the mountain top experiments and would thus be a further strong indication that all such mesons are produced locally. Our figure is actually very similar to that given by Salant, Hornbostel, and Dollman[5] in balloon experiments at 100,000 feet. No estimate has been made yet of the number of ρ-mesons in our plates although these are present.[6]

The projected ranges of the two σ-mesons ejected from stars are 60μ and 700μ. The latter meson, which has an estimated energy of 5.2 Mev,[7] assuming mass 300 m, was emitted in a 3-pronged star, which shows also one short fragment, 4.5μ (probably an α-particle) and a lightly ionizing track which leaves the emulsion before it can be positively identified. A mosaic of photomicrographs of this event is shown in Fig. 1. The ejected meson is long; it suffers two large angle collisions and is finally captured at the end of its range, giving a nuclear disintegration in which only a small fraction of the energy available appears in visible charged fragments.

The initial ionization of the unidentified fragment in the primary star is seen to be very approximately the same as that of the meson. Hence, assuming it is not another meson,

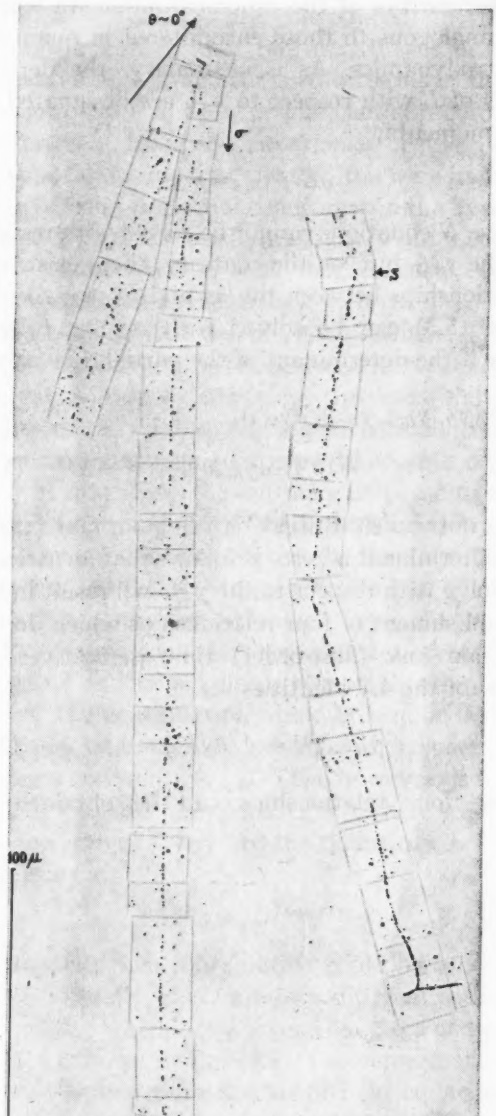

FIG. 1. Mosaic or photomicrographs showing meson ejected from star in Ilford C2, boron loaded emulsion (100μ thick). The meson track is shown in two parts, the points marked S being identical. The approximate direction of the zenith ($\theta=0°$) is indicated.

it could be a proton with energy about 30 Mev. The direction of the zenith (assuming this star to be formed while the aircraft was in level flight) is marked in Fig. 1, and so there is a downward momentum component for the visible fragments. The kinetic energy of the initiating radiation, if a nucleon, must have been more than 200 Mev.

Another point of interest in this event is the long range of the ejected meson. The chance of such a track lying wholly in the emulsion, so that identification is possible, is small. In view of this, and although very few events of this type have been reported yet,[4] we might speculate that an appreciable number of the cosmic stars observed give mesons which leave the emulsion before they can be identified, or are somewhat too energetic to leave a visible record (>about 7 Mev).[8]

We are indebted to the British Overseas Airways Corporation for carrying our plates, to Misses Joan Young, Shirley Young, and Beverly Mear for searching, and to Dr. W. J. Henderson for his interest in the above work.

[1] The plates were exposed on consecutive flights totaling about 400 hours over periods of about six weeks before development. The ceiling was about 25,000 feet.
[2] A. Morrison and E. Pickup, Phys. Rev. **74**, 706 (1948).
[3] Two of these seven events occured in an additional 160 stars of two or more prongs in C2, bismuth loaded emulsions, and one in some C2, unloaded emulsion.
[4] G. P. S. Occhialini and C. F. Powell, Nature **162**, 168 (1948) for σ-mesons from stars; C. F. Franzinetti and R. M. Payne, Nature **161**, 735 (1948) for Li^8 fragments; C. M. G. Lattes *et al.*, Nature **160**, 486 (1947), Table V for π- and σ-mesons.
[5] E. O. Salant, J. Hornbostel, and E. M. Dollman, Phys. Rev. **74**, 694 (1948).
[6] See U. Camerini *et al.*, Nature **162**, 433 (1948).
[7] Using the range energy relation given by Lattes, Occhialini, and Powell, Proc. Phys. Soc. **61**, 173 (1948), p. 181.
[8] We were able to trace back the longest σ-meson we have found, 1100μ with certainty. This corresponds to an energy of 6.8 Mev (for mass 300 m).

The Dielectric Behavior of $BaTiO_3$ Single-Domain Crystals

WALTER J. MERZ
Laboratory for Insulation Research, Massachusetts Institute of Technology, Cambridge, Massachusetts
December 27, 1948

THE measurements of the dielectric constants of $BaTiO_3$ have up to now been made on sintered materials[1] and on multi-domain crystals.[2,3] Once having succeeded in growing single-domain crystals it was of great interest to establish the anisotropy of the dielectric constant by making measurements parallel (ϵ_a) and perpendicular (ϵ_c) to the polar axis. Such a measurement was made by Mason and Matthias[4] and gave the unexpected result that ϵ_a was about 500 times greater than ϵ_c not only in the Curie region but also above the Curie point in the cubic region, where the polar axis disappears.

We have, therefore, repeated these measurements on very thin single-domain crystals of area of the order of a few mm^2. The great majority of crystals have the polar axis perpendicular to the large faces (c-crystals), so that the measurements of ϵ_a could be made only on small

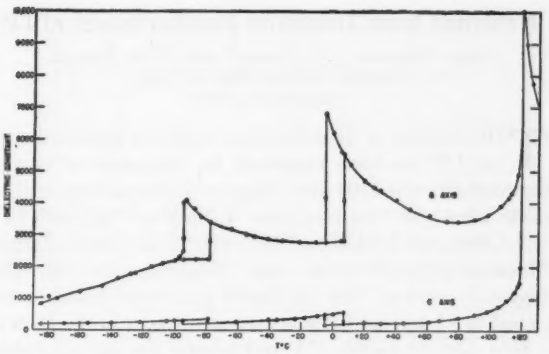

FIG. 1. Dielectric constant of $BaTiO_3$ single-domain crystals.

crystals. As a check, measurements of ϵ_a were also made on c-crystals and the results agreed satisfactorily.

It is seen (Fig. 1) that ϵ_a is greater than ϵ_c but in a more reasonable ratio of about 20:1 at room temperature, and that in particular $\epsilon_a = \epsilon_c$ at the Curie point as required by the transition to the cubic modification. The different behavior of ϵ_a and ϵ_c between the Curie point and the transition point at about 0°C can be explained, as confirmed by optical observations, by the fact that the Ti ion in the oxygen-octahedra has an increasing tendency to displace itself from the eccentric position [001] toward [011], until at the transition point the [011] position becomes suddenly the most stable one. An analogous behavior of the dielectric constant is observed between the transition points at about 0°C and −85°C. Here the stable position of the Ti ion in the oxygen octahedra seems to become the direction of the body diagonal [111]. It is significant that domain formation occurs at both transition points.

Above −5°C, that is, in the tetragonal temperature region, where there are no domains, the results for all the measured crystals are very reproducible. (In Fig. 1 are plotted the values of ϵ_a for the crystal which gave the highest values.) It is not clear whether one should expect theoretically $\epsilon_a \gtrless \epsilon_c$ below −95°C. However, below the transition point at about 0°C the single-domain crystals break up into several domains. This domain structure varies from sample to sample as shown by optical evidence, and the slight variation of the measured results. The appearance of a large thermal hysteresis would seem to substantiate this argument.

In contrast to the result of Mason and Matthias,[4] we have found at room temperature no drop in ϵ_a up to 40 Mc/sec. Furthermore, our hysteresis loops are quite symmetric and saturation is obtained with fields of only about 1000 volts/cm. This indicates that our crystals are more free of internal stresses (at least above −5°C) and contain less impurities than the crystals of Mason and Matthias (mostly Pt impurities).

[1] v. Hippel, Breckenridge, Chesley, and Tisza, Ind. Eng. Chem. **38**, 1097 (1946).
[2] Blattner, Matthias, Merz, and Scherrer, Experientia **3**, 148 (1947).
[3] Bernd T. Matthias, Nature **161**, 325 (1948).
[4] W. P. Mason and B. T. Matthias, Phys. Rev. **74**, 1622 (1948).

Neutrons from Deuteron Bombardment of Li^6

WARD WHALING, J. E. EVANS,* AND T. W. BONNER
The Rice Institute, Houston, Texas
December 27, 1948

THE number of neutrons from deuteron bombardment of Li^6 has been measured for deuterons of energy between 250 and 2200 kev. These neutrons are thought to come from the two reactions: $Li^6+H^2\rightarrow(*Be^8)\rightarrow Be^7+n+3.3$ Mev, and $Li^6+H^2\rightarrow(*Be^8)\rightarrow He^4+He^3+n+1.7$ Mev. Monoenergetic deuterons were obtained with the Rice Institute pressure Van de Graaff generator. Lithium enriched to 95 percent Li^6 was used as a target in the form of a thin film of Li_2SO_4 374 micrograms per sq. cm thick, which is equivalent to 124 kev for a 1-Mev deuteron.[1] The neutrons emitted in the direction of the deuteron beam were detected by means of the argon recoils in a proportional counter filled with argon at atmospheric pressure. The counter was biased to count neutrons of energy greater than 1 Mev. To correct for the Li^7 impurity in the target, the yield of neutrons from a normal Li_2SO_4 target of approximately the same thickness was measured under identical experimental conditions. Knowing the relative amounts of the two isotopes in each target, the contribution of each isotope alone can be determined. Plotted in Fig. 1 are the relative excitation curves for the two isotopes, corrected to indicate the yield of neutrons from targets of equal thickness of the pure isotopes. The units are arbitrary but are the same for both curves. The interval between successive points on the excitation curve is half the target thickness, and each point on the curve represents a count of at least 1280 on the neutron counter.

The angular distribution of the neutrons from lithium has been determined at several deuteron energies by counting the proton recoils from a number of polyethylene foils inside an argon-filled proportional counter. The counter subtended a solid angle of 0.025π at the target, and the neutrons were observed at 15-degree intervals between 0 and 150 degrees to the deuteron beam. The distribution of neutrons from Li^6 is essentially the same at 590, 1000, and 1700 kev, showing a maximum in the forward direction in the laboratory coordinates. The ratio of the counting rate at 0 degrees to that at 150 degrees is 7:4. The angular distribution of the Li^7 neutrons is practically spherical in laboratory coordinates at 605, 700, 820, and 1340 kev. At the 1020-kev resonance, the ratio of the counting rate at 0 and 150 degrees is approximately 2:1. This marked assymetry in the forward direction tends to exaggerate the effect of the 1020 resonance in observations made at 0 degrees.

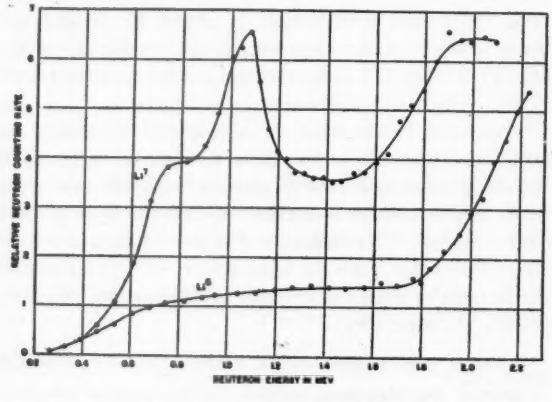

FIG. 1. Relative number of neutrons from separated isotopes of lithium, observed in the direction of the deuteron beam.

When allowance is made for the penetrability of the deuterons through the Coulomb barrier of the Li^6 nucleus, there appears to be a broad energy level in Be^8 excited by s-deuterons of about $\frac{1}{2}$ Mev energy, which corresponds to an excitation energy of 22.5 Mev in the Be^8 compound nucleus. The excitation curves have also been carried out for the two groups of protons from the competing reactions $Li^6+H^2\rightarrow(*Be^8)\rightarrow Li^7+H^1+5.0$ Mev and $Li^6+H^2\rightarrow(*Be^8)\rightarrow *Li^7+H^1+4.5$ Mev, and for the alpha-particles from $Li^6+H^2\rightarrow(*Be^8)\rightarrow He^4+He^4+22$ Mev. In both cases broad maxima in the cross section for disintegration were obtained, and after correcting for the Coulomb penetration, both sets of data indicate a resonance for deuterons of 0.4 Mev. The width of the resonance is about 0.5 Mev. It seems likely that the neutrons, protons, and alpha-particles all come from this same excited state of Be^8. The sharp rise in the neutron counting rate above 1.8 Mev seems to indicate an energy level in Be^8 excited by p-deuterons of energy between 2.5 and 3.0 Mev. The alpha-particle excitation curve does not show a resonance in this region,[2] which would be consistent with the assumption that deuterons with $l=1$ are responsible for this level.

This work was supported by the Research Corporation and by the joint program of the Office of Naval Research and the Atomic Energy Commission.

* Now at Los Alamos Scientific Laboratory.
[1] The enriched Li^6 was kindly furnished by the AEC, Isotopes Branch, Oak Ridge, Tennessee.
[2] N. P. Heydenburg, C. M. Hudson, D. R. Inglis, and W. D. Whitehead, Phys. Rev. **74**, 405 (1948).

Note on the East-West Effect*

A. T. BIEHL, H. V. NEHER, AND WM. C. ROESCH
California Institute of Technology, Pasadena, California
December 27, 1948

IN a recent flight to Peru in a B-29, continuous measurements were made at 3.10 equivalent meters of water barometric pressure (approximately 30,000 feet) of the intensity of cosmic-ray particles at the zenith, 45° west and 45° east. In addition the azimuthal variation was measured over Peru (magnetic latitude zero) at 2.35 m of water (approximately 38,000 feet) for zenith angles of $22\frac{1}{2}$°, 45°, and $67\frac{1}{2}$°. These measurements were made with both 10 cm and 20 cm of lead placed between the counters as well as with *no lead* absorber.** Because of the important bearing that such measurements have on the nature of the primary radiation, some of the preliminary results at the equator are herein reported.

Johnson and Barry[1] measured a west excess at a zenith angle of 60° of only 7 percent above 5 cm of Hg at 20° geomagnetic latitude north. Since this could be accounted

for in terms of the asymmetry in the penetrating component measured near sea level, it was concluded that there was no asymmetry in the soft component and hence that the soft component was due to equal numbers of primary positive and negative electrons. The penetrating component was identified as arising from primary protons.

Janossy and Nicolson[2] agree with this conclusion reached by Johnson, namely that the absence of a large east-west effect at high altitudes argues for two different kinds of primary particles at the equator.

The east-west effect in the penetrating component at intermediate latitudes and altitudes has recently been measured by Schein, Yngre, and Kraybill.[3] In the geomagnetic latitude range 27°–31° north, they report an asymmetry at 45° zenith angle of 0.46±0.07, at a pressure altitude of 34,500 feet, in the particles that can penetrate 22 cm of lead.

In the experiment here reported the asymmetries in both the hard and soft components were measured. The telescopes were the same as used previously by us,[4] except the extreme angles were changed to include ±16° in zenith angle and ±20° in azimuth. Counting rates at the vertical with no absorber were about 500 per minute at the equator at an atmospheric pressure corresponding to 3.10 m of water (32,000 feet). The experiment was performed at approximately 0° geomagnetic latitude and 76° west geographic longitude.

Table I gives a summary of the results at 45° zenith angle. The counting rate has been corrected for dead time of the counters, accidental counts, and for side showers. An indication of the magnitude of the shower correction was obtained by displacing the center tray of counters out of line. A detailed account of these corrections will be published elsewhere.

The following conclusions are drawn from the data in Table I: (a) That at these altitudes the west excess in the total radiation is nearly as large as in the penetrating component. (b) That the percentage asymmetry is increasing with altitude. The fact that the percentage west excess is greater for the more penetrating radiation together with the fact that it decreases with decreasing altitude may be due to scattering suffered by the lower energy particles.

More complete data at the higher altitude were taken. The percentage west excess as a function of zenith angle with and without lead absorber is plotted in Fig. 1. This brings out quite clearly the near equality in the asymmetry of the penetrating and soft components.

The conclusion to be drawn is, that as far as these experiments are concerned, it is not necessary to assume a different primary particle to account for the penetrating and soft components at the equator and that it is quite likely that only one kind of incident, positively charged particle will suffice.

TABLE I. East-west asymmetry over Peru, zenith angle 45°.

M of water equivalent	Thickness of Pb absorber	West excess* (%)
3.1	0	23.3±1.1
	10	27.6±1.3
	20	30.4±1.5
2.35	0	29.1±1.4
	10	33.0±1.6
	20	35.4±1.7

* Computed from the difference between west and east divided by the average.

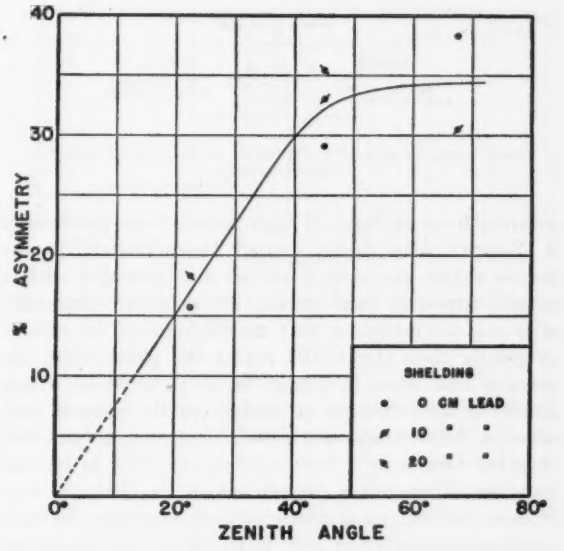

FIG. 1. The west excess in percent as a function of zenith angle with and without lead absorber.

We wish to thank the Office of Naval Research for making these flights possible. We also wish to extend our appreciation to Major W. A. Gustafson and his men of the Air Forces for their cooperation and skillful handling of the plane.

* This work was supported in part by the joint program of the ONR and the AEC.

** Data of 2.35 m of water and zenith angle of 22½° are missing for 10 cm of Pb and at 67½° for 20 cm of Pb because of lack of time.

[1] T. H. Johnson and J. G. Barry, Phys. Rev. 56, 219 (1939).
[2] L. Janossy and P. Nicolson, Proc. Roy. Soc. 192, 99 (1947).
[3] M. Schein, V. H. Yngre, and H. L. Kraybill, Phys. Rev. 73, 928 (1948).
[4] Biehl, Montgomery, Neher, Pickering, and Roesch, Rev. Mod. Phys. 20, 353 (1948).

The Double-Surface Transistor

JOHN N. SHIVE
Bell Telephone Laboratories, Murray Hill, New Jersey
December 28, 1948

IN a series of Letters to the Editor[1] appearing in a recent issue of this journal, there are described the physical construction and proposed theory of operation of a solid state semiconductor triode. This device, which is now called the type *A* transistor, comprises a block of high back-voltage germanium on one of the faces of which are two contacts, side by side with each other and close together. These contacts are called the emitter and collector, respectively. A large area contact to the opposite face of the semiconductor block is called the base contact.

The present communication describes another semiconductor triode, the double-surface transistor, in which the emitter and collector contacts bear on the two opposite faces of a thin wedge or slab of semiconductor. This slab is

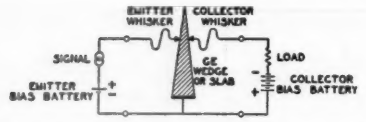

FIG. 1. Electrode geometry and circuit connections for a double-surface transistor.

prepared from an ingot of high back-voltage germanium of N-type.[2] After being ground approximately to the desired shape, the slab is etched and provided with a suitable large-area base contact. For good gain characteristics it is advantageous that the thickness of the slab be no greater than about 0.01 cm at the place where the contacts bear upon it. These contacts should be within about the same distance of coming exactly opposite each other on the two faces of the slab. Tungsten, copper, and phosphor bronze have been used successfully as contact materials. This device, together with its electrical connections for use as a grounded-base amplifier, is illustrated schematically in Fig. 1. In operation a comparatively large d.c. reverse bias (-50 to -100 volts) is applied to the collector, while a comparatively small d.c. forward bias (a few tenths of a volt) is applied to the emitter. Because of positive feed-back effects in the base contact and semiconductor body, the emitter bias voltage-to-base may in some cases be zero or even negative.

The static characteristics of a double-surface transistor are presented in Fig. 2. Families of collector voltage *vs.* collector current curves are given, with constant emitter current as parameter for the solid lines, and with constant emitter voltage as parameter for the dashed lines. Such a plot allows one to make judicious choice of d.c. operating point. It furnishes in addition complete information from which can be obtained, almost by inspection, the dynamic input and output impedances and the forward and backward transfer impedances of the device about any operating point selected.

In the double-surface transistor the emitter and collector points can be separated by surface paths many times longer than those in the type A transistor. It appears that double-

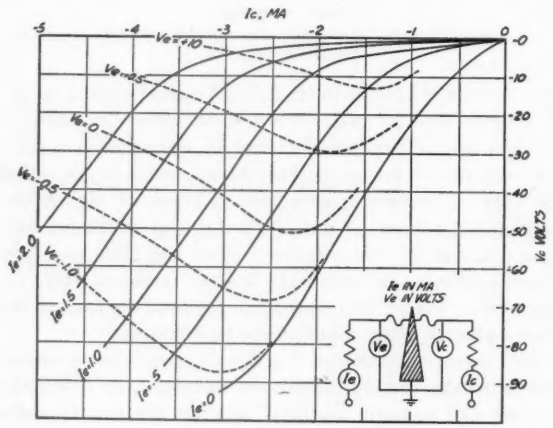

FIG. 2. Static characteristics of a double-surface transistor.

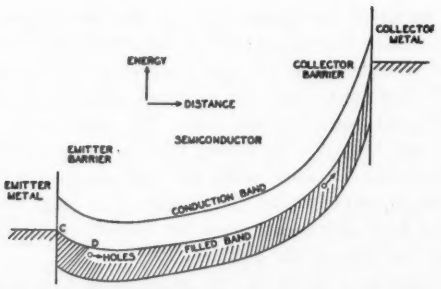

FIG. 3. Energy level diagram illustrating theory of double-surface transistor operation.

surface transistor action takes place through the body of the slab rather than along its surface layers. A tentative explanation of the transfer mechanism in this case is illustrated in the energy level diagram of Fig. 3. An important part of the picture is the bending up of the energy bands of the semiconductor from D to C, either as a result of the contact potential difference between metal and semiconductor,[3] or because of the presence of partly filled surface states on the surface of the semiconductor.[4] It is postulated that the bending up is sufficient to make the topmost levels of the filled band in the germanium accessible for the entry of positive holes from the conduction levels of the emitter metal. The potential of the interior of the semiconductor slab in the neighborhood of D is held at or near the base potential by the low resistance electrical path to the base. Application to the emitter of a positive bias with respect to the base decreases the depth of the barrier from C to D and increases the flow of holes past D into the interior of the slab, whence they are swept away by the collector field. Modulation of the hole current to the collector is thus secure by modulation of the emitter voltage.

A large part of the useful gain of the device is voltage gain resulting from the introduction of current from the emitter at comparatively low impedance and its subsequent withdrawal by the collector at comparatively high impedance. In some regions of the characteristic there is observed also a current amplification $\partial I_c/\partial I_e|_{V_c}$ of magnitude greater than unity. For the example of the unit described in Fig. 2 this current amplification is about 1.5 throughout the useful operating region. Some of this multiplication may be caused by ionizing collisions by holes in transit through the field at the collector barrier, and some by the alteration of this barrier field by the positive hole space charge in such a way as to increase the field emission of electrons from the collector.

The impetus for this development was supplied by the transistor discoveries by J. Bardeen, W. H. Brattain, and W. Shockley. To these men, and to J. A. Becker, the author is indebted for stimulating associations and discussions.

[1] J. Bardeen and W. H. Brattain, Phys. Rev. **74**, 230 (1948); W. H. Brattain and J. Bardeen, Phys. Rev. **74**, 231 (1948); W. Shockley and G. L. Pearson, Phys. Rev. **74**, 232 (1948).

[2] The ingot was prepared by J. H. Scaff and H. T. Theuerer according to the method generally described in H. C. Torrey and C. A. Whitmer's *Crystal Rectifiers* (McGraw-Hill Book Company, Inc., Chapter 12, New York).

[3] N. F. Mott, Proc. Camb. Phil. Soc. **34**, 568 (1938); W. Schottky, Zeits. f. Physik. **113**, 367 (1939); see also Reference 2, Chapters 3 and 4.

[4] John Bardeen, Phys. Rev. **71**, 717 (1947).

Investigation of Hole Injection in Transistor Action

J. R. HAYNES AND W. SHOCKLEY
Bell Telephone Laboratories, Murray Hill, New Jersey
December 28, 1948

THE experiments to be described here were undertaken to furnish direct experimental evidence concerning the nature of the carriers responsible for the impedance decrease which is produced at a collector point by passing current in the forward direction through an emitter point of a transistor.[1]

The sample of germanium used in the experiment was a block of *n*-type high back voltage material having dimensions of 9×3×0.5 mm and provided with plated electrodes at either end. The circuit used is shown in Fig. 1. Current is passed through five emitter points and into the germanium crystal on closing a relay which is actuated sixty times a second. A battery and a key are connected in series across the electrodes so that the electric field in the crystal may be altered.

In series with a collector point is placed a resistance of 5000 ohms and a battery. The collector is negative with respect to the germanium so that the impedance at the contact point is high (order of 0.1 megohm). The current through the 5000-ohm resistance is accordingly closely proportional to the collector point conductance. The voltage across this resistance is connected to the vertical plates of a cathode-ray oscilloscope so that the collector point conductance can be examined as a function of time.

A sketch of the oscilloscope trace obtained when the collector point is placed 1 millimeter from the emitter point is shown in Fig. 2. The dots represent 1-microsecond marker intervals obtained on the oscilloscope trace. An initial short rise in signal voltage is obtained when the relay is closed. This initial rise is primarily due to the potential drop produced by the normal current flow in the germanium.

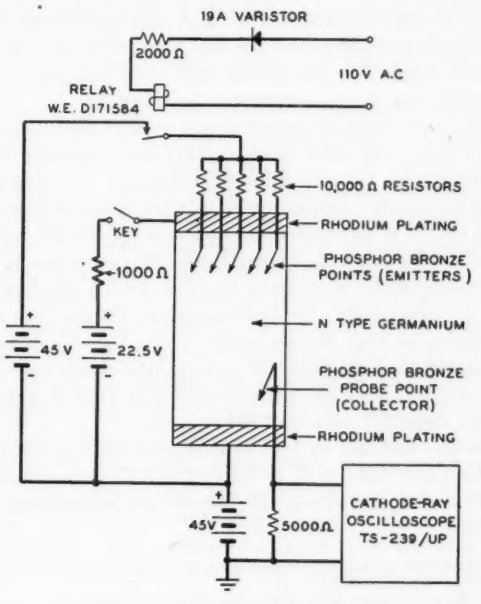

FIG. 1. Circuit arrangement for the investigation of hole injection.

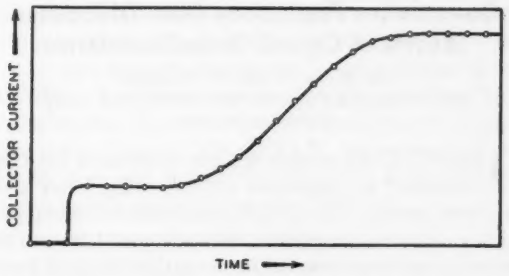

FIG. 2. Oscilloscope trace showing delay of holes in reaching collector.

After this initial rise the current into the collector point remains constant for about five microseconds when a second rise begins. This time delay between the injection of current from the emitter points and the start of current increase in the collector point is found to vanish as the collector point approaches the emitter points. It is evident, therefore, that the delay in this second increase in current through the collector point is due to the finite velocity of some kind of carrier which increases the conductance of the collector point on arrival.

The sign of the charge borne by the carriers was found by closing the key. This decreases the transit time of the carriers when the battery is connected as shown in Fig. 1 and increases it when the battery is reversed. Quantitative investigation of the relationship between electric field, delay, and distance shows that the effect is transmitted as expected for positive particles with a mobility of about 1.2×10^3 cm²/volt sec. in agreement within experimental error with the behavior of holes as established by Hall effect in *p*-type germanium. Further experiments with the collector placed on the opposite side of the block from the emitter points show that the holes are distributed through the interior. These results are consistent with J. N. Shive's observation[2] that transistor action can be obtained with points on the opposite sides of a thin piece of germanium and with those of E. J. Ryder and W. Shockley[3] on resistance in high electric fields.

An estimate of the mean life of positive holes in this sample of germanium has been made by measuring the signal voltage increase produced on hole arrival as a function of time delay. Analysis of the data shows that this voltage decreases exponentially at the rate of $1/e$ in 10 microseconds. This value is evidently also the mean life of the positive holes if it is assumed that the collector conductance is an approximately linear function of hole density.

We are indebted to A. H. White and C. Herring for suggestions regarding the interpretation of the mobility data.

[1] J. Bardeen and W. H. Brattain, Phys. Rev. 74, 230 (1948).
[2] J. N. Shive, Phys. Rev., this issue.
[3] E. J. Ryder and W. Shockley, Phys. Rev. 75, 310 (1949).

Quantitative Predictions from Dislocation Models of Crystal Grain Boundaries

W. SHOCKLEY AND W. T. READ
Bell Telephone Laboratories, Murray Hill, New Jersey
December 28, 1948

DISLOCATION models of grain boundaries have been discussed by numerous authors. This letter shows that these models have certain quantitative consequences which are directly susceptible to experimental test, so that theoretical and experimental investigations of grain boundaries may furnish a direct proof of the presence of particular arrays of dislocations in solids.

Of particular interest are grain boundaries between crystallites differing by a small angular rotation about an important crystallographic direction, such as that shown for a simple cubic model in Fig. 1(A). For this highly symmetrical case, the boundary is equivalent to a row of dislocations (B); if the boundary is parallel to the planes of the left grain, two types of dislocations will be required (C). For any such model there are simple relationships between the arrangement of the dislocations and the orientation of the grains and grain boundary. For Fig. 1(A) we have $\sin(\theta/2)=a/2L$ where a is the slip vector of the dislocation. For $\theta<1°$, L will be >100A so that the dislocation structure of small angle grain boundaries should be resolved by electron microscopy. The writers propose that such dislocation structures have already been optically resolved for very small angle boundaries. In connection with "veining" in aluminum, P. Lacombe[1] has observed that the veins separate regions of slightly different orientation (1.3×10^{-3} radian estimated from Fig. 3[1]); the veins are revealed by rows of similar etch pits. Assuming each etch pit originates on a dislocation, the spacing $L=3\times10^{-4}$ cm (estimated from Fig. 1[1]) gives $\theta=10^{-4}$ radian. The discrepancy of 13 is probably explained by the fact Figs. 1 and 3 correspond to different specimens. The veins shift radically after reannealing at 600°; although they are not straight where they intercept the surface, Fig. 1 shows they extend perpendicularly (within $<0.3°$) straight through the specimen—results consistent with arrays of dislocations.

For larger angle boundaries, minimum energy arrays should give definite interfacial energies; these arrays would be established at high temperatures by interactions between, and motions of, the dislocations and by vacancy diffusion. Figure 1 (A and B) represents the minimum energy array for the simple cubic model; for the approximation of an isotropic model with shear modulus μ and Poisson's ratio σ and for small θ, we find that the interfacial energy is

$$\gamma=[\mu a/4\pi(1-\sigma)]\theta(A-\ln\theta), \qquad (1)$$

where A is a constant depending upon the energy near the dislocation where Hooke's Law fails. (For Nabarro's[2] simple cubic model we find $A\doteq0.8$.) The coefficient of $\theta\ln\theta$ depends only on integrals where the strain is small; hence, it can be calculated without approximations, from the elastic constants and the slip vector "a" of the dislocation used. Similar results will hold for anisotropic materials and more complicated boundaries.

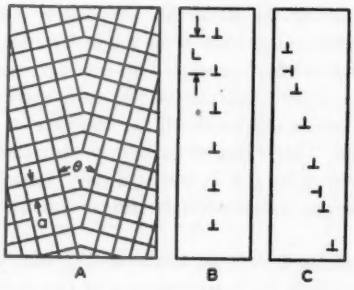

FIG. 1. Simple grain boundaries in cubic model: (A) symmetrical grain boundary, (B) equivalent array of dislocations, and (C) array for unsymmetrical grain boundary.

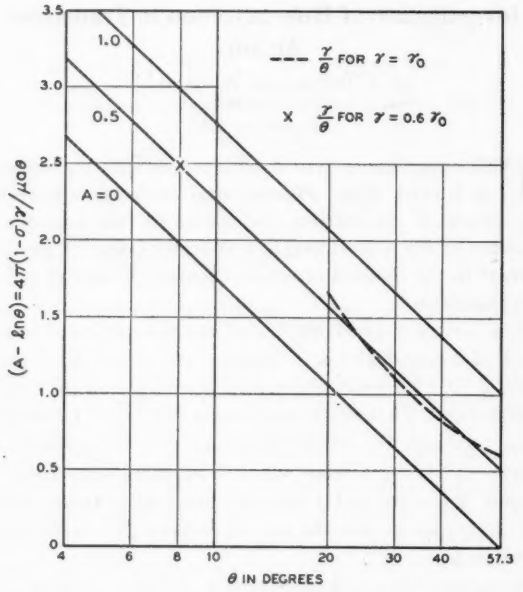

FIG. 2. Predicted dependence of interfacial energy γ upon orientation difference θ.

Thus experimental values of γ/θ should plot *versus* $\ln\theta$ as a straight line with slope $\mu a/4\pi(1-\sigma)$. Recently C. G. Dunn[3] of the General Electric Company has measured grain boundary energies on a relative scale in iron and finds that γ is approximately constant for $\theta>20°$ and for $\theta=8°$ $\gamma=0.6$ times the higher value. This data can be well approximated by a straight line for $A=0.5$ as shown in Fig. 2; surprisingly, the approximation fits the data even for angles as large as one radian. Using Eq. (1) (which is calculated for a simple cubic lattice), the elastic constants for iron, and $a=2.5$A, we estimate that Dunn's approximately constant value is 1300 ergs/cm^2.

We are indebted to J. H. Holloman of the General Electric Company and to C. S. Barrett and C. S. Smith of the Institute for the Study of Metals for stimulating discussions.

[1] P. Lacombe, *Report of Conference on Strength of Solids* (The Physical Society of London, 1948).
[2] F. R. N. Nabarro, Proc. Phys. Soc. **59**, 256 (1947).
[3] We are indebted to C. G. Dunn for this data which is scheduled for the February issue of Journal of Metals.

On the Showers of Mesons and Nucleons

G. WATAGHIN
Universidade de São Paulo, São Paulo, Brasil
January 3, 1949

RECENT experimental results induce us to attempt a revised formulation of the fundamental assumptions proposed in previous papers in order to give a quantitative description of the production of mesons.[1]

1. We assume, of course, that the fundamental process occurring in a high energy collision of nucleons or nuclei is the production of showers of mesons (probably π-mesons and, eventually, other short-lived mesons) and nucleons. The direct production of photons and electrons is assumed to be a secondary phenomenon in most cases (except, perhaps, in the case of highly charged incident nuclei).

2. Indicating by ΔE the fraction of the energy E of the incident nucleon lost in the collision and measured in the terrestrial frame, we assume: $\Delta E/W\sim 1$, and we denote: $av(\Delta E/E)=k$. Considering the possible change of the spin and the charge, we can say that after the collision there will be usually one nucleon having an average energy $E-\Delta E=(1-k)E=qE\sim E$.

3. The energy amount ΔE lost by the incident nucleon will be shared between the created mesons and some nucleons taking part in the collision. We shall consider the center of mass system of this assemblage of mesons and nucleons and apply to it statistical laws. Then, following the deduction indicated in previous work,[1] we find: $\Delta E\geqq An^2+Bn+C$ where A, B, and C are constants having values depending on the masses of the colliding nuclei and n is the number of mesons produced. For large values of n (e.g. $n>100$) we can put $\Delta E\sim An^2$ and thus, approximately, $n\sim(E)^{\frac{1}{2}}$ as pointed out.[1] For smaller showers $10\lesssim n\lesssim 100$ one has: $\Delta E\sim Bn$.

4. The cross section for meson production σ of a primary proton or a fast nucleon with a nucleon at rest is $\sim 3\times 10^{-26}$ cm^2. Thus the collision thickness l for production in cascade of showers of mesons and nucleons by fast nucleons is: $l\sim(M/\sigma)\sim 50$ g/cm^2.

Observations show that almost all energetic showers contain mesons and, therefore, are originated by nucleons. The average value of q can be found from the known value of the frequency of the primary protons and of the fast nucleons at sea level. Indeed, from the assumptions 2 and 4 it follows that the energy of a primary proton is reduced after n collisions by a factor $q^n=q^{x/l}$, where x is the atmospheric depth in g/cm^2. If we neglect the contribution of low energy nucleons, and assume the spectral distribution of the primary protons to be of the type: $dN_P=CE_P^{-\gamma}dE_P$ where $\gamma\geqq 2.5$, the spectral distribution of fast nucleons after n collisions will be: $dN_N=Cq^{n(\gamma-1)}E_N^{-\gamma}dE_N$. Thus the spectral power law is conserved and the reduction factor is: $q^{n(\gamma-1)}=q^{0.03x}$. From the observations we have for the ratio of the primary and the sea-level intensity of fast nucleons a value $\sim 3\times 10^5$. Therefore we obtain $q\sim 0.7$. The resulting approximate description of showers of mesons and nucleons permits one to understand many observed phenomena. Here we want to discuss the remarkable formula giving the number dN' of showers having densities δ in the interval $(\delta, \delta+d\delta)$: $dN'=C'g(\delta)\delta^{-\gamma}d\delta$, where $g(\delta)\to 1$ for high δ, and $\lim_{\delta\to\infty}g(\delta)\delta^{-\gamma'}=0$ and where $\gamma'\sim 2.5$. This spectral distribution is very similar to the distribution of primary protons ($\gamma'=\gamma$). Indeed for local showers the electronic density can be assumed proportional to the meson density. The latter is proportional to the multiplicity n, and thus to $Bn\sim\Delta E\sim E_N$. Comparing the formulas for dN' and dN_N we see: $\gamma'=\gamma$.

[1] G. Wataghin, Phys. Rev. **74**, 975 (1948).

The Isotopic Constitution of Dysprosium

MARK G. INGHRAM, RICHARD J. HAYDEN, AND DAVID C. HESS, JR
Argonne National Laboratory, Chicago, Illinois
December 29, 1948

THE isotopic constitution of dysprosium was first investigated by Aston[1] who found isotopes of masses 161, 162, 163, and 164. He obtained the relative abundances of these isotopes by using a discharge tube with $DyBr_3$ as an ion source, and estimating line intensities on his photographic plates by photometry. Later, Dempster[2] discovered weak isotopes at masses 158 and 160 and estimated the abundance of these isotopes. He did not quote the percentage abundances of the other isotopes. Dempster's values for the percentages of Dy^{158} and Dy^{160} and Aston's values for the heavier isotopes, corrected for the presence of Dy^{158} and Dy^{160}, are given in Table I. Later Wahl[3] made a photometric determination of the abundances of all these isotopes in which he quoted more significant figures than did Aston. Recently[4] two of the authors reported the existence of a stable Dy^{156} isotope present to about one-twentieth of one percent. Because of the discrepancies between the values of Wahl (Table I) and the earlier investigators and because of the large errors inherent in the photometric method, it seemed desirable to measure electrometrically the relative abundances of the dysprosium isotopes. In the course of this work upper limits for the existence of other isotopes were set.

A sample of Dy_2O_3, especially purified with an ion exchange column by Dr. D. H. Harris of the Clinton Laboratories, was analyzed by a filament source mass spectrometer utilizing a recording vibrating reed electrometer to detect the ion beam. The instrument and techniques used in this mass analysis have been described elsewhere.[5] Dysprosium peaks of types Dy^+ and DyO^+ were both observed, but due to the weaker emission in the DyO^+ position, the precision of the measurements at this position was much less. Thus, the values given have been calculated only from the Dy^+ position. The DyO^+ values are, however, consistent with the Dy^+ results. The third row in Table I gives our values for the percentage abundances of the various dysprosium isotopes. The errors quoted are larger than the probable mean deviations in the percentages based on twenty separate determinations. Despite an apparent accuracy of about $\frac{1}{4}$ percent obtained for the probable error calculated on the basis of mean deviations, we do not wish to quote probable errors in any

TABLE I. Isotopic constitution of dysprosium (percent).

Investigator	156	158	160	161	162	163	164
Aston	—	—	—	22.0	24.0	24.0	28.0
Dempster	—	0.1	1.5	—	—	—	—
Wahl	—	0.1 trace	(0.1)	21.1	26.6	24.8	27.3
Inghram, Hayden, and Hess	0.0524 ±0.0005	0.0902 ±0.0009	2.294 ±0.011	18.88 ±0.09	25.53 ±0.13	24.97 ±0.12	28.18 ±0.14

mass to less than ½ percent of the abundance of that mass. This is done because we have been unable to rule out systematic discriminations in mass due to selective emission from the surface ionization source and due to non-linearities in the 10^{10}-ohm collector resistor to a greater precision than this.

The freedom of this dysprosium sample from rare earth impurities allowed upper limits for the natural occurrence of other isotopes of dysprosium to be set. For the possible isotopes we have $Dy^{154}<0.002$ percent, $Dy^{155}<0.002$ percent, $Dy^{157}<0.002$ percent, $Dy^{159}<0.008$ percent, $Dy^{165}<0.011$ percent and $Dy^{166}<0.002$ percent.

A calculation of the chemical atomic weight of dysprosium, based on these isotopic abundances and assuming a packing fraction of -1.0×10^{-4}, gives 162.51. The chemically determined value is 162.46.

[1] F. W. Aston, Proc. Roy. Soc. **A146**, 46 (1934).
[2] A. J. Dempster, Phys. Rev. **53**, 727 (1938).
[3] Wahl, Suomen Kemistiseuran Tiedonatoja **51**, 64 (1942).
[4] D. C. Hess, Jr., and M. G. Inghram, Phys. Rev. **74**, 1724 (1948).
[5] M. G. Inghram, R. J. Hayden, and D. C. Hess, Jr., Phys. Rev. **72**, 967 (1947).

The Vertical Intensity at 10,000 Feet of Ionizing Particles That Produce Penetrating Showers

W. E. HAZEN, C. A. RANDALL, AND O. L. TIFFANY
Randall Laboratory of Physics, University of Michigan, Ann Arbor, Michigan.
December 23, 1948

A LARGE cloud chamber was operated at Echo Lake, Colorado (10,600 ft.) for the purpose of measuring the intensity of ionizing particles that produce showers containing penetrating particles and to study the details of the showers. Since the films were destroyed by fire, it will not be possible to study the showers in detail but an estimate of the intensity can be based on a preliminary survey of the films, which were made in the field.

Collimating telescopes of small solid angle (⅛ sterad.) were placed above the chamber to insure that the events would occur in the useful region of the chamber. Since the events were expected to be rare, six two-counter telescopes were placed side by side, each directed into the useful region of the chamber. A shower tray of eight 1″×30″ G-M tubes, placed below the chamber and shielded on top and sides by two inches of lead, served to detect particles emerging from the chamber. A coincidence between any one of the telescopes and any three or more of the shower counters triggered the chamber and a stereoscopic picture was taken. A one-half inch lead plate was placed above the telescope array to facilitate identification of electrons entering the chamber.

In experiment *A* (Fig. 1), the chamber contained five one-inch lead plates. In a net observation time of 3750 minutes, 30±5 pictures were obtained that showed penetrating showers originating in the lead plates. Assuming that ionizing particles which produce penetrating particle showers are absorbed in lead with a collision path of 180 g/cm², 40 percent of the incident particles will produce showers in 85 g/cm² of lead.[1] This leads to an estimate of 75±15 incident particles in 3750 minutes. Using the same telescope array, but with 3½ inches of lead between the telescope counters, it was found that 31±1 penetrating particles per minute were detected by the telescope array. Hence there was about one shower-producing ionizing particle per 1500 penetrating particles from directions near the vertical. From the well-known intensity of the penetrating component and the above ratio, we obtain $1.1\pm0.3\times10^{-5}$ cm^{-2} sec.$^{-1}$ sterad.$^{-1}$ for the intensity of ionizing, penetrating, shower-producing radiation at Echo Lake. The estimated uncertainty is based on the estimated uncertainty in identification of nuclear disintegrations in the preliminary survey of the data.

If we assume that the majority of the primary cosmic rays can produce nuclear disintegrations of the type we have observed, it is possible to calculate an average absorption path length in air and to estimate an average collision path length. The total intensity of the primary radiation has been calculated by Rossi[2] to be 0.07 cm^{-2} sec.$^{-1}$ sterad.$^{-1}$ for energies greater than 4 Bev for protons. The average absorption path length, assuming exponential absorption, is therefore $L=700/\ln(0.07/1.1\times10^{-5})=80$ g/cm² between the top of the atmosphere and Echo Lake. Tinlot[3] has made direct measurements for the absorption in the atmosphere of locally produced showers of about the same energy as in our case with a result of 118 g/cm². The apparent differences are that Tinlot accepted both charged and uncharged incident particles, the entrance angle was large, and the measurements did not include the top 300 g/cm² of the atmosphere. It is not clear what conclusion might be made from a comparison of the two results.

A collision length in air can be estimated from our results since the primary spectrum presumably is known, and we can therefore take into account the effect of secondaries that can also produce disintegrations. The minimum effective energy for the secondaries is estimated to be one Bev from consideration of the detector and of the com-

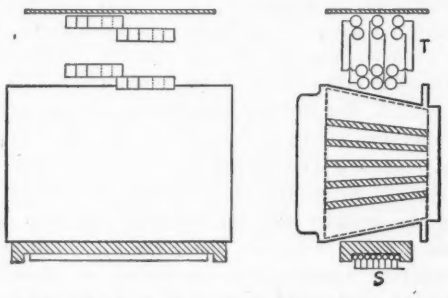

FIG. 1. Back and side elevations of cloud chamber, showing location of telescopes (*T*) and shower tray (*S*). The five lead plates shown are for experiment *A*. These were replaced by four aluminum and two lead plates for experiment *B*.

petition from ionization loss. Therefore, if we assume that the maximum number of energetic, penetrating, shower-producing particles emitted in a disintegration is 5 and that these secondaries receive one-fourth of the energy of the incident particle, the average number of effective generations n is given by: $E/(4\times5)^n=1$ Bev, where E is in Bev. Since the number of particles m in the nth generation is $m=5^n$, we have $\log m=(\log E)\log 5/\log 20=0.54\log E$. If we neglect ionization loss and assume that the secondary rays have the same collision probability as the primaries, the intensity at h is

$$I_h=e^{-h/L}\int_4^\infty m dI(E),$$

where $I(E)$ is the intensity of primary rays with energy above E. The result is $I_h=3I(4)\exp-h/L$ and the value of L, which is now the collision path length, is $L=70$ g/cm².

Arrangement B, in which the top four plates were aluminum, was designed to permit more detailed observation of the mixed showers by making use of the fact that low cascade multiplication of electrons in aluminum would result in lower shower particle densities. In 2570 minutes of observation there were 18 ± 4 pictures of penetrating showers that originated in the aluminum. An estimate of the dependence of collision cross section on atomic number can be made from the relative frequencies of production of penetrating showers in the lead and in the aluminum. The data are consistent with an $A^{\frac{1}{2}}$ variation for the cross section.

The observations were financed in part by the Horace H. Rackham School of Graduate Studies and by the Office of Naval Research. We are grateful for the assistance of Dr. Cohn and Dr. Iona of the University of Denver.

[1] We are indebted to Dr. G. Cocconi for the private communication of the measured value of 180 g/cm².
[2] Bruno Rossi, Rev. Mod. Phys. 20, 573 (1948).
[3] John Tinlot, Phys. Rev. 74, 1197 (1948).

On Electromagnetic Diffraction through a Plane Screen

JOHN W. MILES
Department of Engineering, University of California, Los Angeles, California
December 23, 1948

A POWERFUL variational attack on scalar diffraction through a plane screen[2] has recently been formulated by Schwinger and Levine.[1] Following Schwinger's original variational approach to wave guide diffraction problems (unpublished, M.I.T. Radiation Laboratory, 1944), the writer had independently arrived at a similar (but less powerful) approach to scalar and vector diffraction problems. Results for acoustic diffraction through a circular aperture have been obtained and will be published elsewhere.[3]

An infinite plane screen, consisting of a perforated (aperture) region σ and a perfectly conducting (obstacle) region τ occupies the plane $z=0$. An electromagnetic

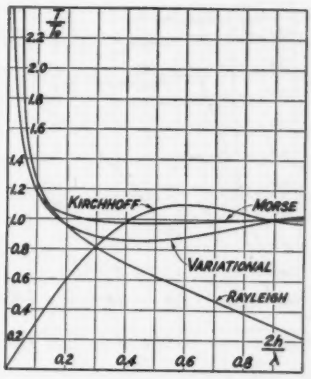

FIG. 1. Transmission cross section (relative to geometric) of slit of width $2h$ for normal incidence of plane wave.

wave ($\mathbf{E}_i$, $\mathbf{H}_i$) is incident from the left ($z<0$). As is well known, the vector fields everywhere may be determined from the tangential electric field over the screen, the representation of the fields in terms of vector eigenfunctions to the wave equations being facilitated by the use of vector transforms.[4] The boundary conditions that the magnetic field be continuous across the aperture and that the electric field vanish on the screen lead to a dual (vector) integral equation for the aperture field, which in turn may be cast in a variational form, a technique due originally to Schwinger.

Let $Z_i=Y_i^{-1}$ be the impedance of the *transverse components of the incident wave*, defined such that

$$\mathbf{H}_i=(\epsilon/\mu)^{\frac{1}{2}}Y_i(\mathbf{k}\times\mathbf{E}_i), \tag{1}$$

where $\mathbf{k}$ is a unit vector along the z axis. An aperture impedance Z_σ is defined as the ratio of the complex power transferred through the aperture to that predicted by geometrical optics, and the ratio of the real part of this parameter to Z_i (which is real if the incident wave is freely propagated) is the ratio of the total transmission cross section to the (projected) geometric area. The variational expression for the reciprocal of the aperture impedance is

$$Y_\sigma=\frac{S_\lambda\{|E_i(\lambda)|^2\}S_\lambda\{Y(\lambda)|E_\sigma(\lambda)|^2\}}{|S_\lambda\{\langle E_i(\lambda)\rangle_{A\sigma}E_\sigma(\lambda)\}|^2}, \tag{2}$$

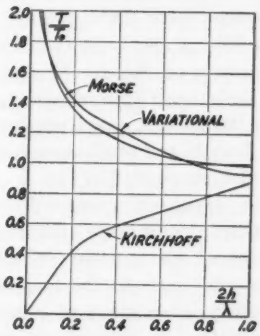

FIG. 2. Transmission cross section of slit for 45° oblique incidence.

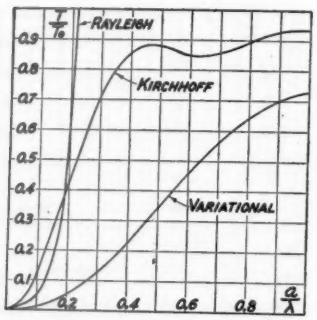

FIG. 3. Transmission cross section of circular aperture of radius a.

where $E_i(\lambda)$ and $E_\sigma(\lambda)$ are the "vector" transforms of the transverse components (parallel to screen) of the incident (at $z=0$) and aperture electric fields, respectively, in the sense of reference 4, the angular brackets with subscript Av denote the complex conjugate, S_λ denotes integration over the entire transform (λ) spectrum, and $Y(\lambda)$ represents the admittance for the eigenmode at a point λ in this spectrum and is defined by

$$Y^{(1)}(\lambda)=[1-(\lambda/k)^2]^{-\frac{1}{2}}, \tag{3a}$$

$$Y^{(2)}(\lambda)=[1-(\lambda/k)^2]^{\frac{1}{2}}, \tag{3b}$$

where the superscripts 1 and 2 denote the TM and TE modes, respectively. k is the wave number (2π/wavelength), and the paths of integration in the λ-spectrum are indented under and over the branch points $-k$ and $+k$, respectively. Equation (2) is variational in the sense that both its real and imaginary parts are stationary with respect to variations of the aperture field about the true solution to the aforementioned integral equation. In the case where only a single class of modes (TM or TE) is excited both the real (G_σ) and imaginary (B_σ) parts of Y_σ are positive definite forms and are therefore absolute minima, while in the more general case only G_σ is an absolute minimum. It is of further interest to remark that *if the approximation $E_\sigma=E_i$ is made in Eq. (2)*, the ratio of the transmission coefficient predicted by Kirchhoff optics to that predicted by geometric optics is given by G_σ/Y_i.

As examples, the problems of diffraction through a slit (magnetic vector parallel to slit) and a circular aperture were considered. The incident field was used to obtain the first variational approximations for the cases of normal and 45° oblique incidence of a plane wave on the slit, and the results are compared with the Kirchhoff, Rayleigh,[5] and exact results[6] in Figs. 1 and 2. In the case of normal incidence of a plane wave on the circular aperture of radius a the field in the variational approximation was adjusted so as to reduce to the known, exact results in the limits of both large wave-length[7] and small wave-length (geometrical optics). The results are plotted in Fig. 3.

An alternative approach, more suitable for the case where the obstacle (τ) is of finite area, is to formulate the problem in terms of the current in the obstacle. The analysis is quite analogous to the foregoing. In the case of a complementary interchange of σ and τ and $\mathbf{E}_i$ and $-\mathbf{H}_i$ this formulation is related to the foregoing by Babinet's principle.[8] Thus, Figs. 1 and 2 give the reflection cross section for a plane wave with the electric vector parallel to a flat strip, and Fig. 3 gives the reflection cross section for a plane wave normally incident on a circular disk.

[1] J. Schwinger and H. Levine, Phys. Rev. **74**, 958–974 (1948).
[2] H. Levine has informed the writer (personal correspondence) that he intends to carry out a similar investigation for the vector problem.
[3] John W. Miles, J. Acous. Soc. Am. (to be published).
[4] John W. Miles, Phys. Rev. **74**, 1531 (1948).
[5] Lord Rayleigh, Phil. Mag. **43**, 259–272 (1897).
[6] P. M. Morse and P. J. Rubenstein, Phys. Rev. **54**, 859–898 (1938).
[7] Lord Rayleigh, Phil. Mag. **44**, 28–52 (1897); H. Bethe, Phys. Rev. **66**, 163–182 (1944).
[8] E. T. Copson, Proc. Roy. Soc. London **A186**, 100–118 (1946).

Hf^{175}, a New Radioactive Isotope of Hafnium

GEOFFREY WILKINSON AND HARRY G. HICKS
Radiation Laboratory and Department of Chemistry, University of California, Berkeley, California
January 3, 1949

A STUDY has been made of hafnium activities produced by bomardment of lutecium with 19-Mev deuterons and 10-Mev protons from the 60-inch Crocker Laboratory cyclotron.

The lutecium used for bombardment was Johnson and Matthey's "Specpure" oxide, prepared by Professor Marsh of Oxford University and purified in this laboratory by ion-exchange resin column separation. Spectroscopic analysis[1] showed absence of yttrium and rare earth contamination. The oxide, with sodium silicate as a binder, was bombarded on a platinum interceptor target placed in the cyclotron beam. After bombardment, the target material was dissolved in boiling, concentrated nitric acid and the insoluble silica residue discarded. After addition of a few milligrams of hafnium carrier, the hot solution was adjusted to $3N$ in nitric acid and the lutecium precipitated by addition of hydrofluoric acid. After centrifuging, the filtrate containing hafnium was scavenged repeatedly by addition of lanthanum carrier solution in order to remove any rare earth contamination. Hold-back carriers for the various radioactivities likely to be formed from the target materials, copper, sodium silicate, etc., were added and the solution adjusted to $3N$ in both nitric and hydrofluoric acids. Excess barium nitrate solution was then added to precipitate barium hafnium fluoride. The washed precipitate was dissolved in hot $8N$ nitric acid saturated with boric acid, and the hafnium hydroxide recovered by addition of ammonium hydroxide. The hydroxide was dissolved in nitric acid, and barium hafnium fluoride reprecipitated. The precipitation of the barium metal fluoride from strongly acid solutions is specific for hafnium and zirconium.

The lutecium and hafnium were finally converted to the oxides for weighing and estimation of chemical yields.

The chemically separated hafnium has been found to contain a single radioactivity, emitting electrons and γ-radiations, which decays with a half-life of 70 ± 2 days. No evidence of zirconium contamination, or shorter-lived

activities, was seen. Standard 3-mg/cm² mica window counters filled with argon-alcohol mixture were used in the measurements. An aluminum absorption curve of an "infinitely thin" hafnium sample, mounted on thin mica, is shown in Fig. 1; the soft quantum radiation background was determined after removal of electrons by a 100-mg/cm² beryllium absorber. The lead absorption curve (Fig. 2) was measured using an unshielded counter. The radiations consist of electrons range 82±2 mg/cm² (300 kev); electromagnetic radiation of half-thicknesses 14.5±0.3-mg/cm² aluminum (8.2 kev), 100±5-mg/cm² lead (55 kev), 2.2±0.1-g/cm² lead (350 kev), and 13.3±0.2-g/cm² lead (1.5 Mev). The energies of the two soft components agree well with those to be expected for lutecium L and K x-radiation.

From the measurements, the intensity ratios of the various radiations were estimated. Corrections were made for absorption of electrons in the counter window, air gap, etc., and counting efficiencies for the 8.2-kev, 55-kev, 350-kev, and 1.5-Mev γ-rays were taken as 5 percent, 0.5 percent, 0.5 percent, and 1.5 percent, respectively. A fluorescence yield of 0.5 for L and 0.8 for K x-radiation was assumed. The fully corrected ratios obtained are:

$$e^-: L \text{ x-rays}: K \text{ x-rays}: 350\text{-kev}\gamma: 1.5\text{-Mev}\gamma = 0.1:0.1:1:0.2:0.05.$$

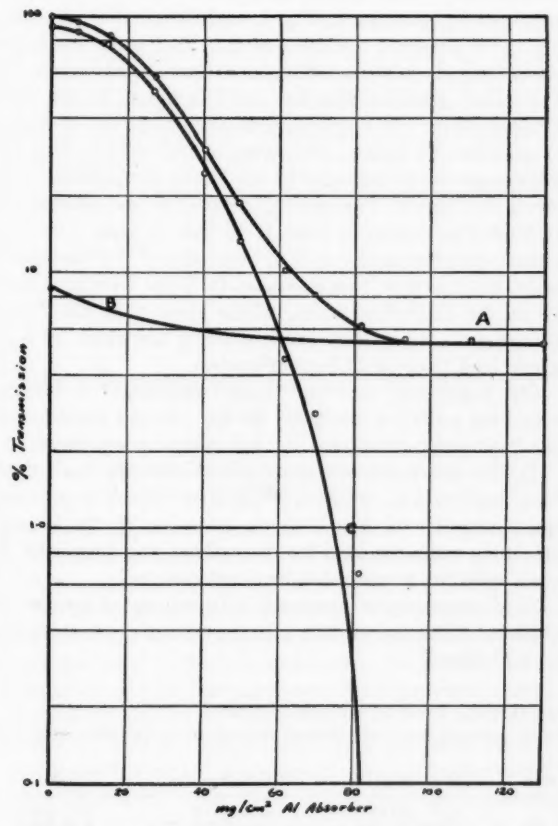

FIG. 1. Aluminum absorption of Hf^{175} radiations: Curve A is the gross absorption curve; curve B, L x-rays, K x-rays, and γ-radiation; curve C, electrons.

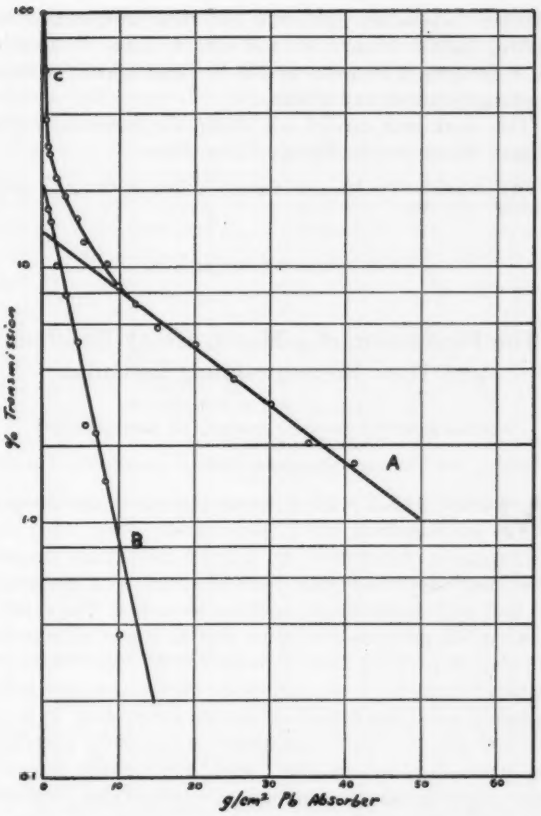

FIG. 2. Lead absorption of Hf^{175} electromagnetic radiations: Curve A represents the hard γ-radiation; Curve B, the resolved unconverted part of the 350-kev γ-ray; Curve C shows the presence of K x-rays.

While it is realized that such ratios may be in error by factors of two or more, more accurate information being difficult, if not impossible, to obtain by the simple counting techniques used, it seems justifiable to attempt to estimate the radiations arising from one disintegration, in order to allow calculation of cross sections of reactions producing the isotope. The isotope thus probably decays by electron capture, mainly to the ground state, and also to two or more excited or metastable levels. The transition from the lower excited state is accompanied by conversion, the coefficient for which is 0.4. The measured energies of the conversion electrons agree with K shell conversion. It is assumed that about 0.1 of the observed K x-rays arise from conversion, and, accordingly, one disintegration by orbital electron capture is represented by 0.9 K quanta corrected for counting efficiency, etc. Using this value, the measured chemical yields, and bombardment data from the cyclotron instruments, the cross sections for the formation of the isotope were calculated. For 10-Mev protons and 19-Mev deuterons on natural lutecium, the cross sections are, respectively, 3×10^{-2} barn and 5×10^{-2} barn. These values are reasonable for the p,n and $d,2n$ reactions, and agree with other measurements for similar reactions in this region.

The new isotope is allocated to mass 175.

We are greatly indebted to Dr. J. G. Hamilton, Mr. T. Putnam, Mr. B. Rossi, and the crew of the 60-inch

Crocker Laboratory cyclotron for their cooperation in making bombardments; we also wish to thank Professors G. T. Seaborg, I. Perlman, and B. B. Cunningham for their continued interest and advice.

This work was carried out under the auspices of the United States Atomic Energy Commision.

[1] We are indebted to Mr. J. G. Conway of this laboratory for spectroscopic analyses.

The Penetration of μ-Meson Decay Electrons and Their Bremsstrahlung Radiation

E. P. Hincks and B. Pontecorvo
National Research Council of Canada, Chalk River Laboratory, Chalk River, Ontario, Canada
January 3, 1949

MEASUREMENTS of the penetration of the charged particles from the 2.2-μsec. meson decay using the arrangement of counters and delayed coincidence circuits previously described[1] have been extended with absorbers of lead and aluminum, in addition to carbon. The results confirm our previous conclusion that at least a substantial number of particles have an energy >25 Mev. Although detailed analysis of the absorption curves does not seem justified, a soft and a hard component are evident. In lead, for example, the "soft" component is essentially absorbed by about 20 g/cm², and the "hard" one is easily detected after 38 g/cm², where its intensity (~1 count/day) is about ten times the casual rate.

While our results will be published in full later, we report here an investigation of the "hard component." First, the arrangement of Fig. 1 was used to determine whether or not the "hard component" is composed of penetrating charged particles. Mesons stopped in 8.5 g/cm² of graphite are detected by the anticoincidence $(AB-C)$. If a decay particle traverses trays C, D, or E, between 1 and 6 μsec. after a meson stops, a delayed coincidence is registered which we designate as $(C)_{del}$, $(D)_{del}$, or $(E)_{del}$. Ordinary coincidence mixers detect the events* $(CD)_{del}$, $(CE)_{del}$, while delayed coincidences of greater complexity are observed by recording all delayed pulses with a ten-pen recorder.

By this technique we have observed that in a run of 103 hr. with 16.4 g/cm² of lead between both C and D, and D and E, there were 9 events of the type $(CDE-B)_{del}$, and 10 of the type $(CE-D-B)_{del}$. We expect in the same time about 8 casual $(CDE-B)_{del}$ events, but only about 0.5 casual $(CE-D-B)_{del}$ events. The experiment when repeated using a similar arrangement with 13.6 g/cm² of graphite between C and D (but lead still between D and E), gave similar results.** This demonstrates the production of a neutral radiation in the lead or carbon absorbers and indicates that most or all of the "hard component" consists, in fact, of photons from bremsstrahlung by the particles of the "soft component."

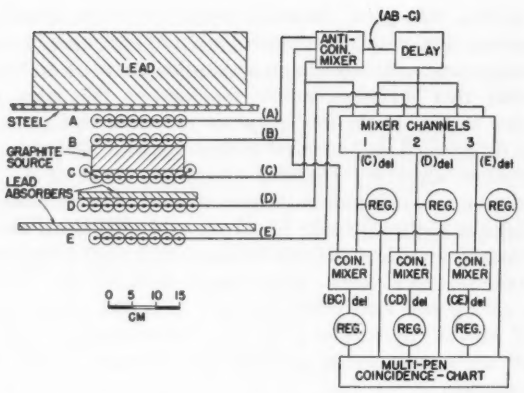

FIG. 1. Experimental arrangement for the detection of bremsstrahlung. Length of counters =40 cm.

To test further this interpretation, we have compared the intensities of production of the "hard component" in elements of different Z, *viz.* carbon and lead. The counter arrangement is shown in Fig. 2, and the circuits are as in Fig. 1. A constant thickness of lead (8.2 g/cm²) is kept above tray E, while an 8.2-g/cm² lead absorber and an 11.0-g/cm² graphite absorber are alternated in the two arrangements: (I), C–graphite–D–lead, and (II), C–lead–D–graphite, as shown. The rates $(CE-D-B)_{del}$, taken as a measure of the intensity of the "hard component," are given in Table I. The ratio (2.8±0.9) of the number of $(CE-D-B)_{del}$ counts in Case II to that in Case I is consistent with the ratio 2 to 3 to be expected*** if the effect is due to radiation from electrons. In Table I we have also given the $(CD-B)_{del}$ rates, which show that the "soft component" is, in fact, more strongly absorbed by 8.2-g/cm² lead than by 11.0-g/cm² carbon.

Our conclusion that the "hard component" is bremsstrahlung radiation produced by the charged particles of the "soft component" has the following consequences:

(1) The charged particles are indeed electrons, for if they were heavier (2 m_e or more) it would be difficult to account quantitatively for the absolute intensity of the bremsstrahlung radiation, and for the ratio of the intensities of such radiation produced in lead and carbon.

(2) Comparison of measured with calculated intensities of bremsstrahlung indicates that the *average* electron energy is >25 Mev;

TABLE I. Results obtained with the two arrangements of Fig. 2 (corrected for casual events).

Absorber between trays C and D	Absorber between trays D and E	Hours of observation	$(CE-D-B)_{del}$/hr.	$(CDE-B)_{del}$/hr.	$(CD-B)_{del}$/hr.
None	None	47	0.11 ±0.05	1.8 ±0.2	5.7 ±0.4
I.—Carbon (11.0 g/cm²)	Lead (8.2+8.2 g/cm²)	392	0.046±0.013	0.02±0.02	1.50±0.07
II.—Lead (8.2 g/cm²)	Carbon (11.0 g/cm²) +lead (8.2 g/cm²)	392	0.13±0.02	0.01±0.02	1.02±0.06

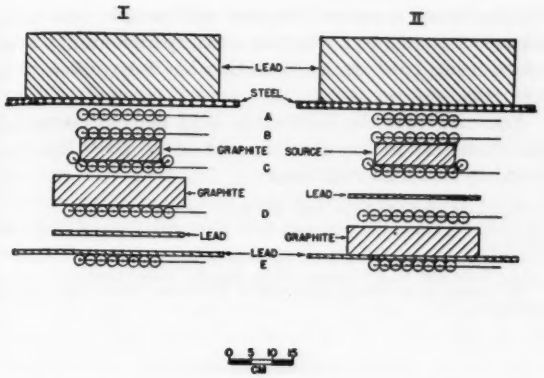

FIG. 2. Two arrangements which were alternated to compare production of bremsstrahlung in carbon (I) and lead (II). For the circuits see Fig. 1.

(3) The presence of bremsstrahlung adds to the difficulties of determining the *maximum* electron energy from absorption measurements;[1] it is clear, however, that to interpret our absorption curves, as well as Steinberger's, there is no need to invoke the presence of electrons of energy >50 Mev.

* The events $(BC)_{del}$ are also recorded and used to cancel some of the *chance* delayed events. Thus if $(CD)_{del}$, $(CE)_{del}$, etc., are accompanied by a discharge of B, they are disregarded: hence the appearance of $-B$ in all the significant rates.

** See also the rates $(CE\text{–}D\text{–}B)_{del}$ and $(CED\text{–}B)_{del}$ in the next experiment (Table I).

*** We have computed the total energy loss by radiation of electrons in the lead and carbon absorbers, as well as the "background" value (constant in both arrangements) of the energy radiated in the brass counter walls of tray C and in the carbon source itself. Assuming that the efficiency of tray E (together with the lead above it) for detecting a photon is proportional to the energy of the photon, the ratio of the $(CE\text{–}D\text{–}B)_{del}$ rates will be approximately equal to the ratio of the total energies radiated in the two cases.

[1] E. P. Hincks and B. Pontecorvo, Phys. Rev. **74**, 697 (1948); for a similar experiment see J. Steinberger, Phys. Rev. **74**, 500 (1948).

Nuclear Gyromagnetic Ratios of Be^9, Rb^{85}, Rb^{87}, and Cs^{133}

JOHN R. ZIMMERMAN* AND DUDLEY WILLIAMS
The Ohio State University, Columbus, Ohio
December 24, 1948

USING the super-regenerative oscillator techniques described in recent notes,[1] we have observed magnetic resonance absorption by the nuclei Be^9, Rb^{85}, Rb^{87}, and Cs^{133} in aqueous solutions of salts. Preliminary results for the gyromagnetic ratios and magnetic moments of these nuclei are listed in Table I and within our present limits of accuracy are in fair agreement with previous results obtained by molecular beam methods.[2–4] It should be pointed out that our preliminary values are based on flux meter measurements of the magnetic fields; the flux meter was calibrated in terms of the proton resonance and we believe the values listed in Table I are accurate to one part in 300. In every case the observed resonance peak was considerably narrower than the corresponding peak obtained in molecular beam experiments. We plan to attempt to improve the accuracy of our results by making simultaneous measurements of the resonance frequency for each nuclear species and the resonance frequency for the proton in the same magnetic field.

One or two remarks about the observed resonance peaks may be in order. The Be^9 peak as observed for a solution of $BeCl_2$ is quite strong, and no difficulties are anticipated in making the proposed direct comparison with the proton peak. An interesting result of our studies of rubidium is that the intensity of the peak observed for the less abundant isotope Rb^{87} is greater than that of the peak observed for the more abundant isotope Rb^{85}. The peak observed for Cs^{133} was weak, and considerable difficulty is anticipated in making the direct comparison with the proton peak.

TABLE I. Preliminary results for gyromagnetic ratios and magnetic moments.

Nucleus	Gyromagnetic ratio g	Spin	Magnetic moment μ
Be^9	0.783	—	—
Rb^{85}	0.536	5/2	1.34
Rb^{87}	1.83	3/2	2.74
Cs^{133}	0.734	7/2	2.57

The work reported here was made possible by research grants from the Ohio State University Development Fund and from the Graduate School.

* Charles A. Coffin Fellow, General Electric Company.

[1] J. R. Zimmerman and D. Williams, Phys. Rev. **74**, 1885 (1948), and **75**, 198 (1949).
[2] P. Kusch, S. Millman, and I. I. Rabi, Phys. Rev. **55**, 666 (1939).
[3] P. Kusch and S. Millman, Phys. Rev. **56**, 527 (1939).
[4] P. Kusch, S. Millman, and I. I. Rabi, Phys. Rev. **55**, 1176 (1939).

The Chain $_{56}Ba^{130}(n,\gamma)_{56}Ba^{131}\rightarrow_{55}Cs^{131}\rightarrow_{54}Xe^{131}$

L. YAFFE, M. KIRSCH, S. STANDIL, AND JEAN M. GRUNLUND
Atomic Energy Project, National Research Council of Canada, Chalk River, Ontario, Canada
December 28, 1948

THE above chain was studied by Katcoff[1] who made the mass assignment of the chain, determined the half-lives, and studied some of the radiation characteristics of the members. Fu-Chun Yu, Gideon, and Kurbatov[2] examined the disintegration schemes of the members of the decay chain. Katcoff gives the decay of Cs^{131} (10.2-day half-life) as occurring by orbital capture, without γ-ray emission. Kurbatov *et al.* find a half-life of 10 ± 0.3 days in fundamental agreement with that of Katcoff. However, they also find an intense radiation of electrons of 112 kev which were identified as conversion electrons of a 145-kev γ-ray emitted by Cs^{131} and estimate its conversion to be about 97 percent. Finkle[3] found that neither Ba^{131} nor Cs^{131} emits positrons.

During the course of irradiation of natural barium we had occasion to examine the above chain. The barium was removed from the cesium by five carbonate precipitations

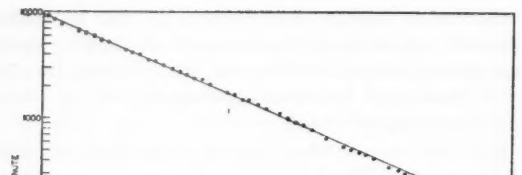

FIG. 1. Decay curve Cs^{131}.

using cesium and barium carriers. The cesium was then separated as the perchlorate and exhaustively purified.

The half-life was measured over a period of six half-lives and found to be 9.6 ± 0.1 days by the method of least squares. The decay curve is shown in Fig. 1. We find, in great abundance, a soft radiation which may be ascribed to the conversion electrons found by Kurbatov *et al.* An absorption curve in aluminum is shown in Fig. 2. This consists of two components, the softer of which is replotted on a larger scale. Assuming that the softer radiation may be treated as though it were similar to a continuous spectrum of β^--radiation, the energy has been determined by back-scattering[4] and found to be 115 kev. The harder component has a half-thickness of 700 mg/cm² and is identical with the 31-kev x-ray found by Katcoff.

If P = the number Ba^{130} atoms irradiated, Q = the number Ba^{131} atoms formed, R = the number Cs^{131} atoms formed, σ = the cross section of Ba^{130} for capture, ρv = neutron flux, t = duration of irradiation, and λ and λ' are the disintegration constants for Ba^{131} and Cs^{131}, respectively, then

$$\sigma=\frac{R}{\rho v P[[(1-e^{-\lambda' t})/\lambda']-[(e^{-\lambda t}-e^{-\lambda' t})/(\lambda'-\lambda)]]}.$$

The Cs^{131} activity obtained was corrected for decay elapsing between removal of the sample from the pile and chemical separation, time elapsing between chemical separation and measurement, chemical recovery, counter efficiency, absorption in sample, in counter window and in air gap between counter window and sample, and back-scattering from tray. The flux was experimentally determined using La^{139}. Its cross section has been taken to be 8.4 barns.[5]

Assuming that the Cs^{131} γ-ray is 97 percent converted, the cross section for neutron capture of Ba^{130} has been found to be 24 ± 8 millibarns.

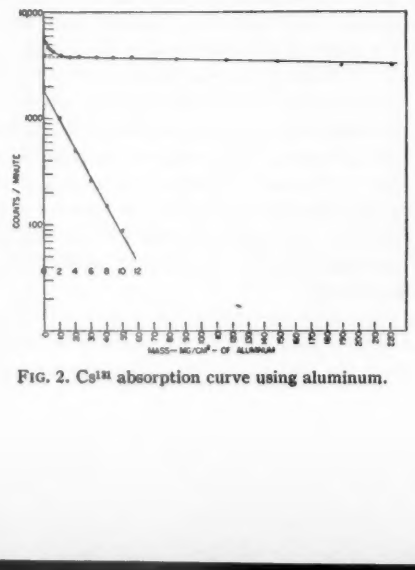

FIG. 2. Cs^{131} absorption curve using aluminum.

[1] Seymour Katcoff, Phys. Rev. **72**, 1160 (1947).
[2] Fu-Chen Yu, D. Gideon, and J. D. Kurbatov, Phys. Rev. **71**, 382 (1947).
[3] Bernard Finkle, Phys. Rev. **72**, 1260 (1947).
[4] L. Yaffe and K. M. Justus, Phys. Rev. **73**, 1400 (1948).
[5] L. Seren, H. N. Friedlander, and S. H. Turkel, Phys. Rev. **72**, 888 (1947).

Table of Interplanar Spacings for Different Target Materials for the Back Reflection Region

SUZANNE VAN DIJKE BEATTY
Westinghouse Research Laboratories, East Pittsburgh, Pennsylvania
January 3, 1949

A TABLE has been computed to expedite the reduction of diffraction patterns obtained in the back reflection region and may be considered a continuation of Research Report R-94602-10-C.

The table gives d values for Mo, Cu, Co, Fe, and Cr targets for every tenth of a degree in 2θ, or five hundredths of θ, to four and five significant figures. The values of the interplanar spacings, d, are computed from the Bragg equation: $n\lambda=2d\sin\theta$ where θ is the glancing angle, λ the wave-length of the diffracted target radiation, and n is taken as unity. The table is computed in angstrom units for the $K\alpha_1$ radiation and factors are given for converting these spacings to those for $K\alpha_2$ and $K\alpha$. Conversion curves from $K\alpha_1$ to kx units are also given for all five target materials over the angular range.

The tables may be obtained directly from the author.

On Mesons π and μ

R. E. MARSHAK
University of Rochester, Rochester, New York
December 23, 1948

SEVERAL papers have recently appeared[1–3] which raise certain doubts about the two-meson hypothesis proposed by the author[4] in order to explain the contradictory behavior of high altitude and sea-level mesons. It seems worth while to clarify the fundamental ideas of the two-meson theory and to discuss briefly its status in the light of the latest experimental results.

The two-meson hypothesis stated: (1) the mesons produced with large cross section at high altitudes are different from the majority of weakly interacting sea-level mesons, (2) the high altitude mesons are strongly coupled to

nucleons, whereas the sea-level mesons are the decay products of the high altitude mesons, (3) a weak coupling of sea-level mesons to nucleons follows from (2). It was not possible to make unique assignments for the spins and masses of the two types of mesons.

The striking experimental discoveries of Powell and his collaborators[5] and the Berkeley group[6] have provided complete confirmation of points (1) and (2). Thus, it is now established that the π-mesons are produced directly in the Berkeley cyclotron and in cosmic-ray stars while the μ-mesons arise indirectly from the decay of the π-mesons. It is furthermore established that π^--mesons are captured by light as well as heavy nuclei in contrast to the μ^--mesons which are only captured by heavy nuclei. These results are contrary to the cloud-chamber evidence[1] for the direct production of μ-mesons and it is likely that visual methods for estimating ionization are not sufficiently accurate to distinguish between π- and μ-mesons.

Definite support for point (3) is provided by the measured value of the half-life for the π–μ-decay, i.e. $0.9^{+0.25}_{-0.15}\cdot 10^{-8}$ sec.,[7] and the fact that nuclear capture of π^- converts an appreciable fraction of its rest energy into star energy,[8] whereas nuclear capture of μ^- converts a negligible fraction of its rest mass into star energy.[8] Both of these facts can be understood on the basis of (3) and assuming that the π-meson is a boson; thus, the scheme for the nuclear capture of μ^- becomes: $\mu^-+P\rightarrow\pi^-+Q+P\rightarrow N+Q$ where P and N are the proton and neutron in the nucleus and Q is the second particle into which the π-meson decays, i.e. $\pi\rightarrow\mu+Q$. The predicted half-life[2,9] for the π–μ-decay agrees well with the measured value considering the uncertainty of the nuclear matrix element. Our original calculation[4] for the half-life treated the π-meson as a fermion for the purposes of illustration; the value of 10^{-8} sec. obtained demonstrates the insensitivity of the half-life to the spin character of the π-meson.

An alternative interpretation of the half-life for π–μ-decay and of the qualitative features of the nuclear capture of negative π- and μ-mesons has been suggested:[2,9] One postulates a direct (weak) coupling between the μ-meson and nucleon and a direct (strong) coupling between the π-meson and nucleon and one *deduces* the π–μ-decay. This is a possible approach but against it two objections may be raised: (1) the calculation of the indirect decay of the π-meson through the virtual creation of nucleons leads to divergence difficulties and (2) the rough quantitative agreement found between the coupling constant for the μ-meson and the nucleon and the β-constant may not be significant in view of the uncertain status of β-decay theory.[10]

Additional experiments have fixed some of the other unknowns in the two-meson theory. The determination[7] of the ratio of masses of the π- and μ-mesons as 1.321 ± 0.006 and the absence of γ-rays[11] associated with the nuclear capture of μ^- prove that the particle Q is a neutrino. Consequently, the μ-meson is a fermion and must possess[12] spin $\frac{1}{2}$. This value of the spin is consistent with the apparently continuous electron spectrum from the μ-decay. The spin of the π-meson is still uncertain.

Major difficulties remain: the possibility of correlating nuclear β-decay with an electron decay of the π-meson appears to be excluded,[6] and it is not at all clear that a correct field theory of nuclear forces can be constructed with only one strongly coupled meson.[4]

[1] G. D. Rochester and C. C. Butler, Proc. Phys. Soc. 61, 307 (1948).
[2] S. Hayakawa, Prog. Theor. Phys. 3, 200 (1948).
[3] J. Tiomno and J. A. Wheeler, Rev. Mod. Phys. 20 (January, 1949, to be published).
[4] R. E. Marshak and H. A. Bethe, Phys. Rev. 72, 506 (1947). S. Sakata and T. Inoue (Prog. Theor. Phys. 1, 143 (1946)) and T. Tanikawa (Prog. Theor. Phys. 2, 220 (1947)) independently introduced a two-meson hypothesis in order to remove the difficulties associated with the electron decay of the meson and its small nuclear scattering; they arrived at a half-life for the decay of the heavy into the light meson many orders of magnitude too small.
[5] G. P. S. Occhialini and C. F. Powell, Nature 162, 168 (1948) and Camerini, Muirhead, Powell, and Ritson, Nature 162, 433 (1948).
[6] E. Gardner and C. M. G. Lattes, Science 107, 270 (1948) and C. M. G. Lattes, Science 108, 588 (1948).
[7] R. Serber, private communication.
[8] See also Sard, Ittner, Conforto, and Crouch, Phys. Rev. 74, 97 (1948).
[9] A. S. Lodge, Nature 161, 809 (1948), L. I. Schiff, Phys. Rev. 74, 1556 (1948), R. F. Christy, private communication.
[10] R. E. Marshak, Phys. Rev. 75, 513 (1949).
[11] O. Piccioni, Phys. Rev. 74, 1236 (1948).
[12] R. F. Christy and S. Kusaka, Phys. Rev. 59, 414 (1941).

Erratum: Thermonuclear Reactions in the Expanding Universe

[Phys. Rev. 74, 1198 (1948)]

R. A. ALPHER AND R. HERMAN
Applied Physics Laboratory, The Johns Hopkins University, Silver Spring, Maryland
AND
G. A. GAMOW
The George Washington University, Washington, D. C.

IT is regretted that Eq. (3) was incorrectly given; it should read:

$$d[\ln x_2]/dt=-pm_2/x_1. \qquad (3)$$

Measurement of the Half-Life and Average Energy of Tritium Decay*

G. H. JENKS, J. A. GHORMLEY, AND F. H. SWEETON
Oak Ridge National Laboratory, Oak Ridge, Tennessee
December 29, 1948

RECENTLY, Novick[1] and Goldblatt *et al.*[2] have found the half-life period of tritium to be considerably less than the 30-year period previously accepted. We have made a determination of the half-life of tritium and obtained a value of 12.46 ± 0.2 years, in agreement with the 12.1 ± 0.5 years reported by Novick. In addition, we have measured the average energy of the tritium decay and found it to be 5.69 ± 0.06 kev.

To determine the half-life of tritium, a sample containing a measured amount of the isotope was prepared and the rate of He^3 evolution, and thus the disintegration rate, of the sample measured. The average energy of the decay was determined by calorimetric study of the quantitative sample.

In preparing the sample, several ml of a mixture of tritium and normal hydrogen were purified by passage through palladium, and the density of the mixture was then compared with that of helium by means of a gas density balance. The volume of the gas sample was then measured and the sample transferred to a Pyrex ampoule containing palladium in which the gas was absorbed. Calorimetric studies of the sample were then carried out.

In the determination of the disintegration rate, advantage was taken of the fairly rapid rate of diffusion of helium through silica glass at room temperature. Following the calorimetric measurement, the sample was converted to water by passage over hot copper oxide and collected and sealed in a small quartz ampoule. A calorimetric measurement of the heat evolved by the sample in this form showed that no significant amount of tritium was lost in the transfer. The sample was then placed in a soft glass container which was held at constant temperature and the He^3, collecting in the container during a two-week period, was measured with a McLeod gauge. These measurements were repeated at two-week intervals until the rate of collection of He^3, after correcting for decay, was constant. The rate was then assumed to be equal to the rate of He^3 formation within the ampoule. The time necessary for the steady-state pressure of He^3 to be built up within the ampoule was appreciably shortened by placing the ampoule in liquid nitrogen for several days prior to starting the measurements.

The gas density balance used in analyzing the sample was constructed of silica glass and the gas controlling system of Pyrex. All valves were of the mercury shut-off type so that no stopcock grease was in contact with the tritium. The absolute density of the tritium-hydrogen mixture was obtained by direct weighing of the reference helium.

The calorimeter was of an isothermal type operating at the temperature of liquid nitrogen and using the rate of evaporation of nitrogen at constant pressure as a measure of the heat input. Calibration of the calorimeter was made with a resistance heater.

Results of the various measurements, adjusted to a reference time, are shown below:

Fraction of tritium in H_2-T_2 mixture	0.497
Total quantity of tritium in sample	2.57_1 ml S.T.P.
Power generated by sample	$2.21_8\times10^{-4}$ watt
Disintegration rate of sample	$2.43_8\times10^{11}$ dis./sec.
Average energy of tritium decay	5.69 kev
Half-life period of tritium	12.46 years

A calorimetric measurement and a disintegration rate measurement were made on a second, smaller sample, and the average energy found in this case agreed within 0.5 percent with the value computed from the above data.

Curran, Angus, and Cockcroft[3] have recently determined the beta-spectrum of tritium from below 1 kev to its maximum, using a proportional counter. From the data presented in their paper, we have estimated the average energy of the distribution to be about 5.5 kev, which is in reasonable agreement with our figure.

An interesting phenomenon observed in the calorimetric study of tritium oxide seems worth mentioning here. The rate of heat evolution by the tritium absorbed in palladium was constant during the course of a measurement extending over a period of 8–10 hours. However, the sample of tritium in the form of the oxide showed an increase of several percent in the rate of heat evolution during the first few hours at −196°C. After the initial increase, the rate of heat evolution became constant and was then in agreement with the value obtained from the same amount of tritium absorbed in palladium. We believe this to indicate that a fraction of the decay energy is stored in the ice at −196°C. in some manner and that the amount stored reaches a steady-state value.

* This document is based on work performed under Contract Number W-7405 eng 26 for the Atomic Energy Project at Oak Ridge National Laboratory.

[1] Aaron Novick, Phys. Rev. **72**, 972 (1947).
[2] M. Goldblatt, E. S. Robinson, and R. W. Spence, Phys. Rev. **72**, 973 (1947).
[3] S. C. Curran, J. Angus, and A. L. Cockcroft, Nature **162**, 302 (1948)

Proceedings of the American Physical Society

Minutes of the Meeting of the Metropolitan Section at Columbia University, New York City on October 22, 1948

THE Fall Meeting of the Metropolitan Section of the American Physical Society was held at Columbia University. The afternoon session consisted of five invited papers on the Solid State:

Ferroelectricity in Barium Titanate. B. T. Matthias and J. N. Richardson, *Bell Telephone Laboratories, Murray Hill, New Jersey.*

Optical and X-Ray Studies of Ferroelectric Domains in Barium Titanate. Elizabeth A. Wood, *Bell Telephone Laboratories, Murray Hill, New Jersey.*

Crystal and Scintillation Counters. R. Hofstadter, *Princeton University, Princeton, New Jersey.*

Characteristics of the Transistor. J. Bardeen and W. H. Brattain, *Bell Telephone Laboratories, Murray Hill, New Jersey.*

The Martensite Reaction. A. W. McReynolds, *The Brookhaven National Laboratory, Long Island, New York.*

Dinner was held in the Columbia Men's Faculty Club. The evening session was a progress report on:

The Present Status of Electron Microscopy. James Hillier, *The Radio Corporation of America Laboratories, Princeton, New Jersey.*

W. F. C. Ferguson
Secretary

THE AMERICAN INSTITUTE OF PHYSICS

INCORPORATED

57 East 55 Street New York 22, N.Y.

MEMBER SOCIETIES:

American Physical Society
KARL K. DARROW, *Secretary*, Columbia University, New York 27, New York.

Optical Society of America
ARTHUR C. HARDY, *Secretary*, Massachusetts Institute of Technology, Cambridge 39, Massachusetts.

Acoustical Society of America
WALLACE WATERFALL, *Secretary*, 57 East 55th Street, New York 22, New York.

Society of Rheology
EARL K. FISCHER, *Secretary*, Institute of Textile Technology, Charlottesville, Virginia.

American Association of Physics Teachers
C. J. OVERBECK, *Secretary*, Northwestern University, Evanston, Illinois.

AFFILIATED SOCIETIES:

American Society for X-Ray and Electron Diffraction
Electron Microscope Society of America
Physical Society of Pittsburgh
Physics Club of Chicago
Physics Club of Philadelphia
Cleveland Physics Society
Physics Club of the Lehigh Valley

ASSOCIATES:

Over seventy-five leading industrial enterprises and other institutions which contribute to the support of the Institute.

JOURNALS:

The Physical Review
JOHN T. TATE, *Editor*, University of Minnesota, Minneapolis, Minnesota.

Reviews of Modern Physics
J. W. BUCHTA, *Editor*, University of Minnesota, Minneapolis, Minnesota.

Journal of the Optical Society of America
GEORGE R. HARRISON, *Editor*, Massachusetts Institute of Technology, Cambridge, Massachusetts.

The Journal of the Acoustical Society of America
FLOYD A. FIRESTONE, *Editor*, 3318 Fessenden Street, N.W., Washington, D. C.

American Journal of Physics
THOMAS H. OSGOOD, *Editor*, Michigan State College, East Lansing, Michigan.

The Review of Scientific Instruments
GAYLORD P. HARNWELL, *Editor*, Randal Morgan Laboratory of Physics, University of Pennsylvania, Philadelphia, Pennsylvania.

The Journal of Chemical Physics
JOSEPH E. MAYER, *Editor*, Kent Chemical Laboratory, University of Chicago, Chicago 37, Illinois.

Journal of Applied Physics
ELMER HUTCHISSON, *Editor*, Case Institute of Technology, Cleveland 6, Ohio.

Physics Today
DAVID A. KATCHER, *Editor*, American Institute of Physics, 57 East 55 Street, New York 22, New York.

OFFICERS

GEORGE R. HARRISON, *Chairman*
Massachusetts Institute of Technology
WALLACE WATERFALL, *Secretary*
The Celotex Corporation
GEORGE B. PEGRAM, *Treasurer*
Columbia University
JOHN T. TATE,
Adviser on Publications
University of Minnesota

GOVERNING BOARD

LUIS W. ALVAREZ
ROBERT B. BRODE
E. U. CONDON
A. J. DEMPSTER
W. F. FAIR, JR.
HARVEY FLETCHER
R. C. GIBBS
GEORGE R. HARRISON
W. V. HOUSTON
PAUL E. KLOPSTEG
F. W. LOOMIS
PHILIP M. MORSE
GEORGE B. PEGRAM
A. H. PFUND (*deceased*)
JOHN T. TATE
WALLACE WATERFALL
M. W. WHITE
A. G. WORTHING

Consultant on Printing
MELVIN LOOS

ADMINISTRATIVE STAFF

HENRY A. BARTON, *Director*
CLEVELAND NORCROSS,
General Manager
THEODORE VORBURGER,
Business Manager
RUTH F. BEVANS,
Publication Manager
BETTY HOFSTADTER, *Office Manager*
EILEEN B. NEUBERGER,
Circulation Manager

THE American Institute of Physics was founded in 1931 as a federation of leading societies in the field of Physics. It combines into one operating agency those functions on behalf of physics which can best be done by the Societies jointly. Its purpose is the advancement and diffusion of physics and its applications to human welfare. To this end it publishes for itself or the Societies the nine journals listed on this page; promotes unity and effectiveness of effort among all who are interested in physics; renders numerous direct services to physicists and to the public; and cooperates with government agencies, national associations, educational institutions, technical industries, and others in such manner as to realize the opportunities and fulfill the responsibilities of physics as an important and constructive human activity.

CONTENTS

THE PHYSICAL REVIEW — SECOND SERIES, VOL. 75, NO. 4 — FEBRUARY 15, 1949

Relative Cross Sections for Nuclear Reactions Induced by High Energy Neutrons in Light Elements . . . . . WILLIAM J. KNOX 537

Thresholds for Several Photo-Nuclear Reactions . . . . . J. MCELHINNEY, A. O. HANSON, R. A. BECKER, R. B. DUFFIELD, AND R. C. TEPPER 542

Neutron-Proton Scattering at 90 Mev . . . . . KEITH BRUECKNER, WALTER HAVENSON, EVANS HAYWARD, AND WILSON M. POWELL 555

Magnetic Refraction of Neutrons at Domain Boundaries . . . . . D. J. HUGHES, M. T. BURGY, R. B. HELLER, AND J. W. WALLACE 563

Electron-Neutrino Angular Correlation in the Beta-Decay of He^6 . . . . . JAMES S. ALLEN, H. R. PANETH, AND A. H. MORRISH 570

Spin Dependence of Slow Neutron Scattering by Deuterons . . . . . E. FERMI AND L. MARSHALL 578

Mixed Cosmic-Ray Showers at Sea Level . . . . . C. Y. CHAO 581

East-West Asymmetry and Latitude Effect of Cosmic Rays at Altitudes up to 33,000 Feet . . . . . W. C. BARBER 590

On the Magnetic Moments of Cl^{35}, F^{19}, Tl^{205}, and Tl^{203} . . . . . H. L. POSS 600

Magnetic Moments of Sunspots . . . . . JAMES W. BROXON 606

Relation of the Cosmic Radiation to Sunspot Magnetic Moments . . . . . JAMES W. BROXON 612

Radioactivities of Some High Mass Isotopes of Cobalt . . . . . THOMAS J. PARMLEY, BURTON J. MOYER, AND ROBERT C. LILLY 619

Quantitative Measurements with Scintillation Counters . . . . . HARTMUT KALLMANN 623

Change in Density of Potassium Chloride Crystals upon Irradiation with X-Rays . . . . . I. ESTERMANN, W. J. LEIVO, AND O. STERN 627

Study of the High Frequency Fundamental Bands in the Spectrum of AsH_3 and AsD_3 . . . . . VIRGINIA MARIE MCCONAGHIE AND HARALD H. NIELSEN 633

Infra-Red Bands in the Spectrum of Difluoromethane . . . . . HUGH B. STEWART AND HARALD H. NIELSEN 640

Quantum Electrodynamics. II. Vacuum Polarization and Self-Energy . . . . . JULIAN SCHWINGER 651

Non-Linear Field Theories . . . . . PETER G. BERGMANN 680

Letters to the Editor:

Emissions of Mesons in Cosmic Stars in Photographic Emulsions . . . . . ERIC PICKUP AND ADAIR MORRISON 686

Dielectric Behavior of $BaTiO_3$ Single-Domain Crystals . . . . . WALTER J. MERZ 687

Neutrons from Deuteron Bombardment of Li^9 . . . . . WARD WHALING, J. E. EVANS, AND T. W. BONNER 688

Note on East-West Effect . . . . . A. T. BIEHL, H. V. NEHER, AND WILLIAM C. ROESCH 688

Double-Surface Transistor . . . . . JOHN N. SHIVE 689

Investigation of Hole Injection in Transistor Action . . . . . J. P. HAYNES AND W. SHOCKLEY 691

Quantitative Predictions from Dislocation Models of Crystal Grain Boundaries . . . . . W. SHOCKLEY AND W. T. READ 692

On the Showers of Mesons and Nucleons . . . . . G. WATAGHIN 693

Isotopic Constitution of Dysprosium . . . . . MARK G. INGHRAM, RICHARD J. HAYDEN, AND DAVID C. HESS, JR. 693

Vertical Intensity at 10,000 Feet of Ionizing Particles that Produce Penetrating Showers . . . . . W. E. HAZEN, C. A. RANDALL, AND O. L. TIFFANY 694

On Electromagnetic Diffraction through a Plane Screen . . . . . JOHN W. MILES 695

Hf^{175}, a New Radioactive Isotope of Hafnium . . . . GEOFFREY WILKINSON AND HARRY G. HICKS 696

Penetration of μ-Meson Decay Electrons and Their Bremsstrahlung Radiation . . . . . E. P. HINCKS AND B. PONTECORVO 696

Nuclear Gyromagnetic Ratios of Be^7, Rb^{85}, Rb^{87}, and Cs^{133} . . . . . JOHN R. ZIMMERMAN AND DUDLEY WILLIAMS 699

Chain $_4Be^{139}(n,\gamma)_4Be^{140}\rightarrow{}_{-1}Cs^{140}\rightarrow{}_{58}X^{140}$ . . . . . L. YAFFE, M. KIRSCH, S. STANDIL, AND JEAN M. GRETHLUND 699

Table of Interplanar Spacings for Different Target Materials for the Back Reflection Region . . . . . SUZANNE VAN DIJKE BEATTY 700

On Meson ν and μ . . . . . R. B. MARSHAK 700

Erratum: Thermonuclear Reactions in the Expanding Universe . . . . . R. A. ALPHER, R. HERMAN, AND G. A. GAMOW 701

Measurement of the Half-Life and Average Energy of Tritium Decay . . . . . G. H. JENKS, J. A. GHORMLEY, AND F. H. SWERTON 701

Proceedings of the American Physical Society:

Minutes of the Meeting of the Metropolitan Section at Columbia University, New York City, October 22, 1948 703

LANCASTER PRESS, INC., LANCASTER, PA.